# University of Southampton

Faculty of Social, Human and Mathematical Sciences

Mathematical Sciences


# Multiscale modelling and experimental estimation of liquid crystals parameters


by

**Thomas Paul Bennett**


Thesis submitted for the degree Doctor of Philosophy

July 2016

UNIVERSITY OF SOUTHAMPTON

ABSTRACT

Faculty of Social, Human and Mathematical Sciences

Mathematical Sciences

# Multiscale modelling and experimental estimation of liquid crystals parameters

by Thomas Paul Bennett

In this thesis we investigate two problems: the measurement of nematic liquid crystal material parameters and the modelling of liquid crystal colloids. Specifically we have developed an optical method of measuring liquid crystal viscosities, and by combining multiple measurements of the transmitted intensity we can measure the variations in boundary pre-tilt and cell thickness across a planar cell. We find that it is possible to measure the rotational viscosity $\gamma_1$ using an amplitude modulated driving potential. This method allows us to probe the dynamics of a nematic liquid crystal across a range of frequencies. In addition we are able to recover the combination of viscosity coefficients $\alpha_4 + \alpha_5$ from high voltage high frequency measurements. The model of a nematic colloid that we have developed is based on the asymptotic homogenisation of a $\mathcal{Q}$-tensor model. These colloidal systems are inherently difficult to model as they contain a large range of physically relevant length-scales. The dopant particles disturb the alignment of the nematic locally and complicate the interaction with externally imposed fields. On the macro-scale both the dopant and nematic realign across a length scale of several microns. By using homogenisation we have derived a set of coupled equations for the evolution of the nematic and dopant alignment. The system consists of a set of cell problems solved on the micro-scale which determine effective material parameters and a set of macroscopic equations in which the influence of the dopant is confined contain to effective material parameters. The theory we obtain is accurate for rather arbitrarily shaped metallic dopants. In particular we are able to directly link the geometry, volume concentration and material parameters of the dopants to the behaviour of the macroscopic system.

# Contents

# List of Figures

# List of Tables

# Declaration of authorship

I, **Thomas Paul Bennett** declare that this thesis entitled **Multiscale modelling and experimental estimation of liquid crystal parameters** and the work presented in it are my own and has been generated by me as the result of my own original research.

I confirm that:

1. This work was done wholly or mainly while in candidature for a research degree at this University;
2. Where any part of this thesis has previously been submitted for a degree or any other qualification at this University or any other institution, this has been clearly stated;
3. Where I have consulted the published work of others, this is always clearly attributed;
4. Where I have quoted from the work of others, the source is always given. With the exception of such quotations, this thesis is entirely my own work;
5. I have acknowledged all main sources of help;
6. Where the thesis is based on work done by myself jointly with others, I have made clear exactly what was done by others and what I have contributed myself;
7. Parts of this work have been published as journal papers and conference proceedings [11, 13] and submitted as a journal paper [12].

**Signed:**

**Date:**

# Record of work

## Chapter 1

Chapter 1 is an introduction to liquid crystal modelling and contains no original work.

## Chapter 2

Chapter 2 sections 2.1 to 2.3 review existing measurement methods. Original work is presented in the remainder of the chapter. Original work is contained in sections 2.4, 2.5 and 2.6. The experimental results analysed in 2.4 were obtained by Dr. M. Proctor, experimental results analysed in 2.5 were obtained by Master students Matthew Sugden and Roger Kirke under the supervision of Dr. M. Proctor. In each section my contribution was to perform theoretical analysis. In particular this involved writing Matlab code to model the experimental system and to process and fit to experimental results under the supervision of Dr. G. D'Alessandro and Prof M. Kaczmarek. Additionally the statistical method developed in 2.5 was developed with the help of Prof. J. Forster. Results from chapter 2 will be submitted to Physical Review Applied.

## Chapter 3

Sections 3.1 and 3.2 contain a literature review. Original work is contained in 3.3 which is based on the work published in [11]. My contribution was to: write Matlab code which solved the homogenised equations, develop Comsol models to model the microscopic problem and cell problems and derived the homogenised equations with the help of Dr. K. Daly. The Matlab code I developed was based upon code previously written by Dr. K. Daly. This work was supervised by Dr. K. Daly and Dr. G. D'Alessandro.

## Chapter 4

Section 4.1 contains an example problem inspired by literature. My contribution to the original work in 4.2 was to: write Matlab code, develop a Comsol model and derive the homogenised equation. The results in this chapter have been submitted to the SIAM journal on applied mathematics. This work was supervised by Dr. K. Daly and Dr. G. D'Alessandro.

# Acknowledgements

I would like to thank my supervisors; Dr Giampaolo D'Alessandro, Professor Malgosia Kaczmarek and Dr Keith Daly for giving me the opportunity to study applied mathematics, for their help and guidance throughout my studies and for many interesting discussions.

I would also like to thank Dr Matthew Proctor for performing the experiments analysed in this thesis.

# Chapter 1

# Introduction

Nematic liquid crystals consist of elongated organic molecules which are arranged with a degree of orientational order but without translational order. This combination produces many interesting and useful physical effects. As the constituent molecules are free to move, liquid crystals flow. This in conjunction with orientational ordering produces a viscous birefringent fluid in which flow and reorientation are tightly coupled. When doped with small nano-to-micrometer size particles the local alignment is disturbed. This further complicates the behaviour and description of the system. Liquid crystals are clearly not easy systems to model and the remainder of this chapter contains background material including a brief introduction to Ericksen-Leslie theory, $\mathcal{Q}$-tensor modelling and optics.

This thesis is primarily concerned with two problems: measuring nematic liquid crystal material parameters and obtaining a macroscopic description of a liquid crystal colloid. Although these problems are seemingly different in nature they do both involve the determination of material parameters, for a pure or doped liquid crystal respectively. This is achieved by analysing experimental data in the former case or through theoretical means in the latter. Estimation of material parameters through experimental data is discussed in chapter 2, while the theoretical model of a colloid is the focus of chapters 3 and 4. More specifically, in chapter 2 we review existing methods of measuring the nematic viscosities and report a new optical method of measuring liquid crystal viscosities using a time varying electric field. We find that it is possible to extract information about both the dynamic viscous behaviour of the system and the elastic behaviour of a liquid crystal by optical means. Chapters 3 and 4 are devoted to the use of mathematical homogenisation to study liquid crystal colloids. In chapter 3 we use homogenisation to obtain the macroscopic response of a nematic liquid crystal containing stationary obstruction of arbitrary shape. We obtain excellent agreement with large-scale finite element simulations. In chapter 4 we extend the model to include rotating obstructions and derive equations that capture

the competing torques on the dopant and nematic. We identify and interpret the various interactions and validate our model against finite element simulations. We summarise our findings in chapter 5 and discuss possible future work for each project.

## 1.1 Describing liquid crystals

Different phases of matter possess different symmetries or equivalently different degrees of order. For instance the atoms in a crystalline solid form a periodic array. This degree of translational and orientational ordering can be identified with a broken symmetry. In this case the symmetry of the Euclidean group is broken by the lattice and only a small subset of possible rotations and translations remains. In general the nature of the broken symmetries determine the type of order parameter. While the order parameter itself encodes the information needed to define the state of the system. For instance to describe a phase with broken orientational symmetry you must at least specify the preferred alignment axes.

The melting transition from a well ordered solid phase to an isotropic fluid phase involves gaining symmetry or equivalently losing order. Certain compounds formed of elongated organic molecules do not show a single melting transition [36]. Instead there exists a temperature window which hosts a variety of phases possessing different symmetries that go under the generic name of liquid crystal (LC) phases, as they have properties intermediate between these two states of matter. These phases possess some of the orientational or positional order of an ordered solid. For example, in a smectic liquid crystal the molecules align along a common direction and form well defined layers. This breaks both part of the translational and orientational symmetry of the isotropic phase and as a result the LC phase has properties characteristic of both a liquid and a crystal. This thesis is concerned with the the non-chiral nematic mesophase, referred to as the nematic phase throughout the remainder of this thesis. Nematic liquid crystals possess only broken rotational symmetry aligning along a spontaneously chosen axis. The centres of mass of the constituent molecules are uncorrelated.

Nematic liquid crystals are characterised by having both the dynamic properties of a fluid, they may be sheared and flow in response to applied stress, and the optical and dielectric properties of a crystalline solid. These properties can be seen to result from the symmetry of the phase. Within the bulk of a nematic liquid crystal the position of the constituent molecules is uncorrelated. However, they align their molecular axis with one another on average. The transition from isotropic fluid to nematic is illustrated in figure 1.1. The full rotational symmetry of the isotropic phase is broken by the transition

into the nematic. This broken symmetry and the resulting anisotropic properties of the nematic phase are responsible for the usefulness of this phase. The director field describes the degree of freedom associated with the broken orientational symmetry. We now discuss in detail the order present within the nematic phase and how it may be described theoretically.

In the absence of external influences a nematic liquid crystal will align into a uniform configuration possessing uniaxial order [64]. Under uniaxial order only a single preferred alignment axis exists, the principal axis or anisotropic axis [110]. The orientation of this axis is often described by a unit vector field $\hat{\boldsymbol{n}}$ called the director [36, 110]. The constituent molecules align their long axis on average with $\hat{\boldsymbol{n}}$ with non-polar order. Non polar order is achieved either because the constituent molecules are non-polar themselves, molecular heads and tails are indistinguishable, or they arrange themselves with an equal number of heads and tails pointing in either direction along $\hat{\boldsymbol{n}}$. As a result both $\hat{\boldsymbol{n}}$ and $-\hat{\boldsymbol{n}}$ represent the same physical state. In a thermotropic liquid crystal the degree of orientational order is temperature dependent, characterised by a scalar order parameter. The interpretation of the scalar order parameter is illustrated in figure 1.2: it measures the width of the angular distribution of molecular axis about the principal axis. For a uniaxial nematic the distribution of molecules about the preferred alignment axis is rotationally symmetric. In a biaxial phase this symmetry is broken and a second principal axis emerges. The degree of ordering along the second principal axis is characterised by the biaxiality parameter. In general the orientational order of a nematic is uniaxial [64], with biaxiality generally confined to the cores of topological defects [97].

Although the director description is widely used there does exists a more complete description of the liquid crystal phase. This can be achieved by combining the two broken symmetries, the principal and secondary axis, with the degree of ordering along each axis. The result is a tensor order parameter, the $\mathcal{Q}$-tensor. In this description the first and second principal axis and order parameters are encoded into a single construct, a traceless symmetric $3 \times 3$ tensor. The $\mathcal{Q}$-tensor is given by [99]

$$\tilde{\mathcal{Q}} = \sqrt{\frac{3}{2}}\tilde{S}\left(\hat{\boldsymbol{n}} \otimes \hat{\boldsymbol{n}} - \frac{1}{3}\mathcal{I}\right) + \sqrt{\frac{3}{2}}\tilde{\beta}\left(\hat{\boldsymbol{l}} \otimes \hat{\boldsymbol{l}} - \hat{\boldsymbol{m}} \otimes \hat{\boldsymbol{m}}\right), \tag{1.1}$$

where $\hat{\boldsymbol{n}}$ is the director, $\hat{\boldsymbol{l}}$ is the biaxial axis and $\hat{\boldsymbol{m}} = \boldsymbol{n} \times \boldsymbol{l}$, the parameters $\tilde{S}$ and $\tilde{\beta}$ measure the scalar and biaxial order respectively. The $\sqrt{3/2}$ factor is present to ensure that in the uniaxial state $\mathrm{Tr}(\tilde{\mathcal{Q}}^2) = \tilde{S}^2$. The eigenvalues of $\mathcal{Q}$ encode information about the degree of ordering while the eigenvectors specify the alignment axes. To quickly determine

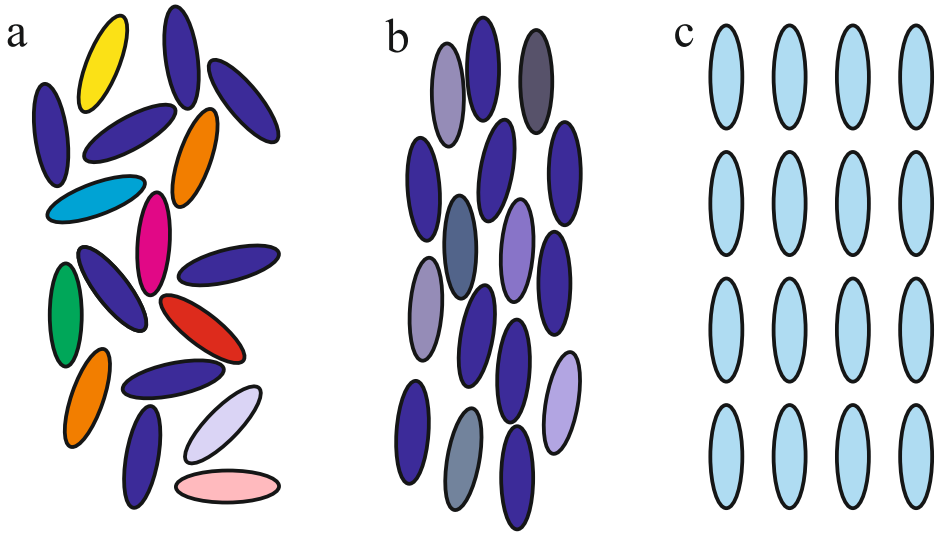


Figure 1.1: Typical molecular configurations in: (a) the isotropic phase (b) the nematic phase and (c) a crystalline phase. The range of colours indicates the degree of ordering. The isotropic phase possesses the highest symmetry and least order. Rotational symmetry is broken and a preferred alignment axis exists in the nematic phase. Both orientational and translational symmetry are broken in the crystalline phase.

if a $\tilde{\mathcal{Q}}$ describes a biaxial state the following function can be used

$$\Delta(\tilde{Q}) = 1 - 6\frac{\mathrm{Tr}(\tilde{\mathcal{Q}}^3)^2}{\mathrm{Tr}(\tilde{\mathcal{Q}}^2)^3}. \tag{1.2}$$

This function can be derived by computing the discriminant of the characteristic equation of the $\tilde{\mathcal{Q}}$-tensor. Function (1.2) has the property that $\Delta(\tilde{\mathcal{Q}}) = 0$ in the uniaxial and $\Delta(\tilde{\mathcal{Q}}) \neq 0$ in the biaxial phase.

Under either the $\mathcal{Q}$-tensor or director description the state of a nematic is not generally uniform throughout space. To determine the configuration a free energy formalism is employed. It is this formalism that is used in chapters 3 and 4 to investigate the properties of a doped nematic system. If the scalar order parameter is constant throughout the sample and the nematic is uniaxial a full $\mathcal{Q}$-tensor description is often unnecessary. In this case the $\mathcal{Q}$-tensor is determined by the unit vector $\hat{\boldsymbol{n}}$, the director. We use Ericksen Leslie theory, a director based formalism that includes the fluid motion of the nematic, in chapter 2 to model the dynamic response of a confined nematic to fast forcing. We now give an overview of director and $\mathcal{Q}$-tensor based modelling of nematic liquid crystals.

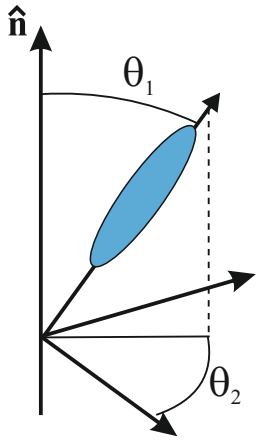


Figure 1.2: For a nematic with director $\hat{\boldsymbol{n}}$ along the vertical axis the ellipse represents a typical molecular alignment. The scalar order parameter measures the clustering of the distribution of molecular alignments with $\theta_1$. The biaxiality parameters measures the clustering of alignments with $\theta_2$. In a uniaxial phase all values of $\theta_2$ are equally likely whereas in a biaxial phase there is a preferred value of $\theta_2$.

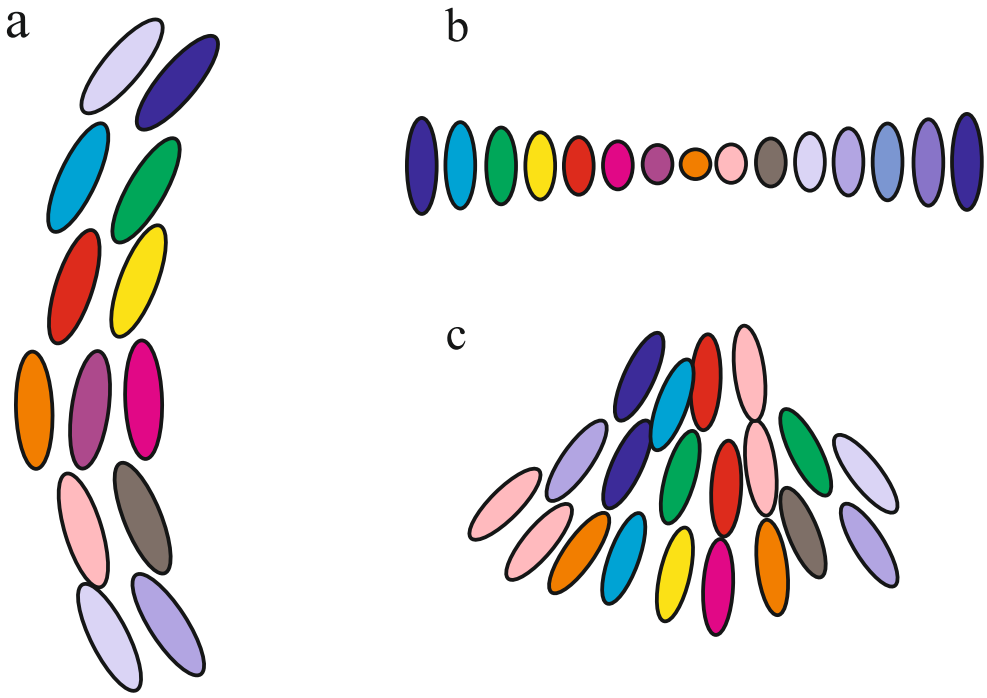


Figure 1.3: Characteristic orientational deformations in a nematic liquid crystal. Each can be identified by considering possible deformations of the director that satisfy $\hat{\boldsymbol{n}} \cdot \hat{\boldsymbol{n}} = 1$ upon travelling away from the origin with $\hat{\boldsymbol{n}}(\mathbf{0}) = (0, 0, 1)$ (see [110] page 16). (a) bend: travel in the direction of $\hat{\boldsymbol{n}}$ deformation is orthogonal to $\hat{\boldsymbol{n}}$ (b) twist: travel orthogonal to $\hat{\boldsymbol{n}}$ deformation is orthogonal to displacement and $\hat{\boldsymbol{n}}$ and (c) splay: travel orthogonal to $\hat{\boldsymbol{n}}$ deformation is in direction of displacement. Each is charactered by an independent elastic constant, it should be noted that in a biaxial nematic additional elastic constants are required.

## 1.2 Director based modelling

Director based modelling of nematic liquid crystals can be used to explore both static and dynamic effects. The origins of the static theory of nematics can be traced back to the work of Frank [40], Oseen [76] and Zocher [119]. A development of both the static and dynamic theory of liquid crystals is presented by Stewart [110]. We summarise this approach here and retain the notation used in [110]. A free energy density $w_F$ which depends on the director field $\hat{\boldsymbol{n}}$ and its gradient $\boldsymbol{\nabla}\hat{\boldsymbol{n}}$ is associated with the nematic. The configuration taken by the nematic in some volume $V$ is that which minimises the total free energy. The total free energy contains contributions from both internal elastic interactions and interaction with externally applied fields. We now detail the construction of such a free energy density. First we obtain the elastic contribution and then the electrostatic term.

The form of the elastic free energy is found by seeking the most general functional that obeys the symmetry requirements of the nematic. These requirements are: that the ordering is non-polar $\hat{\boldsymbol{n}} \equiv -\hat{\boldsymbol{n}}$ and the energy of the system is invariant under a global rotation of $\hat{\boldsymbol{n}}$. These requirement can be enforced by seeking a free energy obeying

$$\begin{aligned} w_F(\hat{\boldsymbol{n}}, \boldsymbol{\nabla}\hat{\boldsymbol{n}}) &= w_F(-\hat{\boldsymbol{n}}, -\boldsymbol{\nabla}\hat{\boldsymbol{n}}), \\ w_F(\hat{\boldsymbol{n}}, \boldsymbol{\nabla}\hat{\boldsymbol{n}}) &= w_F(R\hat{\boldsymbol{n}}, R\boldsymbol{\nabla}\hat{\boldsymbol{n}}R^T), \end{aligned} \tag{1.3}$$

for any constant rotation matrix $R \in SO(3)$. The first requirement enforces nematic rather than polar ordering, the second states that the energy of a given configuration is invariant upon solid body motion provided every point undergoes the same motion. We also require that the free energy is positive semi-definite. The development of such a free energy is summarised by Stewart [110]. The final form of the free energy density is

$$\begin{aligned} w_F =& \frac{1}{2}K_1[\boldsymbol{\nabla}\cdot\hat{\boldsymbol{n}}]^2 + \frac{1}{2}K_2[\hat{\boldsymbol{n}}\cdot(\boldsymbol{\nabla}\times\hat{\boldsymbol{n}})]^2 + \frac{1}{2}K_3\|\hat{\boldsymbol{n}}\times(\boldsymbol{\nabla}\times\hat{\boldsymbol{n}})\|^2 \\ &+ \frac{1}{2}\left(K_2+K_4\right)\boldsymbol{\nabla}\cdot[(\hat{\boldsymbol{n}}\cdot\boldsymbol{\nabla})\hat{\boldsymbol{n}} - (\boldsymbol{\nabla}\cdot\hat{\boldsymbol{n}})\hat{\boldsymbol{n}}], \end{aligned} \tag{1.4}$$

where $K_1$, $K_2$ and $K_3$ are the splay, twist and bend elastic constant, $K_2+K_4$ is the saddle splay constant and is removed from the bulk equations by means of the divergence theorem. The distortions corresponding to pure splay twist and bend are illustrated in figure 1.3. Experimentally, the orientation of a nematic LC is often controlled by an externally driven electric or magnetic field. To describe this interaction we seek an addition to the free energy density to account for applied electric fields. The case of a magnetic field follows in a similar way and can be found in [110, 36].

Nematic liquid crystals acquire a spontaneous polarisation under an applied electric field. The electric displacement field $\boldsymbol{D}$ that results from an applied electric field $\boldsymbol{E}$ is [110]

$$\boldsymbol{D} = \epsilon_0 \epsilon_\perp \boldsymbol{E} + \epsilon_0 \epsilon_a (\hat{\boldsymbol{n}} \cdot \boldsymbol{E}) \hat{\boldsymbol{n}}, \qquad \epsilon_a = \epsilon_\parallel - \epsilon_\perp, \tag{1.5}$$

where $\epsilon_\parallel$ and $\epsilon_\perp$ are the relative dielectric anisotropy measured parallel or perpendicular to the director respectively and $\epsilon_0$ is the vacuum permittivity. The electric energy density of a nematic liquid crystal under a fixed potential drop is given by [110]

$$w_E = -\frac{1}{2} \boldsymbol{D} \cdot \boldsymbol{E}. \tag{1.6}$$

With this addition the electric field acts as a symmetry breaking parameter within the total free energy $w_T = w_F + w_E$ favouring $\hat{\boldsymbol{n}}$ aligned parallel or perpendicular to $\boldsymbol{E}$ for $\epsilon_a$ positive or negative, respectively. The electric field can be determined either by minimising the electrostatic free energy with respect to the electrostatic potential or by employing Maxwell's equations, specifically that the displacement field obeys

$$\boldsymbol{\nabla} \cdot \boldsymbol{D} = 0, \tag{1.7}$$

in the absence of free charges.

The most widely accepted dynamical theory for nematic liquid crystals was developed by Ericksen [38] and Leslie [57] and constitutes a generalisation of the static theory developed by Frank [40], Oseen [76] and Zocher [119]. The Ericksen-Leslie (EL) theory uses the director representation of the nematic. The fluid velocity is specified by a vector field $\boldsymbol{v}$. The governing equations are derived in the isothermal and incompressible regime by Stewart [110]. Here we present an outline of the derivation. The starting point for EL theory are the balance laws for mass, angular and linear momentum. Consider an arbitrary volume $V$ containing nematic liquid crystal subject to externally applied surface and volume forces and moments. The conservation laws can be written in integral form as follows:

$$\frac{D}{Dt} \int_V \rho dV = 0, \tag{1.8}$$

$$\frac{D}{Dt} \int_V \rho \boldsymbol{v} dV = \int_V \rho \boldsymbol{F} dV + \int_{\partial V} \boldsymbol{t} dS, \tag{1.9}$$

$$\frac{D}{Dt} \int_V \rho (\boldsymbol{x} \times \boldsymbol{v}) dV = \int_V \rho (\boldsymbol{x} \times \boldsymbol{F} + \boldsymbol{K}) dV + \int_{\partial V} (\boldsymbol{x} \times \boldsymbol{t} + \boldsymbol{l}) dS, \tag{1.10}$$

where the mass density of the nematic is given by $\rho$, $\boldsymbol{F}$ is the externally applied body force per unit mass, $\boldsymbol{x}$ is the position vector, $\boldsymbol{t}$ is the surface force per unit area, $\boldsymbol{K}$ is

the external body moment per unit mass, $\boldsymbol{l}$ is the surface moment per unit area and $\frac{D}{Dt} = \frac{\partial}{\partial t} + \boldsymbol{v} \cdot \boldsymbol{\nabla}$ is the material time derivative. The surface forces and moments are due to contact with another phase on the boundary of the nematic volume $\partial V$, for instance a submerged solid body or liquid crystal outside of the volume $V$. These surface terms depend on the material parameters of the nematic, the configuration of the nematic at the surfaces and the orientation of the surfaces. This is captured by the stress tensors $t_{ij}$ and couple stress tensor $l_{ij}$ through the relations $t_i = t_{ij}\nu_j$ and $l_i = l_{ij}\nu_j$ where $\boldsymbol{\nu}$ is the unit normal to the surface. The stress and coupled stress tensor contain the, at this stage unknown, material parameters of the nematic.

Equations (1.8)-(1.10) are supplemented by a balance of work hypothesis. The rate at which external forces and moments do work on the system is equal to the rate of change of kinetic and elastic energy in the system plus the total viscous dissipation. Symbolically this is written as

$$\int_V \rho(\boldsymbol{F}\cdot\boldsymbol{V}+\boldsymbol{K}\cdot\boldsymbol{w})dV+\int_{\partial V}(\boldsymbol{t}\cdot\boldsymbol{v}+\boldsymbol{l}\cdot\boldsymbol{w})dS = \frac{D}{Dt}\int_V \left(\frac{1}{2}\rho\boldsymbol{v}\cdot\boldsymbol{v} + w_F\right)dV+\int_V \mathcal{D}dV \quad (1.11)$$

where $\mathcal{D}$ is the viscous dissipation per unit volume and $\boldsymbol{w}$ is the local angular velocity of the director satisfying

$$\frac{D\hat{\boldsymbol{n}}}{Dt} = \boldsymbol{w} \times \hat{\boldsymbol{n}}. \quad (1.12)$$

By putting (1.8)-(1.11) in point form and requiring that the viscous dissipation be positive we find constraints on the possible forms of the stress and coupled stress tensors. The stress tensors must have the form

$$t_{ij} = -p\delta_{ij} - \frac{\partial w_F}{\partial n_{p,j}} n_{p,i} + \tilde{t}_{ij} \quad (1.13)$$

and

$$l_{ij} = \epsilon_{ipq} n_p \frac{\partial w_F}{\partial n_{q,j}} + \tilde{l}_{ij}, \quad (1.14)$$

where $p$ is a pressure arising from the enforced incompressibility, $\tilde{t}_{ij}$ and $\tilde{l}_{ij}$ denote possible dynamic contributions, $\delta_{ij}$ is the Kronecker delta, $\epsilon_{ipq}$ is the Levi-Civita symbol, the notation $f_{,i}$ denotes the partial derivative of $f$ with respect to the $i$-th coordinate and we sum over repeated indices. The dynamic contributions are determined by considering the most general form possible that obeys the symmetries of the nematic and ensures that the dissipation function is positive, see Stewart [110] for details. The dynamic contribution to the coupled stress tensor is zero, while the contribution to the stress tensor $t_{ij}$ contains

six viscosity coefficients coupling the fluid flow to the rotations of the director. The number of viscosities is set by the symmetry requirements of the nematic. By use of the Parodi relations [78] the total number of viscosity coefficients can be reduced to five, as one can show that $\alpha_2 + \alpha_3 = \alpha_6 - \alpha_5$. With this simplification the final form of the viscous dissipation function is

$$\mathcal{D} = \alpha_1(n_i A_{ij} n_j)^2 + 2\gamma_2 N_i A_{ij} n_j + \alpha_4 A_{ij} A_{ji} + (\alpha_2 + \alpha_3 + 2\alpha_5) n_i A_{ij} A_{jk} n_k + \gamma_1 N_i N_i \quad (1.15)$$

with $A_{ij} = \frac{1}{2}(v_{i,j} + v_{j,i})$ the rate of strain, $N_i = n_i - W_{ij} n_j$ the co-rotational time flux of the director, $W_{ij} = \frac{1}{2}(v_{i,j} - v_{j,i})$ the vorticity tensor and $\alpha_i$, $i = 1, ..., 5$ are known as the Leslie viscosity coefficients with $\gamma_1 = \alpha_3 - \alpha_2$ the rotational viscosity and $\gamma_2 = \alpha_2 + \alpha_3$ the torsion coefficient. We now give the final form of the governing equations. By parametrising the director $\hat{\boldsymbol{n}}$ by two angles $\theta_1$ and $\theta_2$ the governing equations may be written in terms of the scaled dissipation function $\hat{\mathcal{D}}(v_{i,j}, \theta_{\alpha,t}, \theta_\alpha) = \frac{1}{2}\mathcal{D}(A_{ij}, N_i, n_i)$, potential energy density $\hat{\Psi}$ and Frank free energy $\hat{w}_F$. The balance of angular momentum is given by [110],

$$\left(\frac{\partial \hat{w}_F}{\partial \theta_{\alpha,i}}\right)_{,i} - \frac{\partial w_F}{\partial \theta_\alpha} - \frac{\partial \hat{\mathcal{D}}}{\partial \theta_{\alpha,t}} + \frac{\partial \hat{\Psi}}{\partial \theta_\alpha} = 0, \qquad \alpha = 1, 2 \quad (1.16)$$

and the balance of linear momentum is

$$\rho \frac{\partial v_i}{\partial t} = \left(\frac{\partial \hat{\mathcal{D}}}{\partial v_{i,j}}\right)_{,j} - \frac{\partial \hat{\mathcal{D}}}{\partial \theta_{\alpha,t}} - \tilde{p}_{,i} \qquad i = 1, 2, 3. \quad (1.17)$$

Here $\rho$ is the mass density, $\tilde{p} = p + \hat{w}_F - \hat{\Psi}$, with $p$ the pressure, $\hat{\Psi}$ the total potential energy density due to electromagnetic and gravitational fields, and summation over repeated indices is implied. By parametrising the governing equations (1.16) and (1.17) using two angles the normalisation condition $\hat{\boldsymbol{n}} \cdot \hat{\boldsymbol{n}} = 1$ is automatically satisfied. The only remaining constraint is that the flow is incompressible,

$$v_{i,i} = 0. \quad (1.18)$$

The Ericksen-Leslie equations (1.16)-(1.17) and constraint (1.18) determine the dynamic evolution of the director. In order to use EL theory the value of the elastic constants and viscosity coefficients must be known. The elastic constants are easily measured by various means. However, measuring the Leslie viscosity coefficients is more difficult. Various existing methods, based around extending traditional viscometer techniques, optical methods and more exotic set-ups, are reviewed at the start of chapter 2. For the remainder

of chapter 2 Ericksen-Leslie theory is used to model the dynamic response of a confined nematic liquid crystal. Optical measurements sensitive to the dynamics of the director are then used to measure combinations of the Leslie viscosity coefficients. We now give an example of applying Ericksen-Leslie theory to a planar liquid crystal system.

### 1.2.1 Planar liquid crystal cell

We illustrate the use of Ericksen-Leslie theory by applying it to a standard problem, the case of a planar liquid crystal. This system is shown in figure 1.4 and consists of a $d \approx 10\ \mu m$ thick glass cell containing nematic liquid crystal of positive dielectric anisotropy. We assume that the nematic is aligned roughly parallel to the upper and lower glass planes at angles $\theta_0$ and $\theta_d$ respectively and that the alignment varies only with $z$ the coordinate into the cell. The nematic is realigned by a high frequency AC field applied orthogonally to the cell walls. Parametrising the director by the tilt angle $\theta(z)$, $\hat{\boldsymbol{n}} = (\cos(\theta), 0, \sin(\theta))$. The governing equations for this system can be found by seeking stationary solutions to the Ericksen-Leslie equations (1.16) to (1.18) and Maxwell's equation for the electric displacement (1.7). The stationary solution is governed by

$$\begin{aligned}[K_1 \cos^2(\theta) + K_3 \sin^2(\theta)]\frac{d^2\theta}{dz^2} + \frac{K_3 - K_1}{2}\left(\frac{d\theta}{dz}\right)^2 \sin(2\theta) \\ + \frac{\epsilon_a \epsilon_0}{2}\left(\frac{d\phi}{dz}\right)^2 \sin(2\theta) = 0,\end{aligned} \tag{1.19a}$$

$$\theta(z=0) = \theta_0, \qquad \theta(z=d) = \theta_d. \tag{1.19b}$$

Maxwell's equation for the electric displacement can be readily integrated to give the potential in the cell

$$\phi(z) = \int_0^z \frac{V}{1 + \frac{\epsilon_a}{\epsilon_\perp}\sin^2(\theta)} dz' \left( \int_0^d \frac{1}{1 + \frac{\epsilon_a}{\epsilon_\perp}\sin^2(\theta)} dz'' \right)^{-1}. \tag{1.20}$$

Here $V$ is the voltage applied to the cell and all other symbols have their usual meanings. The general trend of $\theta$ with increasing voltage $V$ is shown in figure 1.4. As the applied field increases the director realigns itself with $\boldsymbol{E}$, the distortion is greatest at the centre of the cell and saturates at $\pi/2$. At high voltage only the nematic towards the boundaries is not realigned.

In the symmetric case $\theta_0 = \theta_d = 0$ the ground state $\theta(z) = 0\ \forall z$ is a solution of equation (1.19a) for all values of the applied field. However the stability of this solution does depend on the magnitude of the applied voltage. At a critical value of the voltage $\theta = 0$ becomes

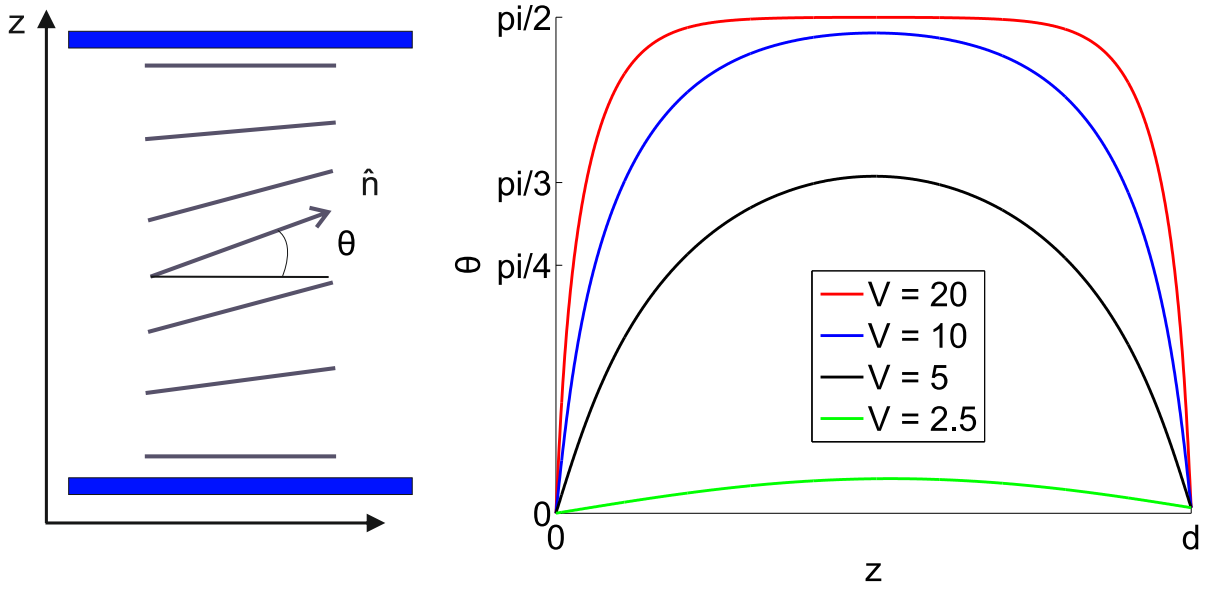


Figure 1.4: (Left) parametrisation of the director within a splay cell by the angle $\theta$. (Right) Tilt angle profile for applied voltages of $V = 2.5, 5, 10, 20$ obtained numerically for pre-tilt values $\theta_0 = 0°$ and $\theta_d = 1°$. The distortion is largest away from the edges of the cell, at high voltage the distortion saturates and the director is aligned with $\boldsymbol{E}$ with the exception of small layers near the boundaries.

unstable and two new stable states emerge from a pitchfork bifurcation. This transition is known as the Frederiks transition. A detailed derivation of the transition voltage for various systems can be found in [110]. Here we show how the transition voltage can be obtained through a linear stability analysis. The governing equations are the linearised Ericksen-Leslie equations. Neglecting fluid flow we find that $\theta$ is governed by

$$K_1 \frac{\partial^2 \theta}{\partial z^2} + \epsilon_a \epsilon_0 \left(\frac{V}{d}\right)^2 \theta = \gamma_1 \frac{\partial \theta}{\partial t}. \tag{1.21}$$

To find the critical value of the voltage we seek a Fourier series solution to equations (1.21)

$$\theta = \sum_{n=1}^{\infty} a_n(t) \sin\left(\frac{n\pi z}{d}\right). \tag{1.22}$$

Substituting (1.22) into (1.21) and projecting onto $\sin\left(\frac{\pi z}{d}\right)$ we find that the fundamental mode $a_1$ is governed by

$$a_1 \left(-\frac{K_1 \pi^2}{d^2} + \epsilon_a \epsilon_0 \frac{V^2}{d^2}\right) = \gamma_1 \frac{\partial a_1}{\partial t}. \tag{1.23}$$

The fundamental mode $a_1$ grows when

$$V > V_{FT} \equiv \pi \sqrt{\frac{K_1}{\epsilon_0 \epsilon_a}}. \tag{1.24}$$

## 1.3 $\mathcal{Q}$-tensor based modelling

In 1.2 we outlined the construction of Ericksen-Leslie theory, a director based model, that includes both static and dynamic effects. In this section we outline the $\tilde{\mathcal{Q}}$-tensor model developed initially by de Gennes [35]. This section is based on the development of the $\tilde{\mathcal{Q}}$-tensor theory reported by Sonnet and Virga [106, 107]. This model will be used in chapters chapters 3 and 4 when studying colloidal suspensions. Throughout this section variables that have a tilde $\sim$ have not been rescaled or non-dimensionalised, this notation was chosen to allow for consistency with chapters 3 and 4. Additionally we distinguish between the free energy densities in the director theory discussed in section 1.2 and the $\tilde{\mathcal{Q}}$-tensor models by using different notation for the various contributions to the free energy density.

To describe the static properties of a nematic we need a free energy density written in terms of $\tilde{\mathcal{Q}}$. The free energy density contains: an elastic contribution written in terms of the gradients of $\tilde{\mathcal{Q}}$, a thermotropic contribution which sets the scalar order parameters and a symmetry breaking contribution which couples the nematic to external fields. To find an expression for the thermotropic free energy contribution Sonnet and Virga [107] seek a polynomial expression in the invariants of the order parameter $\tilde{\mathcal{Q}}$. The invariants of a tensor are defined as the coefficients of the characteristic polynomial [107] and take the same value regardless of the basis in which they are evaluated. This construction guarantees that the free energy, a scalar valued function of a tensor variable, is objective, that is, takes the same value in any reference frame [107]. The thermotropic free energy, which sets the scalar and biaxial order, depends only on $\tilde{\mathcal{Q}}$. The relevant invariants are [107]

$$I_1 = \mathrm{Tr}(\tilde{\mathcal{Q}}), \tag{1.25a}$$

$$I_2 = \mathrm{Tr}(\tilde{\mathcal{Q}}^2), \tag{1.25b}$$

$$I_3 = \mathrm{Tr}(\tilde{\mathcal{Q}}^3). \tag{1.25c}$$

The first invariant is zero by symmetry of the $\tilde{\mathcal{Q}}$-tensor. The expression for the thermotropic free energy density that we will use, often referred to as the Landau de Gennes

free energy [35], is

$$\tilde{\mathcal{F}}_t = \frac{1}{2}A\left(T - T^*\right)\mathrm{Tr}\left(\tilde{\mathcal{Q}}^2\right) - \sqrt{6}B\mathrm{Tr}\left(\tilde{\mathcal{Q}}^3\right) + \frac{1}{2}C\left[\mathrm{Tr}(\tilde{\mathcal{Q}}^2)\right]^2. \tag{1.26}$$

Here $T$ is the temperature, $T^*$ is the temperature at which the isotropic phase becomes unstable, $A$, $B$ and $C$ are the thermotropic coefficients and are assumed to be temperature independent. The temperature dependence in (1.26) is captured entirely by the first term. It is possible to extend (1.26) to include higher order terms in the invariants, this is not pursued here. Finding a general elastic energy density for a $\tilde{\mathcal{Q}}$-tensor based model has been investigated in a number of publications [60, 59, 51, 107]. As there are a large number of elastic constants within a general $\tilde{\mathcal{Q}}$-tensor framework to simplify the exposition we make the single elastic constant approximation. Under this approximation the elastic free energy density is

$$\tilde{\mathcal{F}}_B = \frac{\tilde{L}}{2}\|\tilde{\boldsymbol{\nabla}}\tilde{\mathcal{Q}}\|^2, \tag{1.27}$$

where $\tilde{L}$ is the single elastic constant. It is possible to capture the full elastic anisotropy found in Ericksen-Leslie theory within a $\tilde{\mathcal{Q}}$-tensor theory. However, terms of up to third order in $\tilde{\mathcal{Q}}$, more precisely linear in $\tilde{\mathcal{Q}}$ and quadratic in $\boldsymbol{\nabla}\mathcal{Q}$ [107], must be included. The final two contributions to the free energy density are due to external symmetry breaking interactions. The surface free energy density captures the interaction of the nematic with an external barrier such as an aligning polymer layer. One possible form for this contribution was proposed by [74] which extends the Rapini-Papoular [90] director model to the $\tilde{\mathcal{Q}}$-tensor case. The surface energy density is [74]

$$\tilde{\mathcal{F}}_S = \frac{\tilde{\mu}}{2}\mathrm{Tr}\left[\left(\tilde{\mathcal{Q}} - \tilde{\mathcal{Q}}_S\right)^2\right]. \tag{1.28}$$

Here $\tilde{\mu}$ is the surface anchoring energy density and $\tilde{\mathcal{Q}}_S$ is the preferred surface alignment tensor. This form of the surface free energy has a unique minima when $\tilde{\mathcal{Q}}$ coincides with $\tilde{\mathcal{Q}}_S$. Other anchoring conditions have been proposed such as the planar degenerate case studied by Fournier and Galatola [39] in which any alignment in a chosen plane with given scalar order is a minimum. The final contribution we will need is the electrostatic energy density. This contribution is given by,

$$\tilde{\mathcal{F}}_e = -\frac{1}{2}\tilde{\boldsymbol{E}}\cdot(\epsilon_0\epsilon_r\tilde{\boldsymbol{E}}), \tag{1.29}$$

where $\epsilon_r$ is the relative dielectric permittivity tensor. The relative permittivity can be

written directly in terms of the $\tilde{\mathcal{Q}}$-tensor as

$$\epsilon_r = \epsilon_u \mathcal{I} + \frac{\epsilon_a \sqrt{2}}{\tilde{S}\sqrt{3}} \tilde{\mathcal{Q}}, \tag{1.30}$$

where $\epsilon_u = \frac{2\epsilon_\perp + \epsilon_\parallel}{3}$ is the uniform part of the dielectric permittivity. To describe dynamic effects rather than starting with the conservation of linear and angular momentum and incorporating the dissipating effects due to viscosity by a rate of work hypothesis, as is done for Ericksen-Leslie theory, Sonnet and Virga [106, 107] use a dissipation principle. They formulate the principle of minimum reduced dissipation which can be seen as a generalisation of the classical Rayleigh dissipation principle. The Rayleigh dissipation principle allows frictional forces which are proportional to the velocities within a system to be incorporated within a Lagrangian framework [107, 41]. Roughly speaking the dissipation principle is a requirement that the change in internal energy within a system is balanced by the rate of dissipation. Hence, to employ this methodology both a free energy density and a dissipation function must be constructed. Sonnet and Virga [107] use symmetry considerations to construct a dissipation function for a nematic liquid crystal. Details of this construction can be found in [107], the end result is

$$\begin{aligned} \tilde{\mathcal{R}}(\tilde{\mathcal{D}}, \mathring{\tilde{\mathcal{Q}}}) = &\frac{1}{2}\zeta_1 \mathrm{Tr}(\mathring{\tilde{\mathcal{Q}}}^2) + \zeta_2 \mathrm{Tr}(\tilde{\mathcal{D}}\mathring{\tilde{\mathcal{Q}}}) + \zeta_3 \mathrm{Tr}(\tilde{\mathcal{D}}\mathring{\tilde{\mathcal{Q}}}\tilde{\mathcal{Q}}) + \zeta_4 \mathrm{Tr}(\tilde{\mathcal{D}}^2\tilde{\mathcal{Q}}) \\ &+ \frac{1}{2}\zeta_5 \mathrm{Tr}(\tilde{\mathcal{D}}^2\tilde{\mathcal{Q}}^2) + \frac{1}{2}\zeta_6 (\mathrm{Tr}(\tilde{\mathcal{D}}\tilde{\mathcal{Q}}))^2 + \frac{1}{2}\zeta_7 \mathrm{Tr}(\tilde{\mathcal{D}}^2)\mathrm{Tr}(\tilde{\mathcal{Q}}^2) + \frac{1}{2}\zeta_8 \mathrm{Tr}(\tilde{\mathcal{D}}^2), \end{aligned} \tag{1.31}$$

where $\tilde{\mathcal{D}}$ is the symmetric part of the velocity gradient (denoted $\tilde{A}$ in 1.2 and [110]), $\mathring{\tilde{\mathcal{Q}}} = \dot{\tilde{\mathcal{Q}}} - \tilde{W}\tilde{\mathcal{Q}} + \tilde{\mathcal{Q}}\tilde{W}$ is the co-rotational derivative of the $\tilde{\mathcal{Q}}$ tensor and $\dot{\tilde{\mathcal{Q}}}$ is the material derivative of $\tilde{\mathcal{Q}}$. The viscosities $\zeta_i$, $i = 1, ..., 8$ captures the full range of dynamic coupling within a nematic between the alignment and flow fields that are of second order in $\tilde{\mathcal{D}}$ and $\tilde{\mathcal{Q}}$ [107]. Various simplifications to (1.31) have been proposed Qian and Shen [89] proposed a theory with five viscosities that neatly maps onto the Ericksen-Leslie model that may be obtained from (1.31) by setting $\zeta_3 = \zeta_5 = \zeta_7 = 0$. The associated stress tensor is,

$$\tilde{T} = -\tilde{P}\mathcal{I} - \nabla\tilde{\mathcal{Q}} \odot \frac{\partial \mathcal{F}_B}{\partial \boldsymbol{\nabla}\tilde{\mathcal{Q}}} + \tilde{\mathcal{Q}}\frac{\partial \tilde{R}}{\partial \mathring{\tilde{\mathcal{Q}}}} - \frac{\partial \tilde{R}}{\partial \mathring{\tilde{\mathcal{Q}}}}\tilde{\mathcal{Q}} + \frac{\partial \tilde{R}}{\partial \tilde{\mathcal{D}}}, \tag{1.32}$$

where $\tilde{P}$ is the pressure, $\mathcal{I}$ the identity matrix and the second rank tensor $\tilde{\boldsymbol{\nabla}}\tilde{\mathcal{Q}} \odot \frac{\partial \tilde{\mathcal{F}}_B}{\partial \tilde{\boldsymbol{\nabla}}\tilde{\mathcal{Q}}} = \tilde{\mathcal{Q}}_{kl,i}\frac{\partial \mathcal{F}_B}{\partial \tilde{\mathcal{Q}}_{kl,j}}\boldsymbol{e}_i \otimes \boldsymbol{e}_j$ with $(\boldsymbol{e}_1, \boldsymbol{e}_2, \boldsymbol{e}_3)$ any positively oriented orthogonal frame. The governing

equations for the $\tilde{\mathcal{Q}}$-tensor and velocity field are

$$\frac{\partial \tilde{\mathcal{R}}}{\partial \mathring{\tilde{\mathcal{Q}}}} = \tilde{\boldsymbol{\nabla}} \cdot \frac{\partial \tilde{\mathcal{F}}_V}{\partial \tilde{\boldsymbol{\nabla}} \tilde{\mathcal{Q}}} - \frac{\partial \tilde{\mathcal{F}}_V}{\partial \tilde{\mathcal{Q}}}, \tag{1.33a}$$

$$\tilde{\boldsymbol{\nabla}} \cdot \tilde{T} = 0 \tag{1.33b}$$

where the total volume free energy density is

$$\tilde{\mathcal{F}}_V = \tilde{\mathcal{F}}_B + \tilde{\mathcal{F}}_t + \tilde{\mathcal{F}}_e. \tag{1.34}$$

On the boundary the $\tilde{\mathcal{Q}}$-tensor and velocity field obey,

$$\hat{\boldsymbol{\nu}} \cdot \frac{\partial \tilde{\mathcal{F}}_V}{\partial \tilde{\boldsymbol{\nabla}} \tilde{\mathcal{Q}}} = -\frac{\partial \tilde{\mathcal{F}}_S}{\partial \tilde{\mathcal{Q}}} \tag{1.35a}$$

$$\tilde{\boldsymbol{v}} = \tilde{\boldsymbol{v}}_b, \tag{1.35b}$$

where $\hat{\boldsymbol{\nu}}$ is the outward unit normal on the boundary, $\tilde{\boldsymbol{v}}$ is the flow velocity of the nematic and $\tilde{\boldsymbol{v}}_b$ is the boundary velocity. It should be noted that in (1.33b) we have neglected fluid inertia. This is typical for most liquid crystal applications as the fluid flow equilibrates on a far faster time scale than the director. We investigate this approximation on page 55 in the context of driven oscillations.

## 1.4 Optical modelling

In this section we outline basic results concerning the optics of liquid crystal. These will be used in chapter 2 to model the results of optical measurements. First we describe the experimental set-up that forms the basis of the method developed in chapter 2. Next we model light propagating through a planar liquid crystal cell. We follow the method outlined by Daly [31] where additional details can be found. The final part of this section is dedicated to modelling twisted nematic cells.

### 1.4.1 The cross polarised intensity experiment

Nematic liquid crystals are birefringent possessing two distinct refractive indices $n_o$ and $n_e$ the ordinary and extraordinary index. Linearly polarised light propagating with polarisation parallel to $\hat{\boldsymbol{n}}$ experiences $n_e$, polarisations orthogonal to $\hat{\boldsymbol{n}}$ experiences $n_o$. As a result light propagating through a sample of nematic will experience a different travel

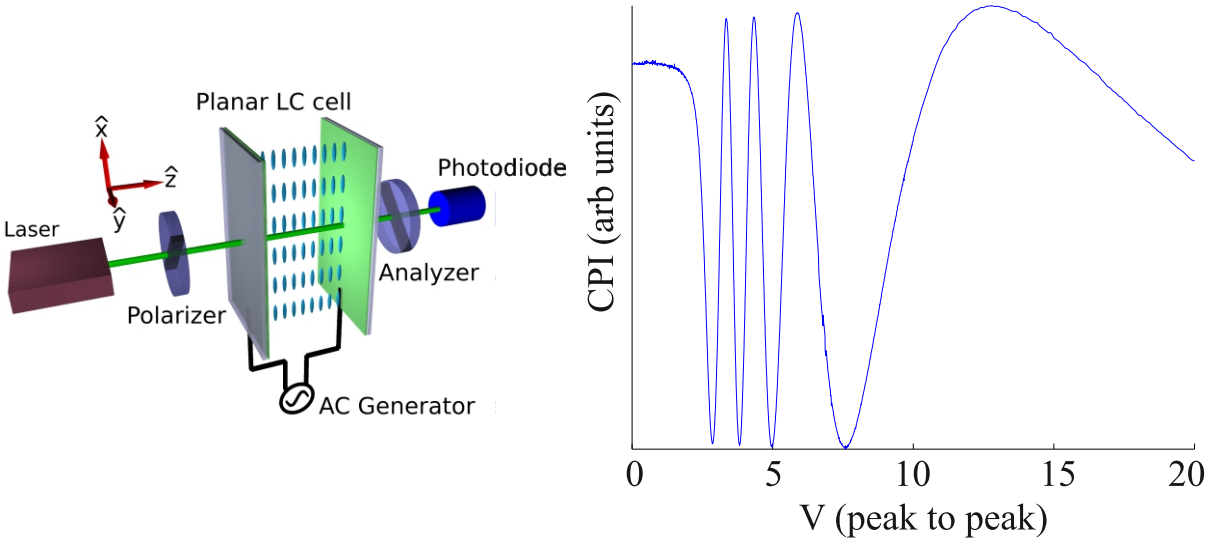


Figure 1.5: (Left) Schematic representation of the experimental set-up used for the cross polarised intensity experiment discussed in chapter 2. The nematic is anchored to the glass substrate by means of a rubbed PI layer. A voltage is applied across the cell reorientating the nematic. Light polarised at 45° to the initial director in transmitted through the cell. Components of the polarisation parallel and orthogonal to the initial director are exposed to different refractive indices. The phase difference determines the exit polarisation, the final polariser and analyser allows this change to be measured as a change in intensity. (Right) a typical CPI trace as a function of peak to peak AC voltage applied to the cell.

time depending on its polarisation. One result of this is that a liquid crystal cell can be used to alter the polarisation state of light. The change in polarisation state is determined by the alignment of the nematic throughout a device. We now describe how, by clever use of polarisers, this change in polarisation state can be detected as a change in intensity.

The experimental set-up used during a cross polarised intensity (CPI) measurement is shown in figure 1.5. Planar liquid crystal cells, in which the director is anchored nearly parallel to the boundary by means of a rubbed polymer layer, are characterised using incident laser light at 532 nm. The incident polarisation is at an angle of 45° with respect to the PI rubbing direction. The phase difference between the two orthogonal components of this beam after passing through the cell is measured by adding an analyser polariser, with transmission axis set orthogonal to the initial polarisation, and observing the resulting changes in intensity using a photodiode. The intensity of transmitted radiation is recorded as a function of applied voltage. A typical trace is shown in figure 1.5.

The plot in the right hand panel of figure 1.5 shows the effect of nematic realignment

with increasing voltage. Initially the intensity is roughly constant before the onset of the Frederiks transition. The transition is slightly smoothed due to the presence of non zero boundary pre-tilt which breaks the symmetry of the bifurcation. As the voltage is increase the phase different increases, the peaks and troughs correspond to total phase changes that are an integer multiple of $\pi$. Finally as the voltage increases and the nematic saturates the transmitted intensity tends asymptotically to zero. In order to extract information from these measurements we must determine the nematic alignment and model the transmission of polarised light through a nematic cell. We address the second point in the following subsection.

### 1.4.2 Light transmission through a liquid crystal cell

We now outline how to model the experiment described in the previous subsection. Light propagating through liquid crystal obeys Maxwell's wave equation, which for a field with time dependence $\exp(-i\omega t)$ is given by [18]

$$\nabla^2 \boldsymbol{E} = -\omega^2 \mu_0 \mu_r \epsilon_0 \epsilon_r \boldsymbol{E}, \tag{1.36}$$

with $\mu_r$ and $\epsilon_r$ the relative permittivity and permeability of the material. Liquid crystals are uni-axial and as a result have two independent permittivities $\epsilon_{\|}$ and $\epsilon_{\perp}$ the permittivity measured parallel and orthogonal to the director respectively. For a liquid crystal the permittivity tensor is related to the director by,

$$\epsilon_r = \epsilon_{\perp} \mathcal{I} + \epsilon_a (\hat{\boldsymbol{n}} \otimes \hat{\boldsymbol{n}}), \tag{1.37}$$

where $\mathcal{I}$ is the identity matrix. The corresponding refractive indices are $n_o$ and $n_e$, the ordinary and extraordinary indices. If biaxiality is present the nematic possesses three distinct refractive indices and the form of the dielectric tensor (1.37) must be modified accordingly. As a result, the phase velocity of light propagating through a liquid crystal cell depends on the angle between the polarisation vector and the director. To model the cross polarised intensity experiment studied in chapter 2 we need to determine this relationship. Choosing a coordinate system aligned with the principle axes of $\epsilon_r$ and by seeking plane wave solutions to (1.36) we arrive at Fresnel equation for wave normals (see [18] page 792)

$$\hat{k}_x^2 (v_p^2 - v_y^2)(v_p^2 - v_z^2) + \hat{k}_y^2 (v_p^2 - v_x^2)(v_p^2 - v_z^2) + \hat{k}_z^2 (v_p^2 - v_x^2)(v_p^2 - v_y^2) = 0 \tag{1.38}$$

where $\hat{k}_x$, $\hat{k}_y$ and $\hat{k}_z$ are the components of the unit wave-vector and $v_p$ is the phase velocity of the wave. As nematics are uniaxial the components of the phase velocity can be written as $v_x = v_y = v_o$ and $v_z = v_e$. Next we write the wave-vector in spherical polar coordinates

$$\hat{\boldsymbol{k}} = \begin{bmatrix} \sin(\theta)\cos(\phi) \\ \sin(\theta)\sin(\phi) \\ \cos(\theta) \end{bmatrix}, \tag{1.39}$$

where $\theta$ and $\phi$ are the spherical polar coordinate angles, $\theta$ being the angle between $\hat{\boldsymbol{n}}$ and $\hat{\boldsymbol{k}}$. Substituting (1.39) into (1.38) we find four solutions

$$\begin{aligned} v_{p1}^2 &= v_o^2, \\ v_{p2}^2 &= v_o^2 \sin^2(\theta) + v_e^2 \cos^2(\theta). \end{aligned} \tag{1.40}$$

The first set of solutions $\{v_{p1}\}$ describes forward and backwards propagation with polarisation orthogonal to the plane containing $\hat{\boldsymbol{n}}$, the second set $\{v_{p2}\}$ describes propagation with polarisation in the plane containing $\hat{\boldsymbol{n}}$. The associated indices can be computed by considering the dielectric ellipsoid of the system [18] and are given by

$$\begin{aligned} n_1 &= n_o, \\ n_{eff} &= \frac{n_e n_o}{\sqrt{n_e^2 \cos^2(\theta) + n_o^2 \sin(\theta)}}. \end{aligned} \tag{1.41}$$

We now return to computing the intensity of transmitted light. The set-up for the cross polarised intensity experiment is shown in figure 1.5. The electric field of a plane polarised ray travelling in the $\hat{z}$ direction arriving with polarisation at $45^{\cdot}$ to the director is given by

$$\boldsymbol{E} = E_0 \exp(i(kz - \omega t)) \frac{1}{\sqrt{2}} \begin{bmatrix} 1 \\ 1 \\ 0 \end{bmatrix}. \tag{1.42}$$

After exiting the cell, the $\hat{x}$ component of the field has acquired a phase shift relative to the $\hat{y}$ component. After transmission through the analyser polariser the field is given by,

$$\boldsymbol{E} = \frac{E_0}{2\sqrt{2}} \exp(i(kz - \omega t))(1 - \exp(i\Delta\phi)) \begin{bmatrix} -1 \\ 1 \\ 0 \end{bmatrix}. \tag{1.43}$$

Computing the intensity $I = \boldsymbol{E}\overline{\boldsymbol{E}}$ where $\overline{\boldsymbol{E}}$ is the complex conjugate of $\boldsymbol{E}$ we find,

$$I = I_0 \sin\left(\frac{\Delta\phi}{2}\right), \tag{1.44}$$

where the accumulated phase lag is calculated by integrating the local phase difference over the cell

$$\Delta\phi = \frac{2\pi}{\lambda}\int_0^d (n_o - n_{eff})dz. \tag{1.45}$$

Here $d$ is the cell width and $\lambda$ is the free space wavelength of the light. Formulas (1.44) and (1.45) suffice for computing the light transmission through a planar cell. To deal with the more general case including a twisted cell we use the extended Jones matrix method [58], [117] although the full $4 \times 4$-Berreman matrix method could also be used [16]. This method involves slicing the sample into thin layers and approximately representing each by a homogeneous medium. Within each layer two transmitted and two reflected waves propagate. The extended Jones matrix method involves neglecting the reflected waves and matching the tangential electric field components across the interface. From this a transmission matrix is formed for the entire system,

$$J = J_N J_{N-1} ... J_1, \tag{1.46}$$

where $J_n$ is the extended Jones matrix for the $n$-th layer [58]. The output wave is related to the input by,

$$\begin{bmatrix} E_x^{out} \\ E_y^{out} \end{bmatrix} = J \begin{bmatrix} E_x^{in} \\ E_y^{in} \end{bmatrix} \tag{1.47}$$

from which the transmittance can be computed. The transmittance of a 90° twisted cell is shown in figure 1.6. Light enters the cell with linear polarisation parallel to the director, the output analyser polariser is orthogonal to the initial polarisation. Under zero applied field the polarisation is effectively rotated by the twisted director. As the applied field increases the nematic reorients parallel to the electric field and the transmitted intensity drops.

In this chapter we have introduced the background material needed to understand chapters chapters 2 to 4. Further details about the liquid crystal modelling can be found in the textbooks by Stewart [110] Chandeskra [27], deGennes [36]

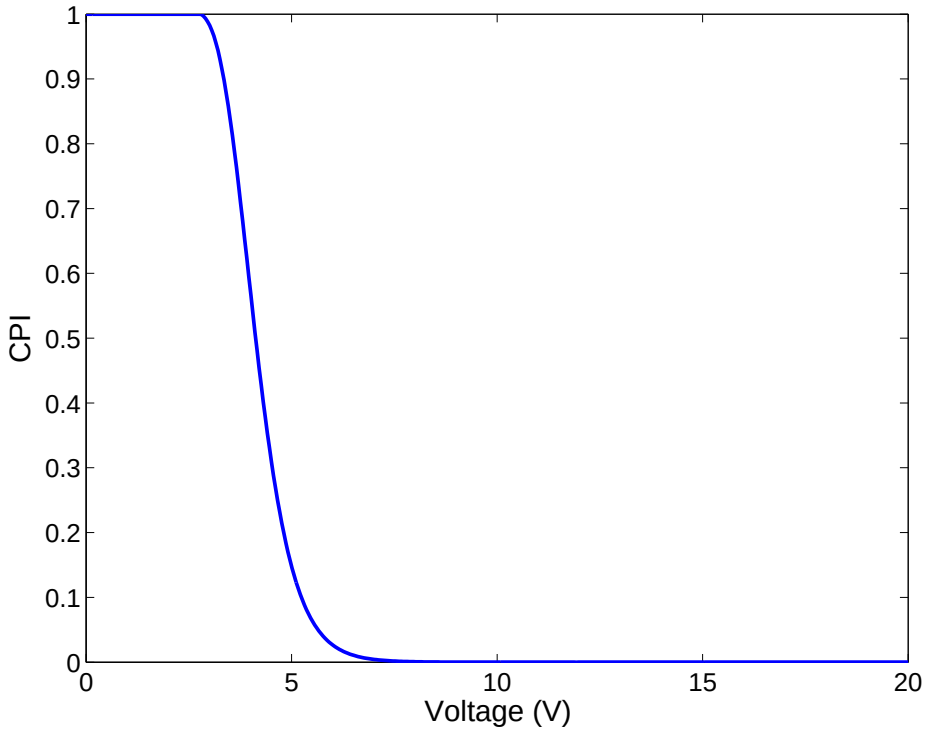


Figure 1.6: Cross polarised intensity for a twisted cell with input polarisation parallel to the initial director. The twisted structure of the director rotates the polarisation of the input beam as a function of the voltage applied to the cell. As the applied field increased the director distorts until it is parallel to the applied field throughout the bulk of the cell. The transmitted intensity was computed using the extended Jones matrix method. The liquid crystal used was E7 with parameters $K_1 = 11.7$ pN, $K_2 = 8$ pN, $K_3 = 19.5$ pN, $\epsilon_{\parallel} = 19.54$, $\epsilon_{\perp} = 5.17$ and $d = 2.4$ $\mu$m.

# Chapter 2

# Measuring liquid crystal properties

## 2.1 Introduction

The Ericksen-Leslie model of a nematic liquid crystal discussed in chapter 1 contains many different material parameters. These material parameters capture the elastic behaviour of a nematic and its dielectric and dynamic properties in a single consistent framework. These parameters take different values for different liquid crystals, are temperature dependent and, in the case dielectric parameters, also frequency dependent. This chapter outlines the work undertaken to develop a new optical measurement techniques to obtain: the elastic constants $K_1$ and $K_3$, the cell thickness and surface pre-tilt, the rotational viscosity $\gamma_1$ and the combination of Leslie viscosities $\alpha_4 + \alpha_5$. The aim of this work was to develop a simple methodology for obtaining relevant parameters using methods that are adapted to the liquid crystal devices investigated in our labs. The methods rely on a simple optical set-up requiring only a stable laser, optical polarisers, a photodiode and a desktop computer outfitted to capture and record the output of the photodiode.

Without an adequate theoretical model it is not possible to obtain a detailed understanding of a given system or to predict its behaviour to new stimuli. Instead the system can be treated as a black box that performs some task, for instance focusing a laser beam. Even in the absence of adequate theory the performance of a system can be still characterised as a function of some externally controlled stimulus. However, using this information to predict the response under different experimental conditions, or combining the results of two separate experiments that utilise a common component is all but impossible without adequate theory. With this observation in mind, reported experimental research can be generally split into two categories, device characterisation and measurement of material parameters.

Device characterisation involves measuring some quantity directly relevant to device

performance such as switching time [111], transition voltage or diffraction efficiency. This can and often is carried out with only a rudimentary understanding of the physics involved. Device characterisation is distinct from the second category measuring material parameters. The latter requires both a valid theoretical model and a fitting procedure. Device characterisation is often pursued to justify investigating a new material, or alternatively, when necessary data or theoretical understanding is lacking. This typically involves two steps: the first is choosing a figure of merit. This is device specific and often has a particular application in mind, for example the switching time [111] for displays or the diffraction efficiency [33] for photo-refractive systems. The second step involves performing a sequence of measurements that can be related to the figure of merit chosen in step one. In the case of a display the switching times, relevant to maximum refresh rate, are often determined by measuring the time taken for a device to undergo a given change in transmitted intensity. By using this methodology it is possible to quantify the change in device performance when different component parts, such as dopant particles, substrate material or liquid crystal mixture, are added or altered, without the need for a complete understanding of the physics involved.

These figures of merit can often be related to material parameter when a valid model is available. This is illustrated by the Frederiks transition and switch on time in a splay cell [110],

$$V_{FT} = \pi\sqrt{\frac{K_1}{\epsilon_0\epsilon_a}}, \tag{2.1a}$$

$$\tau_{on} = \frac{\gamma_1 d^2}{\epsilon_0\epsilon_a\left(V^2 - V_{FT}^2\right)}. \tag{2.1b}$$

respectively where $d$ is the cell thickness, $V$ is the applied voltage, $K_1$ is the splay elastic constant, $\epsilon_0$ is the vacuum permittivity, $\epsilon_a$ the dielectric anisotropy and $\gamma_1$ the rotational viscosity.

Virtually any measurable quantity that is sensitive to the alignment of the liquid crystal, such as the transmitted intensity or capacitance, contains an indication of the Frederiks transition. This typically shows up as a sudden change in the measured variable at around $V = V_{FT}$. As a result the value of $V_{FT}$ is often important for device design and there are many ways to measure to measure its value. However, to move beyond device characterisation and actually determine the values of the material parameters, $K_1$ and $\epsilon_a$, care must be taken to overcome the degeneracy present in equation (2.1a). The simplest way to overcome this problem is to measure the dielectric anisotropy $\epsilon_a$ separately.

This chapter starts with a literature review. Section 2.2 provides a general introduction to some of the main methods used to investigate liquid crystal devices or to measure liquid

crystal material parameters such as: elastic constants, flexo-electric constants, dielectric and conductive properties, cell thickness as-well as boundary pre-tilt and twist angles. Section 2.3 contains a review of methods for measuring the nematic viscosities. In section 2.4 we outline how to obtain many of these parameters from a single optical method. Extensions to the method developed in 2.4 are discussed in section 2.5.

## 2.2 Measuring elastic and dielectric parameters of liquid crystals

Among the methods used to isolate material parameters are: impedance measurements of the complex permittivity [96], chirality induced optical measurements of the flexo-electric effect [26] and capacitive measurements of the dielectric and elastic constants [66]. These techniques all use similar set-ups: liquid crystal filled cells are subjected to externally imposed fields and the optical transmission or impedance of the cell is measured. An example of how elastic constants may be measured is given by Haller [45]. Haller [45] measured the elastic constants $K_1$ and $K_3$ for MBBA by measuring the retardation ($\delta$) of light transmitted through splay and bend cells as a function of the externally applied magnetic field. To determine the elastic constant the relation $H = H_{FT} + b\delta + c\delta^2$ between the phase lag $\delta$ and the applied field $H$ was used. The Frederiks transition field $H_0$ was estimated through least squares fitting to the extrema in the transmitted intensity as a function of applied field $H$. With approximate values for the critical field and existing measurements of the diamagnetic anisotropy, the elastic constants were determined using the expression for the Frederiks transition in the splay or bend geometry. Later in this section we discuss wide area measurements of liquid crystal properties. The method presented is similar to that of Haller but more direct and allows for the determination of $K_1$ and $K_3$ in a single set of measurements without the need to construct different cells.

A similar method was employed by de Jeu *et al.* [50] who determined a full set of elastic constants for the liquid crystals PAA and MBBA. The cross polarised intensity was measured as a function of magnetic field strength and the elastic constants were found from the Frederiks threshold. The threshold itself was determined by extrapolation from measurements made above the threshold. Having found a value for the threshold this was then related to the elastic constant using [50]

$$\left(K_1 + \frac{1}{4}K_3 - \frac{1}{2}K_2\right)\pi^2 = \chi_a H_{FT}^2 d^2, \tag{2.2}$$

where $K_1$, $K_2$ and $K_3$ are the splay, twist and bend elastic constants, $H_c$ is the magnetic Frederiks threshold field, $\chi_a$ is the diamagnetic anisotropy and $d$ is the sample thickness. Hence, after determining the bend and splay elastic constants the value of $K_2$ can be determined. The authors supposed that boundary pre-tilt and weak anchoring effects were the largest sources of error. In particular de Jeu *et al.* [50] note that it was difficult to determine the location of the transition if boundary pre-tilt was present.

To employ either of the above methods, the magnetic anisotropy must be known. The situation is similar if electric fields are used: in this case the dielectric constants are needed. The magnetic susceptibility can be determined by the Faraday-Curie method [22]. This method relies on measuring the force felt by a diamagnetic material in a non-uniform magnetic field through careful use of a balance and an applied field. In such a system the force exerted is directly proportional to the magnetic susceptibility, mass of the sample, field strength and derivative of the field. Hence, measuring the exerted force provides the magnetic susceptibility. Using this technique in the nematic and isotropic phases yields both $\chi_\parallel$ and $\frac{1}{3}\left(\chi_\parallel + 2\chi_\perp\right)$ [22] where $\chi_\parallel$ and $\chi_\perp$ are the magnetic susceptibility measured parallel and perpendicular to $\hat{\boldsymbol{n}}$.

Lastly we discuss measurements of the dielectric constants. The dielectric constants $\epsilon_\parallel$ and $\epsilon_\perp$, which refer to the values obtained with $\boldsymbol{E}$ parallel or orthogonal to $\hat{\boldsymbol{n}}$, may both be obtained from capacitance measurements. The main principle of these measurements is to treat a liquid crystal cell as a planar capacitor and the liquid crystal as the dielectric medium [81]. By measuring the capacitance of a planar cell while under small bias $V$, the value of $\epsilon_\perp$ may be obtained. Similarly under large bias almost all of the liquid crystal is reoriented with the exception of thin layers near the boundaries. Hence, by measuring at high bias it is possible to estimate the value of $\epsilon_\parallel$ [81]. To extract more accurate values the non uniform alignment of the liquid crystal within the cell must be taken into account. This was the approach taken by Meyerhofer [66] who performed capacitance measurements for a mixture of the liquid crystals MBBA and PEBAB [66]. The alignment within a planar cell was computed numerically as a function of voltage. By fitting to the measured capacitance as a function of voltage values for both $\epsilon_\perp$ and $\epsilon_\parallel$ were extracted. The general trend is that the capacitance initially varies linearly with applied voltage $V$, before approaching saturation as $V^{-1}$ [66].

## 2.3 Measuring nematic viscosities: a literature review

The viscosity of an incompressible isotropic Newtonian fluid can be interpreted as its resistance to shearing or tendency to smooth out velocity gradients [110]. The larger the viscosity, the harder it is to shear the fluid. Viscosity also plays a dominating role in determining the interactions of a fluid with a submerged body and the behaviour of a flow near boundaries. In a nematic liquid crystal all of these behaviours are coupled to the orientation of the director. As a result, the viscosity measured in a typical viscometry experiment depends on the alignment of the director. In addition the alignment of the director is itself coupled to the fluid flow. The general picture is that spatially non-uniform reorientation of the nematic induces fluid flow, which can influence the alignment throughout a sample away from the original distortion. The coupling of orientation to fluid flow results in several unusual effects. These include: flow alignment [110] in which the director is aligned relative to the velocity gradient, the optical bounce observed in twisted nematic cells [28] upon removal of a large bias and the asymmetric back-flow [17] responsible for the movement and aggregation of dye particles within a twisted cell.

All of these physical effects are captured by the Ericksen Leslie (EL) theory [38], [57]. The five Leslie viscosity coefficients $\alpha_i$, $i = 1, ..., 5$ introduced in chapter 1 needed to describe these effects can not, in general, be measured independently. Instead experimental results are sensitive to a combination of viscosities determined by the alignment of the nematic throughout the system. By determining which experiments are sensitive to which parameters it is possible to give a physical interpretation to some of the viscosities. In the following section we discuss which combinations of Leslie coefficients allow for such a physical interpretation and how they may be measured. Additional details about the measurement methods cited can be found in the review by Belyaev [9].

### 2.3.1 Mechanical methods

One of the most straightforward ways to understand the physical relevance of the Leslie coefficients is to analyse the behaviour of flow under uniform alignment. By doing this, an analogy can be made to other anisotropic material parameters. For instance, applying an electric field across different crystal axis allows for measurement of different components of the dielectric tensor. This was the approach taken by Miesowicz [67] who performed one of the first experiments to measure the viscosities of a nematic liquid crystal. The Miesowicz viscosities are given in terms of the Leslie viscosities in table 2.1 and are illustrated in

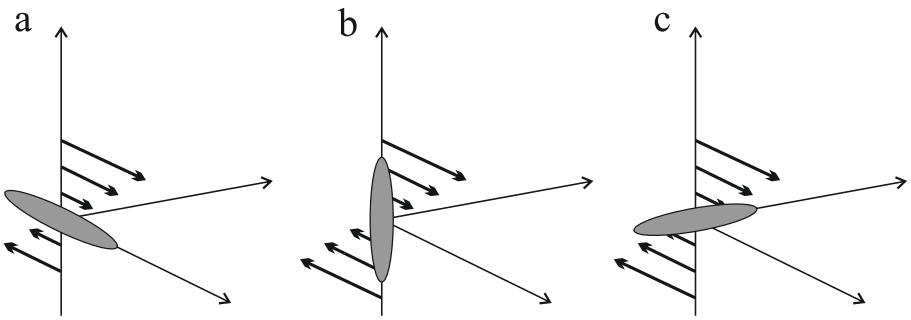


Figure 2.1: Reproduction of figure 4.1 from page 155 of [110] showing the Miesowicz viscosities, arrows represent fluid velocity while the ellipsoids represent the director (a) $\eta_1$, (b) $\eta_2$ and (c) $\eta_3$. We use the convention outlined in [110].

figure 2.1. The Miesowicz viscosities $\eta_1$, $\eta_2$ and $\eta_3$ may be identified with shear flow in which the director is aligned with the velocity, with the velocity gradient or orthogonal to both the velocity and velocity gradient. The fourth Miesowicz viscosity $\eta_{12}$ does not have a simple geometric interpretation and is required to describe the general case of shear flow with arbitrary director configuration [110].

The Miesowicz viscosities can be measured by fixing the orientation of the director with an externally driven magnetic field. Once the alignment of the nematic has been fixed, which constitutes choosing which Miesowicz viscosities to measure, existing viscometery techniques can be employed to measure the chosen viscosity. This method assumes that the chosen alignment is maintained throughout the experiment. One method involves measuring the damping of a submerged oscillating plate under the different director configurations [68]. An alternative experiment used by Beens and de Jeu [8] to measure the two nematic liquid crystals p-methyoxyp′-butylazoxybenze (N4) and p,p′-dibutylazoxybenzene (DIBAB) employs a capillary viscometer. They used a rectangular capillary set-up as shown in figure 2.2. A pressure difference created by gas filled chambers either end of the capillary drives the flow of the nematic through the capillary. As the nematic flows through the capillary, the pressure difference decays exponentially with time. The decay rate of the pressure difference is determined by the viscosity and geometry of the capillary. By measuring the drop in pressure with time the viscosity is inferred. In doing these measurements care must be taken to ensure that the nematic remains in the desired alignment throughout the experiment. Misalignment can be caused by the flow induced torque when measuring $\eta_1$ or $\eta_2$ or by boundary effects more generally. Beens and de Jeu [8] report values from 26°C to 70°C for N4 and from 21°C to 30°C for DIBAB and find that the Parodi relations are satisfied to within experimental error. At 23°C values

found for the LC DIBAB are $\eta_1 = 0.067$, $\eta_2 = 0.015$ and $\eta_3 = 0.025$. The viscosities of N4 are $\eta_1 = 0.0178$, $\eta_2 = 0.024$ and $\eta_3 = 0.047$ at 26°C. For both liquid crystals $\eta_1$ is obtained by using the Parodi relations and direct measurements [8]. For this system the Parodi relations [78] yield

$$\eta_1 = \eta_2 + \gamma_1 \left( \frac{1 + \tan^2(\theta_0)}{1 - \tan^2(\theta_0)} \right). \tag{2.3}$$

Here $\theta_0 \approx 0$ is the flow alignment angle caused by the torque on the director due to the velocity gradient. By using values for $\gamma_1$ obtained by measurements of the dynamics of the Frederiks transition Beens and de Jeu [8] found that the Parodi relations yielded values for $\eta_1$ that are within experimental error.

The dissipation function introduced in the previous chapter (1.15) allows us to identify another viscosity that possesses a physical interpretation, the rotational viscosity $\gamma_1 = \alpha_3 - \alpha_2$. The rotational viscosity is the only viscosity which enters the equations for nematodynamics in the absence of fluid flow. As a result $\gamma_1$ plays a dominant role in setting the typical time scale on which different liquid crystals realign in response to an external stimulus. The Zwetkoff experiment [110] was one of the first methods used to measure the rotational viscosity of a nematic. In it, a cylinder filled with nematic liquid crystal is suspended by a wire along its symmetry axis. A magnetic field is applied orthogonal to the symmetry axis and rotates at constant angular velocity about the cylinder. In such a system, there is negligible fluid flow and the nematic can be considered at rest. The director, however, feels a torque due to the applied field. The nematic transmits the magnetic torque to the cylinder which results in torsion in the suspending wire. The torque is only non-zero because the rotational viscosity is non-zero, that is the director does not equilibrate instantaneously. Instead the director lags behind the rotating magnetic field. Measurements of the torsion in the suspending wire determine the rotational viscosity. Both this experiment and the form of the dissipation function justify interpreting the rotational viscosity as partly defining the time scale on which the nematic reorientates.

This technique has been applied by Prost and Gasparoux [87] to 4′-methoxybenzylidene-4-n-butylanili (MBBA) and 4-n-octyloxyphenyl 4-n-pentyloxybenzoate (8O-O5) for a range of temperatures obtaining the following best fit functional relations

$$\gamma_1 = 3.482 \times 10^{-4} \left( 1 - \frac{T}{319.83} \right)^{0.2942} \exp\left( \frac{841.35}{T - 170.0} \right) \text{ Pa s}, \tag{2.4a}$$

$$\gamma_1 = 1.994 \times 10^{-3} \left( 1 - \frac{T}{357.65} \right)^{0.2783} \exp\left( \frac{590.24}{T - 214.0} \right) \text{ Pa s}, \tag{2.4b}$$

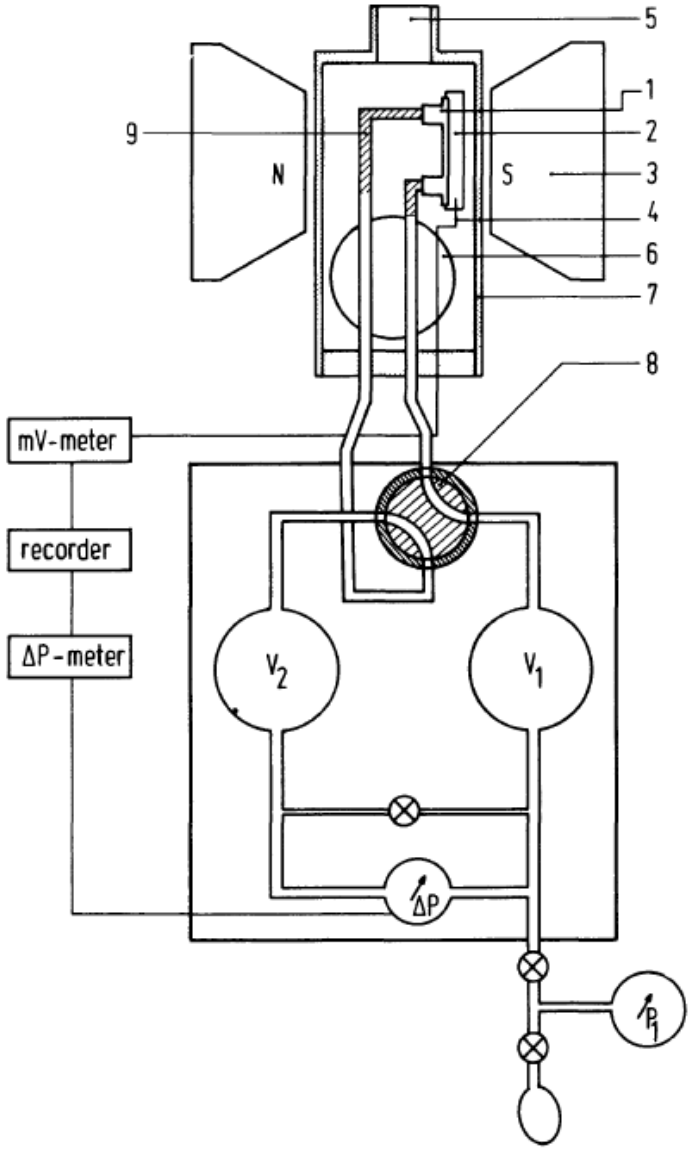


Fig. 5. — Top-view of the set-up for the shear-flow measurements; 1-capillary, 2-brass-holder, 3-magnet, 4-thermocouple, 5-hot air in, 6-hot air out, 7-heated chamber, 8-valve to change pressure direction, 9-liquid crystal.

Figure 2.2: Schematic of experimental set-up originally published by Beens and de Jeu [8]. The nematic is forced through the capillary by the pressure difference created by the two fluid filled volumes $V_1$ and $V_2$. The alignment of the director is controlled by a magnetic field. The rate of flow of nematic through the capillary is related to the pressure difference across the capillary and the viscosity of the nematic. By measuring the decay of the pressure difference the viscosity of the nematic is measured, measured viscosities are given in table 2.3.

| | |
|---|---|
| $\eta_1 = \frac{\alpha_2+2\alpha_3+\alpha_4+\alpha_5}{2}$ | $\eta_A = \frac{\alpha_4}{2}$ |
| $\eta_2 = \frac{\alpha_4+\alpha_5-\alpha_2}{2}$ | $\eta_B = \frac{\alpha_3+\alpha_4+\alpha_6}{2} - \frac{\alpha_3}{2}\left(1+\frac{\gamma_2}{\gamma_1}\right)$ |
| $\eta_3 = \frac{\alpha_4}{2}$ | $\eta_C = \frac{\alpha_4+\alpha_5-\alpha_2}{2} - \frac{\alpha_2}{2}\left(1-\frac{\gamma_2}{\gamma_1}\right)$ |
| $\eta_{12} = \alpha_1$ | |

Table 2.1: Relation between viscosities and Leslie coefficients $\alpha_i$, $i = 1, ..., 5$, Miesowicz viscosities $\eta_1$, $\eta_2$, $\eta_3$ [110] and $\eta_{12}$ and shear wave viscosities $\eta_A$, $\eta_B$ and $\eta_C$ [53].

respectively. In their set-up Prost and Gasparoux [87] fix the magnetic field and rotate the sample.

By taking this approach smaller sample sizes and larger applied fields are possible resulting in greater accuracy.

The final set of mechanical techniques we discuss are the ultrasonic shear wave techniques. Kiry [53] measured the viscosities of PCB by determining its complex shear impedance. Measured viscosities are identified by the same line of reasoning employed to delineate the Miesowicz viscosities. Figure 2.3 taken from Kiry and Martinoty [53] identifies the measured viscosities $\eta_A$, $\eta_B$ and $\eta_C$ defined in table 2.1. Each viscosity is identified by a different relative orientation of the ultrasonic displacement vector and director. The experiment involved measuring the reflection loss and phase change of an acoustic pulse at normal incidence to a nematic quartz interface under different director alignments. The planar alignments were obtained by rubbing the quartz substrate while the homeotropic alignment was obtained by chemical treatment of the surface. The real and imaginary parts of the complex impedance of the sample are related to the impedance of the quartz, reflection loss and phase change [53]. Finally, the viscosity of the nematic is related to the impedance and acoustic frequency. The technique requires precise control over the temperature of the sample in order to accurately measure the phase change. Lastly, this method provides a direct test of the Parodi relations [53, 36]. If the Parodi relations hold, the viscosities $\eta_B$ and $\eta_C$ should be equal. This was confirmed for PCB by Kiry and Martinoty [53].

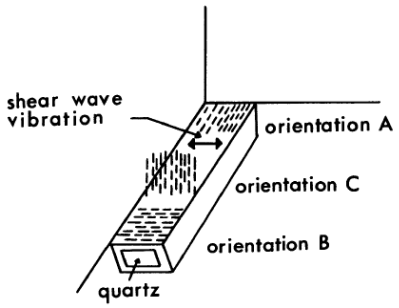


Figure 2.3: Illustration of shear wave viscosities $\eta_A$, $\eta_B$ and $\eta_C$ originally published by Kiry and Martinoty [53].

### 2.3.2 Optical methods

In addition to mechanical measurements various optical techniques exist to determine some combination of viscosity coefficients. It is these newer techniques which generally require smaller sample sizes and do not require specialised viscometry equipment that we will be concerned with for the rest of this section. In general, optical techniques involve measuring the dynamic change in light transmission through a nematic liquid crystal cell. As nematics are birefringent, different polarisations of light are transmitted at different rates. Adjusting the polarisers allow changes in polarisation state, due to the nematic liquid crystal, to be measured as changes in intensity. A typical set-up for a cell with the splay geometry is shown in figure 2.4.

One family of optical techniques involve measuring the change in optical transmission as an applied field is turned on or off. These techniques associate a geometry-dependent time constant $\tau_{on}, \tau_{off}$ with the exponential growth or decay of the director distortions. These time constants, known as switching times, are defined by linearising the governing equations about some initial configuration and seeking exponentially growing/decaying solutions. The switching time is identified as the time constant of the slowest decaying/fastest growing modes. By use of optical set-up similar to figure 2.4, the time dependence of the director translates into a time dependent optical signal. Methods for computing the optical transmission of a liquid crystal cell were discussed in 1.4.2. Calculations of switching times are carried out in [110] for bend and splay geometries with and without fluid flow accounted for. Twisted and super twisted nematic devices are addressed by Tarumi *et al.* [111].

In general, for a cell of thickness $d$ the switch-off time has the form [110]

$$\tau_{\text{off}} = \frac{\gamma_1^* d^2}{K_{eff}}, \tag{2.5}$$

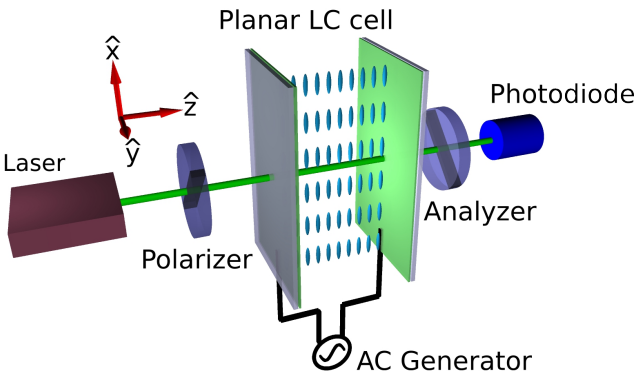


Figure 2.4: Schematic representation of the experimental set-up used for a cross polarised intensity measurement. The nematic is anchored to the glass substrate by means of a rubbed PI layer. A voltage is applied across the cell reorientating the nematic. Light polarised at 45° to the initial director in transmitted through the cell. Components of the polarisation parallel and orthogonal to the initial director are exposed to different refractive indices. The phase difference determines the exit polarisation, the final polariser and analyser allows this change to be measured as a change in intensity.

where $\gamma_1^*$ and $K_{eff}$ are the effective rotational viscosity and elasticity. The exact form is determined by the geometry of the system. The effective viscosity takes into account the flow induced by the evolution of the small deformations. In the splay geometry for small deformations, the effective rotational viscosity differs negligibly from the rotational viscosity. However, this is not the case in the bend and twist geometries. By fitting to measured optical data as a field is applied or removed, values for one or more viscosity coefficients can be measured. This method assumes that the cell-size $d$ and elastic constants $K_{eff}$ can be determined independently. One early optical method optimised for thick $> 150\mu$m homeotropic cells was developed by Pieranski, Brochard and Guyon [20, 80]. Their method involved applying a stepwise magnetic field to a liquid crystal cell and measuring the resulting transient in the transmitted intensity. In these thick cells the transient undergoes many oscillations before decaying. By measuring the time lapse between successive maxima in transmission, a value for the switching time and hence rotational viscosity can be obtained. Wu and Wu [116] used a similar technique to determine the rotational viscosity in a thin $10\mu$m, splay cell. They measured the decay of the phase lag introduced into a linearly polarised light beam by a liquid crystal cell as the nematic relaxed after the application of a stepwise potential. In general, a linear description of the dynamic response is insufficient and the dynamics must be computed by solving the Ericksen Leslie equations numerically. This approach was utilised by Kelly *et al.* [52]: the Ericksen Leslie equations were solved for the response of a twisted nematic device to an applied voltage. By fitting

the time dependent transmission to experimental data, values the values of $\gamma_1$ and $\alpha_4 + \alpha_5$ were found.

A novel method of measuring the rotational viscosity has been suggested by Grinfeld *et al.* [43] which exploits the 'kickback effect' in a splay cell. In the splay geometry, when a large field is applied, the nematic in the centre of the cell aligns. However, at the edges of the cell, a thin layer exists in which the director is rotated through $\pi/2$ radians with respect to the alignment at the centre of the cell in order to obey the boundary conditions. When the external field is switched off, the director first begins to relax at the sides of the cell, where the distortion is large. This reorientation induces shear fluid flow, transferring angular momentum towards the centre of the cell. This results in the counterintuitive situation where the distortion at the centre of the cell initially increases before relaxing. Grinfield *et al.* [43] determined the maximum angle the director is reorientated through by the kickback effect after a large electric/magnetic field is turned off. This angle can be analytically related to the rotational viscosity, bend elastic constant, cell width and the Leslie viscosity coefficients $\alpha_i$ $i = 2, 4, 5$ [43]. Grinfeld *et al.* proposed fitting to the transient in the cross polarised intensity due to the kickback effect, but did not test the technique.

We now examine efforts to accommodate and exploit the temperature dependence of the Leslie viscosities. Wang *et al.* [115] used the work of Haller [46], de Jeu [37] and Imura and Okano [49] to investigate the temperature dependence of the Leslie viscosities. Wang *et al.* [115] included two fundamental effects in their model: variations due to the changing order parameter and variations due to the increased kinetic energy of the molecules. Haller [46] posit the following relation between the scalar order parameter and temperature:

$$S = \left(1 - \frac{T}{T^\dagger}\right)^{\beta_H}. \tag{2.6}$$

Here $T^\dagger$ is a temperature just above the nematic isotropic transition (see Haller [46] for a discussion) and $\beta_H$ (changed from $\beta$ in [46]) a material constant. By measuring the temperature dependence of the refractive index, the authors determined the material constant $\beta$ in (2.6) for E7 and UCF-2. Having determined the relation between order parameter and temperature the authors the relations proposed by Imura and Okano [49] (IO relations) to relate the Leslie coefficients to the order parameter. In these modified relations the Leslie coefficients have a polynomial dependence on the order parameter, as in the original theory developed by Imura and Okano [49]. However, in addition $\alpha_4$ is supposed to have an exponential Arrhenius term to capture the isotropic part of $\alpha_4$. Wang *et al.* [115] also find that $\gamma_1$ is better described by the relation proposed by Wu and Wu [116]. The coefficients

in these expressions are weakly temperature dependent and almost all are universal. As a result they should have the same value for all liquid crystals. By taking advantage of existing MBBA data at a range of temperature Wang *et al.* [115] obtain values for all of the universal parameters viscosity relations. Measurements of the transient optical response of a planar liquid crystal cell at a range of temperatures were used to determine the non-universal parameters. The fitting was done by solving the Ericksen-Leslie dynamic equations to compute the transient response of a splay cell from a highly distorted state. The authors report values for all Leslie viscosities for the liquid crystal mixtures E7 and UCF-02 at $20.3°, 33.3°$ and $46.9°$ for E7 and $70°$ in UCF-02. Though this method is novel and provides a wealth of information there are drawbacks. Firstly the method is not self starting. In order to employ the fitting procedure described in [115] existing temperature dependent data for the Leslie viscosities must be available. This tethers the uncertainty associated with this method to existing data.

We conclude this section, by noting that there exist other classes of measurements. For instance, it is possible to use NMR to probe the relaxation of the director. Bender, Holstein and Geschke [10] used combined magnetic and electric fields to control the director orientation with respect to the magnetic field used by the NMR. For a given set of fields $(B, E)$ different equilibrium configurations are possible. The dynamics of the director as is reaches equilibrium is determined by the fields strength, $\gamma_1$, $\chi_a$, $\epsilon_a$ and the angle between the fields. Using this set-up, they were able to measure different ratios of the rotational viscosity, magnetic and electric susceptibility. By combining their measurements with existing data for $\epsilon_a$, they arrived at values for the rotational viscosity in the temperature range $295 - 325°$ K for the liquid crystal BCH-5 F.F.F.

All of the methods discussed have certain inherent advantages and drawbacks. Mechanical methods are typically very accurate. However, they rely on non standard equipment and require large sample sizes in comparison to optical methods. Existing optical techniques use transient measurements of transmission in various different cell geometries. Though these techniques are simple to apply they place undue weight on the initial director configuration. In section 2.4 we will discuss a new optical method that does not rely on transient measurements. Instead the dynamic optical response of the nematic to a rapidly varying electric field is used.

## 2.4 A new optical method for viscosity measurement

In this section we report a new method for measuring some of the Leslie viscosities of a nematic liquid crystal using a time dependent electric field. We explain in detail how to

extend the standard CPI experiment discussed in 1.4 to measure viscosities and we present results for various different liquid crystals. The viscosity measurements reported in this section were performed by Dr Matthew Proctor (Physics and Astronomy) and the text is partly based on a draft joint paper that we have co-written that will be submitted to Phys. rev. applied.

### 2.4.1 Modelling the nematic response to periodic forcing

Our method is built on a typical cross polarised intensity (CPI) measurements used to determine elastic constants, pre-tilt, birefringence and/or cell thickness as discussed in 1.4. We extend this method by using a time dependent driving potential to probe the dynamics of the liquid crystal. This drives oscillations of the director about an average deflection, determined by the amplitude of the applied field, which lead to modulations of the light phase lag. These are detectable in the standard deviation of the CPI. The director oscillations are coupled to the fluid flow within the cell and as a result optical measurements are sensitive to multiple viscosity coefficients. We have found that for low average deflections, the measurements are sensitive only to the rotational viscosity $\gamma_1$, so that this regime can be used to measure $\gamma_1$. With $\gamma_1$ determined, the oscillations about a larger average deflections can be used to determine $\alpha_4 + \alpha_5$.

We start by examining the equations governing the evolution of the director under the application of a time dependent potential. The director field $\hat{\boldsymbol{n}}$ is parametrised by the angle $\theta$ that it forms with the $x$-axis, $\hat{\boldsymbol{n}} = [\cos(\theta(z)), 0, \sin(\theta(z))]$ where $x$ and $z$ are defined in figure 2.4. In this configuration the fluid velocity of the nematic is given by $\boldsymbol{v} = [v, 0, 0]$. The governing equations take the form of two non-linear coupled partial differential equations that describe the director and fluid dynamics [110]. The governing equation for the director describes a balance between electrostatic torque and the elastic restoring force in the nematic and includes a term coupling the director rotation to the fluid flow. The fluid flow is due entirely to the reorientation of the director. In dimensional form, the governing equations are [110]:

$$[K_1 \cos^2(\theta) + K_3 \sin^2(\theta)]\frac{\partial^2\theta}{\partial z^2} + \frac{K_3 - K_1}{2}\left(\frac{\partial\theta}{\partial z}\right)^2 \sin(2\theta) + \frac{\epsilon_a\epsilon_0}{2}\left(\frac{\partial\phi(z,t;\omega)}{\partial z}\right)^2 \sin(2\theta) - m(\theta)\frac{\partial v}{\partial z} = \gamma_1\frac{\partial\theta}{\partial t}, \tag{2.7}$$

$$\frac{\partial}{\partial z}\left[g(\theta)\frac{\partial v}{\partial z} + m(\theta)\frac{\partial\theta}{\partial t}\right] = 0, \tag{2.8}$$

with

$$m(\theta) = \frac{1}{2}\left[(\alpha_3 - \alpha_2) + (\alpha_3 + \alpha_2)\cos(2\theta)\right], \tag{2.9}$$

and

$$g(\theta) = \frac{1}{2}(\alpha_3 + \alpha_2)\cos(2\theta) - \frac{\alpha_1}{8}\cos(4\theta) + \frac{1}{2}(\alpha_3 + \alpha_4 + \alpha_5 + \alpha_1/4)\ . \tag{2.10}$$

The boundary and initial conditions are,

$$\begin{aligned} &\theta(z=0,t) = \theta_0 \\ &\theta(z=d,t) = 0 \\ &\theta(z,t=0) = \theta_0(1 - \frac{z}{d}) \end{aligned} \tag{2.11}$$

The electric potential is given by

$$\phi(z,t;\omega) = \int_0^z \frac{V(t;\omega)}{1 + \frac{\epsilon_a}{\epsilon_\perp}\sin^2(\theta)} dz' \left( \int_0^d \frac{1}{1 + \frac{\epsilon_a}{\epsilon_\perp}\sin^2(\theta)} dz'' \right)^{-1}. \tag{2.12}$$

In these equations $K_1$ and $K_3$ are the splay and bend elastic constants, $\epsilon_0$ is the vacuum permittivity and $\epsilon_a = \epsilon_\parallel - \epsilon_\perp$ the dielectric anisotropy of the nematic, with $\epsilon_\parallel$ and $\epsilon_\perp$ the component of permittivity along and orthogonal to the director respectively. The rotational viscosity $\gamma_1$ is related to the Leslie viscosity coefficients $\alpha_i$, $i = 1, ..., 5$ by $\gamma_1 = \alpha_3 - \alpha_2$. For most liquid crystals $\alpha_1$ and $\alpha_3$ are small in comparison to the other viscosity coefficients. In formulating our model we have neglected fluid inertia, this is typical and can be justified by analysing the ratio of time scales involved (see [98] chapter 5). The ratio of time scales is set by the number

$$\mathrm{Nr} = \frac{\mathrm{Re}}{\mathrm{Er}} = \frac{\rho K_1}{\gamma_1^2} \tag{2.13}$$

where the Reynolds number is defined as $\mathrm{Re} = \frac{\rho u d}{\gamma_1}$ and the Ericksen's number are defined as $\mathrm{Er} = \frac{\gamma_1 u d}{K_1}$ with $u$ is a characteristic velocity. For a typical liquid crystal with parameters $\gamma_1 \sim 100$ mPas, $\rho = 1000$ kgm$^{-3}$ and $K_1 = 10$ pN we have $\mathrm{Nr} = 10^{-6}$. Hence any effect due to fluid inertia is negligible and the flow equilibrates one million times faster than the director does. With a given solution for $\theta(z,t)$, the cross polarised intensity is given by equation (1.44). The oscillations in the director lead to modulations in the phase shift across the cell detectable in the dynamics of the CPI trace. The standard deviation of the CPI gives a measure of the dynamic response of the nematic and can be used to measure its viscosities.

In order to do this, it is important to understand the role played by the major viscosities in equation (2.7) and (2.8). First we note that $\alpha_1$ and $\alpha_3$ are in general small in comparison to the other Leslie coefficients. As discussed in section 2.3 page 47 $\gamma_1 = \alpha_3 - \alpha_2$ sets the time scale on which the director responds to an applied field and in conjunction with $\gamma_2 = \alpha_3 + \alpha_2 \approx -\gamma_1$ determines the strength of the coupling function $m(\theta)$. From the form of $g(\theta)$ in equation (2.10) we can see that the combination $\alpha_4 + \alpha_5$ plays a role in setting the magnitude of the velocity gradient regardless of the orientation of the nematic. For a sinusoidal applied field, the measured signal is, in general, sensitive to both $\gamma_1$ and $\alpha_4 + \alpha_5$ and these two parameters cannot be determined independently from CPI data. As an example, figure 2.5 shows the standard deviation of $\theta(z,t)$ and the velocity profile for different values of $\gamma_1$ and $\alpha_4 + \alpha_5$, each of which produces the same value for the standard deviation of the CPI. To produce figure 2.5 the governing equations (2.7) and (2.8) were solved numerically using spectral collocation [113] to discretise in space and an implicit variable step algorithm (Matlab routine ode15s) to integrate in time. The oscillations in $\theta$, shown in figure 2.5, towards the edges of the cell are driven directly by the alternating potential: here the LC alignment is not saturated by the strength of the electric field and the time variations of the latter can induce fluctuations in the former. These, in turn, induce the fluid flow responsible for driving the oscillations at the centre of the cell. Decreasing the value of $\gamma_1$ primarily increases the oscillations at the edge of the cell, as the nematic is more able to follow the alternating potential, while $\alpha_4 + \alpha_5$ governs the overall velocity gradient which plays a dominant role in setting the amplitude of the oscillations at the centre of the cell. Degeneracy in the measurement of $\gamma_1$ and $\alpha_4 + \alpha_5$ is present because the optical measurements are insensitive to the region the oscillations are taking place in, and as a result it is possible to compensate for a change in $\gamma_1$ by changing $\alpha_4 + \alpha_5$.

The degeneracy shown in figure 2.5 can also be detected by examining the relevant minimisation landscape. When performing fits it is typical to minimise the sum of the squared difference between theoretical and experimental values. For a two parameter fit this process is equivalent to finding the lowest point on a landscape whose height is the residual of the square distance, the minimisation landscape. Figure 2.6 shows the minimisation landscape for simulations of the standard deviation of the CPI for voltage values 3 to 20 V peak to peak at a frequency of 500 Hz. For the left plot the true values of the viscosities were chosen to be $(\gamma_1, \alpha_4 + \alpha_5) = (269.8, 296.7)$ mPas, for the right $(\gamma_1, \alpha_4 + \alpha_5) = (242.8, 445)$ mPas. The landscapes have a clear valley structure and shows saturation at large $\alpha_4 + \alpha_5$. The valley structure indicates the same degeneracy as in figure 2.5. The for the left-hand plot in figure 2.6 moving along the valley corresponds

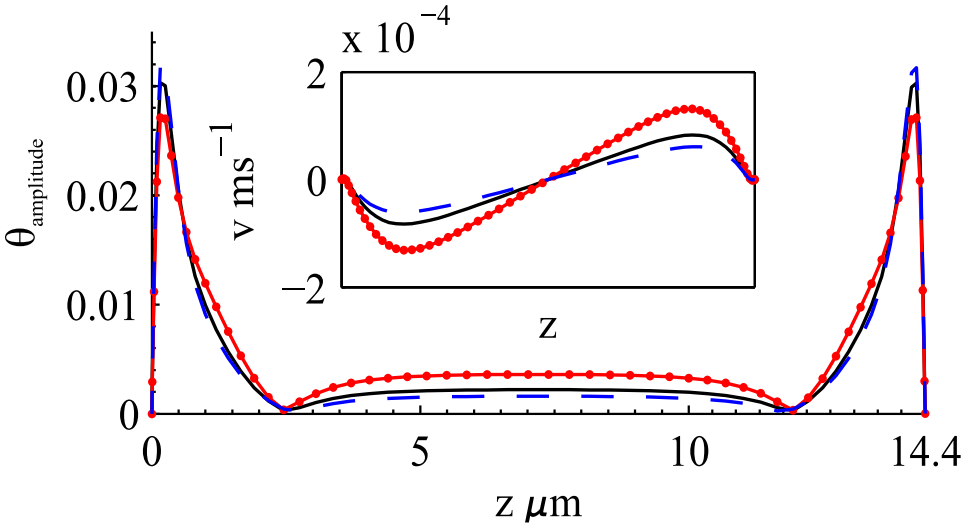


Figure 2.5: Amplitude of the director oscillations and velocity profiles across a standard cell. The cell is driven by a 500 Hz sinusoidal voltage with a 20 V peak to peak amplitude. For the solid black line $\gamma_1 = 203.6$ mPas and $\alpha_4 + \alpha_5 = 431$ mPas. The red dash-dot and the blue dash lines correspond to a change of $\gamma_1$ of $\pm 10\%$ respectively. In both cases $\alpha_4 + \alpha_5$ has been adjusted so that the standard deviations of the CPI was *unchanged*.

to compensating for a change in $\gamma_1$, which alters the oscillations at the edges of the cell, by changing $\alpha_4 + \alpha_5$, which effects the oscillations at the centre of the cell. There is a slightly different feature apparent in the right-hand plot. The valley becomes vertical for large $\alpha_4 + \alpha_5$ because at large $\alpha_4 + \alpha_5$ there is very little fluid flow and as a result the oscillations at the centre of the cell shown in figure 2.5 are negligible. Hence, increasing $\alpha_4 + \alpha_5$ further does not alter the behaviour of the nematic significantly. With this in mind we may also interpret $\alpha_4 + \alpha_5$ as controlling the (inverse) strength of the coupling between the director and velocity field. At low values the coupling is strong and fluid flow is easily induced.

However, it is possible to break this degeneracy by operating at a low voltage. To measure $\gamma_1$ we require that equation (2.7) is uncoupled from the flow velocity of the nematic, as in this way only $\gamma_1$ enters the governing equation for $\theta$. This can be achieved if the velocity gradient is small. From equation (2.8) we see that it is driven by the source term $m(\theta)\frac{\partial \theta}{\partial t}$. Examining equation (2.9) and using the assumption that $\alpha_3$ is small, a value of $\theta \approx 0$ will cause $m(\theta)$, and hence the source term in equation (2.8), to vanish.

As a result, oscillations in the director close to the $\theta = 0$ state are sensitive only to $\gamma_1$ and their amplitude can be used to estimate this parameter. Once $\gamma_1$ is known, $\alpha_4 + \alpha_5$ can be estimated by the CPI oscillation amplitude at high voltage. We explore these two regimes theoretically in the next subsection before presenting experimental results.

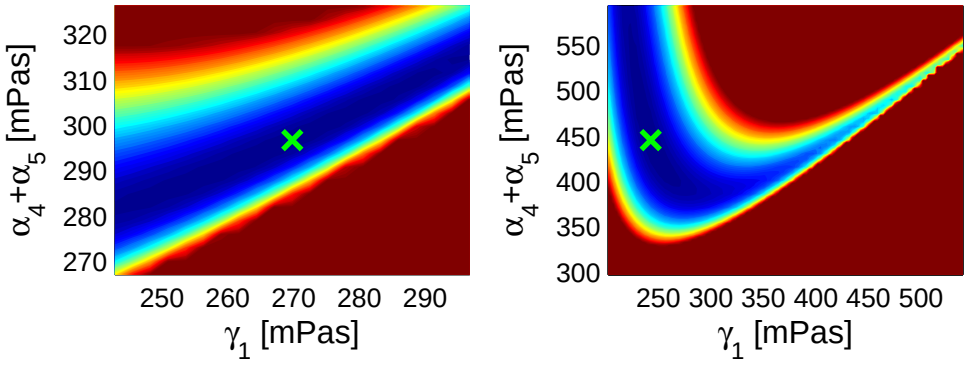


Figure 2.6: Optimisation landscapes for two different sets of viscosity values. Colour indicates the residual of the least square distance, blue being $\approx 10^{-6}$ and red being $> 10^{-3}$. The green cross indicates the true value of the viscosities used. The main feature is the valley structure showing a degeneracy between $\gamma_1$ and $\alpha_4 + \alpha_5$. In particular for a liquid crystal with low $\gamma_1$ and high $\alpha_4 + \alpha_5$ the valley is aligned with the $\alpha_4 + \alpha_5$ axis.

### 2.4.2 Low voltage measurement regime

To determine $\gamma_1$ we use a modulated potential of the form

$$V(t) = V_a \cos(2\pi f_H t) \left[1 + V_b \cos(2\pi f_l t)\right], \tag{2.14}$$

where $f_H \gg f_l$ is chosen so that the liquid crystal is unable to follow the rapid oscillations. This choice also has the additional benefit of minimising ion movement. This form of the potential is chosen so that the mean deflection can be set independently from the oscillations of the director. Figure 2.7 shows the general trend in the standard deviation of the oscillations of the CPI for mean deflection just above the Frederiks threshold. The mean CPI is shown as an inset, the red region shows the range of the oscillations. The oscillation amplitude varies as $1/\omega$ and saturates at low frequency. At saturation the director is able to follow the oscillating potential almost perfectly. To determine $\gamma_1$ we use the linear regime.

### 2.4.3 High Voltage measurement regime

To obtain value for $\alpha_4 + \alpha_5$ we seek a regime with large coupling to the flow. To this end we have used both numerical and analytical approaches. As noted previously at low deflection there is negligible coupling between the liquid crystal alignment and the fluid flow. Using the method of matched asymptotic expansions to seek high voltage solutions

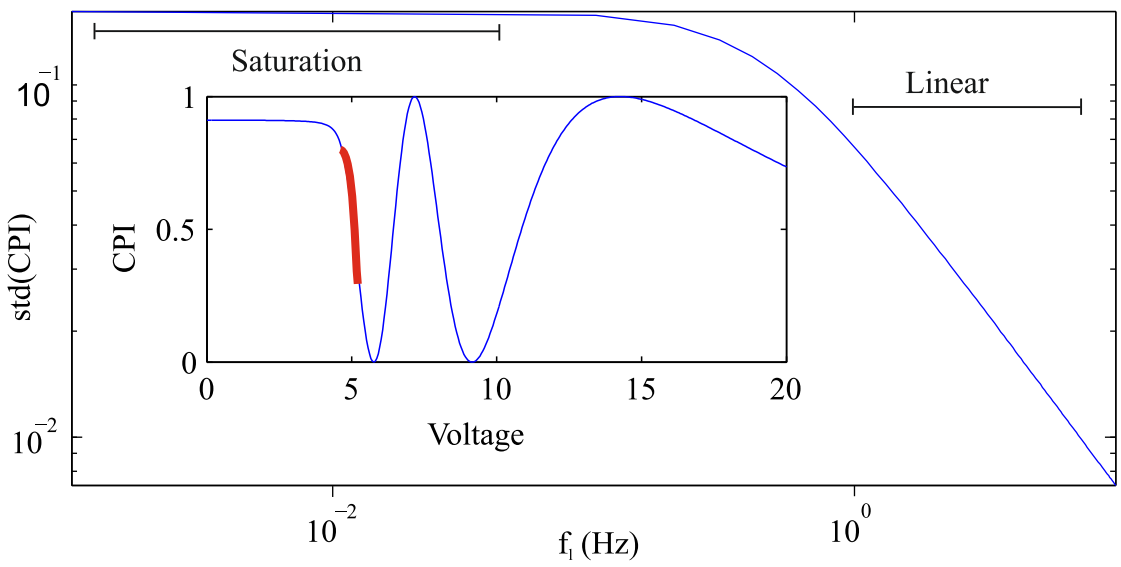


Figure 2.7: Trend followed by the oscillations of the director as a function of the frequency $f_l$. The inset shows the corresponding mean CPI, the red region bounds the typical range of the oscillations. The linear regime is used to obtain values for $\gamma_1$.

to equations (2.7) and (2.8) we obtain leading order expressions for the deflection of the director and the velocity of the nematic. The details of the derivation are in appendix A.1 and the main results are given by equations A.27.

Figure 2.8 shows the agreement between the matched asymptotics and numerical results for the director oscillations and fluid flow. The asymptotics capture the shape and magnitude of the oscillations well, however, the asymptotics predict that there are times at which the amplitude of the director oscillations vanishes everywhere throughout the cell simultaneously. This feature is not present in the numerical simulations. For this reason we do not use the analytical results when fitting to experimental data. This is likely caused by a simplifying assumption in which the full detail of boundary layer structure present in the mean deflection was neglected when computing the boundary layer in the oscillations.

### 2.4.4 Experimental method

This section summarises the CPI experiments performed by Dr. M. Proctor. The experimental set-up is identical to that outlined in section 1.4.1.

Standard LC cells were prepared using ITO glass substrates, coated with rubbed polyimide (PI). They were filled with one of the three LCs chosen for this investigation. The choice of LCs (E7, TL205, ZLI4792) was driven by the availability in the literature of their

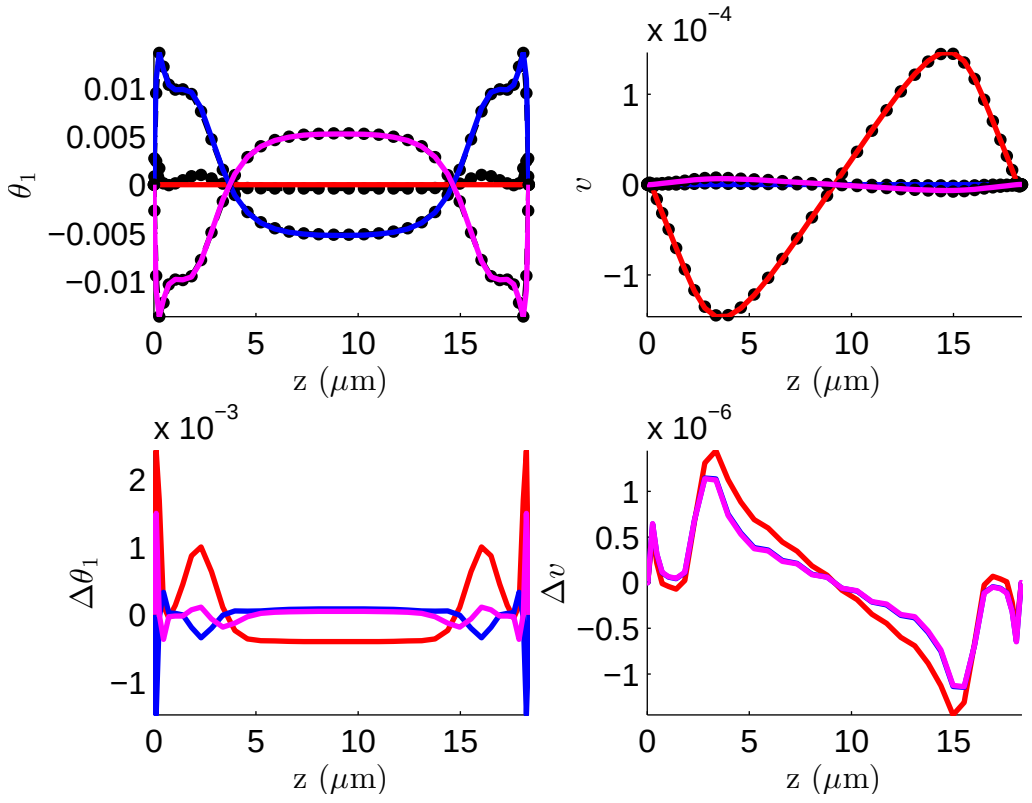


Figure 2.8: Comparison of the solution to equation (A.26) and of equation (A.27) to numerical simulations for an 18 $\mu$m cell filled with the liquid crystal E7. (Left) $\theta_1$ the oscillations in $\theta$ and $\Delta\theta_1$ the difference between numerical and asymptotic solutions. (right) Comparison of velocity profiles $v$ and point-wise errors $\Delta v$. The results from the matched asymptotic expansions are in red, the blue points/broken line are from numerical simulations, different curves correspond to 1/4, 1/2 and 3/4 of a period. The agreement of the velocity shown on the right hand panels is excellent and ,due to symmetry, the blue curve in $\Delta v$ is masked by the purple curve. However, the oscillations in $\theta$ shown on the left panels predicted by the matched asymptotics fail to account for the relative phase of the oscillations at different points in the cell.

physical, electrical and optical parameters, so our results could be compared with them and verified. In order to test the method using a range of cell thickness, different sized spacer beads were used.

The experiment had three aims: to determine the static parameters of the liquid crystal namely $K_1$ and $K_3$, to determine $\gamma_1$ and to determine $\alpha_4 + \alpha_5$. The first step was to ramp the amplitude of a 10 kHz voltage from 0-20 V peak to peak, and measure the average intensity at each voltage; the resulting data were used to fit values for $K_1$, $K_3$, the cell thickness, and pre-tilt. The fitting procedure for all of the experimental data is described in more detail in 2.4.5.

To measure $\gamma_1$ we used the potential given by equation (2.14). As discussed previously this allows independent tuning of the mean deflection and oscillations as well as minimising ion movement. Values of $V_a$ and $V_b$ that result in a large variation of the CPI while inducing only a small variation of $\theta$ were chosen. Typically the voltage would vary by $\sim 5\%$ about a point close to the Frederiks transition. The frequency $f_H$ was set to 10 kHz, while the frequency $f_l$ was ramped in steps of 0.5 Hz from 0.1 Hz to 9.6 Hz. $\gamma_1$ was then used to fit to the data. This corresponds to the linear region in figure 2.7.

The measurement of $\alpha_4+\alpha_5$ was performed by ramping the amplitude of a 500 Hz signal from 0 V to 20 V peak to peak in steps of 0.02 V(E7), 0.04 V(ZLI4792) and 0.05 V(TL205), waiting 5 s for the transient to elapse and measuring the crossed polarised intensity at each voltage value for 0.02 s. The standard deviation of the signal at each point was extracted, and the resulting data were fitted by varying $\alpha_4 + \alpha_5$, and using the previously measured value of $\gamma_1$.

### 2.4.5 Fitting and Validation

In order to compute the cross polarised intensity, the governing equations (2.7) and (2.8) were solved in Matlab using the method detailed by Mottram et al [70] to reduce the coupled governing equations (2.7) and (2.8) to a single equation for $\theta$ containing a non local source term representing the flow. A spectral collocation method [113] was used to discretise space, and an implicit variable step algorithm (Matlab routine ode15s) to integrate in time. As noted previously $\alpha_1$ and $\alpha_3$ are generally very small in comparison to the other viscosities and so we have taken $\alpha_1 = 0$ mPas bad $\alpha_3 = 0$ mPas.

To compute the cross-polarised intensity the integral in equation (**??**) was computed using a Clenshaw-Curtis quadrature [113]. Its average and standard deviation were extracted to compare it with the experimental data.

Fitting of the experimental data was done in two steps. First, the average of the cross polarised intensity taken at 500 Hz and 10 kHz was fitted giving values for the cell size,

| | $d$ | $\theta_0$ | $K_1$ | $K_3$ | $\gamma_1$ | $\alpha_4 + \alpha_5$ |
|---|---|---|---|---|---|---|
| E7 [115] | 14.4 $\mu$m | 0.5° | 10.9 pN | 18.0 pN | 203.6 mPa s (280.8 mPa s) | 431 mPa s (316.8 mPa s) |
| TL205 | 15.0 $\mu$m | 1.22° | 16.5 pN | 20.3 pN | 303.0 mPa s (367 mPa s) | 403.0 mPa s |
| ZLI4792 [52] | 11.7 $\mu$m | 1.78° | 14.8 pN | 19.8 pN | 109.6 mPa s (95.0 mPa s) | 133.4 mPa s (115.0 mPa s) |

Table 2.2: Cell and material parameters for fitted viscosities for E7, TL205 and ZLI4792 obtained from the fits shown in figures 2.9-2.11. The available literature values are reported in parenthesis below the corresponding fitted values. The literature parameters were measured at 20.3°C, 20°C and "room temperature" respectively for the three LCs. The TL205 literature datum is from the corresponding Merck data sheet.

| | $n_0$ | $n_e$ | $\epsilon_\parallel$ | $\epsilon_\perp$ | $V_a$ | $V_b$ |
|---|---|---|---|---|---|---|
| E7 | 1.5282 | 1.7558 | 19.54 | 5.17 | 2.875 | 0.0365 |
| TL205 | 1.527 | 1.744 | 9.1 | 4.1 | 5.54 | 0.018051 |
| ZLI4792 | 1.4794 | 1.5763 | 8.3 | 3.1 | 5.6750 | 0.0485 |

Table 2.3: Optical, dielectric and voltage parameters used for numerical simulation. $V_a$ and $V_b$ define the voltage form given by equation (2.14) and $V_a$ is peak to peak.

elastic constants and pretilt. These values were then used when fitting the viscosities to the standard deviation of the oscillations of the CPI measured in the two regimes. The cell thickness $d$ determines the maximum polarisation phase shift in propagation. The pretilt $\theta_0$ regulates how sharp the Frederiks transition is and, in conjunction with $d$, determines the zero voltage intensity. The splay elastic constant $K_1$ locates the Frederiks transition and controls the low voltage portion of the trace. The bend elastic constant $K_3$ only affects the high voltage behaviour.

Fitting was done using a least square algorithm (Matlab routine `lsqrcurvefit`) as follows: first the cell thickness, pretilt and splay elastic constant were fitted to the low voltage portion of the trace (up to just above the Frederiks transition). With the values of the cell thickness and pretilt fixed the entire data trace was fitted using the two elastic constants as fitting parameters. The fitted values of thickness, pretilt and elastic constants determined from the average of the 500 Hz or 10 kHz data were used for subsequent fits to the standard deviation of the 500 Hz and amplitude modulated data.

Once thickness, pretilt and elastic constants were known, the viscosities were obtained by a least square fit minimisation. The fit was performed using the Matlab constrained optimisation function `fmincon` and the `active-set` and `sqp` algorithms. Where available, we have used literature values of the viscosities as starting point for the minimisation process (see table 2.2). Otherwise, reasonable guesses were used. To ensure convergence, we have used an iterative fitting procedure. The low voltage, low frequency measurements were fitted using only $\gamma_1$ as a fitting parameter and keeping $\alpha_4 + \alpha_5$ fixed. With $\gamma_1$ thus found, the high voltage data was used to determine $\alpha_4 + \alpha_5$. With these updated values for $\gamma_1$ and $\alpha_4 + \alpha_5$, the process was repeated to ensure convergence. The final fitted values of $\gamma_1$ and $\alpha_4 + \alpha_5$ are shown in table 2.2 and the values of the non fitted parameters are shown in table 2.3.

We have verified that the fitted values of $\gamma_1$, deduced from the low frequency measurements, are independent of $\alpha_4 + \alpha_5$. To this end we have determined the minimisation landscape in a neighbourhood of the fitted values for $\gamma_1$ and $\alpha_4 + \alpha_5$. The degeneracy between these two sets of parameters discussed in section 2.4.1 implies that the landscape has the shape of a valley steep in one direction, but fairly flat in the other. As discussed in section 2.4, in general, increasing $\gamma_1$ while decreasing $\alpha_4 + \alpha_5$ just moves the minimisation point along the floor of the valley thus making it impossible to determine independently these two sets of parameters. However, in the case of the low frequency measurements that we have used to determine $\gamma_1$, the minimisation valley is approximately parallel to the $\alpha_4 + \alpha_5$ direction so that the fit is several orders of magnitude more sensitive to $\gamma_1$ than $\alpha_4 + \alpha_5$, as expected (and desired).

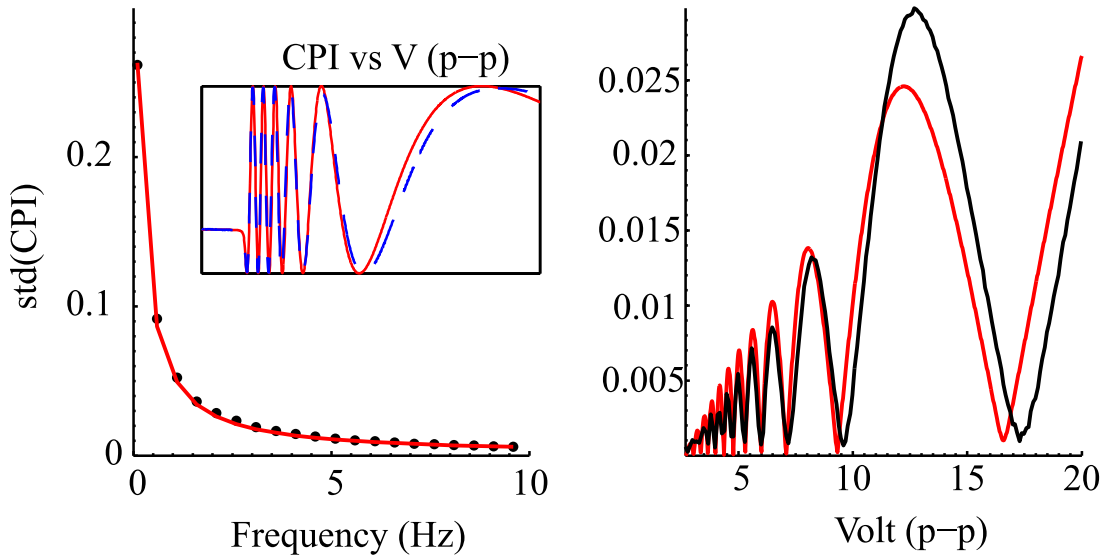


Figure 2.9: Fit to average and standard deviation of cross polarised intensity for E7. Left: low frequency regime, solid red curve is theoretical fit black points are experimental. Right: high frequency regime, solid black line is experimental data solid red curve is theoretical fit. Insert: average CPI as a function of peak to peak amplitude: solid red line is theoretical fit broken blue line is experimental data.

The experimental data along with the fits to Ericksen–Leslie theory are shown in figures 2.9-2.11 while the fitted parameters and comparison with the literature values are reported in Table 2.2. In general the theoretical fits agree well with the experimental results and the obtained viscosity values are physically reasonable and in good agreement with the literature.

### 2.4.6 Conclusions

We have presented a versatile and elegant technique, based on a familiar experimental set-up, that quickly yields values for $\gamma_1$ and $\alpha_4 + \alpha_5$. The method was verified for some well known liquid crystals, such as E7, TL205 and ZLI4792, providing values of $\gamma_1$ and $\alpha_4 + \alpha_5$ that are in good agreement to those found in the literature, as well as elastic constants, cell thickness, and pretilt. This is done by working in a regime where $\alpha_4 + \alpha_5$ does not affect the fluid flow, followed by working in a regime where both coefficients are relevant. Time constants can then easily be calculated using the fitted parameters. Discrepancies between measured and literature values can be attributed to experimental conditions, most likely the differences in the temperature at which the time constant was measured. As an added

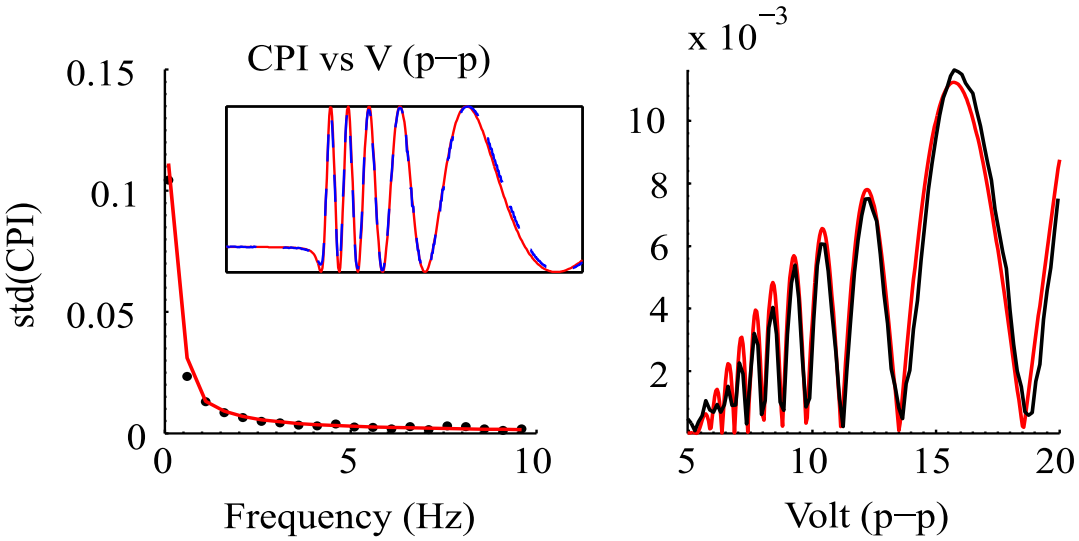


Figure 2.10: As in figure 2.9, except that the LC is TL205.

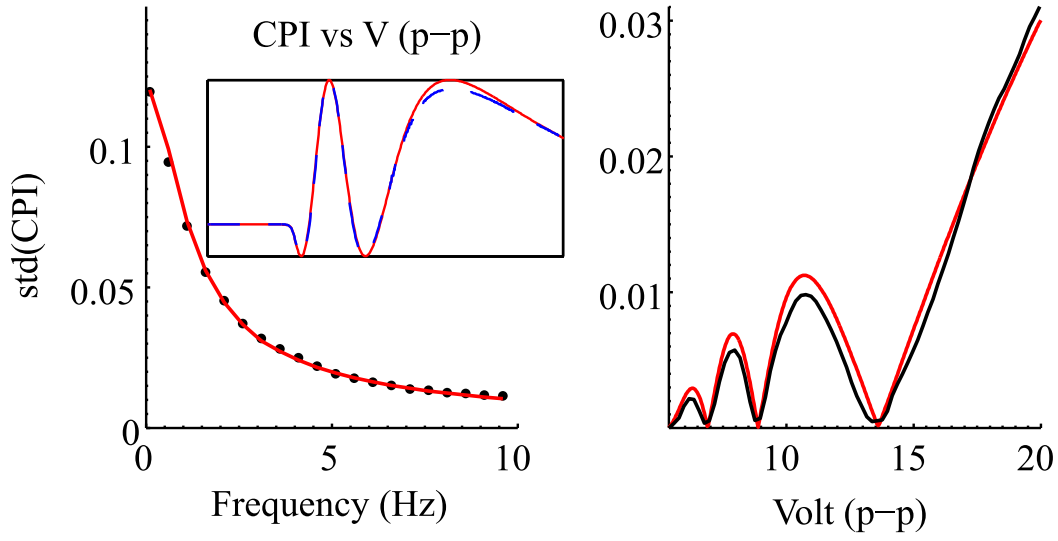


Figure 2.11: As in figure 2.9, except that the LC is ZLI4792.

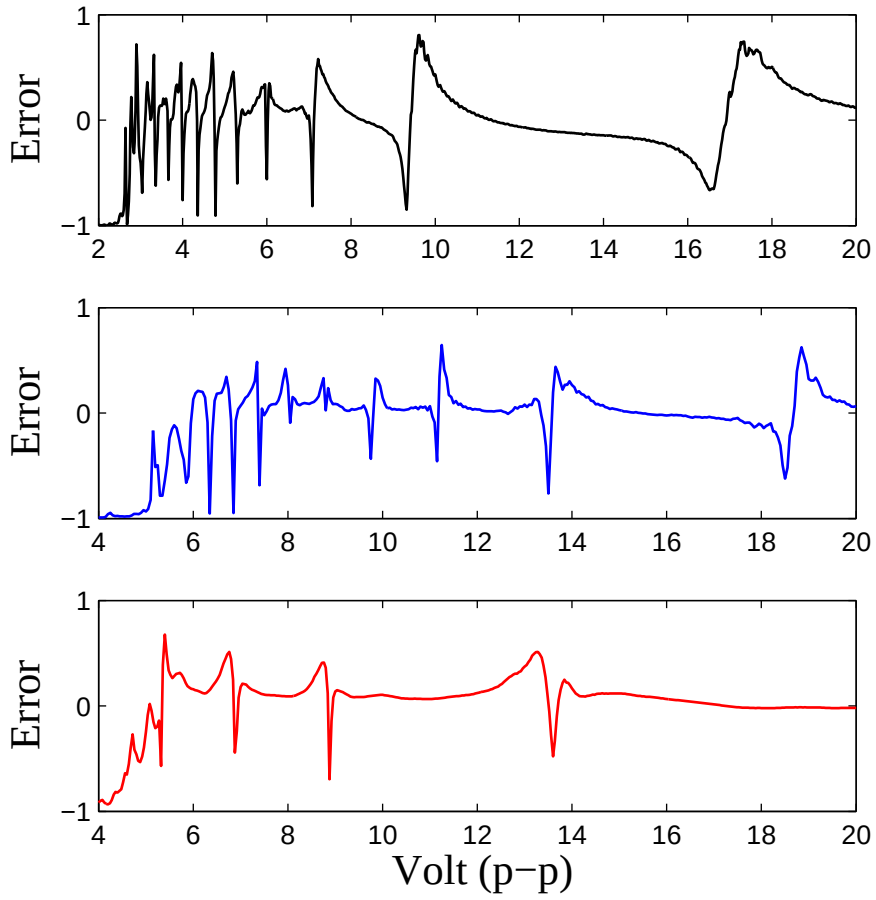


Figure 2.12: The relative error on the high voltage 500 Hz measurements of the CPI from top to bottom E7 (black), TL205 (blue) and ZLI4792 (red). The error is defined as the ratio of the difference between experimental and theoretical values divided by their sum.

bonus, the analysis of the measurement procedure and the complementary roles of $\gamma_1$ and $\alpha_4 + \alpha_5$ give a very clean and insightful example in the complex, but rewarding world of fluid dynamics of liquid crystalline materials.

The method described here is very general and could be extended in some fashion to different geometries, e.g. twisted cells, and LCs, including novel materials such as nematic LCs doped with nano-particles [24]. The main issue with extending this method to alternative geometries is retaining the ability to separate the viscosities. We now explore how this method may be extended to characterise devices by using multiple measurements taken at different points on the LC cell.

## 2.5 Wide area measurements of liquid crystal and cell parameters

In this section we investigate how to use multiple measurements of the CPI taken at different points on the cell to obtain information about the splay and bend elastic constants of the liquid crystal, cell thickness and pre-tilt. We also discuss the use of statistical methods to obtain effective bounds on the measured parameters. The measured CPI data used in this section was obtained by Master students Matthew Sugden and Roger Kirke under the supervision of Dr. M. Proctor and Prof. M. Kaczmarek. The statistical methodology was devised with the help of Prof J. Forster.

The aim of this project is to measure variations in material parameters of a LC filled cell over a relatively wide area. This system is composed of two components: the liquid crystal and the cell hosting the liquid crystal. All parameters related to the liquid crystal must necessarily be constant across measurements performed using a particular cell. Hence, significant variations in the measured CPI indicate non-uniformities in the cell itself. In addition to detecting non-uniformities the method developed here allows for a more accurate determination of the liquid crystal elastic constants and an estimate of the error on the measured parameters.

In the following subsections we detail the numerical model of the nematic, the statistical methods used to analyse the data and finally we discuss the initial results of this project.

### 2.5.1 Theoretical modelling of the cross-polarised intensity measurements

The steady director field at a given voltage is determined from Frank-Oseen theory discussed in chapter 1 and the electric potential is modelled by Maxwell's equation for the

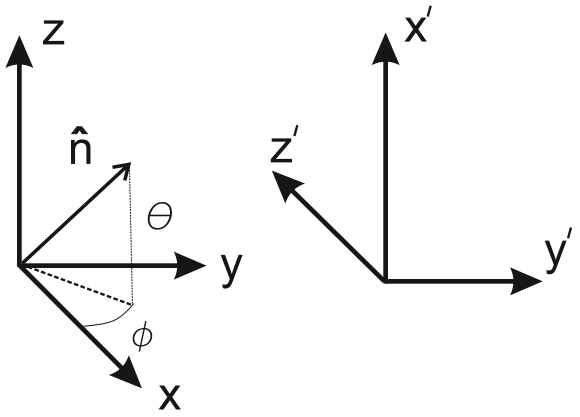


Figure 2.13: The relation between the unprimed coordinate system used in 2.4 and that used to account for pre-twist at the boundary.

electric displacement field. We minimise the Frank free energy given by equation (1.4) for the general case of a director field within a twisted cell. If the standard spherical coordinate angles $(\theta, \phi)$ shown in figure 2.13 are used to parametrise the director the twist angle becomes undefined when $\theta = \frac{\pi}{2}$. To avoid this problem we used a rotated coordinate system given by

$$\begin{bmatrix} x \\ y \\ z \end{bmatrix} = \begin{bmatrix} 0 & 0 & -1 \\ 0 & 1 & 0 \\ 1 & 0 & 0 \end{bmatrix} \begin{bmatrix} x' \\ y' \\ z' \end{bmatrix}, \tag{2.15}$$

where the unprimed and primed systems are shown in figure 2.13. The polar coordinate angles associated with the primed system are $(\alpha, \beta)$. Using this system the director is given by $\hat{\boldsymbol{n}} = (-\sin(\beta), \cos(\beta)\sin(\alpha), \cos(\beta)\cos(\alpha))$ where $\alpha$ is measured up from the $x'$-$y'$ plane and $\beta$ is measured from the $x'$ axis within the $x'$-$y'$ plane. By using this coordinate system we do not encounter a coordinate singularity provided the net twist does not exceed 90°. The Frank-Oseen equations where solved using spectral collocation to discretise in space and the implicit MATLAB routine ode15s to integrate in time. To compute the transmitted intensity we use the extended Jones matrix method, details may be found in the papers by Lien [58] and Yu and Kwok [117].

### 2.5.2 Fitting and statistical methods

We use a statistical model to obtain an estimate of the variation of $d$ and pre-tilt across a large area of the cell. We assume that the data measured at each site corresponds to sampling from an unknown multivariate normal distribution $\mathcal{N}(\boldsymbol{\mu}(\boldsymbol{x}, V), \Sigma(V))$ with mean vector $\boldsymbol{\mu}(V)$ and covariance matrix $\Sigma(V)$, with $V = V_i, i = 1, 2, ..., N_V$ the voltage values

at which the CPI is measured and $\boldsymbol{x}$ the position on the cell. It is important to note that we have assumed the covariance matrix does not depend on position within the cell. We have allowed for the mean intensity to vary with position to account for variations in thickness, pre-tilt or other parameters. Conversely sources of error, which are captured by the covariance matrix, are assumed to be identical at every point.

To obtain accurate estimates of the cell and material parameters we estimate both $\boldsymbol{\mu}$ and $\Sigma$ for low voltages only, as we extract cell size and pre-tilt from the low voltage part of the CPI. This involves fitting to multiple data traces measured at different locations on the cell. Once we have estimated $\boldsymbol{\mu}$ and $\Sigma$, a parametric bootstrap method is used to obtain error estimates on $d$ and pre-tilt. The bootstrapping process involves generating a large number of traces with mean $\boldsymbol{\mu}(\boldsymbol{x}, V)$ for each cell site $\boldsymbol{x}$ with noise determined by $\Sigma$. By fitting to these traces we obtain a range of values for $d$ and pre-tilt for each cell site, from which we infer standard errors on both parameters. In other words we estimate the distribution governing the experimental data and use this to estimate uncertainties in $d$ and pre-tilt. We now describe the procedure used to estimate $\boldsymbol{\mu}$ and $\Sigma$.

The first stage in the analysis of the experimental traces is to perform a least squares fit to obtain the material and cell parameters $K_1$, $K_3$, $d$ and pre-tilt. As the elastic constants $K_1$ and $K_3$ are properties of the liquid crystal used, they must not vary from measurement to measurement. To enforce this constraint we divide the data for each cell into $N_s$ subsets containing $N_t$ traces and fit to each subset using $N_t$-independent values for $d$ and pre-tilt and a single value for $K_1$ and $K_3$. For this portion of the fitting only we utilise the full range of voltage values measured, several hundred points in the range $0 \leq V \leq 20$ Volts. From the $N_s$ values for the elastic constants we compute the sample means $\hat{K}_1$, $\hat{K}_3$ which we take as an estimate of the true value of $K_1$ and $K_3$. Next we fit to the low voltage portion of the traces using the values obtained for the splay and bend constants in the previous step.

The covariance matrix $\Sigma(V)$ is estimated as [112]

$$\hat{\Sigma} = \frac{1}{N_p} \sum_{i=1}^{N_p} \left( \boldsymbol{I}_{exp}(\boldsymbol{x}_i, \boldsymbol{V}) - \boldsymbol{g}(\boldsymbol{x}_i, \boldsymbol{V}) \right) \left( \boldsymbol{I}_{exp}(\boldsymbol{x}_i, \boldsymbol{V}) - \boldsymbol{g}(\boldsymbol{x}_i, \boldsymbol{V}) \right)^T . \tag{2.16}$$

Here $N_p$ is the number of measurement points on the cell, $\boldsymbol{I}_{exp}(\boldsymbol{x}_i, \boldsymbol{V})$ is the experimental CPI at point $\boldsymbol{x}_i$ on the cell for the range of voltages $\boldsymbol{V} = [V_1, V_2, ..., V_{N_V}]$ and $\boldsymbol{g}(x_i, \boldsymbol{V})$ its theoretical counterpart. Having computed $\hat{\Sigma}$ a set of $m$ traces is generated for each cell site. The traces are formed by drawing $m$ instances from the distribution $\mathcal{N}(\hat{\boldsymbol{\mu}}(\boldsymbol{x}, \boldsymbol{V}), \hat{\Sigma}(\boldsymbol{V}))$ for each $\boldsymbol{x}$ position on the cell. Finally we perform a least squares fit using cell size and pre-tilt as fitting parameters.

### 2.5.3 Results and analysis

Selected experimental traces and fits computed using the method discussed in subsection 2.5.2 are shown in figure 2.14. The remainder of the data and fits are in appendix A.2. The agreement at low voltage is excellent and the deviations of theory from experiment are confined to the high voltage portion of the trace.

At high voltage there are two features present in the E7 data in figure 2.14: the final maxima in the top left experimental trace does not reach a normalised intensity of 1 and the predicted asymptotic decrease in the CPI is more rapid in nearly all traces. The first feature, lifting off of the final maxima, is present in only the top left trace in figure 2.14 and is most likely caused by scattering losses. The second feature, disagreement at high voltage seen in most traces, is more of an anomaly and indicates that the distortion of the nematic increases more rapidly with increasing voltage in the theory than in practise. At these voltage values ($V > 10$ V) the nematic is aligned orthogonally throughout most of the cell. The only region that is not aligned is at the boundaries. For this reason we have attempted to determine what additional physics may be governing the alignment at the boundaries under high voltage.

One possible contributing factor to both the lifting off, and incorrect asymptotic behaviour in our model is a small boundary pre-twist. The effect of including pre-twist is shown in figure 2.15. Introducing a pre-twist changes the predicted traces in several ways. The zero voltage intensity is shifted, the maxima and minima exhibit lifting off and the final portion of the trace is shifted. The lifting off due to pre-twist shown in figure 2.15 mostly alters the final minima. As we do not observe this feature in the experimental data we can bound the pre-twist to only a few degrees. This also eliminates the pre-twist as a possible explanation of the lifting off in 2.14. The pre-twist does influence the final portion of the trace and shifts the final maxima to lower voltage. We have found that pre-twist cannot account for the deviation at high voltage. The pre-twist needed is too large and causes lifting off where non is present in the experimental traces.

The second factor is finite anchoring effects. These may be added to our model by using weak anchoring conditions derived from the Rapini-Papoular surface free energy density [90] (see [110] for an exposition in English). Finite anchoring has the effect of stretching and shifting the CPI towards lower voltages. Unfortunately attempting to fit to each of the traces in figure 2.14 using finite anchoring strength does not reduce the error at high voltage. It is possible that a combination of pre-twist and weak anchoring is responsible. However, this leads to a proliferation of parameters we would need to determine: the boundary pre-twist, pre-tilt, in-plane and out of plane anchoring energy densities. We have not attempted to fit using all of these parameters.

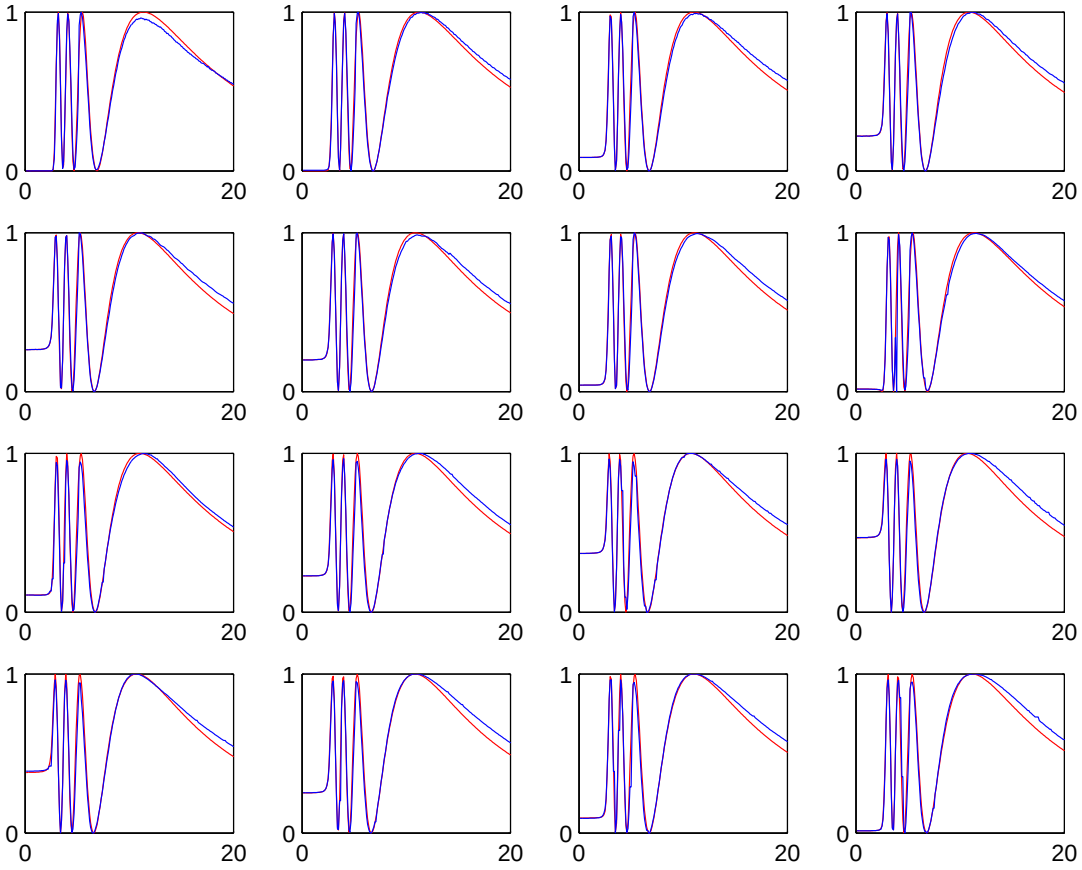


Figure 2.14: Examples of the crossed-polarised intensity as a function of the peak-to-peak amplitude of the applied voltage measured at different point in the cell, red lines are theory blue lines are experimental data. The fits shown correspond to one subset of data used during the first step of the fitting process which involved subdividing the data and fitting for $K_1$, $K_3$, $d$ and pre-tilt. The liquid crystal used was E7 with planar alignment and PI/PVK alignment layer.

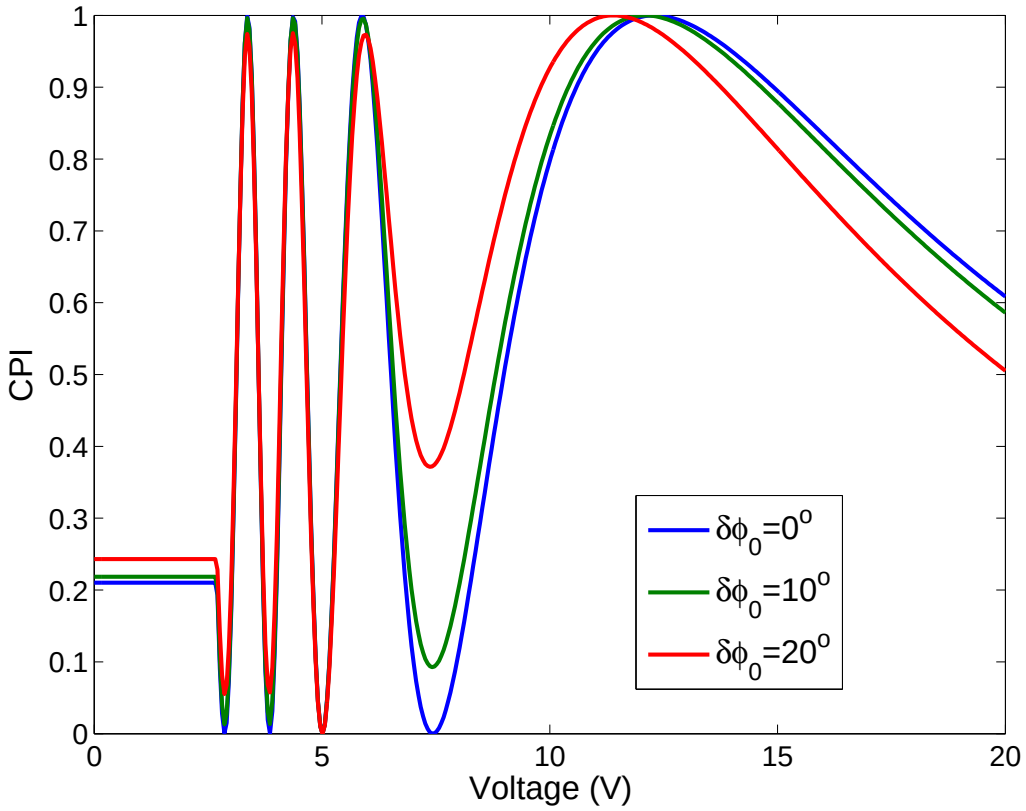


Figure 2.15: Trend of CPI for different pre-twist angles $\delta\phi_0 = 0°, 10°, 20°$ degrees for a 12 $\mu$m, E7 cell with $K_1 = 11.7$ pN, $K_2 = 8$ pN and $K_3 = 19.5$ pN with zero pre-tilt as a function of peak-to-peak voltage. The initial intensity is shifted, there is lifting off, most notably of the final minima, and the final portion of the trace is shifted.

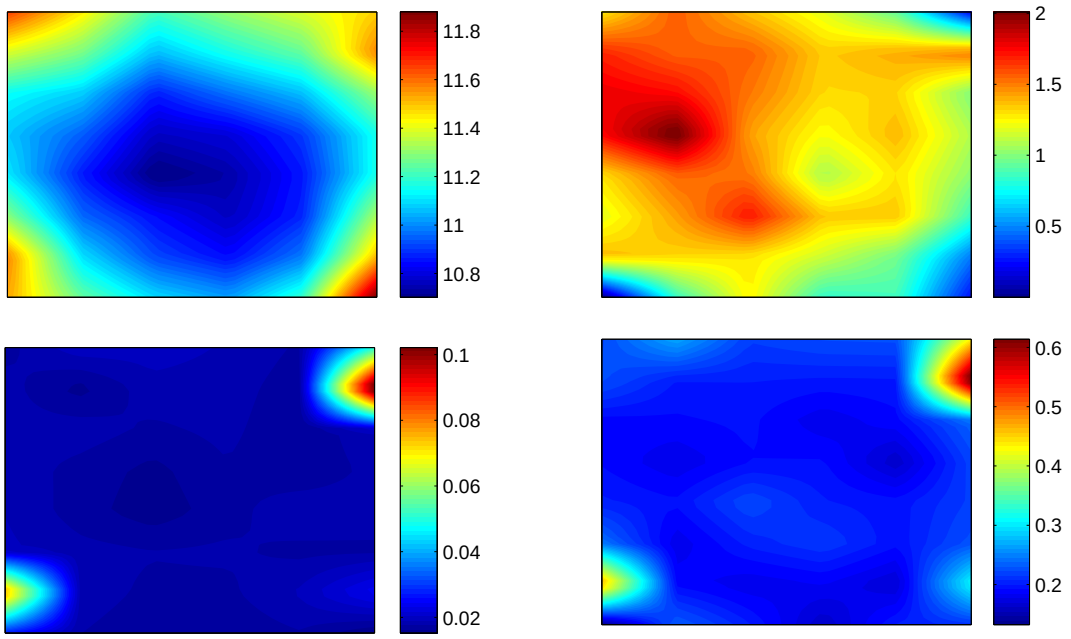


Figure 2.16: Cell thickness in microns (Top left), pre-tilt in degrees (Top right), error on cell thickness ($\mu$m) (bottom left) and error on pre-tilt (degrees) (bottom right) for an E7 cell with PI-PI alignment layer. The points at which the CPI was measured formed a $8 \times 6$ grid.

The resulting thickness and pre-tilt maps for a typical LC cell filled with E7 or TL205 are shown in figures 2.16 and 2.17. The colour of the map indicates thickness (pre-tilt), with blue colours indicating lower thicknesses (pre-tilt). The data was taken over a year before it was analysed. As a result when figure 2.17 was constructed the data did not appear to be lie on a $8 \times 6$ grid as had been recorded. Instead upon closer inspection based on the periodicity of the data the TL205 data appeared to have been taken on a $12 \times 4$ grid. For both of the cells there is a clear indication that the thickness is lowest in the centre of the cell, and is thicker near the corners (where the spacers were introduced between the two glass slides). There is no obvious correlation between the cell thickness and the pre-tilt however the point-wise errors on the cell thickness and pre-tilt are well correlated in space for both cells. The elastic constants and estimated errors are shown in table 2.4. The error bars were obtained by taking the standard deviation of the values of $K_1$ and $K_3$ obtained by subsetting.

A sample of the results from the parametric bootstrapping process are shown in figure 2.18. Figure 2.18 shows the results of fitting for the cell size and pre-tilt to the data generated by the parametric bootstrap. In general there is a clear elliptical shape to the distribution showing a correlation between changes in the cell thickness and pre-tilt as the result of noise generated by the parametric bootstrap. This is expected as both of these

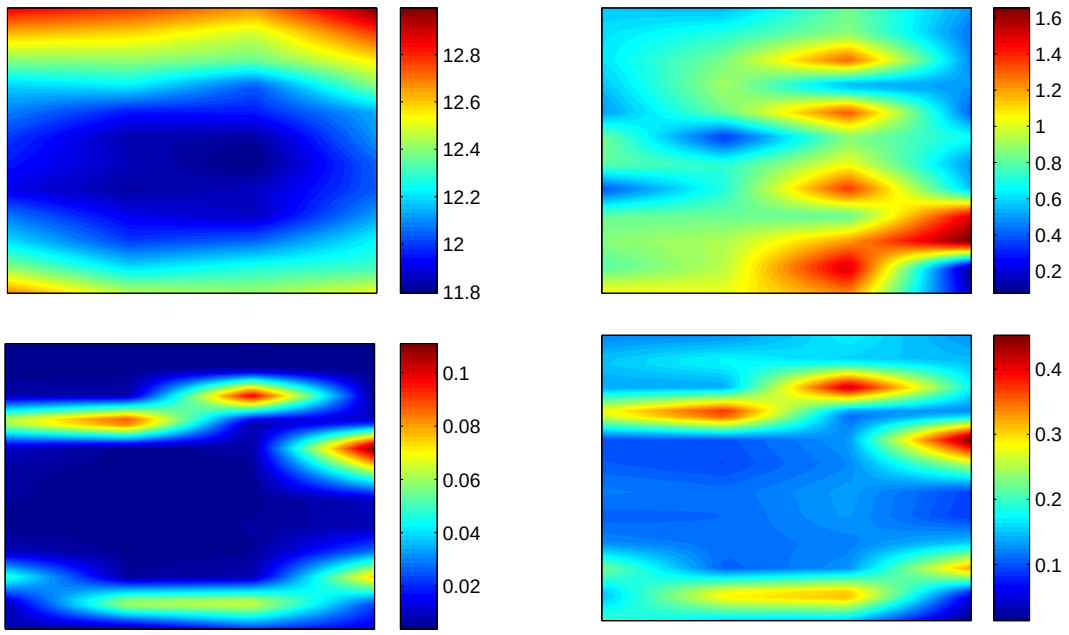


Figure 2.17: Cell thickness in microns (Top left), pre-tilt in degrees (Top right), error on cell thickness ($\mu$m) (bottom left) and error on pre-tilt (degrees) (bottom right) for an TL205 cell with PI-PI alignment layer. The points at which the CPI was measured formed a $12 \times 4$ grid.

| | $K_1$ | $K_3$ | $\sigma(K_1)$ | $\sigma(K_3)$ |
|---|---|---|---|---|
| E7 | 11.8 pN | 15.7 pN | 0.11 pN | 0.107 pN |
| TL205 | 16.6 pN | 23 pN | $9.52 \times 10^{-2}$ pN | 1 pN |

Table 2.4: Splay and bend elastic constants for the liquid crystals E7 and TL205, the standard deviation is also shown.

parameters influence the initial intensity. There is a correspondence between the plots shown in figure 2.14 and figure 2.18. Comparing the first and second plots from the top left of figure 2.14 and figure 2.18 we see that if the initial intensity is close to zero then the nature of the distribution is altered. In the second case the parametric bootstrap process produces two families of curves those with an additional minima and those without, this is responsible for the clustering shown. This does not occur in the first subfigure as the zero volt intensity is too close to zero and the noise added to the phase lag by the parametric bootstrap cannot produce a new minima.

We have demonstrated that it is possible to combine multiple measurements of the CPI to obtain information about the variations in cell thickness and pre-tilt across a liquid crystal cell. Work by Treidel [7] has shown that it is possible to vary the thickness of a liquid crystal cell using mechanical pressure, the resulting thickness profile is qualitatively similar to those found here. Our method has the added advantage of being able to measure

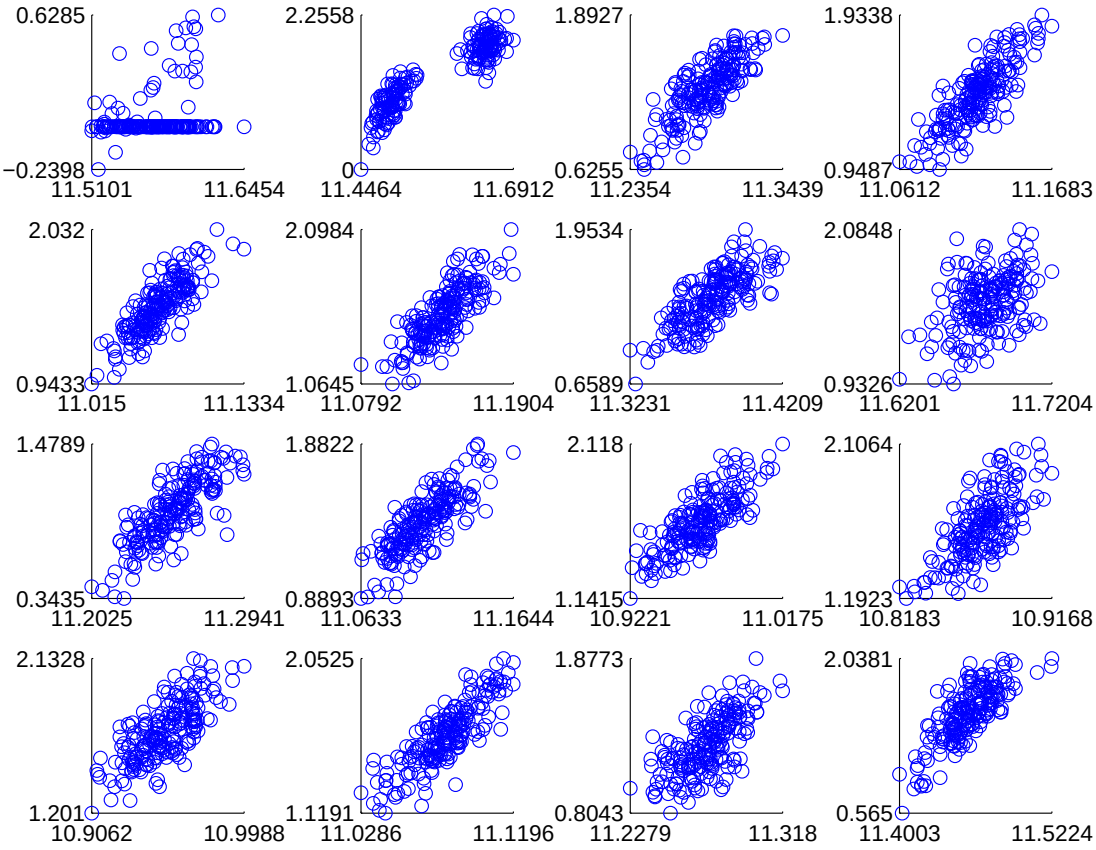


Figure 2.18: Scatter plot of fitted values for the cell thickness ($x$-axis measured in $\mu$m) and pre-tilt ($y$-axis measured in degrees). There is a one to one correspondence between the subplots in this figure and in figure 2.14.

the pre-tilt and elastic constants as well as providing error bounds on the parameters.

## 2.6 User friendly measurement procedure

We are aiming to implement the measurement methods discussed in 2.4 and 2.5 into a single device. As a first step we have collected the algorithms needed to perform the data analysis into a graphical user interface (GUI). This section provides a brief overview of the existing software.

The main GUI is shown in figures 2.19. The software is split into two user interfaces: the first allows the user to import experimental data from text files, view and smooth the data, the second performing the numerical fitting. The first GUI is shown in figure 2.20.

The main GUI 2.19 allows the user to fit $K_1$, $K_3$ the cell size and pre-tilt to the mean CPI. The fitting algorithm involves essentially two steps: firstly when data is imported into the GUI a peak detection algorithm is used to identify the maxima and minima in the data (see figure 2.23). This allows bounds to be placed on the cell size and splits the trace into the low and high voltage sections. The interface allows the user to manually correct any mistakes in the peak detection process. Secondly the least squares fit is run with fitting parameters as selected by the user. The low voltage part of the fit determines $K_1$, the cell size and pre-tilt, the high voltage section only determines $K_3$. The routine automatically samples the data to reduce computation time. A larger number of points are used at low voltage where the data is sensitive to multiple parameters. At high voltage only the extrema are needed. Fitting to the low and high frequency oscillations is implemented in a similar way although without the need for peak detection. The wide area measurements interface uses the procedure outlined in section 2.5.2 to split the multiple traces into subsets. The results can be visualised via scatter plots (see for example 2.18), line graphs or surface plots as depicted in figure 2.22.

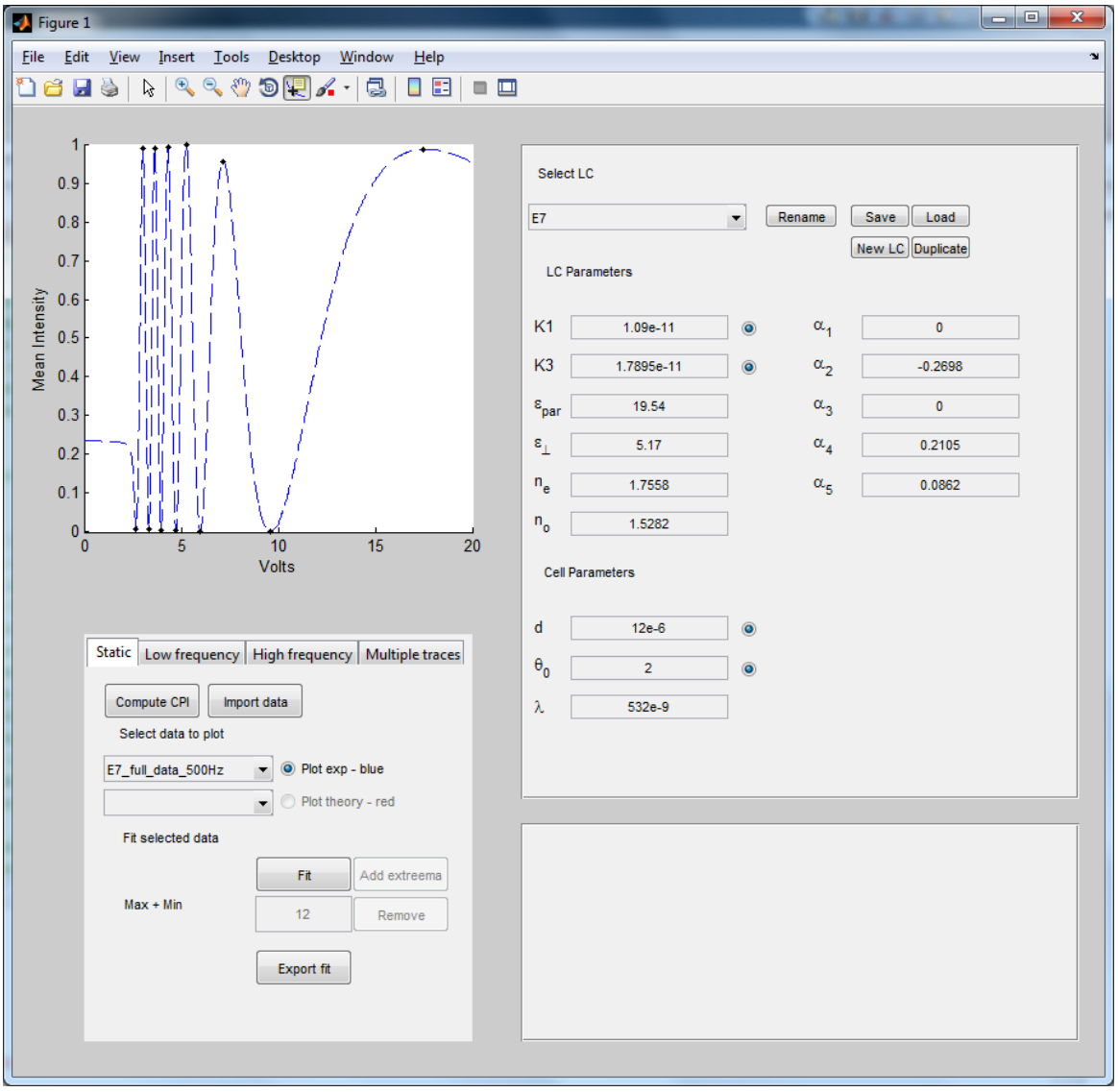


Figure 2.19: Main GUI panel with a single set of static CPI data displayed. The user can input material parameters for an arbitrary liquid crystal or select from the database included with the software using the right hand panel of the GUI. Selecting which results to display as well as initiating fits is handled by the panel in the bottom left.

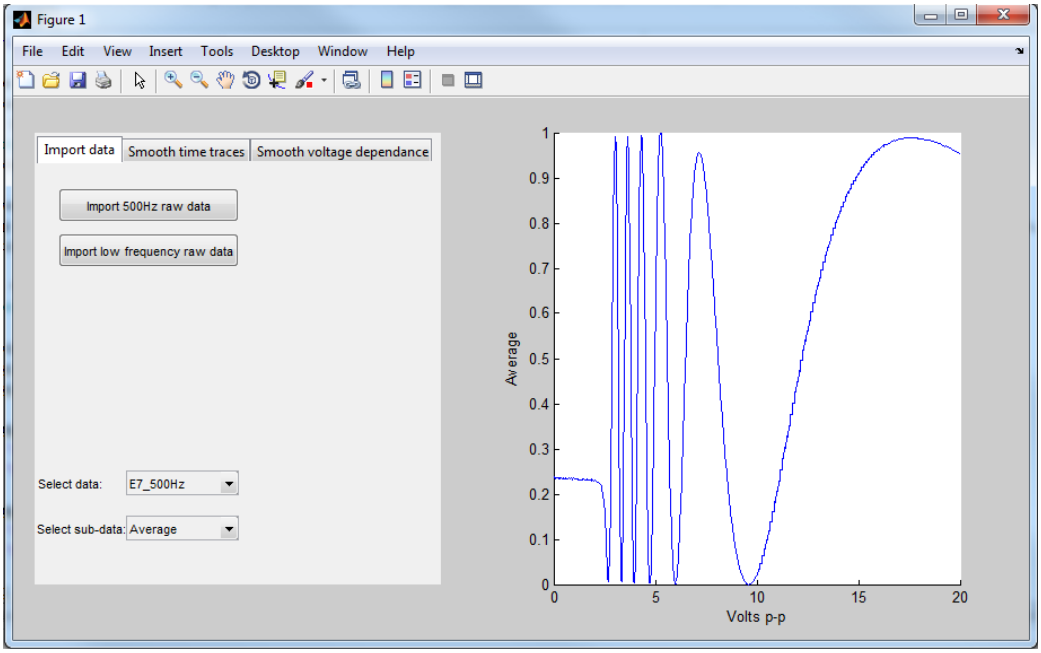


Figure 2.20: Graphical user interface used to import CPI data from text files and produce standardised MATLAB data files for use in the main GUI. This interface allows the user to smooth both the mean CPI, the time-dependent CPI and the standard deviation of the oscillations. The standard deviation in the CPI is automatically extracted from time dependent data. The data is smoothed using either a moving average of the moving least squares Savitzky-Golay filter, both of these are implemented using the MATLAB function smooth.

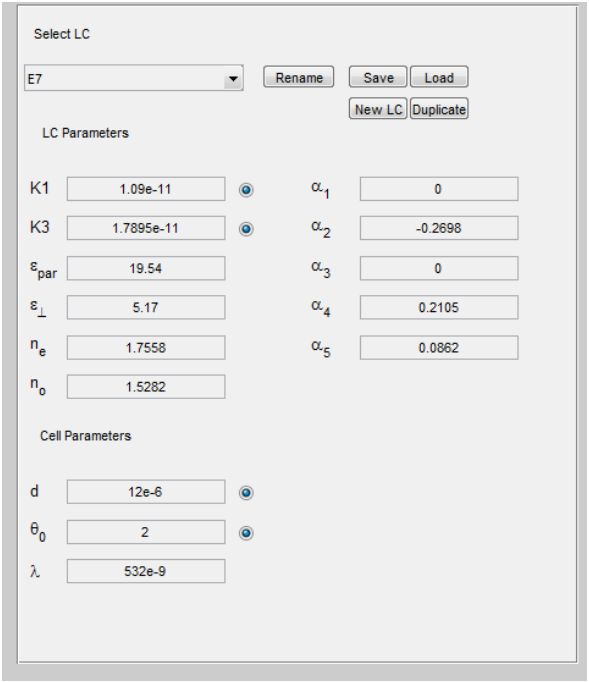


Figure 2.21: The materials panel allows the user to select, edit, save and load liquid crystal material parameter data. In addition when performing fits to the static part of the CPI the user has the option of fitting using any combinations of the elastic constants, cell thickness and pretilt as fitting parameters.

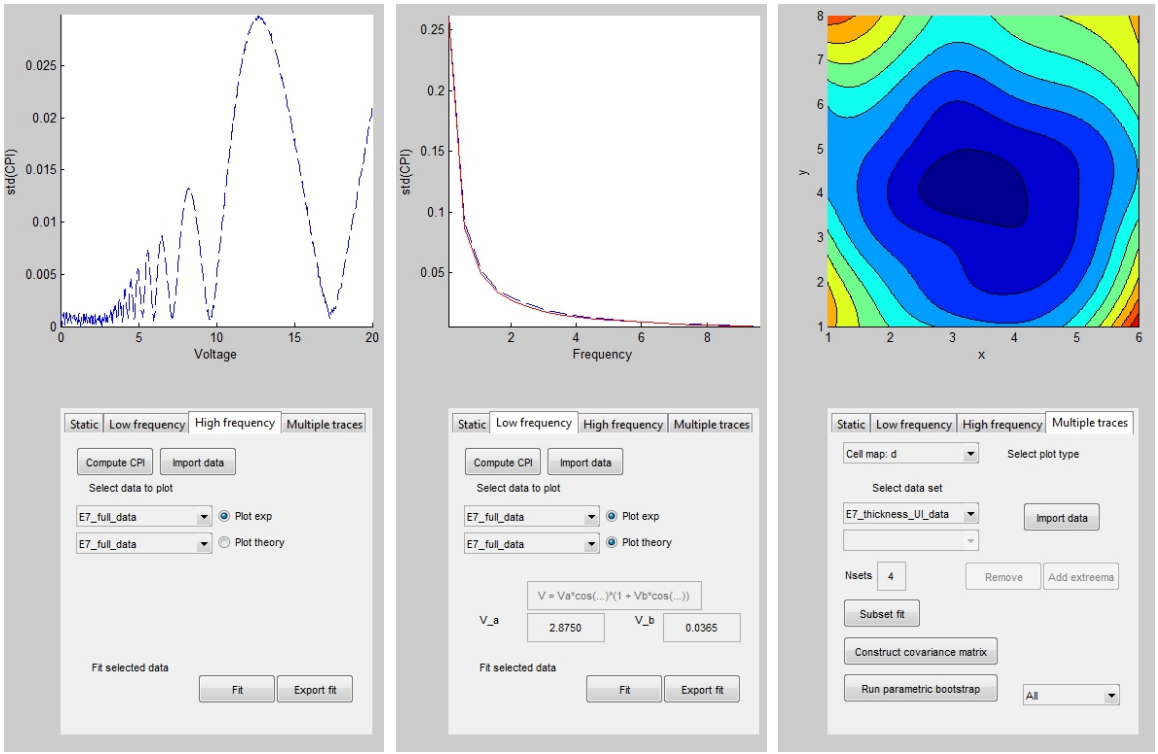


Figure 2.22: The high and low frequency part of the interface and the multiple point analysis panel. Each allows the user to import data, run fits for the relevant parameters as well as viewing and exporting the results.

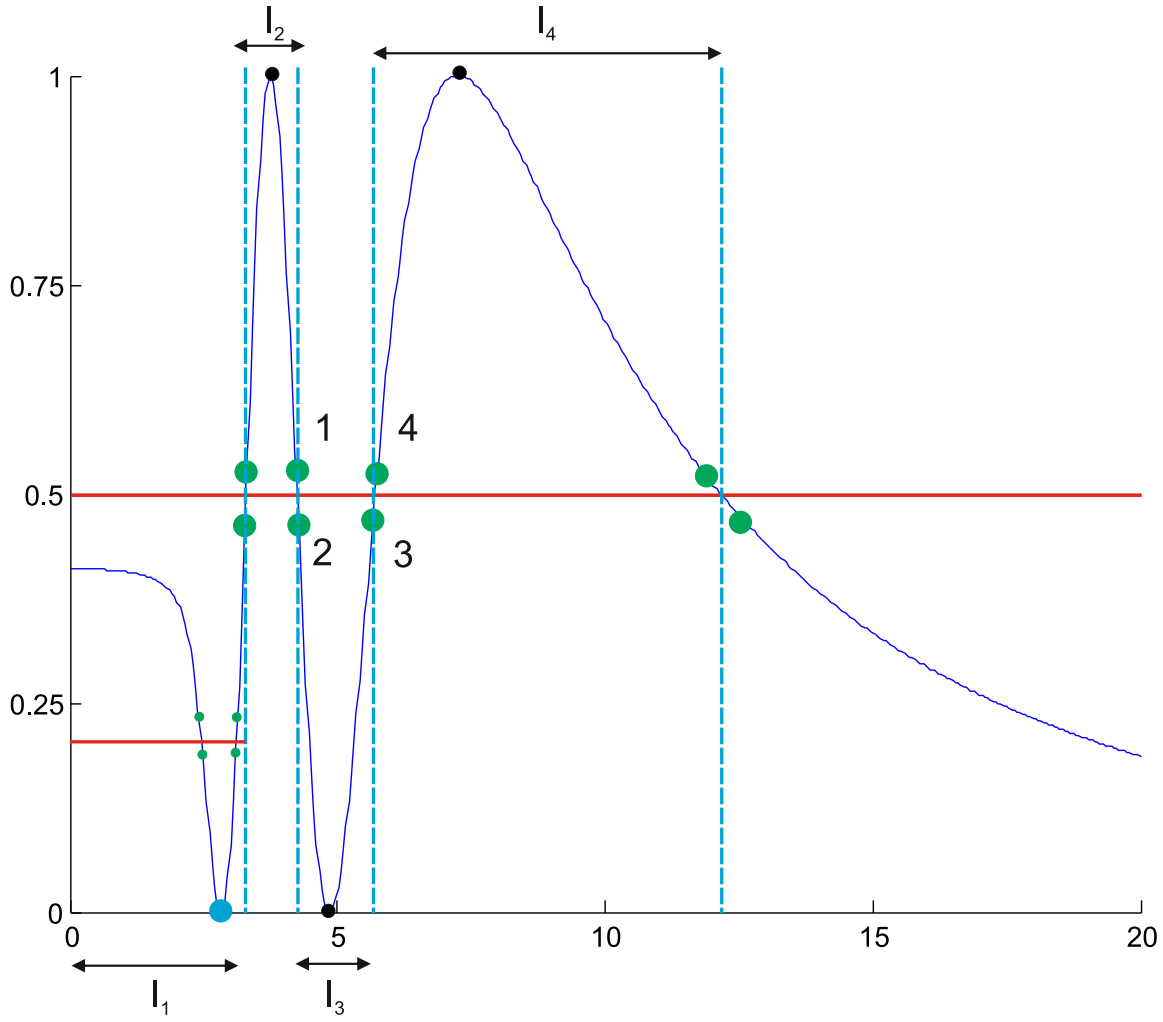


Figure 2.23: A graphical illustration of the peak detection algorithm. First, all data points that lie immediately before and after the line $I = 0.5$ (shown in red) are identified. A subset of these are labelled 1, 2, 3 and 4 in the figure. This allows the data trace to be broken up into subintervals $I_n$ for $n = 1, .., N$. Each of these subintervals contains either a maxima or minima, for instance the interval $I_3$ which contains a single minima. In general for all but the first and last subinterval it suffices to use the maximum/minimum value attained within the interval to identify the peaks. The first subinterval is treated using the same process as shown by the second red line. In the case shown an initial minima is detected. This process is also applied to the final subinterval.

## 2.7 Conclusions

We have demonstrated that a new optical technique which probes the dynamics of a nematic liquid crystal in the frequency domain can provide measurements of the Leslie viscosities $\gamma_1$ and $\alpha_4 + \alpha_5$. Although we do not find particularly good agreement between the measured values for E7 and those from the literature we have not controlled the temperature during these experiments which is likely the largest source of error. This could be applied to doped nematics in which case the ability to control the frequency of the driving field may reveal information that is not easily accessed by transient methods.

By combining the data from several measurements of the cross polarised intensity we have devised a robust statistical method which us to incorporate: global constraints, $K_1$ and $K_3$ are identical between measurements, and the computation of point-wise and global errors. We have found that there is no spatial correlation between cell thickness and pre-tilt. However, there is a rather strong spatial correlation between their uncertainties. Additionally the cells appear to bow in towards the middle.

# Chapter 3

# Homogenisation of systems with static micro-structure

This chapter is the first of two dedicated to the use of homogenisation theory to study the interaction between a nematic liquid crystal and dopant particles. In this chapter first we review existing approaches to modelling nematic colloids in section 3.1, in section 3.2 we explain the homogenisation method using the example of diffusion in spatially inhomogeneous media finally in section 3.3 we apply homogenisation to the problem of a nematic liquid crystal hosting *fixed* metallic inclusions.

## 3.1 Literature review

In this section we review existing literature related to colloidal or doped nematics. We begin in 3.1.1 by discussing the basic physical facts of these systems before reviewing existing approaches to deriving effective medium theories. In the 3.1.2 we discuss the method of mathematical homogenisation.

### 3.1.1 Nematic colloids

Colloidal nematic systems are formed from a suspension of nanometre to micron sized particles held within nematic liquid crystal. These systems are typically manufactured to alter the properties of the host nematic. Alternatively, the nematic component of the system may act as a lab or tunable background medium to investigate the properties of dopant particles. We are primarily interested in the first case.

The nature of the inclusions used ranges from simple metallic or dielectric particles to more exotic ferroelectric [61, 62] or ferromagnetic [19, 23, 24, 83] particles. In general the

dopants interact with both the nematic director and any imposed electromagnetic field. The end result of this interplay is that the suspension possesses altered electric or magnetic properties and, in addition, their ground state is no longer uniform. Instead, the director is distorted due to the presence of dopant particles.

It is possible to roughly split nematic colloidal research into two regimes: strong and weak anchoring. In the former particles typically induce topological defects in the nematic. These are singularities in the director field that emerge due to the incompatibility between particle anchoring and the uniform ground state of the nematic. In the latter the dopant acts to enhance the response of the nematic to electromagnetic fields. In both regimes a primary question is the stability of different colloidal suspensions. In the weak anchoring regime this often means estimating the aggregation time, for strong anchoring this means determining which of the many defect structures has the lowest free energy.

In the strong anchoring regime for homeotropic anchoring to a spherical particle Stark [108] has shown that the stability of the dipole, Saturn ring and surface ring states depend on the size, anchoring strength and strength of the applied field (see also the review by Stark [109]). For weak anchoring Ruhwandl and Terentjev [94] studied the interaction between a pair of spherical colloidal particles with homeotropic anchoring conditions. By deriving a linearised theory valid at low anchoring or small particle size they obtained a rough estimate of the particle aggregation time. This is proportional to the elastic constant and viscosity of the nematic and inversely proportional to the square of the anchoring energy. These results concern the interaction of individual or pairs of particles with the nematic, we now examine suspensions.

When the anchoring is strong the nematic alignment is significantly disturbed and the distortions mediate long range interparticle interactions. These systems often contain complex defect networks stretching between particles. Numerical work by Araki and Tanaka [3] predicted the formation of disclination loops encircling multiple particles. These loops mediate complex interparticle interactions. Subsequent experimental [55, 101, 65] and theoretical [114] studies have investigated the formation of disclination loops in various colloidal systems. Defect structures formed around nano particles can also be used within self assembly. Senyuk *et al.* [100] show that gold nano particles can be trapped by the defects induced by large spherical colloidal dopants and demonstrate assembly of chains and other structures through use of optical tweezers.

In this thesis we are primarily interested in the weak anchoring regime. This occurs for systems with low anchoring energy density or small particles [95] in this regime topological defects are absent. In this case the dopants alter the elastic, electrostatic and thermal response of the nematic [85, 88] producing a new material. Despite the lack of disclinations

and large elastic distortions the dopants can still have a non-trivial effect on the response of the nematic. Various classes of particles have been considered, here we consider gold, ferroelectric and ferromagnetic.

*Gold*

Gold inclusions have been shown to lower the nematic-isotropic transition temperature and increase the conductivity albeit at the loss of conductivity anisotropy [85]. When used in frequency modulated displays gold particles have been shown to result in faster switching speeds [69] than pure nematics. Gold inclusions have also been used to tune the dielectric anisotropy [88] resulting in lower operating voltages for liquid crystal devices. Alternatively liquid crystals have been used as a host medium to study and tune the plasmon resonance of the gold particles [86]. In this case it is the dielectric environment provided by the nematic that alters the response of the inclusions. Recently nanoparticle structures [100] have been explored as candidate tunable metamaterials. Podoliak *et al.* [82] found that low concentration gold nano particle are sufficient to enhance optical nonlinearity and also lead to altered anchoring strength and pretilt values.

*Ferromagnetics*

One class of colloidal nematics that have attracted a large amount of attention from both theorists and experimentalists are systems doped with ferromagnetic particles. Interest in these systems was initially raised by Brochard and de Gennes [19]: they found that the addition of dopants alters the response of the nematic host to external fields. The nematic experiences a torque due to the surface anchoring to the dopants. As a result the orientation of the dopants is correlated with the director. The dopant particles interact strongly with the applied field. The end result is an altered interaction between the nematic and the magnetic field.

An effective medium theory for ferromagnetic systems was initially developed by Brochard and de Gennes [19] and has been extended by Burylov and Raikher [23, 24] to include finite anchoring strength and re-derived more formally by Calderer *et al.* [25]. The Burylov and Raikher model has been experimentally tested by Podoliak *et al.* [83]. They find that at low particle concentration there is good agreement with the Burylov and Raikher [23, 24] model, at higher concentrations evidence of particle aggregation is found through microscopy. We now outline the main features of the effective medium theories for ferromagnetic suspensions.

A free energy for the colloidal system was proposed by considering the interactions

between the nematic and a single dopant particle [19, 23, 24]. The torque exerted by the nematic on the dopant particles and vice versa are estimated for cylindrical dopants. Surface interaction are shown to align the dopants parallel or perpendicular to the director. The stability of each state depends on whether the anchoring is planar or homeotropic. The final form of the free energy contains contributions due to the magnetic energy of the dopants, mixing entropy and anchoring with the nematic. The free energy is derived under the assumption that the dopants are already magnetised. Within this framework the director $\hat{\boldsymbol{n}}$, dopant concentration $f$ and dopant dipole $\hat{\boldsymbol{m}}$ are found by minimising the total free energy. Burylov and Raikher [23] predict a segregation effect, a non-uniform distribution of particles will form under an applied field. This effect occurs because, in an appropriate geometry, a uniform applied magnetic field will result in a non uniform director distribution. The dopants then migrate to regions where the elastic and magnetic energies are at a minima. More recently Calderer *et al.* [25] derived the effective free energy proposed by Burylov and Raikher [23] through a more rigorous homogenisation procedure.

The addition of ferromagnetic particles to a nematic liquid crystal can have additional effects beyond simply altering material parameters. Zadorozhnii [118] found that for homeotropic anchoring the interactions between magnetic field, director and dopants lead to a range of possible switching behaviours. For weakly coupled dopants there is an inverse Frederiks effect in which the distortion first increases before decreasing and vanishing at a critical field. In chapter 4 we find a similar change in switching behaviour for a nematic liquid crystal doped with metallic particles.

*Ferroelectrics*

Ferro-electric particles are nano to micrometer sized particles that poses a permanent electric dipole. Theoretical work has shown that ferroelectric suspensions posses reduced Frederiks thresholds [91, 103], asymmetric Frederiks behaviour [30], increased [61] nematic isotropic transition temperatures and an increase in nematic order [61, 42]. In general many of these effects depend on the composition of the suspension. Reshetnyak *et al.* [91] assumed the anchoring was strong enough that the dopant particles align with dipoles parallel or anti parallel to the director. The free energy is modified to take into account the mixing entropy of the particles and the interaction of permanent particle dipoles with an applied field. The dopants are assumed to see an effective field given by the field in the nematic multiplied by a local field correction, a phenomenological parameter. The model predicts a decrease in the Frederiks transition due to the dopants. The model put forward by Shelestiuk *et al.* [103] improves upon [91]. An effective medium theory is used to replace the phenomenological local field correction factor with effective dielectric constants.

Shelestiuk *et al.* [103] note that the effective permittivity entering the nematic free energy differs from that which would be measured experimentally via capacitance measurements due to the non-uniform nature of the material. This is because the spatial averages $< \boldsymbol{E} \cdot \boldsymbol{D} >$ and $< \boldsymbol{E} > \cdot < \boldsymbol{D} >$ are not in general equal in non-uniform materials [103]. Lopatina and Selinger developed a statistical mechanical model of ferro electric nano particles in liquid crystals [61]. The starting point for their model is the interaction energy between a liquid crystal and the dipole field of a spherical nano particle. They argue that near the nano-particle the nematic director cannot follow the rapid variations in the electric field. Hence, the director is assumed to be constant in the vicinity of each nano particle. In general the dipoles are not all aligned in the same direction throughout space and hence the free energy density is written in terms of the nano particle order tensor [61], which expresses the mean orientation of the dipoles. Using this model Lopatina and Selinger find that the nematic-isotropic transition temperature increases. The local interaction between particle and host also couples the scalar order parameter to the applied field [61]. Although ferroelectric particles can increase the transition temperature the dilution effect modelled by Gorkunov and Osipov [42] results in decrease of the transition temperature for spherically isotropic particles.

Suspensions formed of liquid crystal TL205 or 18523 and ferro electric barium titanate (BTO) or tin thiohypodiphosphate (SPS) particles were investigated by Podoliak *et al.*[84]. The dielectric, elastic and dynamic properties of these suspensions were investigated. In total three different particle species were investigated: milled BTO, milled SPS and ablated BTO the concentration by weight was estimated at $\approx 1\%$. The milled particle retain the ferroelectric state while the ablated particle appeared dielectric in nature, possibly due to heating during ablation [84]. The dielectric response was measured by a capacitance method and an increase in the dielectric anisotropy was found when ferroelectric particles were added [84]. The splay elastic constant $K_1$ was measured by cross polarised intensity measurements near the Frederiks transition. For the ferroelectric particles the splay elastic constant decreased by approx 10% in 18523, larger decrease of up to 20% was observed in TL205. This change in elastic behaviour was further investigated, the role of the surfactant introduced to alongside the dopants was ruled out by manufacturing cells with small amounts of surfactant and solvent added to the liquid crystal. In this case the change in dielectric and elastic behaviour was not observed [84]. To further probe the origin of the changing elastic behaviour $K_1$ was measured for TL205 doped with the dielectric ablated BTO particles, $K_1$ was found to decrease by $\approx 15\%$. Finally the switching time in a twisted cell was found to follow a more complicated relation with applied voltage than for a pure liquid crystal [84]. Depending on the magnitude of the applied field the

doped LC suspensions were found to reorient faster or more slowly than undoped cells [84]. Experimental work by Cook *et al.* [30] showed that low concentration ferronematics show hysteresis behaviour in the DC Frederiks transition. This was postulated to be caused by the reorienting of the dopant particles under the applied field. After cycling a cell from 0 to $V$ volts the dopant are aligned by the field, as a result when the cycle is reversed ($V$ to 0 volts) a shift is observed in the Frederiks threshold of up to 0.8 Volts. The shift originates from the internal field generated by the dopants.

### 3.1.2 Homogenisation literature

In the previous section we reviewed the existing approaches to deriving effective medium theories for doped nematics. These suspensions are inherently multi-scale systems, that is they involve physics which takes place across multiple different length scales, the scale of the dopant particles themselves and the larger length-scale of the device or sample. One method for treating this class of problems in and general manner is homogenisation theory. This collection of formal up-scaling methods has proven to be effective when applied to various multi-scale systems.

Homogenisation theory allows complex, often though not always periodic, multiple scale problems to be decomposed into two sets of problems posed on two disparate length scales. These two sets are referred to as the cell problems, capturing the small scale physics, and the macroscopic or homogenised equations, representing the large length scale behaviour of the system. In general, when dealing with periodic systems the cell problems capture the physics occurring within a unit cell while the homogenised equations predict the large scale variation across many such cell in response to external or internal forcing. An introduction to the method of asymptotic homogenisation can be found in the book by Pavliotis and Stuart [79], application to porous material is explored by Hornung [47], the history is explored by Tartar [63]. Here we review the existing literature pertaining to homogenisation and specifically homogenisation and liquid crystals.

The methods of homogenisation theory have been developed to study the solutions of partial differential equations that involve a rapidly varying microstructure. This structure is captured by some combination of the domain of the problem, whose geometry is often complex and multiply connected, rapidly oscillating coefficients in the equations themselves. The challenge in each of these case is to obtain effective equations describing the limiting case of vanishing microstructure. This results in a macroscopic or homogenised descriptions in which the effect of the microstructure has been smoothed out. Formally a general homogenisation problem can be stated as follows [1, 79]. A sequence of problems

for some field $u_\eta$ is posed

$$\mathcal{L}_\eta u_\eta = f_\eta \qquad \boldsymbol{x} \in \Omega \tag{3.1}$$

along with sufficient boundary conditions. Here the parameter $\eta$ gives the scale separation in our problem, $\mathcal{L}_\eta$ is a sequence of differential operators and $f_\eta$ is a source term. For periodic homogenisation $\eta$ is the dimensionless period of the microstructure or the period of oscillations in $\mathcal{L}_\eta$. The task is then to obtain effective equations in the limit as $\eta$ tends to zero in some appropriate weak sense. The resulting equation for $u$, the limit of the sequence $u_\eta$, contains additional terms that represent the contribution from the microscopic variations. This is often accomplished by using multiple scale expansions in the parameter $\eta$. We now briefly outline the development of homogenisation theory.

In general homogenisation applies to quite general non-periodic multi-scale systems. In this case relatively weak results are found by difficult formal methods. Typically these results include bounds on material parameter and it is not usually possible to arrive at more explicit expressions or to determine governing equations [63]. Major work in the general area has been carried out by Tartar and Spagnolo who developed specialised notions of weak convergence [102, 63]. Progress towards developing more useful techniques was made during the 1970's. A less formal approach was developed [4, 5, 6, 79], this approach known as multiple-scale expansions allows one to guess the form of the homogenised equations and cell problem by use of asymptotic expansions.

In addition to being a practical tool for finding governing equations the multiple scale expansion method lead to the development of the two-scale convergence method by Nguetseng and Allaire [72, 1]. Their method applies to periodic problems and utilises the periodic structure more efficiently by making use of the results of multiple scale expansions. The end result is twofold a proof of convergence and an alternative form of the homogenisation problem referred to as the two scale system. The two scale system contains contribution from both the micro-scale and macro-scale. From a practical point of view the notion of two-scale convergence allows for a justification of the guess made when employing multiple-scale expansions (see [79] page 26, Lemma 2.34). Additional work has been carried to further simplify the proofs of convergence such as the periodic unfolding method developed by Cioranescu *et al.* [29]. Two-scale convergence has also been extended by Nguetseng [73] beyond the periodic case.

The method used in this thesis is that of multiple-scale expansions. This is often the first step used in a formal proof of convergence and in addition the method has been extended beyond the periodic case to include more general problems. These include materials in which the periodic lattice is distorted, this is realised by e.g. biological systems and spatially amorphous systems [21, 92] are in which there are slow variations

in the microstructure, e.g. diffusion problems [21] and in ion transport within batteries [93, 21].

Homogenisation is applied to a wide range of physical phenomena. It is used to model flow in porous media [56, 48], charge and discharge of batteries [93], study electrical activity in biological systems [92], obtain effective mass theorems for crystalline solids [2] and model the elastic deformation of perforated bodies [75]. In each of these cases the main result is a computationally efficient model of the system being studied that provides a direct and self consistent link between macroscopic parameters and microstructure. In fluid flow problems this is typically realised by obtaining an equation for the macroscopic flow velocity containing various terms describing the viscous interaction with the porous microstructure. In the case of deformable materials there is often feedback between the effective parameters, obtained by means of cell problems, and the macroscopic behaviour. For a liquid crystal colloid the cell problems allow the extrapolation of macroscopic properties from the local interaction of dopant particles with the nematic.

Existing literature [104, 14, 15] proves under general conditions the convergence of the homogenization scheme based on the director representation of the nematic liquid crystal. Shen and Calderer [104] considers a system of periodic inclusions representing polymer fibers anchoring to the liquid crystal via a Rapini-Papoular surface potential [110] under application of a uniform magnetic field. By using the method of two-scale convergence [1] a free energy is derived for the system in the limit of vanishing microstructure. The resulting free energy contains an effective elasticity tensor and a polymer alignment term representing the anchoring effect of the inclusions. This formalism has been extended to non-periodic geometries [14] and random inclusions [15].

At first glance it is not obvious if the more formal approach offered by homogenisation is entirely separate to the ad hoc methods employed in the physics literature or if one or both of these approaches may be obtained as the limiting case of the other. Firstly both the approach taken in the physics literature [23, 24, 91, 103] and the more formal approach taken in the applied mathematics literature [104, 14, 15] describe the system using a free energy approach. Where the approaches differ is in how additional degrees of freedom are introduced and constrained. The method followed by Brochard and de Gennes [19] consists of making free energy considerations to determine the preferred alignment of the magnetic filaments within the nematic. Next a new free energy is proposed to describe a ferro-nematic at low volume fractions under the assumption that grains align with the director. The modified free energy contains an altered magnetic susceptibility for magnetic misalignment and an entropy term. No changes are made to the elastic free energy of the nematic to account for dilution. Burylov *et al.* [23, 24] follows a similar approach but

allows for misalignment of the director and dopant particles. The initial attempts to study ferro electric systems by Reshetnyak *et al.* [91] followed a similar method.

A typical homogenisation scheme involves a more formal process, we focus on the method of two-scale expansions. An example of applying this method is given in section 3.2, the general procedure involves extracting a series of cell problems and a macroscopic average equation from the governing equations of the full system by means of asymptotic expansions. Physics included in the governing equations of the full system generates cell problems and representative terms in the homogenised equation. As we will show in 3.3 under a homogenisation scheme an anisotropic elasticity tensor drops out of the analysis (see [104, 14, 15, 11]) as an inevitable consequence of the volume excluded by the inclusions. The form of the elasticity tensor is computed directly from the microscopic geometry, no unknown phenomenological parameters are introduced. All parameters introduced are computed from their accompanying cell problem in a self consistent manner. As a result it is possible to compute the new material parameters as a function of inclusions geometry and composition. In addition interaction that occur across length scales can also be captured. The downside is that more work is required to include the breadth of physics found in a mean field theory without sacrificing the generality of the geometry considered. This is a particular problem in systems that are not truly periodic where additional work has be undertaken to account for variations over the macroscopic scale.

To conclude, approaches based on homogenisation theory provide a set of microscopic cell problems and a set of macroscopic equations or equivalently a macroscopic free energy density. In general these governing equations must be solved simultaneously to determine the system behaviour. The parameters introduced into the macroscopic equations, such as the elasticity tensor, are defined by the cell problems. Each cell problem captures one or more physical affects of the dopants on the nematic and explicitly includes the geometry of the dopants. Thanks to this direct link to the microscopic geometry, different inclusions geometries can be treated in a straight forward manner. Conversely the effective medium theories of Burylov *et al.* [23, 24] produce a single free energy density containing new variables representing the configuration of the dopants. The microscopic details such as the size and shape of the dopants are confined to phenomenological parameters. Treating differently shaped dopants would require additional work on a case by case basis under such an approach. The trade off when employing homogenisation is an increase in mathematical complexity in return for increased geometric generality and a self consistent method of computing phenomenological terms.

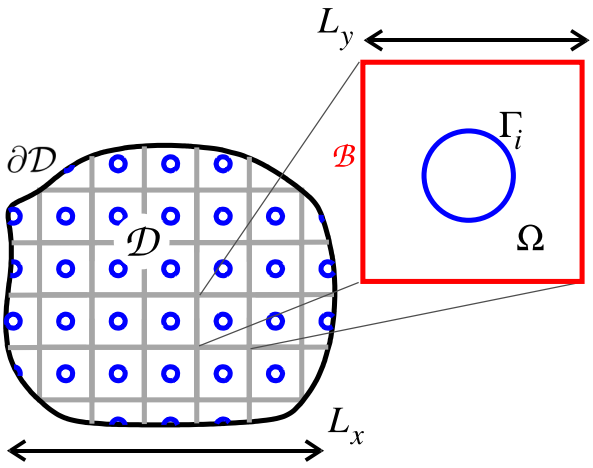


Figure 3.1: Domains used in defining scale separation. The macroscopic domain consists of an open region $\mathcal{D}$, with external boundary $\partial\mathcal{D}$, constructed from unit cells $\Omega$ with outer boundaries $\mathcal{B}$ and impermeable boundary $\Gamma_i$.

## 3.2 The method of homogenisation

In this section we provide an overview of the method of asymptotic homogenisation.

### 3.2.1 An example problem: The diffusion equation

Next we look at a simple example problem in homogenisation. The standard textbook examples are, see for example [79, 47], diffusion in spatially varying media and homogenisation of a uniformly elliptic PDE. We illustrate the method of homogenisation through the problem of diffusion in a punctured domain, similar examples can be found in [79, 47]. The governing equations for such a process, after appropriate non-dimensionalisation are,

$$\nabla^2 u = \frac{\partial u}{\partial t} \qquad \boldsymbol{x} \in \mathcal{D}, \tag{3.2a}$$

$$\hat{\boldsymbol{\nu}} \cdot \boldsymbol{\nabla} u = 0 \qquad \boldsymbol{x} \in \Gamma_i, \tag{3.2b}$$

$$u\left(\boldsymbol{x}\right) = u_b \qquad \boldsymbol{x} \in \partial\mathcal{D}. \tag{3.2c}$$

Here $u$ is the concentration of diffusing particles, $\hat{\boldsymbol{\nu}}$ is the unit normal on the obstruction surface, the obstructions $\Gamma_i$ represent impermeable regions in the domain of the problem 3.1 and we have assumed that the diffusion time-scale is $\mathcal{O}(1)$. The aim of performing a homogenisation of (3.2) is to remove the complex microscopic details of the geometry and obtain a system of governing equations in which the geometric details have been confined

to effective material parameters. To accomplish this a small parameter is defined, $\eta = \frac{L_y}{L_x}$ where $L_y$ is the size of a unit cell and $L_x$ is the macroscopic size of the system. Next we define a second spatial coordinate $\boldsymbol{y} = \frac{\boldsymbol{x}}{\eta}$. The $\boldsymbol{y}$ coordinate can be thought of as tracking position within each cell. We assume that all fields are functions of $\boldsymbol{x}$ and $\boldsymbol{y}$. We expand all fields and operators in the small parameter $\eta$,

$$u = u_0 + \eta u_1 + \eta^2 u_2 + \mathcal{O}(\eta^3), \tag{3.3a}$$

$$\boldsymbol{\nabla} = \boldsymbol{\nabla}_{\boldsymbol{x}} + \frac{1}{\eta}\boldsymbol{\nabla}_{\boldsymbol{y}}, \tag{3.3b}$$

$$\nabla^2 = \nabla^2_{\boldsymbol{x}} + \frac{1}{\eta}(\boldsymbol{\nabla}_{\boldsymbol{x}} \cdot \boldsymbol{\nabla}_{\boldsymbol{y}} + \boldsymbol{\nabla}_{\boldsymbol{y}} \cdot \boldsymbol{\nabla}_{\boldsymbol{x}}) + \frac{1}{\eta^2}\nabla^2_{\boldsymbol{y}}. \tag{3.3c}$$

To constrain the additional degrees of freedom we require all functions to be periodic in $\boldsymbol{y}$. Next we substitute (3.3) into (3.2) and equate coefficients of powers of $\eta$. At each order we extract information about the behaviour of $u_0$. The order $\eta^{-2}$ terms give,

$$\nabla^2_{\boldsymbol{y}} u_0 = 0 \qquad \boldsymbol{y} \in \Omega, \tag{3.4a}$$

$$\hat{\boldsymbol{\nu}} \cdot \boldsymbol{\nabla}_{\boldsymbol{y}} u_0 = 0 \qquad \boldsymbol{y} \in \Gamma_i. \tag{3.4b}$$

Here we have used the decomposition of the macroscopic domain $\mathcal{D}$ into a repetition of unit cells $\Omega$. The resulting problem for the order $\eta^{-2}$ terms (3.4) is solved within a single cell subject to periodic boundary conditions. The solution to (3.4a) subject to periodic boundary conditions is any function independent of the micro-scale, in other words $u_0 = u_0(\boldsymbol{x})$. Proceeding to order $\mathcal{O}(\eta^{-1})$ we find,

$$\nabla^2_{\boldsymbol{y}} u_1 = 0 \qquad \boldsymbol{y} \in \Omega, \tag{3.5a}$$

$$\hat{\boldsymbol{\nu}} \cdot \boldsymbol{\nabla}_{\boldsymbol{x}} u_0 + \hat{\boldsymbol{\nu}} \cdot \boldsymbol{\nabla}_{\boldsymbol{y}} u_1 = 0 \qquad \boldsymbol{y} \in \Gamma_i. \tag{3.5b}$$

First we ensure that the solvability condition for $u_1$ is satisfied. The solvability condition is found by projecting (3.5a) onto the kernel of the adjoint of the operator defined by $\mathcal{L} = \nabla^2_{\boldsymbol{y}}$ and equiped with periodic boundary conditions. The kernel is spanned by functions of $\boldsymbol{x}$ only, without loss of generality we write the solvability condition as

$$\int_\Omega \nabla^2_{\boldsymbol{y}} u_1 dV = 0 \tag{3.6}$$

Next we apply the divergence theorem and boundary condition (3.5b)

$$\begin{aligned}\int_\Omega \nabla_{\boldsymbol{y}}^2 u_1 dV &= \int_\Gamma \hat{\boldsymbol{\nu}} \cdot \boldsymbol{\nabla}_{\boldsymbol{y}} u_1 dS, \\ &= -\int_\Gamma \hat{\boldsymbol{\nu}} \cdot \boldsymbol{\nabla}_{\boldsymbol{x}} u_0 dS, \\ &= -\int_\Omega \boldsymbol{\nabla}_{\boldsymbol{y}} \cdot \boldsymbol{\nabla}_{\boldsymbol{x}} u_0 dV, \\ &= 0. \end{aligned} \tag{3.7}$$

We see that the solvability condition is automatically satisfied provided $u_0$ is independent of $\boldsymbol{y}$.

To uncouple the problem for $u_1$ in (3.5) we make the ansatz $u_1(\boldsymbol{x}, \boldsymbol{y}) = \chi_k(\boldsymbol{y}) \frac{\partial u_0}{\partial x_k}(\boldsymbol{x})$, where all of the macroscopic dependence is absorbed into the derivative of $u_0$. Substituting for $u_1$ we find the cell problem

$$\nabla_{\boldsymbol{y}}^2 \chi_k = 0 \qquad \boldsymbol{y} \in \Omega, \tag{3.8a}$$

$$\hat{\boldsymbol{\nu}} \cdot \boldsymbol{\nabla}_{\boldsymbol{y}} \chi_k = -\hat{\boldsymbol{\nu}} \cdot \hat{\boldsymbol{e}}_k \qquad \boldsymbol{y} \in \Gamma_i. \tag{3.8b}$$

The cell problem (3.8) is solved inside a unit cell subject to periodic boundary conditions. The solution to (3.8) is defined up to a constant, the value of this constant does not influence the final solution. Finally at order $\mathcal{O}(\eta^0)$ we find

$$\nabla_{\boldsymbol{x}}^2 u_0 + \boldsymbol{\nabla}_{\boldsymbol{x}} \cdot \boldsymbol{\nabla}_{\boldsymbol{y}} u_1 + \boldsymbol{\nabla}_{\boldsymbol{y}} \cdot \boldsymbol{\nabla}_{\boldsymbol{x}} u_1 + \nabla_{\boldsymbol{y}}^2 u_2 = \frac{\partial u_0}{\partial t} \qquad \boldsymbol{y} \in \Omega, \tag{3.9a}$$

$$\hat{\boldsymbol{\nu}} \cdot \boldsymbol{\nabla}_{\boldsymbol{x}} u_1 + \hat{\boldsymbol{\nu}} \cdot \boldsymbol{\nabla}_{\boldsymbol{y}} u_2 = 0 \qquad \boldsymbol{y} \in \Gamma_i. \tag{3.9b}$$

The solvability condition for (3.9a) is given by

$$\int_\Omega \nabla_{\boldsymbol{x}}^2 u_0 + \boldsymbol{\nabla}_{\boldsymbol{x}} \cdot \boldsymbol{\nabla}_{\boldsymbol{y}} u_1 + \boldsymbol{\nabla}_{\boldsymbol{y}} \cdot \boldsymbol{\nabla}_{\boldsymbol{x}} u_1 + \nabla_{\boldsymbol{y}}^2 u_2 dV = \int_\Omega \frac{\partial u_0}{\partial t} dV, \tag{3.10}$$

as before we apply the divergence theorem and use the boundary conditions (3.9b).

$$\int_\Omega \nabla_{\boldsymbol{x}}^2 u_0 + \boldsymbol{\nabla}_{\boldsymbol{x}} \cdot \boldsymbol{\nabla}_{\boldsymbol{y}} u_1 dV = \int_\Omega \frac{\partial u_0}{\partial t} dV, \tag{3.11}$$

Next we substitute for $u_1$ from the cell problem. The homogenised equation for the

diffusion problem is

$$\boldsymbol{\nabla}_{\boldsymbol{x}} \cdot (\mathcal{D}\boldsymbol{\nabla}_{\boldsymbol{x}} u_0) = \frac{\partial u_0}{\partial t}, \tag{3.12}$$

where the effective diffusion tensor is given by

$$\mathcal{D}_{ij} = \frac{1}{\|\Omega\|} \int_{\Omega} \delta_{ij} + \frac{\partial \chi_j}{\partial y_i} dV. \tag{3.13}$$

Equation (3.12) gives the large scale dependence of the concentration of the diffusing species. The original problem (3.2) required that we solve the isotropic diffusion equation in a complex geometry containing multiple inclusions. Instead the homogenised equation is solved in the same domain in the absence of any inclusions.

The presence of inclusions is captured entirely by the diffusion tensor (3.13). As would be expected from symmetry considerations the diffusion tensor is isotropic for a regular cubic array of spheres. For ellipsoids with major axis aligned with any coordinate $\mathcal{D}_{ij}$ is diagonal, off axis alignment or arbitrarily shaped inclusions produce large off-diagonal terms. $\mathcal{D}_{ij}$ captures the effect excluded volume has on the diffusion of the particle species.

Other typical problems that can easily be treated using homogenisation include: determining the response of composite materials, fluid flow through porous media and advection-diffusion problems [79, 47].

We now apply the method illustrated in this section to the more complicated problem of a liquid crystal hosting metallic inclusions.

## 3.3 Homogenisation of liquid crystal colloids

In this section we use homogenisation theory to develop a model for a nematic liquid crystal hosting metallic inclusions. This section is heavily based on a published paper produced in conjunction with Dr. G. D'Alesandro and Dr. K. R Daly [11]. The main difference between this section and [11] is that here we have altered the derivation. We first derive the homogenised equations before extracting the slow manifold dynamics rather than undertaking both of these problems simultaneously as in [11]. In subsection 3.3.1 we outline the microscopic model of the system, in subsection 3.3.2 we estimate the parameter region of validity for our model, we derive the homogenised equations in subsection 3.3.3.

### 3.3.1 Modelling a liquid crystal with inclusions

We model the evolution of the nematic alignment using the $\mathcal{Q}$-tensor formalism discussed in 1.3. In constructing our model we make several assumptions about our system. In order to apply homogenization we assume periodicity, i.e. the inclusions form a periodic array of unit cells as shown in figure 3.2 with period $L_y$. Each cell consists of a volume $\Omega$, the hashed region shown in figure 3.2, containing liquid crystal and a metallic inclusion of volume $\Omega_{np}$ with boundary $\Gamma_i$, where the subscript $i$ labels the inclusions. We label the external boundary of a cell $\mathcal{B}$. The macroscopic domain $\mathcal{D}$ consists of an array of unit cells, with macroscopic boundary $\partial\mathcal{D}$. The system has a separation of scales which we quantify by the smallness parameter $\eta = \frac{L_y}{L_x}$, where $L_x$ is the size of the macroscopic system. The homogenization process involves studying the limiting behaviour of a system as $\eta$ tends to zero while the total size of the system remains constant. We consider a system of constant size $L_x$ as the size of the periodic microstructure $L_y$ tends to zero and the number of inclusions diverges. The inclusions are assumed to remain in fixed positions and orientations, but, we pose no restrictions on their geometry.

We are interested in the case where neither the surface energy nor the bulk energy dominates the behaviour of the system. We expect that in this regime there will be a richer interplay between the two constituents, particles and liquid crystal, that will show the potential of homogenization theory to obtain realistic macroscopic equations. To this end we require that the ratio of bulk to surface energy remains constant as $\eta$ tends to zero. This imposes constraints on the strength of the surface anchoring in the system because the total surface area of the inclusions tends to infinity as $\eta$ tends to zero. To determine the scaling of the anchoring energy we estimate the total bulk elastic and surface energy in the system. For the system pictured in figure 3.2 the dimensional bulk elastic energy $\tilde{F}_B$ and surface energy $\tilde{F}_S$ are given by,

$$\tilde{F}_B = \int_{\mathcal{D}} \frac{\tilde{L}}{2} \|\tilde{\boldsymbol{\nabla}}\tilde{\mathcal{Q}}\|^2 dV \sim V_{lc}\frac{\tilde{L}}{2}, \tag{3.14a}$$

$$\tilde{F}_S = \sum_i \int_{\Gamma_i} \frac{\tilde{\mu}}{2}\left(\tilde{\mathcal{Q}} - \tilde{\mathcal{Q}}_S\right)^2 dS \sim A_\Gamma \frac{\tilde{\mu}}{2}, \tag{3.14b}$$

with $V_{lc}$ the total volume of liquid crystal, $A_\Gamma$ the total contact area with the inclusions, $\tilde{\mathcal{Q}}_S$ is the preferred surface alignment, $\tilde{L}$ is an elastic constant and $\tilde{\mu}$ is the anchoring energy density. For spherical inclusions of radius $r = \eta r_0$ the total surface area of the inclusions is $A_\Gamma = 4\pi r_0^2 \eta^2 N$ where $N$ is the total number of inclusions. The total number of inclusions in the system is $N = \frac{1}{\eta^3}$, hence the surface energy $\tilde{F}_S$ scales as $\tilde{\mu}\eta^{-1}$. The total bulk elastic energy is independent of $\eta$, hence, for a system with a constant ratio of

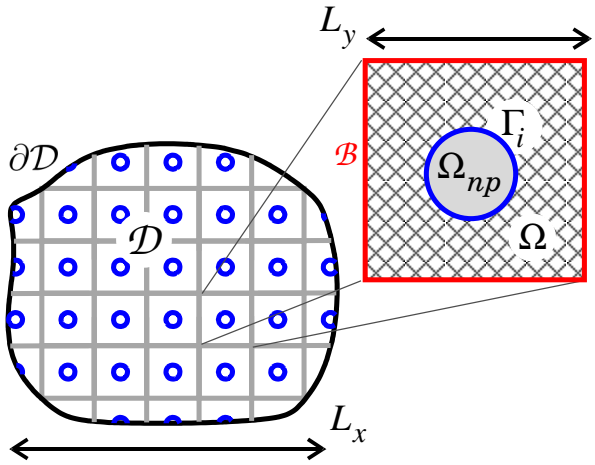


Figure 3.2: Domains used in defining scale separation. The macroscopic domain consists of an open region $\mathcal{D}$, with external boundary $\partial\mathcal{D}$, constructed from unit cells $\Omega$ with outer boundaries $\mathcal{B}$ and inclusions of volume $\Omega_{np}$ and boundary $\Gamma_i$.

surface to bulk free energy the anchoring energy density $\tilde{\mu}$, must scale as $\eta$. In addition to this global constraint on the total surface interaction energy we also require that the anchoring on each inclusions is weak enough as to not induce defects. Taking the results of Kuksenok [54] as a guide, no defects form if $\tilde{\mu}r/\tilde{L} \ll 4$. As both $\tilde{\mu}$ and $r$ scale with $\eta$ this relation is always satisfied in the homogenization limit, $\eta \to 0$.

### 3.3.2 Microscopic governing equations and a priori estimates

We describe the alignment of the nematic by the $\mathcal{Q}$-tensor [35] introduced in equation (1.1) and discussed in 1.3. We define the electrostatic tensor

$$\tilde{\mathcal{E}} = \sqrt{\frac{3}{2}}\left[\tilde{\boldsymbol{\nabla}}\tilde{\phi} \otimes \tilde{\boldsymbol{\nabla}}\tilde{\phi} - (\tilde{\boldsymbol{\nabla}}\tilde{\phi} \cdot \tilde{\boldsymbol{\nabla}}\tilde{\phi})\frac{\mathcal{I}}{3}\right], \tag{3.15}$$

where $\tilde{\phi}$ is the electrostatic potential. We follow the approach outlined by Sonnet *et al.* [105] and express the scaled $\mathcal{Q}$-tensor, preferred surface alignment tensor $\mathcal{Q}_S$ and electrostatic tensor $\tilde{\mathcal{E}}$ on the basis of traceless symmetric tensors. The components on this basis are

$$\tilde{a}_m = \mathrm{Tr}\left[\mathcal{T}^{(m)}\tilde{\mathcal{Q}}\right], \tag{3.16a}$$

$$\tilde{e}_m = \mathrm{Tr}\left[\mathcal{T}^{(m)}\tilde{\mathcal{E}}\right], \tag{3.16b}$$

$$\tilde{a}_{Sm} = \mathrm{Tr}\left[\mathcal{T}^{(m)}\tilde{\mathcal{Q}}_S\right], \tag{3.16c}$$

which form the $m$-th components of the vectors $\tilde{\boldsymbol{a}}$, $\tilde{\boldsymbol{e}}$ and $\tilde{\boldsymbol{a}}_S$, where $\mathcal{T}^{(m)}$, $m = 1, ..., 5$ are a basis of traceless symmetric tensors defined by equations (3.17).

$$\mathcal{T}^{(1)} = \frac{1}{\sqrt{6}} \left( -\hat{\boldsymbol{e}}_1 \otimes \hat{\boldsymbol{e}}_1 - \hat{\boldsymbol{e}}_2 \otimes \hat{\boldsymbol{e}}_2 + 2\hat{\boldsymbol{e}}_3 \otimes \hat{\boldsymbol{e}}_3 \right), \tag{3.17a}$$

$$\mathcal{T}^{(2)} = \frac{1}{\sqrt{2}} \left( \hat{\boldsymbol{e}}_1 \otimes \hat{\boldsymbol{e}}_1 - \hat{\boldsymbol{e}}_2 \otimes \hat{\boldsymbol{e}}_2 \right), \tag{3.17b}$$

$$\mathcal{T}^{(3)} = \frac{1}{\sqrt{2}} \left( \hat{\boldsymbol{e}}_1 \otimes \hat{\boldsymbol{e}}_2 + \hat{\boldsymbol{e}}_2 \otimes \hat{\boldsymbol{e}}_1 \right), \tag{3.17c}$$

$$\mathcal{T}^{(4)} = \frac{1}{\sqrt{2}} \left( \hat{\boldsymbol{e}}_1 \otimes \hat{\boldsymbol{e}}_3 + \hat{\boldsymbol{e}}_3 \otimes \hat{\boldsymbol{e}}_1 \right), \tag{3.17d}$$

$$\mathcal{T}^{(5)} = \frac{1}{\sqrt{2}} \left( \hat{\boldsymbol{e}}_2 \otimes \hat{\boldsymbol{e}}_3 + \hat{\boldsymbol{e}}_3 \otimes \hat{\boldsymbol{e}}_2 \right), \tag{3.17e}$$

The governing equations for the alignment of the nematic can be derived from the dissipation principle discussed in 1.3. Here we neglect fluid flow and set all viscosities in (1.31) to zero except for $\zeta_1$. In non-dimensional form the governing equations are

$$\xi_0^2 \nabla^2 \boldsymbol{a} + \chi_a \boldsymbol{e} + M(\boldsymbol{a})\boldsymbol{a} = \frac{\partial \boldsymbol{a}}{\partial t} \qquad \boldsymbol{x} \in \mathcal{D}, \tag{3.18a}$$

$$\hat{\boldsymbol{\nu}} \cdot \boldsymbol{\nabla} \boldsymbol{a} = W \left( \boldsymbol{a}_S - \boldsymbol{a} \right) \qquad \boldsymbol{x} \in \Gamma_i, \tag{3.18b}$$

$$\boldsymbol{a} = \boldsymbol{b}\left(\boldsymbol{x}\right) \qquad \boldsymbol{x} \in \partial\mathcal{D}, \tag{3.18c}$$

where $\boldsymbol{b}(\boldsymbol{x})$ is the prescribed value of $\boldsymbol{a}(\boldsymbol{x})$ on the macroscopic boundary $\partial\mathcal{D}$, $\hat{\boldsymbol{\nu}}$ is the unit normal on $\Gamma_i$. The non-dimensional elastic constant is given by $\xi_0^2 = \frac{9C\tilde{L}}{2B^2 L_x^2}$, $\chi_a = \frac{9\epsilon_0 \Delta\epsilon C^2 \tilde{V}}{2L_x^2 B^3}$ is the dimensionless dielectric anisotropy, $W = \frac{\tilde{\mu} L_x}{2\tilde{L}}$ is the dimensionless anchoring strength and $\tilde{V}$ is a characteristic potential. The non-dimensional time $t$ and spatial position $\boldsymbol{x}$ are $t = \frac{2B^2}{9C\zeta_1}\tilde{t}$ and $\tilde{\boldsymbol{x}} = L_x \boldsymbol{x}$, with $\tilde{\boldsymbol{x}}$ the dimensional spatial position. The components of the $\mathcal{Q}$-tensor and electrostatic potential are scaled according to $\tilde{\boldsymbol{a}} = \frac{2B}{3C}\boldsymbol{a}$, $\tilde{\boldsymbol{a}}_S = \frac{2B}{3C}\boldsymbol{a}_S$, $\tilde{\phi} = \tilde{V}\phi$ and $\tilde{\boldsymbol{e}} = \frac{2B}{3C}\boldsymbol{e}$. The non-linear thermotropic contribution to the evolution equations are

confined to the thermotropic term $M(\boldsymbol{a})$ given by (3.19).

$$M(\boldsymbol{a}) = T\mathcal{I} + \begin{bmatrix} 3a_1 & -3a_2 & -3a_3 & \frac{3}{2}a_4 & \frac{3}{2}a_5 \\ -3a_2 & -3a_1 & 0 & \frac{3}{2}\sqrt{3}a_4 & -\frac{3}{2}\sqrt{3}a_5 \\ -3a_3 & 0 & 3a_1 & \frac{3}{2}\sqrt{3}a_5 & \frac{3}{2}\sqrt{3}a_4 \\ \frac{3}{2}a_4 & \frac{3}{2}\sqrt{3}a_4 & \frac{3}{2}\sqrt{3}a_5 & \frac{3}{2}a_1 + \frac{3}{2}\sqrt{3}a_2 & \frac{3}{2}\sqrt{3}a_3 \\ \frac{3}{2}a_5 & -\frac{3}{2}\sqrt{3}a_5 & \frac{3}{2}\sqrt{3}a_4 & \frac{3}{2}\sqrt{3}a_3 & \frac{3}{2}a_1 - \frac{3}{2}\sqrt{3}a_2 \end{bmatrix}, \tag{3.19}$$

and

$$T = -T_0 - 2\sum_{k=1}^{5} a_k^2. \tag{3.20}$$

The electric field is governed by Maxwell's equation $\boldsymbol{\nabla} \cdot \boldsymbol{D} = 0$. We model the gold inclusions as macroscopic ideal conductors, ignoring finite size effects. The electric potential is hence subject to a floating potential on the metallic inclusions. Expressed in terms of the non-dimensional electrostatic potential $\phi$ this reads

$$\boldsymbol{\nabla} \cdot [(\mathcal{I} + \alpha\mathcal{Q})\, \boldsymbol{\nabla}\phi] = 0 \qquad \boldsymbol{x} \in \mathcal{D}, \tag{3.21a}$$

$$\phi = V_0(\boldsymbol{x}) \qquad \boldsymbol{x} \in \partial\mathcal{D}, \tag{3.21b}$$

$$\phi = \mathrm{C}_i \qquad \boldsymbol{x} \in \Gamma_i, \tag{3.21c}$$

$$\int_{\Gamma_i} \hat{\boldsymbol{\nu}} \cdot (\mathcal{I} + \alpha\mathcal{Q})\, \boldsymbol{\nabla}\phi dS = 0 \qquad \boldsymbol{x} \in \Gamma_i, \tag{3.21d}$$

where $\alpha = \sqrt{\frac{2}{3}}\frac{\Delta\epsilon}{\epsilon_u}\frac{2B}{3C}$ with $\epsilon_u$ the isotropic dielectric coefficient. $C_i$ is the constant potential attained on the surface $\Gamma_i$ of the $i$-th inclusion. The value of this constant is determined by the macroscopic boundary conditions (3.21b). $V_0(\boldsymbol{x})$ is the prescribed value of the potential on the macroscopic boundary $\partial\mathcal{D}$. The non-dimensional elastic constant $\xi_0^2$ and dielectric anisotropy $\chi_a$ are very small. For a typical liquid crystal mixture with parameters given by table 3.1 $\xi_0^2 = 4.39 \cdot 10^{-7}$ and $\chi_a = 5.13 \cdot 10^{-6}$. Conversely the thermotropic term $M(\boldsymbol{a})\boldsymbol{a}$ is $\mathcal{O}(1)$ indicating that the liquid crystal dynamics, equation (3.18a) has at least two different time scales [34]. Evolution on the fast time scale is determined by the thermotropic term $M(\boldsymbol{a})\boldsymbol{a}$ which drives the $\mathcal{Q}$-tensor into the uniaxial state [34]. We are interested in the reorientation of the liquid crystal due to the elastic and electrostatic energies. The reorientational dynamics occurs on a far slower time-scale as they are driven by the weaker elastic and electrostatic terms.

Given the natural time-scale separation present in (3.18a) we split the derivation into

| $K = 15$ pN | $S = \frac{3+\sqrt{9-8T_0}}{4}$ |
|---|---|
| $A = 0.13 \cdot 10^6$ JK$^{-1}$m$^{-3}$ | $\epsilon_\perp = 4.1$ |
| $B = 1.6 \cdot 10^6$ JK$^{-1}$m$^{-3}$ | $\epsilon_\parallel = 9.1$ |
| $C = 3.9 \cdot 10^6$ JK$^{-1}$m$^{-3}$ | $L_x = 32 \cdot 10^{-6}$ m |
| $T_0 = -10$ | $\gamma_1 = 0.081$ Pa s |
| $\tilde{\mu} = 3.23 \cdot 10^{-8} W$ Jm$^{-2}$ | $\tilde{\xi}_0^2 = 4.631 \cdot 10^{-8}$ |
| $\chi_a = 7.221 \cdot 10^{-7}$ | |

Table 3.1: Parameters used in numerical simulations, values represent a typical liquid crystal.

two steps. Firstly, we apply the methods of homogenisation to confine the details of the microscopic geometry to effective material parameters. Secondly we utilise the method of multiple scales to simplify the dynamics of our system [34].

As discussed earlier, in this chapter we consider the case where the ratio of surface to bulk energy remains constant as $\eta \to 0$. As $\eta \to 0$ the total surface area tends to infinity. We have shown, using equations (3.14) that in order for the total surface energy to remain finite the surface anchoring energy density must scale linearly with $\eta$, in other words $W$ is $\mathcal{O}(\eta)$. We therefore define a scaled anchoring energy $W_1$ as $W = \eta W_1$. Although under this scaling the surface anchoring energy density tends to zero as $\eta \to 0$ it should be noted that the total surface energy remains finite, and in general, non-zero.

Before we proceed to apply homogenisation theory to our system we identify the physically relevant range of anchoring energies that our model applies to. We assume inclusions are fixed and do not nucleate defects. As noted previously the weak anchoring condition [54] always holds in the homogenisation limit. Assuming fixed inclusions is likely to be valid provided inclusions do not aggregate on the experimental time scale. In a real system $\eta \neq 0$, hence, we now estimate values of $W_1$ that do not induce defects.

Using the parameters in table 3.1 we find that the anchoring energy density scales as $\tilde{\mu} = 3.28 \cdot 10^{-8} \eta W_1$ Jm$^{-2}$. For a typical liquid crystal cell used in our numerical simulations $L_x = 32$ $\mu$m, $L_y = 1$ $\mu$m and a particle of radius 50 nm, weak anchoring corresponds to $W_1 \ll 40000$.

Ruhwandl and Terentjer [94] identify the aggregation time using a director based model by considering the elastic interaction between separated colloidal particles. The aggregation time is given by [94]

$$\tau_{ag} = \frac{0.5 L \nu}{\tilde{\mu}^2} \left( \frac{1}{c^{7/3}} - \frac{1}{c_m^{7/3}} \right) \tag{3.22}$$

where $\nu$ is a characteristic viscosity taken to be $\nu = 0.1$Pa s and $c_m = 0.74$ is the maximum colloidal packing fraction. Using table 3.1 and the above parameters, the volume fraction

of particles is $c = 5 \cdot 10^{-4}$ giving an aggregation of $\tau_{ag} \approx 25$ weeks for $W_1 = 100$. We expect the theory developed here to apply to low volume concentrations, i.e. $c \leq 0.01$. However for the purpose of numerical verification it is easier to simulate systems containing larger inclusions, and hence larger volume fractions. To summarise our model is tailored towards systems in which the anchoring to an individual inclusion is weak enough to not induce defects and in which the overall effect of the anchoring on the nematic alignment does not dominate the system.

### 3.3.3 Static inclusions Homogenisation

To homogenize equations (3.18) and (3.21) we use a perturbation expansion in the small parameter $\eta$. We define a microscopic scale $\boldsymbol{y}$ by the relation $\boldsymbol{y} = \frac{\boldsymbol{x}}{\eta}$ and assume that all fields are, a priori functions of $\boldsymbol{x}$ and $\boldsymbol{y}$. We use the chain rule and expand $\phi$, $\boldsymbol{a}$, $\mathcal{Q}$, $\boldsymbol{e}$, the floating potentials $C_i$ and the spatial derivatives as a series in $\eta$:

$$\boldsymbol{\nabla} = \frac{1}{\eta}\boldsymbol{\nabla}_{\boldsymbol{y}} + \boldsymbol{\nabla}_{\boldsymbol{x}}, \tag{3.23a}$$

$$\boldsymbol{a} = \boldsymbol{a}_0 + \eta\boldsymbol{a}_1 + \eta^2\boldsymbol{a}_2 + \mathcal{O}(\eta^3), \tag{3.23b}$$

$$\phi = \phi_0 + \eta\phi_1 + \eta^2\phi_2 + \mathcal{O}(\eta^3), \tag{3.23c}$$

$$\mathcal{Q} = \mathcal{Q}_0 + \eta\mathcal{Q}_1 + \eta^2\mathcal{Q}_2 + \mathcal{O}(\eta^3), \tag{3.23d}$$

$$\boldsymbol{e} = \frac{\boldsymbol{e}_0}{\eta^2} + \frac{\boldsymbol{e}_1}{\eta} + \boldsymbol{e}_2 + \mathcal{O}(\eta), \tag{3.23e}$$

$$C_i = C_{0i} + \eta C_{1i} + \eta^2 C_{2i} + \mathcal{O}(\eta^3). \tag{3.23f}$$

where $\boldsymbol{e}_0$, $\boldsymbol{e}_1$ and $\boldsymbol{e}_2$ have components given by (3.24).

$$e_{0i} = \mathrm{Tr}\left(\sqrt{\frac{3}{2}}\left[\boldsymbol{\nabla}_{\boldsymbol{y}}\phi_0 \otimes \boldsymbol{\nabla}_{\boldsymbol{y}}\phi_0\right]\mathcal{T}^{(i)}\right), \tag{3.24a}$$

$$e_{1i} = \mathrm{Tr}\left(\sqrt{\frac{3}{2}}\left[\boldsymbol{\nabla}_{\boldsymbol{x}}\phi_0 \otimes \boldsymbol{\nabla}_{\boldsymbol{y}}\phi_0 + \boldsymbol{\nabla}_{\boldsymbol{y}}\phi_0 \otimes \boldsymbol{\nabla}_{\boldsymbol{x}}\phi_0 + \boldsymbol{\nabla}_{\boldsymbol{y}}\phi_0 \otimes \boldsymbol{\nabla}_{\boldsymbol{y}}\phi_1 + \boldsymbol{\nabla}_{\boldsymbol{y}}\phi_1 \otimes \boldsymbol{\nabla}_{\boldsymbol{y}}\phi_0\right]\mathcal{T}^{(i)}\right), \tag{3.24b}$$

$$e_{2i} = \mathrm{Tr}\left(\sqrt{\frac{3}{2}}\left[\boldsymbol{\nabla}_{\boldsymbol{y}}\phi_0 \otimes (\boldsymbol{\nabla}_{\boldsymbol{y}}\phi_2 + \boldsymbol{\nabla}_{\boldsymbol{x}}\phi_1) + (\boldsymbol{\nabla}_{\boldsymbol{x}}\phi_0 + \boldsymbol{\nabla}_{\boldsymbol{y}}\phi_1) \otimes (\boldsymbol{\nabla}_{\boldsymbol{x}}\phi_0 + \boldsymbol{\nabla}_{\boldsymbol{y}}\phi_1)\right.\right.$$
$$\left.\left. + (\boldsymbol{\nabla}_{\boldsymbol{y}}\phi_2 + \boldsymbol{\nabla}_{\boldsymbol{x}}\phi_1) \otimes \boldsymbol{\nabla}_{\boldsymbol{y}}\phi_0\right]\mathcal{T}^{(i)}\right), \tag{3.24c}$$

for $i = 1, ..., 5$.

As discussed in section 3.3.2 we set $W = \eta W_1$ to ensure that our model captures the weak anchoring limit. The method of homogenisation is as follows: we substitute equations (3.23) into (3.18) and (3.21) and solve the resulting equations in ascending powers of $\eta$. In doing so we impose appropriate solvability conditions at each order in $\eta$, requiring that all equations have a solution. This requirement imposes constraints on the terms in (3.23). Once we have proceeded to $\mathcal{O}(\eta^2)$ we will have sufficient constraints to determine the leading order behaviour of the system.

### The $\mathcal{O}(1)$ equations

Substituting equations (3.23) into (3.18) and (3.21) and retaining terms of order $\mathcal{O}(1)$ we obtain

$$\xi_0^2 \nabla_{\boldsymbol{y}}^2 \boldsymbol{a}_0 + \chi_a \boldsymbol{e}_0 = 0 \qquad \boldsymbol{y} \in \Omega, \tag{3.25a}$$

$$\hat{\boldsymbol{\nu}} \cdot \boldsymbol{\nabla}_{\boldsymbol{y}} \boldsymbol{a}_0 = 0 \qquad \boldsymbol{y} \in \Gamma_i. \tag{3.25b}$$

The leading order electric potential is governed by,

$$\boldsymbol{\nabla}_{\boldsymbol{y}} \cdot \left[\left(\mathcal{I} + \alpha \mathcal{Q}_0\right) \boldsymbol{\nabla}_{\boldsymbol{y}} \phi_0\right] = 0 \qquad \boldsymbol{y} \in \Omega, \tag{3.26a}$$

$$\phi_0 = C_{0i} \qquad \boldsymbol{y} \in \Gamma_i, \tag{3.26b}$$

$$\int_{\Gamma_i} \left[\left(\mathcal{I} + \alpha \mathcal{Q}_0\right) \boldsymbol{\nabla}_{\boldsymbol{y}} \phi_0\right] \cdot d\boldsymbol{S} = 0 \qquad \boldsymbol{y} \in \Gamma_i. \tag{3.26c}$$

Notice that $\phi_0 = \phi_0(\boldsymbol{x})$ and $\boldsymbol{a}_0 = \boldsymbol{a}_0(\boldsymbol{x})$ solve (3.25) and (3.26) provided that the condition,

$$\phi_0 = C_{0i} \qquad \boldsymbol{y} \in \Gamma_i, \tag{3.27}$$

are satisfied. Condition (3.27) constrains the potential to a constant unknown value on the surface of the $i$-th inclusions. If $\phi_0$ varies only on the macroscopic scale $\boldsymbol{x}$ there will be

a small change in its value, of $\mathcal{O}(\eta)$ across a unit cell: as a result condition (3.27) cannot be satisfied and needs to be modified slightly. We Taylor expand $\phi_0$ about a point $\boldsymbol{x}_i$ on $\Gamma_i$

$$\begin{aligned}\phi_0(\boldsymbol{x}) =&\phi_0(\boldsymbol{x}_i) + (\boldsymbol{x}-\boldsymbol{x}_i)\cdot\boldsymbol{\nabla}_{\boldsymbol{x}}\phi_0(\boldsymbol{x}_i) + (\boldsymbol{x}-\boldsymbol{x}_i)^T\mathcal{H}(\phi_0)(\boldsymbol{x}_i)(\boldsymbol{x}-\boldsymbol{x}_i)\\ &+\mathcal{O}\left((\boldsymbol{x}-\boldsymbol{x}_i)^3\right),\end{aligned} \tag{3.28}$$

where $[\mathcal{H}_\phi]_{nm} = \left[\frac{\partial^2\phi_0}{\partial x_n \partial x_m}\right]_{\boldsymbol{x}=\boldsymbol{x}_i}$. By using the relation $\boldsymbol{x} = \eta\boldsymbol{y}$ we obtain,

$$\begin{aligned}\phi_0(\boldsymbol{x}) =&\phi_0(\boldsymbol{x}_i) + \eta(\boldsymbol{y}-\boldsymbol{y}_i)\cdot\boldsymbol{\nabla}_{\boldsymbol{x}}\phi_0(\boldsymbol{x}_i) + \eta^2(\boldsymbol{y}-\boldsymbol{y}_i)^T\mathcal{H}(\phi_0)(\boldsymbol{x}_i)(\boldsymbol{y}-\boldsymbol{y}_i)\\ &+\mathcal{O}\left(\eta^3\right).\end{aligned} \tag{3.29}$$

Hence we modify the boundary condition (3.27) to,

$$\phi_0(\boldsymbol{x}_i) = C_{0i} \qquad \boldsymbol{y}\in\Gamma_i. \tag{3.30}$$

Substituting equation (3.29) and (3.23c) into equation (3.21d) and using (3.23f) we obtain an appropriate boundary condition for $\phi_1$,

$$\phi_1 = -(\boldsymbol{y}-\boldsymbol{y}_i)\cdot\boldsymbol{\nabla}_{\boldsymbol{x}}\phi_0 + C_{1i} \qquad \boldsymbol{y}\in\Gamma_i \tag{3.31}$$

The value of the constant $C_{0i}$ will be fixed at higher order using the macroscopic boundary conditions.

### The $\mathcal{O}(\eta)$ equations

At $\mathcal{O}(\eta)$ using $\boldsymbol{a}_0 = \boldsymbol{a}_0(\boldsymbol{x})$ and $\phi_0 = \phi_0(\boldsymbol{x})$ we find,

$$\nabla^2_{\boldsymbol{y}}\boldsymbol{a}_1 = 0 \qquad \boldsymbol{y}\in\Omega, \tag{3.32a}$$

$$\hat{\boldsymbol{\nu}}\cdot\boldsymbol{\nabla}_{\boldsymbol{y}}\boldsymbol{a}_1 + \hat{\boldsymbol{\nu}}\cdot\boldsymbol{\nabla}_{\boldsymbol{x}}\boldsymbol{a}_0 = 0 \qquad \boldsymbol{y}\in\Gamma_i, \tag{3.32b}$$

and

$$\boldsymbol{\nabla}_{\boldsymbol{y}}\cdot[(\mathcal{I}+\alpha\mathcal{Q}_0)\boldsymbol{\nabla}_{\boldsymbol{y}}\phi_1] = 0 \qquad \boldsymbol{y}\in\Omega, \tag{3.33a}$$

$$\phi_1 = -(\boldsymbol{y}-\boldsymbol{y}_i)\cdot\boldsymbol{\nabla}_{\boldsymbol{x}}\phi_0 + C_{1i} \qquad \boldsymbol{y}\in\Gamma_i, \tag{3.33b}$$

$$\int_{\Gamma_i}[\mathcal{I}+\alpha\mathcal{Q}_0](\boldsymbol{\nabla}_{\boldsymbol{y}}\phi_1 + \boldsymbol{\nabla}_{\boldsymbol{x}}\phi_0)\cdot d\boldsymbol{S} = 0 \qquad \boldsymbol{y}\in\Gamma_i, \tag{3.33c}$$

where summation over repeated indices is implied. We have simplified equations (3.32)-(3.33) using the constraints on $\boldsymbol{a}_0$ and $\phi_0$ found at $\mathcal{O}(1)$. We note that the electric field contribution, $\boldsymbol{e}_1$, which would appear in equation (3.32a), is zero as $\phi_0$ is independent of $\boldsymbol{y}$. To ensure solvability for $\boldsymbol{a}_1$ we integrate equation (3.32a) over the volume of a cell and use the divergence theorem along with boundary conditions (3.32b). The solvability condition is found by integrating (3.32a)

$$\int_\Omega \nabla^2_{\boldsymbol{y}} \boldsymbol{a}_1 dV = 0 \tag{3.34}$$

using the divergence theorem and boundary conditions (3.32b) we find

$$\begin{aligned}\int_\Omega \nabla^2_{\boldsymbol{y}} \boldsymbol{a}_1 dV &= \int_\Gamma \hat{\boldsymbol{\nu}} \cdot \boldsymbol{\nabla}_{\boldsymbol{y}} \boldsymbol{a}_1 dS \\ &= -\int_\Gamma \hat{\boldsymbol{\nu}} \cdot \boldsymbol{\nabla}_{\boldsymbol{x}} \boldsymbol{a}_0 dS \\ &= 0\end{aligned} \tag{3.35}$$

which is automatically satisfied. We now proceed to find the solution of equation (3.32a) subject to (3.32b). We use the ansatz

$$\boldsymbol{a}_1(\boldsymbol{x}, \boldsymbol{y}) = \chi_k(\boldsymbol{y}) \frac{\partial \boldsymbol{a}_0}{\partial x_k}(\boldsymbol{x}), \tag{3.36}$$

where we have absorbed the long scale spatial dependence of $\boldsymbol{a}_1$ into the derivative of $\boldsymbol{a}_0$. Substituting equation (3.36) into (3.32a) and (3.32b) we obtain the standard cell problem for elliptic homogenisation,

$$\nabla^2_{\boldsymbol{y}} \chi_k = 0 \qquad \boldsymbol{y} \in \Omega, \tag{3.37a}$$

$$\hat{\boldsymbol{\nu}} \cdot \boldsymbol{\nabla}_{\boldsymbol{y}} \chi_k = -\hat{\boldsymbol{\nu}} \cdot \boldsymbol{e}_k \qquad \boldsymbol{y} \in \Gamma_i, \tag{3.37b}$$

The cell problem (3.37) is solved numerically inside a unit cube with periodic boundary conditions on the outer sides, denoted $\mathcal{B}$ in figure 3.2.

Turning to equation (3.33) the solvability condition is obtained by integrating (3.33a) over a unit cell and applying the divergence theorem,

$$\int_{\Gamma_i} \left(\mathcal{I} + \alpha \mathcal{Q}_0\right) \boldsymbol{\nabla}_{\boldsymbol{y}} \phi_1 \cdot d\boldsymbol{S} = 0. \tag{3.38}$$

Substituting equation (3.33b) into (3.38) we find that the solvability condition is satisfied.

To obtain the cell problem for $\phi_1$ we make the ansatz,

$$\phi_1 = \sum_{k=1}^{3} R_k\left(\boldsymbol{x}, \boldsymbol{y}\right) \frac{\partial \phi_0}{\partial x_k} + \bar{\phi}_1\left(\boldsymbol{x}\right). \tag{3.39}$$

Substituting equation (3.39) into (3.33) we find the cell problem

$$\left[\delta_{ij} + \alpha \mathcal{Q}_{0ij}\right] \frac{\partial^2 R_k}{\partial y_i \partial y_j} = 0 \qquad \boldsymbol{y} \in \Omega, \tag{3.40a}$$

$$R_k = -(y_k - y_{0k}), \qquad \boldsymbol{y} \in \Gamma_i \tag{3.40b}$$

$$\int_{\Gamma_i} \left(\mathcal{I} + \alpha \mathcal{Q}_0\right) \boldsymbol{\nabla}_{\boldsymbol{y}} R_k(\boldsymbol{y}) \cdot d\boldsymbol{S} = 0, \qquad \boldsymbol{y} \in \Gamma_i \tag{3.40c}$$

where $k = 1, 2, 3$ and we have set $\bar{\phi}_1 = C_{1i}$. The final cell problem (3.40) can be solved numerically subject to periodic boundary conditions on $\mathcal{B}$ (see figure 3.2) once the leading order alignment tensor $\mathcal{Q}_0$ is known. Unlike for equations (3.32) a separation of scales is impossible and we cannot obtain a cell problem that is completely independent of the macroscopic variable $\boldsymbol{x}$. While this may appear to be a problem it suffices to solve (3.40) for a discrete set of $\mathcal{Q}_0$ and interpolate.

### The $\mathcal{O}(\eta^2)$ equations

As a final step we collect terms of $\mathcal{O}(\eta^2)$,

$$\begin{aligned} &\xi_0^2 \left(\nabla_{\boldsymbol{y}}^2 \boldsymbol{a}_2 + \boldsymbol{\nabla}_{\boldsymbol{x}} \cdot \boldsymbol{\nabla}_{\boldsymbol{y}} \boldsymbol{a}_1 + \boldsymbol{\nabla}_{\boldsymbol{y}} \cdot \boldsymbol{\nabla}_{\boldsymbol{x}} \boldsymbol{a}_1 + \nabla_{\boldsymbol{x}}^2 \boldsymbol{a}_0\right) \\ &\quad + M_0 \boldsymbol{a}_0 + \chi_a \boldsymbol{e}_2 = \frac{\partial \boldsymbol{a}_0}{\partial t} \qquad \boldsymbol{y} \in \Omega, \end{aligned} \tag{3.41a}$$

$$\hat{\boldsymbol{\nu}} \cdot \boldsymbol{\nabla}_{\boldsymbol{y}} \boldsymbol{a}_2 + \hat{\boldsymbol{\nu}} \cdot \boldsymbol{\nabla}_{\boldsymbol{x}} \boldsymbol{a}_1 = W_1 \left(\boldsymbol{a}_S - \boldsymbol{a}_0\right) \qquad \boldsymbol{y} \in \Gamma_i, \tag{3.41b}$$

$$\begin{aligned} &\boldsymbol{\nabla}_{\boldsymbol{y}} \cdot \left[\left(\mathcal{I} + \alpha \mathcal{Q}_0\right) \left(\boldsymbol{\nabla}_{\boldsymbol{y}} \phi_2 + \boldsymbol{\nabla}_{\boldsymbol{x}} \phi_1\right) + \alpha \mathcal{Q}_1 \boldsymbol{\nabla}_{\boldsymbol{y}} \phi_1 + \alpha \mathcal{Q}_1 \boldsymbol{\nabla}_{\boldsymbol{x}} \phi_0\right] \\ &+ \boldsymbol{\nabla}_{\boldsymbol{y}} \cdot \left[\alpha \mathcal{Q}_2 \boldsymbol{\nabla}_{\boldsymbol{y}} \phi_0\right] + \boldsymbol{\nabla}_{\boldsymbol{x}} \cdot \left[\left(\mathcal{I} + \alpha \mathcal{Q}_0\right) \left(\boldsymbol{\nabla}_{\boldsymbol{x}} \phi_0 + \boldsymbol{\nabla}_{\boldsymbol{y}} \phi_1\right)\right] \\ &\quad + \boldsymbol{\nabla}_{\boldsymbol{x}} \cdot \left[\alpha \mathcal{Q}_1 \boldsymbol{\nabla}_{\boldsymbol{y}} \phi_0\right] = 0 \qquad \boldsymbol{y} \in \Omega, \end{aligned} \tag{3.42a}$$

$$\int_{\Gamma_i} \left[\left(\mathcal{I} + \alpha \mathcal{Q}_0\right)\left(\boldsymbol{\nabla}_{\boldsymbol{y}} \phi_2 + \boldsymbol{\nabla}_{\boldsymbol{x}} \phi_1\right) + \alpha \mathcal{Q}_1 \left(\boldsymbol{\nabla}_{\boldsymbol{x}} \phi_0 + \boldsymbol{\nabla}_{\boldsymbol{y}} \phi_1\right)\right] \cdot d\boldsymbol{S} = 0 \qquad \boldsymbol{y} \in \Gamma_i. \tag{3.42b}$$

Here

$$M_0 = M(\boldsymbol{a}_0), \tag{3.43}$$

and the matrix valued non-linear function $M$ is defined by equation (3.19). As before we require that equations (3.41a) and (3.42a) have solutions. We start by projecting (3.41a) onto the kernel of the operator $\nabla^2_{\boldsymbol{y}}$ (equipped with periodic boundary conditions) which is spanned by constants. The equation governing the alignment of the nematic is,

$$\int_\Omega \left[\xi_0^2(\nabla^2_{\boldsymbol{y}}\boldsymbol{a}_2 + \boldsymbol{\nabla}_{\boldsymbol{x}}\cdot\boldsymbol{\nabla}_{\boldsymbol{y}}\boldsymbol{a}_1 + \boldsymbol{\nabla}_{\boldsymbol{y}}\cdot\boldsymbol{\nabla}_{\boldsymbol{x}}\boldsymbol{a}_1 + \nabla^2_{\boldsymbol{x}}\boldsymbol{a}_0) + M_0\boldsymbol{a}_0 + \xi_0^2\chi\boldsymbol{e}_2\right]dV = \int_\Omega \frac{\partial \boldsymbol{a}_0}{\partial t}dV \tag{3.44}$$

Next using the definition of $\boldsymbol{e}_2$ we have,

$$\int_\Omega \boldsymbol{e}_{2i}dV = \mathrm{Tr}\left[\boldsymbol{\nabla}_{\boldsymbol{x}}\phi_0 \otimes \boldsymbol{\nabla}_{\boldsymbol{x}}\phi_0\left(|\Omega| + 2|\Omega_{np}|\right)\mathcal{T}^{(i)} + \int_\Omega \boldsymbol{\nabla}_{\boldsymbol{y}}\phi_1 \otimes \boldsymbol{\nabla}_{\boldsymbol{y}}\phi_1 dV\mathcal{T}^{(i)}\right], \tag{3.45}$$

where $|\Omega|$ is the volume of liquid crystal contained in a unit cell and $|\Omega_{np}|$ is the volume of an inclusion and we have used

$$\int_\Omega \nabla_{\boldsymbol{y}}\phi_1 d^3y = \sum_{k=1}^{3}\hat{\boldsymbol{e}}_k\cdot\boldsymbol{\nabla}_{\boldsymbol{x}}\phi_0(\boldsymbol{x})\int_\Omega \boldsymbol{\nabla}_{\boldsymbol{y}}R_k(\boldsymbol{y})d^3y, \tag{3.46}$$

and using the divergence theorem and boundary conditions (3.40b) it can be shown that

$$\int_\Omega \boldsymbol{\nabla}_{\boldsymbol{y}}R_k\left(\boldsymbol{y}\right)d^3y = \int_{\Gamma_i} R_k\left(\boldsymbol{y}\right)\hat{\boldsymbol{\nu}}dS = |\Omega_{np}|\hat{\boldsymbol{e}}_k \tag{3.47}$$

Using boundary condition (3.41b) to remove $\boldsymbol{a}_2$ and (3.45) we find the homogenised equation is

$$\begin{aligned}&\xi_0^2\boldsymbol{\nabla}_{\boldsymbol{x}}\cdot(\mathcal{K}\boldsymbol{\nabla}_{\boldsymbol{x}}\boldsymbol{a}_0) + M_0\boldsymbol{a}_0 + \chi_a\left(\boldsymbol{e}_M\left(1 + 2\frac{\|\Omega_{np}\|}{\|\Omega\|}\right) + \boldsymbol{p}\right)\\ &+ \frac{\xi_0^2 W_1}{\|\Omega\|}\int_\Gamma\left(\boldsymbol{a}_S - \boldsymbol{a}_0\right)dS = \frac{\partial \boldsymbol{a}_0}{\partial t}.\end{aligned} \tag{3.48}$$

Here

$$\mathcal{K}_{ij} = \frac{1}{|\Omega|}\int_\Omega\left(\delta_{ij} + \frac{\partial\chi_j}{\partial y_i}\right)d^3y, \tag{3.49}$$

and the components of the macroscopic electric field $\boldsymbol{e}_M$ and induced polarisation field $\boldsymbol{p}$ are,

$$e_{Mi} = \mathrm{Tr}\left[\boldsymbol{\nabla}_{\boldsymbol{x}}\phi_0 \otimes \boldsymbol{\nabla}_{\boldsymbol{x}}\phi_0\mathcal{T}^{(i)}\right], \tag{3.50}$$

$$p_i = \frac{1}{|\Omega|}\int_\Omega \mathrm{Tr}\left[\boldsymbol{\nabla}_{\boldsymbol{y}}\phi_1 \otimes \boldsymbol{\nabla}_{\boldsymbol{y}}\phi_1 \mathcal{T}^{(i)}\right] dV, \tag{3.51}$$

The solvability condition for the electric potential is

$$|\Omega|\boldsymbol{\nabla}_{\boldsymbol{x}}\cdot\left[\left(\mathcal{I}+\alpha\mathcal{Q}_0\right)\boldsymbol{\nabla}_{\boldsymbol{x}}\phi_0\right] + \boldsymbol{\nabla}_{\boldsymbol{x}}\cdot\left[\left(\mathcal{I}+\alpha\mathcal{Q}_0\right)\int_\Omega \boldsymbol{\nabla}_{\boldsymbol{y}}\phi_1 d^3y\right] = 0. \tag{3.52}$$

Using (3.47) we find that the homogenised equation for the electric potential is

$$\boldsymbol{\nabla}_{\boldsymbol{x}}\cdot\left[\left(|\Omega|+|\Omega_{np}|\right)\left(\mathcal{I}+\alpha\mathcal{Q}_0\right)\boldsymbol{\nabla}_{\boldsymbol{x}}\phi_0\right] = 0. \tag{3.53}$$

### Reduced manifold dynamics

As mention previously the liquid crystal dynamics occur across two separate time-scales. We now apply multiple scale analysis to extract the slow dynamics from equation (3.48). Firstly using $\xi_0^2$ as the small parameter equation (3.48) can be rewritten as,

$$\begin{aligned}&\xi_0^2\nabla_x\cdot\left(\mathcal{K}\nabla_x\boldsymbol{a}_0\right) + M_0\boldsymbol{a}_0 + \xi_0^2\chi\left(\boldsymbol{e}_M\left(1+2\frac{\|\Omega_{np}\|}{\|\Omega\|}\right)+\boldsymbol{p}\right)\\ &+\frac{\xi_0^2 W_1}{\|\Omega\|}\int_\Gamma\left(\boldsymbol{a}_S-\boldsymbol{a}_0\right)dS = \frac{\partial\boldsymbol{a}_0}{\partial t},\end{aligned} \tag{3.54}$$

where $\chi_a = \chi\xi_0^2$. Now we expand $\boldsymbol{a}_0$ in a series in $\xi_0^2$

$$\boldsymbol{a}_0 = \boldsymbol{a}_{00} + \xi_0^2\boldsymbol{a}_{01} + \mathcal{O}(\xi_0^4), \tag{3.55}$$

and replace the time derivative in (3.54) using the chain rule

$$\frac{\partial}{\partial t} = \xi_0^2\frac{\partial}{\partial t_1}, \tag{3.56}$$

where we have discarded the fast time-scale of the thermotropic free energy and track only the dynamics occuring on the slow elastic time-scale $t_1$. The leading order dynamics produce

$$M_{00}\boldsymbol{a}_{00} = 0, \tag{3.57}$$

where recalling that $M_0$ is a matrix valued function of $M_{00} = M_0(\boldsymbol{a}_{00})$. It follows from (3.57) that the leading order scalar and biaxial order parameters are $|\boldsymbol{a}_{00}| = S_0$ and $\beta_0 = 1 - \frac{6\mathrm{Tr}^2(\mathcal{Q}_0^3)}{\mathrm{Tr}^3(\mathcal{Q}_0^2)} = 0$ [34]. $S_0$ is determined by the temperature, $S_0 = \frac{3+\sqrt{9-8T_0}}{4}$. Condition (3.57) fixes $\boldsymbol{a}_{00}$ onto the solution manifold consisting of uniaxial tensors of order parameter $S_0$. The remaining degrees of freedom will be determined at higher order in $\xi_0^2$. At order

$\xi_0^2$ we find

$$\begin{aligned}&\boldsymbol{\nabla}_{\boldsymbol{x}}\cdot(\mathcal{K}\boldsymbol{\nabla}_{\boldsymbol{x}}\boldsymbol{a}_{00})+M_{00}\boldsymbol{a}_{01}+\left(\frac{\partial M_{00}}{\partial a_{00k}}a_{01k}\right)\boldsymbol{a}_{00}\\&+\chi\left(\boldsymbol{e}_M\left(1+2\frac{\|\Omega_{np}\|}{\|\Omega\|}\right)+\boldsymbol{p}\right)+\frac{W_1}{\|\Omega\|}\int_\Gamma(\boldsymbol{a}_S-\boldsymbol{a}_{00})\,dS=\frac{\partial\boldsymbol{a}_{00}}{\partial t},\end{aligned}\tag{3.58}$$

where

$$\frac{\partial M_{00}}{\partial a_{00k}}=\left.\frac{\partial M}{\partial a_k}\right|_{\boldsymbol{a}=\boldsymbol{a}_{00}}.\tag{3.59}$$

To ensure solvability for $\boldsymbol{a}_{01}$ we project (3.58) onto the vectors $\boldsymbol{V}^{(k)}$,

$$\begin{aligned}\boldsymbol{V}^{(1)}&=\begin{bmatrix}0&-2a_{003}&2a_{002}&-a_{005}&a_{004}\end{bmatrix},\\\boldsymbol{V}^{(2)}&=\begin{bmatrix}-\sqrt{3}a_{004}&a_{004}&a_{005}&\sqrt{3}a_{001}-a_{002}&-a_{003}\end{bmatrix},\\\boldsymbol{V}^{(3)}&=\begin{bmatrix}\sqrt{3}a_{005}&a_{005}&-a_{004}&a_{003}&-\sqrt{3}a_{001}-a_{002}\end{bmatrix},\end{aligned}\tag{3.60}$$

where $a_{00k}$, $k=1,...,5$ are the components of $\boldsymbol{a}_{00}$. The vectors defined in (3.60) which span the kernel of the operator $M_{00}$. In the case of the nematic liquid crystal these vectors have the additional properties of spanning the kernel of the Hessian of the thermotropic part of the free energy density and being tangent to the solution manifold defined by (3.57) [34]. First we recognise from (3.58) that the $i$-th component of the thermotropic contribution can be written as

$$(M_{00}\boldsymbol{a}_{01}+\left(\frac{\partial M_{00}}{\partial a_{00k}}a_{01k}\right)\boldsymbol{a}_{00})_i=\left((M_{00})_{ij}+\left(\frac{\partial M_{00}}{\partial a_{00j}}\right)_{iq}a_{00q}\right)a_{01j}\tag{3.61}$$

We recognise the bracketed terms $\mathcal{H}_{ij}=\left((M_{00})_{ij}+\left(\frac{\partial M_{00}}{\partial a_{00j}}\right)_{iq}a_{00q}\right)$ as the Hessian of the thermotropic free energy. The vectors $V^{(k)}$ span kernel of $\mathcal{H}_{ij}$ and are orthogonal to $\boldsymbol{a}_0$. Projecting we find the final form of our governing equation is

$$\boldsymbol{V}^{(k)}\cdot\frac{\partial\boldsymbol{a}_{00}}{\partial t}=\boldsymbol{V}^{(k)}\cdot\left[\xi_0^2\boldsymbol{\nabla}_{\boldsymbol{x}}\cdot(\mathcal{K}\boldsymbol{\nabla}_{\boldsymbol{x}}\boldsymbol{a}_{00})+\chi_a\left(\boldsymbol{e}_M\left(1+2\frac{|\Omega_{np}|}{|\Omega|}\right)+\boldsymbol{p}\right)+W_1\xi_0^2\boldsymbol{q}\right],\tag{3.62}$$

for $k=1,2,3$, with the constraint that $|\boldsymbol{a}_{00}|^2=S_0^2$, that the leading order biaxiality is

zero and where

$$\boldsymbol{q} = \frac{1}{|\Omega|}\int_{\Gamma} \boldsymbol{a}_S dS. \tag{3.63}$$

### 3.3.4 Validation

In order to validate equations (3.53) and (3.62) we compare their predictions with numerical simulations of the full system, for two cases of inclusions in a twisted cell. In a twisted cell the director is parametrised by

$$\hat{\boldsymbol{n}} = (\sin(\theta_H)\cos(\phi_H), \sin(\theta_H)\sin(\phi_H), \cos(\theta_H))\,, \tag{3.64}$$

(see [110] page 101) with the $x_3$-axis measuring distance into the cell. The tilt angle $\theta_H$ is measured down from the $x_3$-axis and the twist angle $\phi_H$ counter-clockwise from the $x_1$-axis. The first case consists of spherical particles with an applied electric field and the second case ellipsoidal particles in the absence of an applied field, see figure 3.3. The cells are of thickness $L_x = 32\mu$m, the particles are assumed evenly distributed with separation $L_y = 1\mu$m, and the material parameters used are given in table 3.1. In the first case (a) the spherical particles are of radius $0.3\mu$m; in the second case (b) the semi major axis of the ellipsoids is $0.3\mu$m and the two minor axes are $0.1\mu$m, the ellipsoids orientation is given by $(\theta_p, \phi_p) = (45^o, 30^o)$. With $\theta_p$ is measured down from the $x_3$-axis and the twist angle $\phi_p$ counter-clockwise from the $x_1$-axis.

We apply a potential difference across the LC cell and compare the director profile obtained by solving the full system of equations (3.18) and (3.21) using Comsol multiphysics, a finite element package, to that obtained from the approximate system (3.53) and (3.62). The full $\mathcal{Q}$-tensor equations were implemented as a general form PDE in Comsol while Maxwell's equation for the electric displacement were implemented using the electrostatics package. The metallic inclusions were modelled using the floating potential condition to ensure that the electrostatic potential was constant across each inclusion. The weak anchoring condition was implemented by specifying the flux of $\boldsymbol{a}$ on each inclusion. The geometry consists of an array of unit cells along the $x_3$-axis each containing a single inclusion. We imposed periodic boundary conditions on the exterior sides parallel to the $x_3$-axis and strong anchoring conditions with zero pretilt and pre-twist on the sides parallel to the $x_1$-$x_2$ plane. A free tetrahedral mesh of custom mesh size was used in the bulk of the domain and a free triangular mesh was applied on the boundaries. We used the time dependent solver with relative and absolute tolerances of $10^{-4}$, the default MUMPS linear system solver and the solution to the homogenised equations as initial conditions.

To solve the homogenised equations we used a pseudo spectral code as described in

[34] and we solved the cell problems (3.37) and (3.40) using Comsol. To compute (3.51) the cell problem (3.40) must be solved as $\mathcal{Q}_0$ varies throughout the cell. We did this by solving (3.40) for a range of values of $\mathcal{Q}_0$ and interpolating. We also computed the response of an undoped cell for comparison using a spectral method. Figure 3.3 shows a comparison between the homogenisation predictions, the full finite element simulation and an undoped solution corresponding to the case where no particles are present. We see that there is very good agreement between the homogenised equations and numerical simulations for both spherical and ellipsoidal particles as shown in figure 3.3. In the case of ellipsoidal inclusions (b) the alignment of the inclusions acts to break the symmetry of the twisted nematic. This is visible as an asymmetry in plot (b) of figure 3.3.

### 3.3.5 Doped liquid crystals in a splay geometry

Having validated the homogenised equations, we now use them to study the effect of dopants on two characteristic features of liquid crystal cells in a splay geometry, namely the Fredericks transition, and the switch-on and switch-off times. In the splay geometry the director is confined to the $x_1$-$x_3$ plane and varies only in the $x_3$ direction with $x_3 \in [0,1]$. The director is parametrised by the angle $\theta_H(x_3,t)$ measured from the $x_3$-axis, $\hat{\boldsymbol{n}} = (\sin(\theta_H), 0, \cos(\theta_H))$; with this parametrisation the constraints on the order parameters are automatically met. The governing equations (3.62) reduces to a zero twist constraint and a governing PDE for the director angle $\theta_H$. The director angle satisfies

$$\begin{aligned}\frac{\partial \theta_H}{\partial t} = \xi_0^2 \mathcal{K}_{33} \frac{\partial^2 \theta_H}{\partial x_3^2} + \frac{\chi_a}{2S_0}\left(\frac{\sqrt{3}}{3}F_2(\theta_H) - F_1(\theta_H)\right)\sin(2\theta_H)\left(\frac{\partial \phi_0}{\partial x_3}\right)^2 \\ + \frac{\chi_a\sqrt{3}}{3S_0}\cos(2\theta_H)F_4(\theta_H)\left(\frac{\partial \phi_0}{\partial x_3}\right)^2 + \frac{\xi_0^2 W}{3S_0}\sin(2\theta_H)\left(\frac{\sqrt{3}}{2}q_2 - \frac{3}{2}q_1\right) \\ + \frac{\sqrt{3}\xi_0^2 W}{3S_0}\cos(2\theta_H)q_4,\end{aligned} \tag{3.65a}$$

$$\begin{aligned}\left[\xi_0^2 W q_3 + \chi_a F_3(\theta_H)\left(\frac{\partial \phi_0}{\partial x_3}\right)^2\right]\left(\cos^2(\theta_H) - 1\right) \\ -\frac{\sin(2\theta_H)}{2}\left[\xi_0^2 W q_5 + \chi_a F_5(\theta_H)\left(\frac{\partial \phi_0}{\partial x_3}\right)^2\right] = 0\end{aligned} \tag{3.65b}$$

$$\begin{aligned}\chi_a\left(\sin(\theta_H)F_3(\theta_H) + \cos(\theta_H)F_5(\theta_H)\right)\left(\frac{\partial \phi_0}{\partial x_3}\right)^2 \\ + \xi_0^2 W\left(q_3\sin(\theta_H) + q_5\cos(\theta_H)\right) = 0\end{aligned} \tag{3.65c}$$

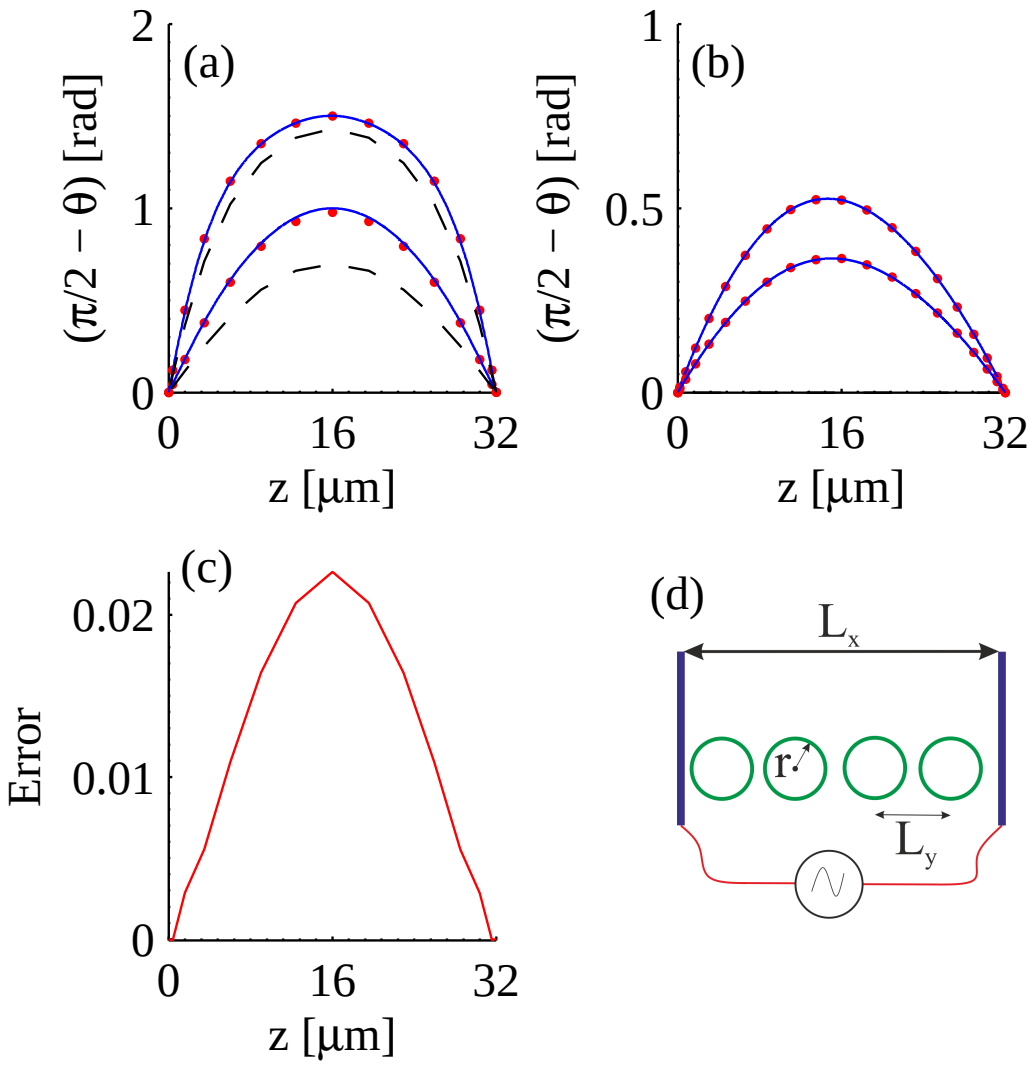


Figure 3.3: Comparison of numerical simulation of the full and homogenised equations for spherical and ellipsoidal particles inside a twisted geometry, zero pretilt at boundaries and homeotropic anchoring on dopants. (a) Spherical particles of radius $r = 0.3\,\mu$m at applied voltages of 1.5 V and 3 V (lower and upper curves respectively). (b) Ellipsoidal dopants $V = 0$ with anchoring energy $W_1 = 50$ (bottom) and $W_1 = 100$ (top) orientation given by $(\theta_p, \phi_p) = (45^o, 30^o)$. The semi major axis of the ellipsoids is $0.3\,\mu$m the two minor axes are $0.1\,\mu$m. (a) & (b) Red points are from homogenisation, broken black line is undoped and blue line from Comsol numerical simulations. (c) Absolute error Error $= |\theta_H - \theta_N|$ where $\theta_H$ is the tilt angle from the homogenised equations and $\theta_N$ is extracted from numerical simulations of the full system. (d) Schematic diagram of the system studied: planar cell of size $L_x$ with spherical/ellipsoidal dopants with spacing $L_y$.

$$\theta_H(0,t_2) = \theta_H(1,t_2) = \frac{\pi}{2}, \tag{3.65d}$$

where $\mathcal{K}_{33}$ is defined in (3.49). Both $\mathcal{K}_{33}$ and $q_i$ (3.63), $i = 1, ..., 5$ may be computed once the cell problem (3.37) is solved using Comsol. The functions $F_i(\theta_H)$, $i = 1, ..., 5$ can be expressed in-terms of $R_k$, $k = 1, ..., 5$ the solutions to equations (3.40) (the electrostatic cell problem). The relations are

$$\begin{aligned} F_1(\theta_H) = 1 + \frac{1}{|\Omega|}\int_\Omega -\frac{1}{2}\left(\frac{\partial R_3}{\partial y_1}\right)^2 - \frac{1}{2}\left(\frac{\partial R_3}{\partial y_2}\right)^2 \\ + \left(\frac{\partial R_3}{\partial y_3}\right)^2 + 2\left(\frac{\partial R_3}{\partial y_3}\right) dV, \end{aligned} \tag{3.66a}$$

$$F_2(\theta_H) = \frac{1}{|\Omega|}\int_\Omega \frac{\sqrt{3}}{2}\left[\left(\frac{\partial R_3}{\partial y_1}\right)^2 - \left(\frac{\partial R_3}{\partial y_2}\right)^2\right] dV, \tag{3.66b}$$

$$F_3(\theta_H) = \frac{1}{|\Omega|}\int_\Omega \sqrt{3}\left(\frac{\partial R_3}{\partial y_1}\right)\left(\frac{\partial R_3}{\partial y_2}\right) dV, \tag{3.66c}$$

$$F_4(\theta_H) = \frac{1}{|\Omega|}\int_\Omega \sqrt{3}\left(\frac{\partial R_3}{\partial y_1}\right)\left(\frac{\partial R_3}{\partial y_3} + 1\right) dV. \tag{3.66d}$$

$$F_5(\theta_H) = \frac{1}{|\Omega|}\int_\Omega \sqrt{3}\left(\frac{\partial R_3}{\partial y_2}\right)\left(\frac{\partial R_3}{\partial y_3} + 1\right) dV, \tag{3.66e}$$

We compute (3.66) over a uniformly spaced grid of $\theta_H$ values in the interval $[0, \pi/2]$ and interpolate. We use a spectral collocation method to solve (3.65) [113].

We consider two microscopic geometries: a regular array of spheres of radius $R$ and an array of ellipsoids of semi axes $r_1, r_2, r_3$ of various orientations. Figure 3.4 shows how the Fredericks transition depends on the particle radius for spherical dopants and on the aspect ratio at constant surface area for ellipsoidal dopants. Figure 3.5 shows how the source term and elasticity tensor vary with particle size/orientation for the systems in figure 3.4. Spherical inclusions always reduce the Fredericks transition: the excluded volume effect reduces the elasticity and the presence of metallic particles forces the potential to drop across a smaller region of liquid crystal giving a larger field. Moreover for spherical dopants there is no source term $\boldsymbol{q}$ present to stabilise the zero voltage configuration. Ellipsoidal particles break the symmetry of the Fredericks bifurcation unless their major axis is aligned parallel or orthogonal to the initial director configuration. The Fredericks transition may

be lowered or raised depending on the competition between the excluded volume effects in $\mathcal{K}_{ij}$, the source term $\boldsymbol{q}$ and the enhanced electric fields $\boldsymbol{e}_M$ and $\boldsymbol{p}$. By linearising (3.65a) about the zero voltage solution, $\theta_H = \pi/2$, we can obtain an algebraic expression for the Fredericks transition,

$$V_{FT} = \sqrt{\frac{\xi_0^2\left(3\mathcal{K}_{33}\pi^2 S_0 + \sqrt{3}Wq_2 - 3Wq_1\right)}{\chi_a\left(-F_2\sqrt{3} + \sqrt{3}\frac{\partial F_4}{\partial \theta_H} + 3F_1\right)_{\theta_H=\pi/2}}}. \tag{3.67}$$

This formula is valid only if neither the electric field nor the inclusion alignment field $\boldsymbol{q}$ induce a twist and $\theta_H = \pi/2$ remains a solution. These constraints follow from the governing equations (3.65). Substituting $\theta_H = \pi/2$ into (3.65a) we must have

$$q_4 = F_4 = 0. \tag{3.68}$$

The zero twist condition is given by equations (3.65b) and (3.65c), these are satisfied for arbitrary $\theta_H$ provided

$$q_3 = q_5 = F_3 = F_5 = 0. \tag{3.69}$$

For ellipsoidal particles (3.69) restricts the major axis of the ellipsoids to the plane containing the director. If the major axis of the ellipsoids were to leave the plane the preferred anchoring on the inclusions and fringe fields would force the director out of plane and the chosen parametrisation would no longer describe the system. The second constraint, (3.68), guarantees that there is a perfect bifurcation and is satisfied by ellipsoids with homeotropic anchoring provided they are aligned with the initial director or perpendicular to it. If (3.68) is not satisfied the Fredericks transition is softened as if there were pretilt at the boundaries.

To obtain expressions for the switch-on and switch-off times from the uniform state we linearise (3.65a) about $\theta_H = \pi/2$ and consider the evolution of a small perturbation satisfying (3.65d). For the case of zero applied voltage we obtain the non-dimensional switch-off time while for an applied voltage exceeding the Fredericks threshold we obtain the switch-on time (see [110] pages $220 - 222$)

$$\tau_{\text{on}} = \frac{3S_0}{\chi_a\left(3F_1 - \sqrt{3}F_2 + \sqrt{3}\frac{\partial F_4}{\partial \theta_H}\right)_{\theta_H=\pi/2}(V^2 - V_{FT}^2)}, \tag{3.70}$$

$$\tau_{\text{off}} = \frac{3S_0}{3S_0\pi^2\xi_0^2\mathcal{K}_{33} - \xi_0^2 W\left(3q_1 - \sqrt{3}q_2\right)}. \tag{3.71}$$

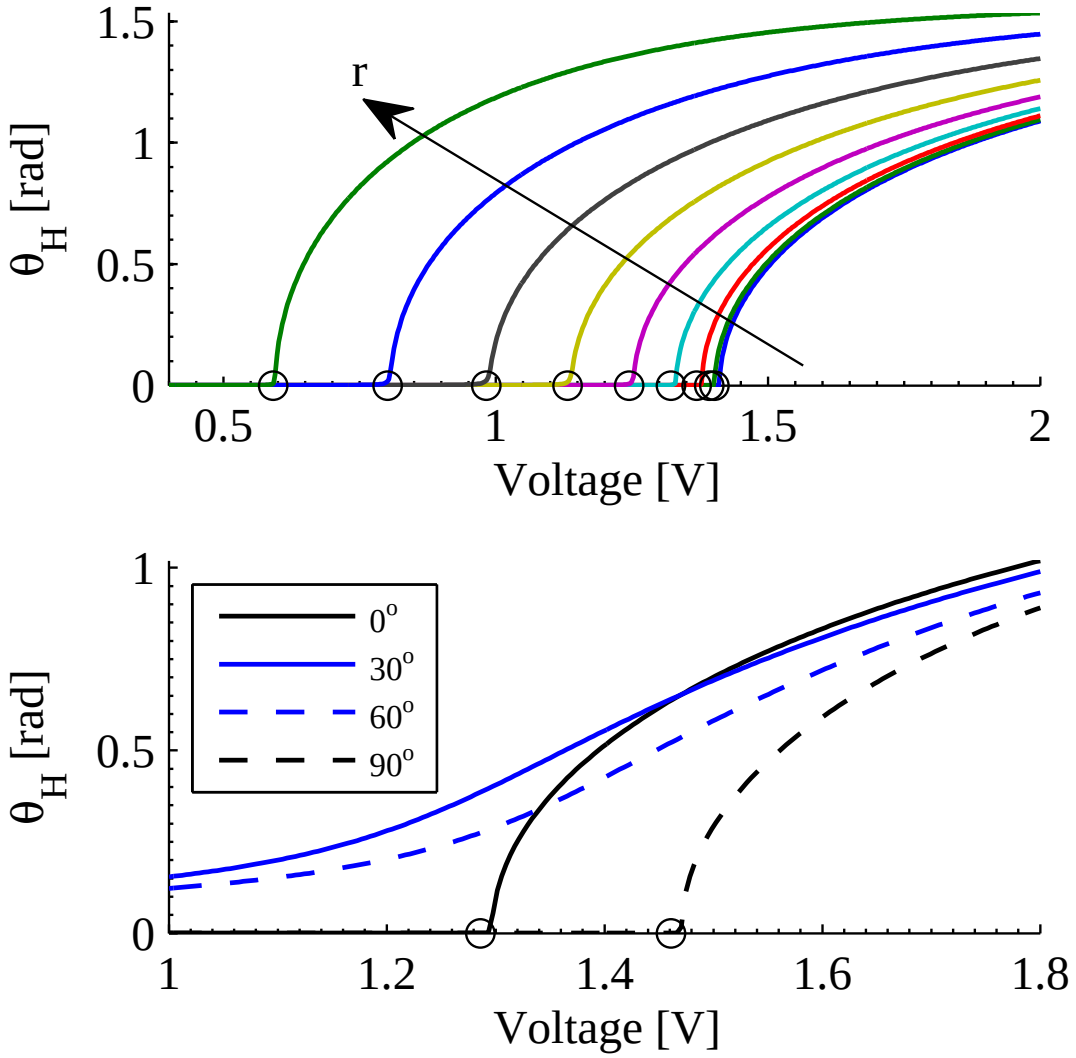


Figure 3.4: Bifurcation diagrams for spherical and ellipsoidal inclusions. Top spheres of radius from $0.05\mu$m in steps of $0.05\,\mu$m to $0.45\,\mu$m. Bottom: ellipsoids with major axis $r_1 = 0.3\,\mu$m and minor axis' $r_2 = r_3 = 0.1\,\mu$m, oriented in the plane of the director at an angle of $0^o, 30^o, 60^o$ and $90^o$ to the initial director alignment. Circles indicate the position of the Fredericks transition computed using equation (3.67).

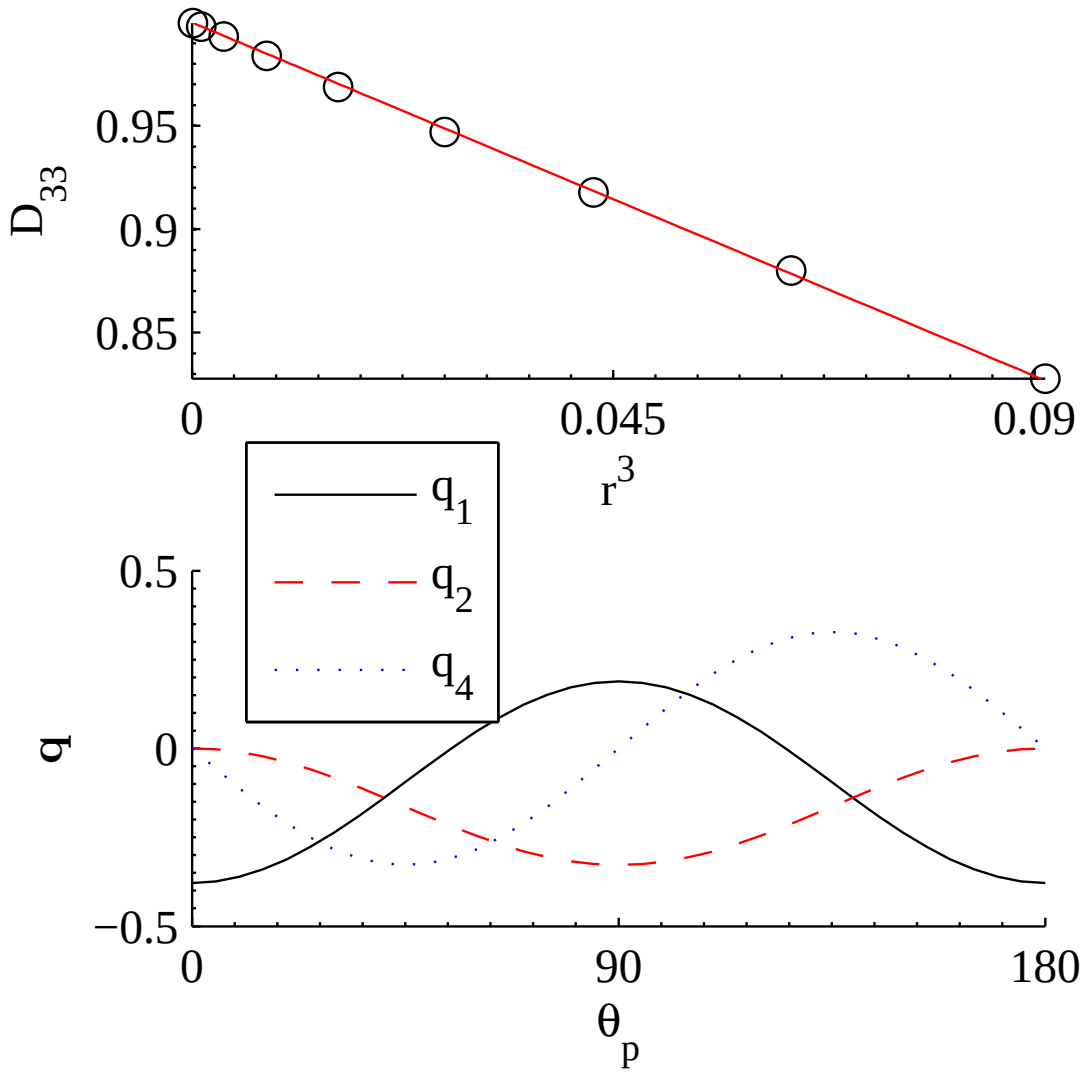


Figure 3.5: Diagonal component of the elasticity tensor for spherical inclusions and components of the source term $\boldsymbol{q}$ for ellipsoidal particles confined to the $x_1$-$x_3$ plane. The angle $\theta_p$ is measured from the ellipsoids major axis to the $x_3$ axis, $q_3 = q_5 = 0$ (not shown). The approximate linear relation between $\mathcal{K}_{33}$ and $r^3$ indicates that the excluded volume effect is dominant.

It should be noted that even though we have neglected fluid flow in these formulae the correction to the switch-on times due to induced fluid flow within a planar cell is minimal for most liquid crystals (see [110] page 228), likewise the correction to the switch-off time from a slightly distorted state is small. Figure 3.6 shows how the switching times vary with aspect ratio for a range of ellipsoidal particles with homeotropic anchoring. Particles are either aligned with the initial director or orthogonal to it. In the case of alignment with the initial director the homeotropic anchoring destabilises the zero voltage solution and we see a decrease in the switch-on time and an increase in the switch-off time. This situation is not completely reversed for particles aligned parallel to the initial director. In this case the effective field acts as a restoring force and decreases the switch-off time. However the enhanced electric field dominates and the switch-on time decreases as well, despite the reduced elastic constant and unfavourable source term. This example illustrates how doping with particles may be used to tailor the properties of the LC to specific applications. The simplicity and computational efficiency of the homogenisation method makes optimising these properties a realistic prospect.

Equation (3.67) suggests that by carefully choosing both the inclusions geometry and anchoring strength it may be possible to obtain an extremely low value for the Frederiks transition. In general the value of $V_{FT}$ is lower for larger inclusions, because of reduced elasticity and increased effective susceptibility, and for inclusions whose anchoring $\boldsymbol{q}$ reduces the stability of the zero voltage ground state. Similar considerations can be applied to the switching times given by equations (3.70) and (3.71). The switch-on time is shorter, leading to faster devices, if the effective susceptibility is increased or the Frederiks transition is decreased. To summarise $V_{FT}$ and $\tau_{\text{on}}$ are smaller for larger volume fraction inclusions, stronger anchoring with inclusions aligned so that $q_1$ is large and $q_2$ is small. As in a pure nematic these requirements are nearly reversed when we try to minimise the switch-off time. The switch-off time is shortest for: stiffer systems, favouring smaller inclusions, and inclusions aligned so that $q_2$ is large and $q_1$ is small.

In the limit of vanishing inclusions all of the results obtained reduce to the classical results. The anchoring term $\boldsymbol{q}$ vanishes, $\mathcal{K}$ reduces to the identity, the particle volume fraction tends to zero and the induced dipole field $\boldsymbol{p}$ vanishes.

### 3.3.6 Conclusions

In this section we have studied the alignment of a nematic liquid crystal which is confined by a set of periodic metal inclusions. Using the method of homogenisation we have derived a set of approximate equations which describe the alignment of the liquid crystal subject to an applied external electric field and weak anchoring on the surface of the inclusions.

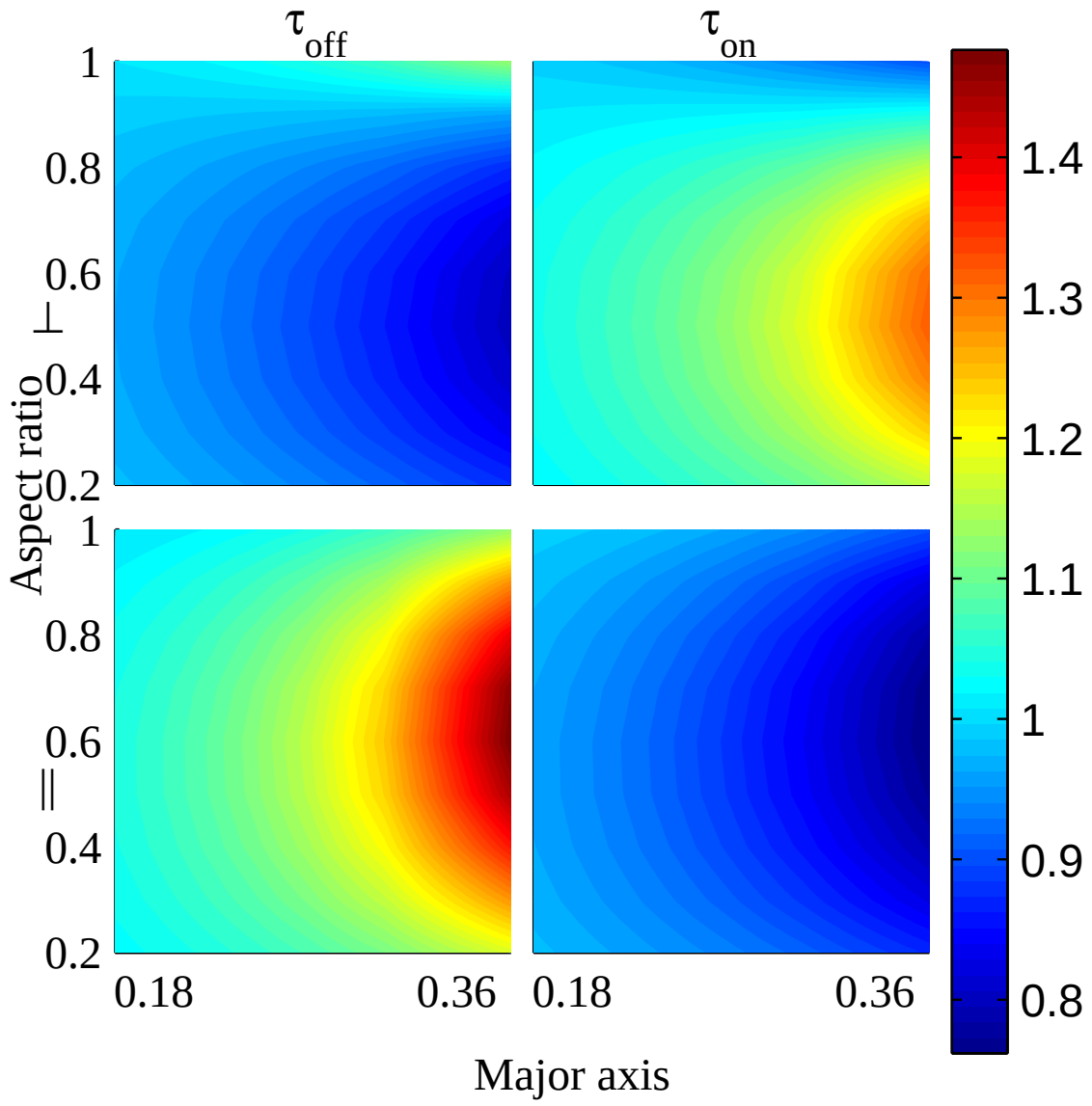


Figure 3.6: Switch-off (left) and on (right) time at $V = 2$V for colloidal nematic with ellipsoidal particles as a fraction of undoped on/off times in the splay geometry. Ellipsoids oriented orthogonal (top) or parallel (bottom) to initial director with homeotropic anchoring on inclusions and anchoring strength $W_1 = 10$. Vertical dopants reinforce stability of the $\theta_H = 0$ state while horizontal dopants reduce it.

The inclusions we consider are of arbitrary shape but are assumed to vary on a scale much smaller than the macroscopic length scale of interest. Hence, these inclusions may be identified as either a periodic micro structure or a set of dopant particles. The key advantage of this method is that we are able to link the macroscopic properties to the micro-scale structure through a representative cell problem rather than explicitly considering the full geometry.

The derivation of these equations is based on several assumptions regarding the physical and geometric properties of the system. Specifically we consider only metal particles which we consider to be uniformly distributed across the device. The choice of material is not a limitation of the theory developed here and this method could be extended to include dielectric, ferroelectric or ferromagnetic particles. The result of this would be that the cell problem for the electrostatic field would be different and there would potentially be a coupling between the cell problems for the liquid crystal and electric field. It is also possible to improve upon our existing model for gold. We have assumed that the gold inclusions can be modelled as ideal conductors, this could be relaxed to include a finite skin depth under DC conditions. Additionally the optical response of gold nano particles of 5 nm-100 nm in diameter can be modelled macroscopically [44]. This is achieved by including scattering contributions to the complex dielectric permittivity. The assumption that the particles are uniformly distributed allows us to simplify the cell problem using the assumption of periodicity. Similarly assuming that the particles are of fixed position and orientation reduces the interactions that we have to consider.

These approximations are appropriate for the case of a periodically patterned micro structure. However, for the case in which the inclusions take the form of particles these assumptions may break down and random distributions of particles and particle movement will need to be considered. Random inclusions can be dealt with for low volume fraction materials simply by assuming that any deviation from periodicity will simply induce an error of $O(\eta)$. However, a more accurate approximation could be obtained using methods for general random media as used, for example, in [47]. The particle rotation and motion, due to fluid flow or elastic and electrostatic forces, is a more complicated issue. Rigid body rotation of porous structures has been considered in the context of elasticity [48], in which case a non-linear elasticity theory is derived. A general approach to non-uniform but nearly periodic microstructures has been developed by Richardson, Chapman and Bruna [21, 92, 93] which we employ in chapter 4 to the problem of a rotating microstructure with limited fluid flow. The drift of particles could also be included assuming that the motion is sufficiently slow compared to the reorientation. However, we expect that in this case the correction to our existing results will be small. Dropping the weak anchoring

approximation is another possible extension of this project. Doing so would not be trivial, but may ultimately lead to a detailed comparison to the periodic systems discussed by Musevic [71].

The final homogenised equations (3.53) and (3.62) capture the effects of the underlying geometry in terms of an effective elastic tensor and a forcing term which acts to align the liquid crystal to the average preferred direction on the surface of the inclusions. We have found excellent agreement between large scale numerical simulations in which the full geometry is included and the predictions of our model. The homogenised equations require significantly less computation time than the full geometry. The elasticity cell problem for the liquid crystal only needs to be solved once to parametrise the equations and takes less than 10 seconds on a desktop PC for a spherical particle. The cell problem for the electric field (3.40) must be solved for a range of $\mathcal{Q}_0$ to parametrise the equations. However, the solution for each configuration takes under 10 seconds to compute and need only be done once for any particular dopant. The corresponding simulation of the full geometry takes approximately 15 hours on a single 16 core node of the Iridis 4 supercomputing cluster at the University of Southampton.

By computing the effective material parameters of the nematic as a function of inclusion geometry we can quantify the effect of these inclusions on the Fredericks transition and the switch-on and switch-off times for the liquid crystal. We have shown that using simple ellipsoidal inclusions with a preferred homeotropic anchoring the switch-on and switch-off times can be either increased or decreased. The link which this method provides between the macroscopic behaviour of the liquid crystal and the underlying geometry will be of fundamental importance in the design of composite liquid crystal materials with optimal material parameters.

# Chapter 4

# Homogenisation of systems with moving micro-structure

This chapter concerns the modelling of moving metallic particles within a nematic liquid crystal. We extend the model developed in chapter 3 by incorporating rotating particles and limited fluid dynamics within a homogenisation framework. We obtain a macroscopic model of the suspension. The microscopic interaction between the nematic and dopant is captured by cell problems which are solved on the micro-scale. These provide a self consistent way of computing material parameters. In section 4.1 we briefly discuss the relevant literature that addresses non-periodic system. We provide a simple example of applying this non-periodic homogenisation to a diffusion problem in section 4.1.1. In section 4.2 we derive a model of a nematic suspension, this section is based heavily on a paper written in conjunction with Dr. G. D'Alessandro and Dr. K. R. Daly that has been submitted to the SIAM journal on applied mathematics.

## 4.1 Homogenisation of material with deformable microstructures

There have been various attempts to extend the method of multiple scales to non-periodic systems. In this section we outline some of these methods.

The methods in the literature can be roughly categorised according to how they modify the periodicity requirement as follows: deviations from an ideal lattice [92] and microstructure variation between cells [93, 21].

Deviations from an ideal lattice can be handled by using curvilinear coordinates. Richardson and Chapman [92] used this method to model the electrical activity of cardiac

tissue. The non-uniformity of the tissue was accounted for by transforming the configuration according to $\boldsymbol{x}'' = B(\boldsymbol{x}, t)$ where $\boldsymbol{x}$ is the Eulerian position of a point within the hear tissue, the deformed configuration, and $\boldsymbol{x}''$ is the corresponding position in the non-deformed reference configuration. The reference configuration is periodic. Hence, by expressing the micro-scale variable $\boldsymbol{y}$ in terms of position within the reference configuration $\boldsymbol{y}'' = B(\boldsymbol{x}, t)$ the non-periodic problem can be mapped into a periodic one. This approach was used to derive the bidomain equations [92]. The disadvantage of this method is that the cell problems now depend on macroscopic position within the system. As a result they must be solved for each configuration [92].

To model changes in the microscopic structure from cell to cell the relation between the local microscopic configuration the macroscopic coordinate can be defined implicitly by a level set function. This method has been applied by Bruna and Chapman [21] and Richardson *et al.* [93]. By defining the location of the inclusion surface by a level set, $\chi_{LS}(\boldsymbol{x}, \boldsymbol{y}) = 0$, it is possible to treat the varying microstructure as a slow function of the macroscopic variable. This is the method that we illustrate in the next section and use to model of nematic suspension in section 4.2.

### 4.1.1 Diffusion beyond the periodic setting

Recall the example model discussed in the previous chapter of diffusion in a perforated domain. In this section we illustrate how to extend this model to account for variations in orientation of the inclusions. This is accomplished using the methods outlined in [21, 93]. The problem is defined by,

$$\nabla^2 u = \frac{\partial u}{\partial t} \qquad \boldsymbol{x} \in \mathcal{D}, \tag{4.1a}$$

$$\hat{\boldsymbol{\nu}} \cdot \boldsymbol{\nabla} u = 0 \qquad \boldsymbol{x} \in \Gamma(\boldsymbol{x}), \tag{4.1b}$$

$$u\left(\boldsymbol{x}\right) = u_b \qquad \boldsymbol{x} \in \partial\mathcal{D}. \tag{4.1c}$$

Here $u$ is again the concentration and the impermeable barriers $\Gamma(\boldsymbol{x})$ have orientation which depends on the macroscopic position $\boldsymbol{x}$. This is captured by the level set function

$$\chi_{LS}(\boldsymbol{x}, \boldsymbol{y}) = \boldsymbol{y}^T R(\boldsymbol{x}) A R^T(\boldsymbol{x}) \boldsymbol{y} - 1, \tag{4.2}$$

where the rotation is given by $R : \mathbb{R}^3 \to SO(3)$ the position of the boundaries is given by

$$\Gamma(\boldsymbol{x}) = \{\boldsymbol{y} \mid \chi_{LS}(\boldsymbol{x}^{(j)}, \boldsymbol{y}) = 0\}. \tag{4.3}$$

We proceed as normal expanding the field $u$ and the gradient and Laplacian operator.

$$u = u_0 + \eta u_1 + \eta^2 u_2 + \mathcal{O}(\eta^3), \tag{4.4a}$$

$$\boldsymbol{\nabla} = \boldsymbol{\nabla}_{\boldsymbol{x}} + \frac{1}{\eta}\boldsymbol{\nabla}_{\boldsymbol{y}}, \tag{4.4b}$$

$$\nabla^2 = \nabla^2_{\boldsymbol{x}} + \frac{2}{\eta}\boldsymbol{\nabla}_{\boldsymbol{x}} \cdot \boldsymbol{\nabla}_{\boldsymbol{y}} + \frac{1}{\eta^2}\nabla^2_{\boldsymbol{y}}. \tag{4.4c}$$

In addition we expand the unit normal $\hat{\boldsymbol{\nu}}$. Using the level set we can define the unit normal as,

$$\begin{aligned} \hat{\boldsymbol{\nu}} &= \frac{(\boldsymbol{\nabla}_{\boldsymbol{x}} + \frac{1}{\eta}\boldsymbol{\nabla}_{\boldsymbol{y}})\chi_{LS}}{|(\boldsymbol{\nabla}_{\boldsymbol{x}} + \frac{1}{\eta}\boldsymbol{\nabla}_{\boldsymbol{y}})\chi_{LS}|}, \\ &= \hat{\boldsymbol{\nu}}_0 + \eta\left(\frac{\boldsymbol{\nabla}_{\boldsymbol{x}}\chi_{LS}}{|\boldsymbol{\nabla}_{\boldsymbol{y}}\chi_{LS}|} - \hat{\boldsymbol{\nu}}_0\frac{\hat{\boldsymbol{\nu}}_0 \cdot \boldsymbol{\nabla}_{\boldsymbol{x}}\chi_{LS}}{|\boldsymbol{\nabla}_{\boldsymbol{y}}\chi_{LS}|}\right) + \mathcal{O}(\eta^2), \end{aligned} \tag{4.5}$$

where the leading order unit normal is $\hat{\boldsymbol{\nu}}_0 = \frac{\boldsymbol{\nabla}_{\boldsymbol{y}}\chi_{LS}}{|\boldsymbol{\nabla}_{\boldsymbol{y}}\chi_{LS}|}$. Substituting equations (4.4) and (4.5) into (4.1) and collecting powers of $\eta$ we find at order $\mathcal{O}(\eta^{-2})$. The order $\mathcal{O}(\eta^{-2})$ terms from equation (4.1a) are,

$$\nabla^2_{\boldsymbol{y}} u_0 = 0, \qquad \boldsymbol{y} \in \Omega(\boldsymbol{x}) \tag{4.6a}$$

$$\hat{\boldsymbol{\nu}}_0 \cdot \boldsymbol{\nabla}_{\boldsymbol{y}} u_0 = 0, \tag{4.6b}$$

as in the previous example we find that $u_0 = u_0(\boldsymbol{x})$. Continuing to order $\mathcal{O}(\eta^{-1})$ next order we find,

$$\nabla^2_{\boldsymbol{y}} u_0 = 0, \qquad \boldsymbol{y} \in \Omega(\boldsymbol{x}) \tag{4.7a}$$

$$\hat{\boldsymbol{\nu}}_0 \cdot \boldsymbol{\nabla}_{\boldsymbol{y}} u_1 + \hat{\boldsymbol{\nu}}_0 \cdot \boldsymbol{\nabla}_{\boldsymbol{x}} u_0 + \boldsymbol{\nu}_1 \cdot \boldsymbol{\nabla}_{\boldsymbol{y}} u_0 = 0. \tag{4.7b}$$

As $u_0 = u_0(\boldsymbol{x})$ the solvabillity condition is identical to that found in 3.2.1 and is automatically satisfied. Making the ansatz $u_1 = \chi_k(\boldsymbol{x}, \boldsymbol{y})u_{0,k} + \overline{u}_1(\boldsymbol{x})$ we find the cell problem,

$$\nabla^2_{\boldsymbol{y}} \chi_k = 0, \qquad \boldsymbol{y} \in \Omega(\boldsymbol{x}) \tag{4.8a}$$

$$\hat{\boldsymbol{\nu}}_0 \cdot \boldsymbol{\nabla}_{\boldsymbol{y}} \chi_k = -\hat{\boldsymbol{\nu}}_0 \cdot \hat{\boldsymbol{e}}_k. \tag{4.8b}$$

Here $\hat{\boldsymbol{e}}_k$, $k = 1, 2, 3$ form the standard set of Cartesian basis vectors. The solution to this cell problem depends on the macroscopic variable $\boldsymbol{y}$ through the domain $\Omega(\boldsymbol{x})$. Continuing to the next order the $\mathcal{O}(\eta^0)$ terms from equation (4.1a) are

$$\nabla^2_{\boldsymbol{x}} u_0 + \boldsymbol{\nabla}_{\boldsymbol{x}} \cdot \boldsymbol{\nabla}_{\boldsymbol{y}} u_1 + \boldsymbol{\nabla}_{\boldsymbol{y}} \cdot \boldsymbol{\nabla}_{\boldsymbol{x}} u_1 + \nabla^2_{\boldsymbol{y}} u_2 = \frac{\partial u_0}{\partial t}, \tag{4.9a}$$

$$\hat{\boldsymbol{\nu}}_0 \cdot \boldsymbol{\nabla}_{\boldsymbol{y}} u_2 + (\hat{\boldsymbol{\nu}}_0 \cdot \boldsymbol{\nabla}_{\boldsymbol{x}} + \boldsymbol{\nu}_1 \cdot \boldsymbol{\nabla}_{\boldsymbol{y}}) u_1 + (\boldsymbol{\nu}_1 \cdot \boldsymbol{\nabla}_{\boldsymbol{x}} + \boldsymbol{\nu}_2 \cdot \boldsymbol{\nabla}_{\boldsymbol{y}}) u_0 = 0. \tag{4.9b}$$

Integrating equation (4.9a) over a generic cell $\Omega(\boldsymbol{x})$, using the divergence theorem and boundary condition (4.9b) we find

$$\int_{\Omega(\boldsymbol{x})} \nabla^2_{\boldsymbol{x}} u_0 + \boldsymbol{\nabla}_{\boldsymbol{x}} \cdot \boldsymbol{\nabla}_{\boldsymbol{y}} u_1 dV - \int_{\Gamma(\boldsymbol{x})} \boldsymbol{\nu}_1 \cdot (\boldsymbol{\nabla}_{\boldsymbol{y}} u_1 + \boldsymbol{\nabla}_{\boldsymbol{x}} u_0)\, dS = |\Omega| \frac{\partial u_0}{\partial t}, \tag{4.10}$$

next we apply Reynolds transport theorem to move the differential operator $\boldsymbol{\nabla}_{\boldsymbol{x}}$ outside of the integral,

$$\begin{aligned} &\boldsymbol{\nabla}_{\boldsymbol{x}} \cdot \int_{\Omega(\boldsymbol{x})} (\boldsymbol{\nabla}_{\boldsymbol{x}} u_0 + \boldsymbol{\nabla}_{\boldsymbol{y}} u_1) dV + \int_{\Gamma(\boldsymbol{x})} (\boldsymbol{\nabla}_{\boldsymbol{x}} u_0 + \boldsymbol{\nabla}_{\boldsymbol{y}} u_1) \cdot (\boldsymbol{\nabla}_{\boldsymbol{x}} \boldsymbol{r} \cdot \hat{\boldsymbol{\nu}}_0) dS \\ &- \int_{\Gamma(\boldsymbol{x})} \boldsymbol{\nu}_1 \cdot (\boldsymbol{\nabla}_{\boldsymbol{y}} u_1 + \boldsymbol{\nabla}_{\boldsymbol{x}} u_0)\, dS = |\Omega| \frac{\partial u_0}{\partial t}, \end{aligned} \tag{4.11}$$

Here $\boldsymbol{r}$ is the position vector on $\Gamma(\boldsymbol{x})$. Next using the level set function and the implicit function theorem we can write

$$\begin{aligned} (\boldsymbol{\nabla}_{\boldsymbol{x}} \boldsymbol{r} \cdot \hat{\boldsymbol{\nu}}_0)_i &= \frac{\partial r_i}{\partial x_j} \hat{\boldsymbol{\nu}}_{0i}, \\ &= -\frac{\partial \chi_{LS}}{\partial x_j} \frac{1}{|\boldsymbol{\nabla}_{\boldsymbol{y}} \chi_{LS}|}, \end{aligned} \tag{4.12}$$

where we have used the fact that $\boldsymbol{r}$ is the restriction of the microscopic $\boldsymbol{y}$-coordinate to the the boundary $\Gamma(\boldsymbol{x})$. Next using

$$\boldsymbol{\nu}_1 = \left( \frac{\boldsymbol{\nabla}_{\boldsymbol{x}} \chi_{LS}}{|\boldsymbol{\nabla}_{\boldsymbol{y}} \chi_{LS}|} - \hat{\boldsymbol{\nu}}_0 \frac{\hat{\boldsymbol{\nu}}_0 \cdot \boldsymbol{\nabla}_{\boldsymbol{x}} \chi_{LS}}{|\boldsymbol{\nabla}_{\boldsymbol{y}} \chi_{LS}|} \right), \tag{4.13}$$

and boundary condition (4.7b) we find that the terms generated by the transport theorem and the level set expansion of the unit normal due to the non-uniform nature of the microstructure cancel. The homogenised equation is given by

$$\boldsymbol{\nabla}_{\boldsymbol{x}} \cdot (\mathcal{D}(\boldsymbol{x}) \boldsymbol{\nabla}_{\boldsymbol{x}} u_0) = \frac{\partial u_0}{\partial t}, \tag{4.14}$$

where the effective diffusion tensor now depends on $\boldsymbol{x}$ and is given by

$$\mathcal{D}_{ij}(\boldsymbol{x}) = \frac{1}{\|\Omega\|} \int_{\Omega(\boldsymbol{x})} \delta_{ij} + \frac{\partial \chi_j}{\partial y_i} dV. \tag{4.15}$$

In this simple case we have shown that including a slow variation in the microstructure does not alter the form of the homogenised equation. Instead the effective diffusion tensor depends on the macroscopic variable $\boldsymbol{x}$. The terms generated by using Reynolds transport theorem exactly cancel those that arise from the expansion of the unit normal. In the following sections we explore applying this method to a nematic suspension.

## 4.2 Nematic liquid crystal suspension with rotating metallic particles.

We study the behaviour of nematic liquid crystal doped with ideally conductive metallic particles. The particles are distributed across a regular lattice however we allow their orientation to change throughout space. In 4.3 we derive the microscopic equations that describe the liquid crystal-dopant interaction, in 4.4 we obtain homogenised equations, we validate the model in 4.5, discuss the model and present conclusions in 4.6.

## 4.3 Microscopic model

In this section we derive the microscopic equations governing the liquid crystal suspension that we are going to study in the following sections. We consider a nematic liquid crystal in a two-dimensional planar geometry incorporating perfectly conductive particles that have rotational but not translational freedom.

### 4.3.1 Representing the system

Metallic dopant particles added to a nematic liquid crystal act to alter the elastic and dielectric properties of the nematic. To determine the governing equations for the nematic and dopant particles we use a free energy and dissipation principle. We consider a nematic liquid crystal doped with small particles. We assume that the particles are sufficiently dispersed that we may approximate them as lying on a periodic lattice. The system we consider, illustrated in figure 4.1, is made of a periodic array of freely rotating particles contained within a volume of liquid crystal. The system, particles and nematic liquid crystal, is infinitely extended in the $x_3$ direction. The kinetic energy of a uniform flat disc of radius $\tilde{r}$ rotating at angular velocity $\tilde{\omega}$ is

$$T = \frac{1}{2}\frac{\tilde{\rho}\pi\tilde{r}^4}{2}\tilde{\omega}^2 \tag{4.16}$$

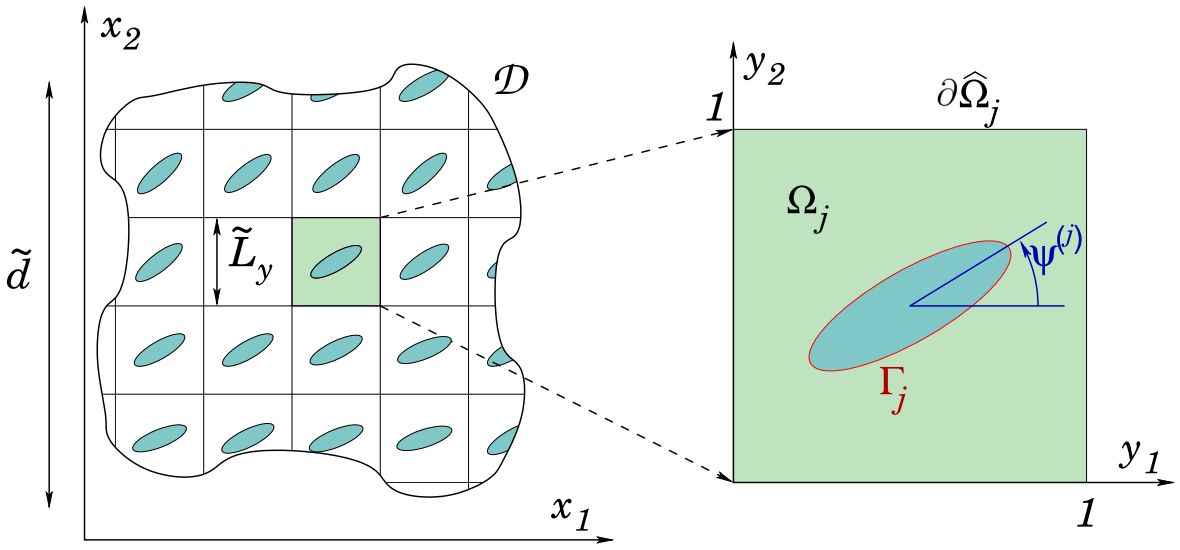


Figure 4.1: Schematic of the system, the macroscopic domain $\mathcal{D}$ consists of several unit cells $\Omega$ with boundary $\Gamma$. The angle $\psi^{(j)}$ measures the orientation of the $j-th$ particle within the system.

where $\tilde{\rho}$ is the mass density. The moment of inertia depends on the fourth power of the pillar radius. Conversely the viscous drag depends on the perimeter of the inclusions and is hence linear in the radius. For this reason we neglect the kinetic energy throughout this chapter. The total free energy of the system per unit length is (neglecting the kinetic energy of the pillars)

$$\tilde{F}_{\text{tot}} = \int_{\mathcal{D}} \left( \tilde{\mathcal{F}}_B + \tilde{\mathcal{F}}_E \right) d\tilde{S} + \int_{\cup_j \Gamma_j} \tilde{\mathcal{F}}_S d\tilde{l}, \tag{4.17}$$

with $\tilde{\mathcal{F}}_S$, $\tilde{\mathcal{F}}_E$ $\tilde{\mathcal{F}}_B$ the surface, electrostatic and volume free energy densities respectively. The macroscopic domain $\mathcal{D}$ is an open subset of $\mathbb{R}^2$ and is a tessellation of unit cells $\Omega_j \subset \mathbb{R}^2$, $j \in \mathbb{N}$. The boundary of the unit cells is split into two parts, $\partial\Omega_j = \Gamma_j \cup \partial\hat{\Omega}_j$, where $\Gamma_j$ is the boundary of the $j$-th inclusion and $\partial\hat{\Omega}_j$ is the boundary shared with the neighbouring unit cells. We represent the orientation of the nematic using the $\mathcal{Q}$-tensor [36]. We assume that the nematic is uni-axial and that the principal axis of the nematic is oriented within the $x_1$-$x_2$ plane. Hence we can describe the nematic liquid crystal using a two dimensional $\mathcal{Q}$-tensor theory. For a nematic locally aligned with a director $\hat{\boldsymbol{n}}$, the $\tilde{\mathcal{Q}}$-tensor is given by

$$\tilde{\mathcal{Q}} = \sqrt{2}\tilde{S}\left( \hat{\boldsymbol{n}} \otimes \hat{\boldsymbol{n}} - \frac{1}{2}\mathcal{I} \right) \tag{4.18}$$

where $\tilde{S}$ the scalar order parameter and $\mathcal{I}$ is the $2 \times 2$ identity matrix. The normalization in equation (4.18) is chosen so that $\mathrm{Tr}(\tilde{\mathcal{Q}}^2) = \tilde{S}^2$. The space of traceless symmetric $2 \times 2$ tensors forms a two-dimensional vector space. Following Sonnet *et al.*[105], we expand the $\mathcal{Q}$-tensor as $\tilde{\mathcal{Q}} = \sum_{i=1}^{2} \tilde{a}_i \mathcal{T}^{(i)}$ where $\mathcal{T}^{(i)}$ form the basis of the matrix space an are given by

$$\begin{aligned} \mathcal{T}^{(1)} &= \frac{1}{\sqrt{2}} \begin{bmatrix} 0 & 1 \\ 1 & 0 \end{bmatrix}, \\ \mathcal{T}^{(2)} &= \frac{1}{\sqrt{2}} \begin{bmatrix} -1 & 0 \\ 0 & 1 \end{bmatrix}, \end{aligned} \tag{4.19}$$

and $\tilde{a}_i = \mathrm{Tr}(\tilde{\mathcal{Q}}\mathcal{T}^{(i)})$ are the components of $\tilde{\mathcal{Q}}$ on this basis. The dimensional bulk free energy density in the single elastic constant approximation is

$$\tilde{\mathcal{F}}_B = \frac{\tilde{L}}{2} \|\tilde{\boldsymbol{\nabla}} \tilde{\boldsymbol{a}}\|^2 + \frac{1}{2} A \left(T - T^*\right) |\tilde{\boldsymbol{a}}|^2 + \frac{1}{2} C |\tilde{\boldsymbol{a}}|^4, \tag{4.20}$$

where $\tilde{L} \equiv \frac{K}{4\tilde{S}^2}$, $K$ is the single elastic constant chosen to coincide with Ericksen-Leslie theory [110], $\tilde{\boldsymbol{a}} = [\tilde{a}_1 \ \tilde{a}_2]^T$ is a vector formed from the components of the $\tilde{\mathcal{Q}}$ tensor on the basis of traceless symmetric tensors $\mathcal{T}^{(i)}, i = 1, 2$, $A$ and $C$ are thermotropic coefficients, $T$ is the absolute temperature with $T^*$ the pseudo critical temperature at which the isotropic phase becomes unstable. The dielectric energy density written in terms of the electric field $\tilde{\boldsymbol{E}}$ and relative dielectric tensor $\epsilon$ is given by

$$\tilde{\mathcal{F}}_E = -\frac{1}{2} \tilde{\boldsymbol{E}} \cdot (\epsilon_0 \epsilon \tilde{\boldsymbol{E}}) \text{ with } \epsilon = \left( \epsilon_u \mathcal{I} + \frac{\Delta\epsilon}{\tilde{S}} \frac{1}{\sqrt{2}} \tilde{\mathcal{Q}} \right), \tag{4.21}$$

Here $\epsilon_u$ is the uniform dielectric constant, $\Delta\epsilon$ is the dielectric anisotropy in the fully nematic phase ($\tilde{S} = 1$) and $\epsilon_0$ is the permittivity of free space. We adopt this notation to make it easier to compare the predictions of our model with an equivalent Ericksen-Leslie model with dielectric anisotropy $\Delta\epsilon$. The surface energy density is given by

$$\tilde{\mathcal{F}}_S = \frac{\tilde{\mu}}{2} |\tilde{\boldsymbol{a}} - \tilde{\boldsymbol{a}}_S|^2. \tag{4.22}$$

Here $\tilde{\mu}$ is the anchoring energy density and $\tilde{\boldsymbol{a}}_S$ the preferred alignment on the particle surface. The dynamics are given by the dissipation function $\tilde{R}$, the energy lost per unit

volume and unit time due to viscous dissipation,

$$\tilde{R} = \frac{1}{2}\zeta_1 \left| \frac{\partial \tilde{\boldsymbol{a}}}{\partial \tilde{t}} \right|^2 + \frac{\zeta_3}{2}\tilde{\mathcal{D}} : \tilde{\mathcal{D}}. \tag{4.23}$$

Here $\tilde{\mathcal{D}}_{ij} = \frac{1}{2}\left(\tilde{v}_{i,j} + \tilde{v}_{j,i}\right)$ is the symmetric part of the velocity gradient, $\tilde{v}_{i,j} = \frac{\partial \tilde{v}_i}{\partial \tilde{x}_j}$, $\zeta_3$ (up to a factor of 1/2) is the isotropic part of the nematic viscosities and $\zeta_1 \equiv \frac{\gamma_1}{2\tilde{S}^2}$ with $\gamma_1$ is the rotational viscosity. We use a simplified version of the dissipation function proposed by Sonnet and Virga [106] and include only two terms in the dissipation: the rotational viscosity of the nematic, which sets the time scale of $\tilde{\mathcal{Q}}$, and the isotropic viscosity, which sets the time scale of the particles. To simplify the resulting equations we have neglected the coupling between the nematic alignment and the fluid flow. This is typically valid when reorientation of the director occurs slowly or when there is uniform reorientation throughout the nematic.

In addition to neglecting the coupling of the flow to the $\mathcal{Q}$-tensor we also neglect convection and model the fluid flow using Stokes equation. We can do this, because for this system requiring that the Reynolds number is small

$$\mathrm{Re} = \frac{2\rho|\boldsymbol{v}|\tilde{d}}{\zeta_3} \ll 1 \tag{4.24}$$

where $\rho$ is the density of the nematic, $\boldsymbol{v}$ the fluid velocity and $\tilde{d}$ the characteristic size of the system gives $|\boldsymbol{v}| \lesssim 10^2$ ms$^{-1}$, a condition that is easily satisfied in most liquid crystal devices.

Finally, to obtain the torque on the dopants caused by fluid flow and the electric field we use the viscous stress tensor,

$$\tilde{T}^{(N)} = -\tilde{p}\mathcal{I} + \zeta_3\tilde{\mathcal{D}}, \tag{4.25}$$

and the Maxwell stress tensor

$$\tilde{T}^{(M)} = \tilde{\boldsymbol{E}} \otimes \tilde{\boldsymbol{D}} - \frac{1}{2}\left(\tilde{\boldsymbol{E}} \cdot \tilde{\boldsymbol{D}}\right)\mathcal{I}. \tag{4.26}$$

where $\tilde{\boldsymbol{D}} = \epsilon_0\epsilon\tilde{\boldsymbol{E}}$ is the electric displacement field.

### 4.3.2 Nondimensionalisation

We now nondimensionalise equations (4.20), (4.21), (4.22) and (4.23). All the scaling parameters and some typical values are listed in table 4.1. The bulk and surface non-

dimensional free energy density and the total free energy are given by

$$\mathcal{F}_B = \frac{\xi_0^2}{2}\|\boldsymbol{\nabla a}\|^2 + \frac{T_0}{2}|\boldsymbol{a}|^2 + \frac{1}{2}|\boldsymbol{a}|^4, \tag{4.27a}$$

$$\mathcal{F}_E = -\chi_c\left[\boldsymbol{E}\cdot(\hat{\epsilon}\boldsymbol{E})\right], \tag{4.27b}$$

$$\mathcal{F}_S = \frac{\beta}{2}|\boldsymbol{a}_S - \boldsymbol{a}|^2, \tag{4.27c}$$

$$F = \int_{\mathcal{D}} \mathcal{F} dS - \sum_{\forall j}\int_{\Gamma_j} \mathcal{F}_S dl, \tag{4.27d}$$

where

$$\mathcal{F} = \mathcal{F}_B + \mathcal{F}_E. \tag{4.28}$$

We have scaled $\tilde{\boldsymbol{a}} = \left(\frac{2B}{3C}\right)\boldsymbol{a}$, $\tilde{\boldsymbol{E}} = \frac{\tilde{V}_0}{\tilde{d}}\boldsymbol{E}$ and $\tilde{\boldsymbol{x}} = \tilde{d}\boldsymbol{x}$ and $\tilde{V}_0$ is a typical voltage value taken to be 1 Volt. The non-dimensional elastic constant is $\xi_0^2 = \frac{9C}{4B^2}\frac{L}{\tilde{d}^2}$, the non-dimensional electric susceptibility is $\chi_c = \frac{\epsilon_0\epsilon_u\tilde{V}_0^2}{C\tilde{d}^2}\left(\frac{3C}{2B}\right)^4$, $T_0$ is the reduced temperature and the non-dimensional anchoring strength is $\beta = \frac{\tilde{\mu}}{C\tilde{d}}\left(\frac{3C}{2B}\right)^2$. The non-dimensional dissipation function is given by

$$R = \frac{1}{2}\left|\frac{\partial \boldsymbol{a}}{\partial t}\right|^2 + \frac{1}{2}\zeta'\mathcal{D}:\mathcal{D}, \tag{4.29}$$

where the reduced viscosity is $\zeta' = \frac{\zeta_3}{\zeta_1}\left(\frac{3C}{2B}\right)^2$ and time has been scaled as $\tilde{t} = \frac{\zeta_1}{C}\left(\frac{3C}{2B}\right)^2 t$. The Maxwell and viscous stress tensors (4.25) and (4.26) become,

$$T^{(M)} = \chi_c\left[\boldsymbol{E}\otimes\boldsymbol{D} - \frac{1}{2}(\boldsymbol{E}\cdot\boldsymbol{D})\mathcal{I}\right], \tag{4.30a}$$

$$T^{(N)} = -p\mathcal{I} + \zeta'\mathcal{D}. \tag{4.30b}$$

Here the pressure is scaled $\tilde{p} = C\left(\frac{2B}{3C}\right)^2 p$, the velocity is scaled $\tilde{\boldsymbol{v}} = \frac{\tilde{d}}{\tau}\boldsymbol{v}$, the electric displacement field is $\tilde{\boldsymbol{D}} = \frac{\tilde{V}_0}{\tilde{d}}\boldsymbol{D}$ which is related to the non-dimensional electric field by $\boldsymbol{D} = \hat{\epsilon}\boldsymbol{E}$ where the reduced dielectric tensor is $\hat{\epsilon} = \frac{\epsilon}{\epsilon_u}$. We now derive the equations governing the nematic LC, fluid flow, dopants and applied potential.

### 4.3.3 The nematic equations

The equations governing the nematic liquid crystal dynamics are given by,

$$\frac{\partial R}{\partial\frac{\partial \boldsymbol{a}}{\partial t}} = \boldsymbol{\nabla}\cdot\frac{\partial\mathcal{F}}{\partial\boldsymbol{\nabla a}} - \frac{\partial\mathcal{F}}{\partial\boldsymbol{a}} \tag{4.31}$$

in the bulk and

$$\hat{\boldsymbol{\nu}} \cdot \frac{\partial \mathcal{F}}{\partial \boldsymbol{\nabla a}} = -\frac{\partial \mathcal{F}_S}{\partial \boldsymbol{a}} \qquad \boldsymbol{x} \in \Gamma_i \tag{4.32}$$

on the $i$-th particle with $\hat{\boldsymbol{\nu}}$ the outward unit normal from $\Omega_j$. Substituting the total non-dimensional free energy density from (4.27) and the dissipation function from equation (4.29) into (4.31) and (4.32) we find the nematic is governed by,

$$\frac{\partial \boldsymbol{a}}{\partial t} = \xi_0^2 \nabla^2 \boldsymbol{a} + \chi_a \boldsymbol{e} - \boldsymbol{a} T_0 - 2\boldsymbol{a}|\boldsymbol{a}|^2 \qquad \boldsymbol{x} \in \Omega_j, \tag{4.33a}$$

$$\hat{\boldsymbol{\nu}} \cdot \boldsymbol{\nabla a} = W\left(\boldsymbol{a}_S - \boldsymbol{a}\right) \qquad \boldsymbol{x} \in \Gamma_j, \tag{4.33b}$$

where $\chi_a = \frac{\epsilon_0 \Delta\epsilon}{2SC}\left(\frac{3C}{2B}\right)^4 \left(\frac{\tilde{V}_0}{\tilde{d}}\right)^2$ and $W = \frac{\beta}{\xi_0^2}$.

### 4.3.4 The particle equations

To determine the governing equations for the particles we balance the torques due to the fluid flow, nematic liquid crystal and electric fields. These torques can each be determined using the appropriate stress tensor, free energy or dissipation function. We use the latter to derive the nematic torques and the former to determine the electrostatic contribution. The torque on particle $j$ due to elastic distortions and surface orientations is equal to minus the derivative of the nematic elastic and surface free energy density with respect to particle orientation,

$$\begin{aligned}\tilde{\tau}_N^{(j)} = &-\int_{\Gamma_j} \left\{ \frac{\xi_0^2}{2}\|\boldsymbol{\nabla a}\|^2 + \frac{T_0}{2}|\boldsymbol{a}|^2 + \frac{1}{2}|\boldsymbol{a}|^4 \right\} \left(\hat{\boldsymbol{\nu}} \cdot \frac{\partial \boldsymbol{r}}{\partial \psi^{(j)}}\right) dl - \int_{\Gamma_j} \beta\left(\boldsymbol{a}_S - \boldsymbol{a}\right) \cdot \frac{\partial \boldsymbol{a}_S}{\partial \psi^{(j)}} \\ &+ \frac{\beta^2}{\xi_0^2}\left(\hat{\boldsymbol{\nu}} \cdot \frac{\partial \boldsymbol{r}}{\partial \psi^{(j)}}\right)\left(\boldsymbol{a}_S - \boldsymbol{a}\right)^2 + \frac{\beta\kappa}{2}\left(\hat{\boldsymbol{\nu}} \cdot \frac{\partial \boldsymbol{r}}{\partial \psi^{(j)}}\right)\left(\boldsymbol{a}_S - \boldsymbol{a}\right)^2 dl, \end{aligned} \tag{4.34}$$

where $\psi^{(j)}$ is the alignment of the $j$-th particle and we have used Reynolds transport theorem (see appendix A.3). Here $\kappa$ is the principal curvature of the particles surface and $\boldsymbol{r}$ is the position vector on the particle surface with respect to a given origin. To compute the torque due to the electric field we use the Maxwell stress tensor (4.30a). The $x_3$ component of the torque is

$$\tau_E^{(j)} = -\int_{\Gamma_j} r_{\perp k} \hat{\nu}_m T_{km}^{(M)} dl, \tag{4.35}$$

where we sum over repeated indices with the indices ranging from 1 to 2. Here $\boldsymbol{r}_\perp = [-x_2 \;\; x_1]^T$ and $\epsilon_{ipk}$ is the Levi-Civita symbol. The torque or drag due to fluid flow acts to resist the particle motion and, as will be shown in 4.4.2, introduces time dependence into

the particle dynamics. The time-scale on which the particle reorients is hence determined by a balance between this drag term and the other torques. In non-dimensional units the flow velocity $\boldsymbol{v}$ is governed by

$$\frac{\zeta'}{2}\nabla^2\boldsymbol{v} = \boldsymbol{\nabla}p, \qquad \boldsymbol{\nabla}\cdot\boldsymbol{v} = 0, \qquad \boldsymbol{x}\in\Omega_j, \tag{4.36a}$$

$$\boldsymbol{v} = \frac{\partial\psi^{(j)}}{\partial t}\boldsymbol{r}_\perp, \qquad \boldsymbol{x}\in\Gamma_j. \tag{4.36b}$$

We can now compute the drag on the particle from the dynamic stress tensor. Following the same method as for the Maxwell stress we find,

$$\begin{aligned}(\tau_v)_i^{(j)} &= -\int_{\Gamma_j} r_{\perp k}\hat{\nu}_m T^{(N)}_{mk}\,dl \qquad k=1,2,\\ &= -\int_{\Gamma_j}\boldsymbol{r}_\perp\cdot(-p\hat{\boldsymbol{\nu}}+\zeta'\mathcal{D}\hat{\boldsymbol{\nu}})\,dl\end{aligned} \tag{4.37}$$

Summarizing, the particle dynamics are governed by

$$\begin{aligned}&\int_{\Gamma_j}\boldsymbol{r}_\perp\cdot(-p\hat{\boldsymbol{\nu}}+\zeta'\mathcal{D}\hat{\boldsymbol{\nu}})\,dl = -\int_{\Gamma_j}\left\{\frac{\xi_0^2}{2}\|\boldsymbol{\nabla a}\|^2+\frac{T_0}{2}|\boldsymbol{a}|^2+\frac{1}{2}|\boldsymbol{a}|^4\right\}\left(\hat{\boldsymbol{\nu}}\cdot\frac{\partial\boldsymbol{r}}{\partial\psi^{(j)}}\right)dl\\ &-\int_{\Gamma_j}\beta\,(\boldsymbol{a}_S-\boldsymbol{a})\cdot\frac{\partial\boldsymbol{a}_S}{\partial\psi^{(j)}}+\frac{\beta^2}{\xi_0^2}\left(\hat{\boldsymbol{\nu}}\cdot\frac{\partial\boldsymbol{r}}{\partial\psi^{(j)}}\right)(\boldsymbol{a}_S-\boldsymbol{a})^2+\frac{\beta\kappa}{2}\left(\hat{\boldsymbol{\nu}}\cdot\frac{\partial\boldsymbol{r}}{\partial\psi^{(j)}}\right)(\boldsymbol{a}_S-\boldsymbol{a})^2dl\\ &-\int_{\Gamma_j} r_{\perp k}\hat{\nu}_l T^{(M)}_{lk}dl.\end{aligned} \tag{4.38}$$

### 4.3.5 The potential equations

The electric potential is governed by Maxwell's equation for the electric displacement field. We assume that there are no free charges in the system and impose a floating potential condition on the electrostatic potential on the surface of the inclusions. In nondimensional form the equations governing the electric potential are

$$\boldsymbol{\nabla}\cdot([\mathcal{I}+\alpha\mathcal{Q}]\,\boldsymbol{\nabla}\phi) = 0 \qquad \boldsymbol{x}\in\Omega_j, \tag{4.39a}$$

$$\phi|_{\Gamma_j} = \text{Constant and } \int_{\Gamma_j}\hat{\boldsymbol{\nu}}\cdot([\mathcal{I}+\alpha\mathcal{Q}]\,\boldsymbol{\nabla}\phi)\,dl = 0 \qquad \boldsymbol{x}\in\Gamma_j. \tag{4.39b}$$

Equations (4.33), (4.36), (4.38) and (4.39) govern the nematic, fluid flow, particles and electric field in our system. We have assumed that the particles are fixed in position but are allowed to rotate freely, thus neglecting any effect due to concentration gradients. The

| | |
|---|---|
| $K = 15$ pN | $L = \frac{K}{4\tilde{S}^2} \approx 13.4$ pN |
| $S = \sqrt{\frac{-T_0}{2}} = \sqrt{5} \approx 2.236$ | $\tilde{S} = \frac{2B}{3C}S \approx 0.6116$ |
| $A = 0.13 \cdot 10^6$ JK$^{-1}$m$^{-3}$ | $\zeta = 280.8$ mPa s |
| $B = 1.6 \cdot 10^6$ JK$^{-1}$m$^{-3}$ | $\zeta_3 = 224.7$ mPa s |
| $C = 3.9 \cdot 10^6$ JK$^{-1}$m$^{-3}$ | $\tilde{d} = 32 \cdot 10^{-6}$ m |
| $T_0 = -10$ | $\tau = \frac{\zeta}{C}\left(\frac{3C}{2B}\right)^2 \approx 9.625 \times 10^{-7}$ s |
| $\tilde{\mu} = 10^{-7}$ to $10^{-5}$Jm$^{-2}$ | $\xi_0^2 = \frac{9C}{4B^2}\frac{L}{\tilde{d}^2}$ |
| $\tilde{v}_c = \frac{\tilde{d}}{\tau}$ | $\beta = \frac{\tilde{\mu}}{C\tilde{d}}\left(\frac{3C}{2B}\right)^2$ |
| $W = \frac{\beta}{\xi_0^2} \approx 12$ to $0.12$ | $\eta = \frac{L_y}{\tilde{d}}$ |
| $\chi_a = \frac{\epsilon_0 \Delta\epsilon}{2SC}\left(\frac{3C}{2B}\right)^4\left(\frac{\tilde{V}_0}{\tilde{d}}\right)^2$ | $\kappa_0 = \frac{1}{2}\frac{\zeta_3}{\zeta_1}\left(\frac{3C}{2B}\right)^2$ |
| $\alpha = \frac{\Delta\epsilon}{\sqrt{2}S\epsilon_u}$ | $\chi_c = \frac{\epsilon_0\epsilon_u}{C\tilde{d}^2}\left(\frac{3C}{2B}\right)^4 V_0^2$ |
| $\tilde{p} = C\left(\frac{2B}{3C}\right)^2 p$ | $\tilde{v} = \frac{\tilde{d}}{\tau}v$ |

Table 4.1: Parameters used during nondimensionalisation, values represent a typical LC.We have used the same nondimensionaliation scheme as was employed in chapter 3.

particles themselves are treated as ideal conductors and we use a continuum model for the nematic which bounds the minimum particle size that we may consider. Additionally by decoupling the nematic from the fluid flow we have included only limited dynamics. We perform a multiple scale analysis of these equations and by using a level set representation of the particles we derive homogenised equations. Following this we use a second method of multiple scales to extract the slow dynamics of the nematic.

## 4.4 Homogenization

In our system we have equations for the particles, the liquid crystal, the applied field and the fluid flow. As the size of the particles varies linearly with $\eta$ to avoid the surface term dominating we postulate that the anchoring energy density scales linearly with $\eta$ ($\tilde{\mu} = \mathcal{O}(\eta)$). A rough physical interpretation of this condition is that we have weak anchoring on the particle surface. More precisely in the limit $\eta \to 0$ the total boundary area between nematic and dopant diverges. As a result unless we postulate a decrease in the anchoring energy density we find that the surface anchoring dominates the particle dynamics. This is roughly physically equivalent to maintaining a constant volume of surfactant as the number of particles diverges. This way even though the total interaction area increases the surface energy density decreases. In any real application of the theory

developed here $\eta$ is small but non-zero. The equations derived here are valid for small $\eta$ provided that the total surface energy density is of the order of the bulk energy or smaller and that the anchoring on each individual particle is weak enough to not induce defects.

In order to represent arbitrary particles undergoing rotational motion correctly within the homogenization scheme we use the level set method first employed by Bruna and Chapman [21] and Richardson [93] to compute the expansion of the unit normal vector and the value of the term $\hat{\boldsymbol{\nu}} \cdot \frac{\partial \boldsymbol{r}}{\partial \psi^{(j)}}$. For ease of notation, we drop the particle index $j$ in the remainder of this subsection. We express the location of the particle surface as a level set $\chi_{LS}(\psi(\boldsymbol{x}), \boldsymbol{y}) = 0$. The expansion of the unit normal is given by

$$\begin{aligned} \hat{\boldsymbol{\nu}} &= \frac{\boldsymbol{\nabla}_{\boldsymbol{x}}\chi_{LS} + \frac{1}{\eta}\boldsymbol{\nabla}_{\boldsymbol{y}}\chi_{LS}}{|\boldsymbol{\nabla}_{\boldsymbol{x}}\chi_{LS} + \frac{1}{\eta}\boldsymbol{\nabla}_{\boldsymbol{y}}\chi_{LS}|} \\ &= \hat{\boldsymbol{\nu}}_0 + \eta\left(\frac{\boldsymbol{\nabla}_{\boldsymbol{x}}\chi_{LS}}{|\boldsymbol{\nabla}_{\boldsymbol{y}}\chi_{LS}|} - \hat{\boldsymbol{\nu}}_0\frac{\hat{\boldsymbol{\nu}}_0 \cdot \boldsymbol{\nabla}_{\boldsymbol{x}}\chi_{LS}}{|\boldsymbol{\nabla}_{\boldsymbol{y}}\chi_{LS}|}\right) + \mathcal{O}(\eta^3), \end{aligned} \tag{4.40}$$

where the leading order unit normal is

$$\hat{\boldsymbol{\nu}}_0 = \frac{\boldsymbol{\nabla}_{\boldsymbol{y}}\chi_{LS}}{|\boldsymbol{\nabla}_{\boldsymbol{y}}\chi_{LS}|}. \tag{4.41}$$

We now determine the "speed" of the boundary i.e. $\frac{\partial \boldsymbol{r}}{\partial \psi}$. As mentioned in section 4.3.4, $\boldsymbol{r}$ is the position vector of a point on the surface of a given particle. In the context of homogenization, $\boldsymbol{r}$ is a rapidly varying quantity and hence a function of the $\boldsymbol{y}$ coordinates. We can therefore use the implicit function theorem on the level set definition of the particle boundary to obtain

$$\frac{\partial r_i}{\partial \psi} = -\frac{\partial \chi_{LS}}{\partial \psi}\left(\frac{\partial \chi_{LS}}{\partial y_i}\right)^{-1}. \tag{4.42}$$

By utilizing the following symmetry of $\chi_{LS}$ in its two arguments

$$\chi_{LS}(0, R^T(\psi(\boldsymbol{x}))\boldsymbol{y}) = \chi_{LS}(\psi(\boldsymbol{x}), \boldsymbol{y}) \tag{4.43}$$

and using the chain rule we find

$$\frac{\partial \chi_{LS}}{\partial \psi} = -\boldsymbol{r}_\perp \cdot \boldsymbol{\nabla}_{\boldsymbol{y}}\chi_{LS}. \tag{4.44}$$

Hence

$$\frac{\partial \boldsymbol{r}}{\partial \psi} \cdot \hat{\boldsymbol{\nu}}_0 = \boldsymbol{r}_\perp \cdot \hat{\boldsymbol{\nu}}_0. \tag{4.45}$$

### 4.4.1 Scaling of equations

As the size of the particles decreases so does the magnitude of the torques on the particles. To make the analysis as transparent as possible we make the $\eta$ dependence of the terms in (4.38) explicit. This amounts to mapping the domain of integration from a domain that scales with $\eta$ to a fixed domain of size one. The line element and position vector on the particle both scale linearly with $\eta$, surface elements scale with $\eta^2$ and the curvature scales as $\frac{1}{\eta}$. With these postulated scalings the particle governing equation is

$$\begin{aligned}\eta \int_{\Gamma_j} \boldsymbol{r}_\perp \cdot (-p\hat{\boldsymbol{\nu}} + \zeta' \mathcal{D}\hat{\boldsymbol{\nu}})\, dl = &- \int_{\Gamma_j} \eta^2 \left\{ \frac{\xi_0^2}{2} \|\boldsymbol{\nabla a}\|^2 + \frac{T_0}{2}|\boldsymbol{a}|^2 + |\boldsymbol{a}|^4 \right\} \left( \hat{\boldsymbol{\nu}} \cdot \frac{\partial \boldsymbol{r}}{\partial \psi^{(j)}} \right) dl \\ &- \eta^2 \beta \int_{\Gamma_j} (\boldsymbol{a}_S - \boldsymbol{a}) \cdot \boldsymbol{a}_{S\perp} + \eta^2 \frac{\beta}{\xi_0^2} (\hat{\boldsymbol{\nu}} \cdot \boldsymbol{r}_\perp)(\boldsymbol{a}_S - \boldsymbol{a})^2 + \frac{\kappa}{2} (\hat{\boldsymbol{\nu}} \cdot \boldsymbol{r}_\perp)(\boldsymbol{a}_S - \boldsymbol{a})^2 dl \\ &- \eta^2 \chi_c \int_{\Gamma_j} r_\perp \cdot (\hat{\boldsymbol{\nu}} \cdot T_M) dl.\end{aligned} \tag{4.46}$$

The fluid flow obeys

$$\frac{\zeta'}{2} \nabla^2 \boldsymbol{v} = \boldsymbol{\nabla} p, \qquad \boldsymbol{\nabla} \cdot \boldsymbol{v} = 0, \qquad \boldsymbol{x} \in \Omega_j, \tag{4.47a}$$

$$\boldsymbol{v} = \eta \frac{\partial \psi^(j)}{\partial t} \boldsymbol{r}_\perp, \qquad \boldsymbol{x} \in \Gamma_j. \tag{4.47b}$$

The nematic obeys

$$\frac{\partial \boldsymbol{a}}{\partial t} = \xi_0^2 \nabla^2 \boldsymbol{a} + \chi_a \boldsymbol{e} - \boldsymbol{a} T_0 - 2\boldsymbol{a}|\boldsymbol{a}|^2 \qquad \boldsymbol{x} \in \Omega_j, \tag{4.48a}$$

$$\hat{\boldsymbol{\nu}} \cdot \boldsymbol{\nabla a} = \eta W (\boldsymbol{a}_S - \boldsymbol{a}) \qquad \boldsymbol{x} \in \Gamma_j. \tag{4.48b}$$

The equation governing the electrostatic potential (4.39) is unchanged.

All the ingredients needed for carrying out the homogenization procedure are now in place. The next step consists in solving the drag equation to eliminate the fluid velocity. This is possible because we have neglected the back-coupling between the director alignment and fluid flow so that the fluid velocity is driven only by the particle orientation. We will carry out this step in the next subsection and then move onto homogenise the remaining equations.

### 4.4.2 Expanding the drag

First we note that, by assumption, the fluid flow is coupled only to the particle orientation. Dealing with the fluid flow will then allow us to simplify (4.46) and determine an explicit set of equations for the particle motion. We make the usual expansions of the gradient, the Laplacian and fields,

$$\boldsymbol{\nabla} = \boldsymbol{\nabla}_{\boldsymbol{x}} + \frac{1}{\eta}\boldsymbol{\nabla}_{\boldsymbol{y}}, \tag{4.49a}$$

$$\nabla^2 = \nabla^2_{\boldsymbol{x}} + \frac{2}{\eta}\boldsymbol{\nabla}_{\boldsymbol{x}} \cdot \boldsymbol{\nabla}_{\boldsymbol{y}} + \frac{1}{\eta^2}\nabla^2_{\boldsymbol{y}}, \tag{4.49b}$$

$$\boldsymbol{v} = \boldsymbol{v}_0 + \eta\boldsymbol{v}_1 + \eta^2\boldsymbol{v}_2, \tag{4.49c}$$

$$\mathcal{D} = \frac{1}{\eta}\mathcal{D}_0 + \mathcal{D}_1 + \eta\mathcal{D}_2, \tag{4.49d}$$

$$p = p_0 + \eta p_1 + \eta^2 p_2. \tag{4.49e}$$

Substituting equations (4.49) into Stokes' equation (4.47) we obtain a sequence of problems at different orders in $\eta$. Solving these in ascending powers of $\eta$ we will derive the cell problem for the fluid flow and use the result to simplify the drag term which forms the left-hand side of equation (4.46), namely

$$F = \eta \int_{\Gamma_j} \boldsymbol{r}_\perp \cdot (-p\hat{\boldsymbol{\nu}} + \zeta' \mathcal{D}\hat{\boldsymbol{\nu}})\, dl. \tag{4.50}$$

#### Leading order

At leading order the fluid obeys

$$\begin{aligned} &\nabla^2_{\boldsymbol{y}}\boldsymbol{v}_0 = 0, \qquad \boldsymbol{\nabla}_{\boldsymbol{y}} \cdot \boldsymbol{v}_0 = 0 \qquad \boldsymbol{y} \in \Omega_j, \\ &\boldsymbol{v}_0 = \boldsymbol{0}, \qquad \boldsymbol{y} \in \Gamma_j, \end{aligned} \tag{4.51}$$

subject to periodic boundary conditions on $\partial\hat{\Omega}_j$, the outer cell walls. This system has solution $\boldsymbol{v}_0 = 0$. As a results, $\mathcal{D}_0 = 0$.

#### First order

At this order the fluid obeys

$$\begin{aligned} &\frac{\zeta'}{2}\nabla^2_{\boldsymbol{y}}\boldsymbol{v}_1 = \boldsymbol{\nabla}_{\boldsymbol{y}} p_0, \qquad \boldsymbol{\nabla}_{\boldsymbol{y}} \cdot \boldsymbol{v}_1 = 0, \qquad \boldsymbol{y} \in \Omega_j, \\ &\boldsymbol{v}_1 = \frac{\partial\psi}{\partial t}\boldsymbol{r}_\perp, \qquad \boldsymbol{y} \in \Gamma_j, \end{aligned} \tag{4.52}$$

subject to periodic boundary conditions on $\partial\hat{\Omega}_j$. We make the ansatz $\boldsymbol{v}_1 = \boldsymbol{u}_1 \frac{\partial \psi}{\partial t}$ and $p_0 = P_0 \frac{\partial \psi}{\partial t}$ where both $P_0$ and $\boldsymbol{u}_1$ depend on $\boldsymbol{y}$. The system of equations for $\boldsymbol{u}_1$ is

$$\begin{aligned} &\nabla_{\boldsymbol{y}}^2 \boldsymbol{u}_1 = \boldsymbol{\nabla}_{\boldsymbol{y}} P_0, \qquad \boldsymbol{\nabla}_{\boldsymbol{y}} \cdot \boldsymbol{u}_1 = 0, \qquad \boldsymbol{y} \in \Omega_j, \\ &\boldsymbol{u}_1 = \boldsymbol{r}_\perp, \qquad \boldsymbol{y} \in \Gamma_j. \end{aligned} \tag{4.53}$$

Equations (4.53) are the cell problem for $\boldsymbol{u}_1$ and can be solved numerically. The order $\eta^0$ rate of shear tensor is given by

$$\mathcal{D}_1 = \frac{1}{2}\left[\boldsymbol{\nabla}_{\boldsymbol{y}} \boldsymbol{v}_1 + (\boldsymbol{\nabla}_{\boldsymbol{y}} \boldsymbol{v}_1)^T\right]. \tag{4.54}$$

and the drag on the $j$-th particle can be expanded as

$$\int_{\Gamma_j} \boldsymbol{r}_\perp \cdot (\zeta' \mathcal{D}_1 \hat{\boldsymbol{\nu}}_0 - \hat{\boldsymbol{\nu}}_0 p_0)\, dl = \frac{\partial \psi^{(j)}}{\partial t} \int_{\Gamma_j} \boldsymbol{r}_\perp \cdot (\zeta' \mathcal{D}_1' \hat{\boldsymbol{\nu}}_0 - \hat{\boldsymbol{\nu}}_0 P_0)\, dl + \mathcal{O}(\eta). \tag{4.55}$$

where

$$\mathcal{D}_1' = \frac{1}{2}\left[\boldsymbol{\nabla}_{\boldsymbol{y}} \boldsymbol{u}_1 + (\boldsymbol{\nabla}_{\boldsymbol{y}} \boldsymbol{u}_1)^T\right]. \tag{4.56}$$

Using equation (4.55) we simplify the particle equation (4.46) to

$$\begin{aligned} \kappa_0' \frac{\partial \psi^{(j)}}{\partial t} = &- \int_{\Gamma_j} \left\{ \frac{\xi_0^2}{2} \|\boldsymbol{\nabla} \boldsymbol{a}\|^2 + \frac{T_0}{2} |\boldsymbol{a}|^2 + |\boldsymbol{a}|^4 \right\} \left( \hat{\boldsymbol{\nu}} \cdot \frac{\partial \boldsymbol{r}}{\partial \psi} \right) dl \\ &- \beta \int_{\Gamma_j} (\boldsymbol{a}_S - \boldsymbol{a}) \cdot \boldsymbol{a}_{S\perp} + \eta^2 W (\hat{\boldsymbol{\nu}} \cdot \boldsymbol{r}_\perp)(\boldsymbol{a}_S - \boldsymbol{a})^2 + \frac{\kappa}{2} (\hat{\boldsymbol{\nu}} \cdot \boldsymbol{r}_\perp)(\boldsymbol{a}_S - \boldsymbol{a})^2 dl \\ &- \chi_c \int_{\Gamma_j} \boldsymbol{r}_\perp \cdot (\hat{\boldsymbol{\nu}} \cdot T_M) dl, \end{aligned} \tag{4.57}$$

where

$$\kappa_0' = \int_{\Gamma_j} \boldsymbol{r}_\perp \cdot (\zeta' \mathcal{D}_1' \hat{\boldsymbol{\nu}}_0 - \hat{\boldsymbol{\nu}}_0 P_0)\, dl. \tag{4.58}$$

As we are only interested in the leading order time dynamics of $\psi$ we do not consider higher order terms in the expansion of the drag equations.

### 4.4.3 Nematic dynamics and the electric field

Having obtain a simplified equation for the particles (4.57), we now proceed to homogenise equations (4.39) and (4.48). As in the previous section, we expand derivatives, equations

(4.49), and fields

$$\boldsymbol{a} = \sum_{k=0}^{k=\infty} \boldsymbol{a}_k \eta^k, \qquad \boldsymbol{e} = \sum_{k=0}^{k=\infty} \boldsymbol{e}_k \eta^k. \tag{4.59}$$

**Leading order**

The leading order expansion of the nematic equations (4.48) is

$$\xi_0^2 \nabla_{\boldsymbol{y}}^2 \boldsymbol{a}_0 + \chi_a \boldsymbol{e}_0 = 0, \qquad \boldsymbol{y} \in \Omega_j, \qquad \forall j, \tag{4.60a}$$

$$\hat{\boldsymbol{\nu}}_0 \cdot \boldsymbol{\nabla}_{\boldsymbol{y}} \boldsymbol{a}_0 = 0, \qquad \boldsymbol{y} \in \Gamma_j, \qquad \forall j, \tag{4.60b}$$

subject to periodic boundary conditions on the outer boundaries of the unit cell. Similarly, the leading order expansion of Maxwell's equations for the electric potential is

$$\boldsymbol{\nabla}_{\boldsymbol{y}} \cdot \left( \left[ \mathcal{I} + \alpha \mathcal{Q}^{(0)} \right] \boldsymbol{\nabla}_{\boldsymbol{y}} \phi_0 \right) = 0, \qquad \boldsymbol{y} \in \Omega_j, \qquad \forall j, \tag{4.61a}$$

$$\phi_0 = C_j \text{ and } \int_{\Gamma_j} \left( \left[ \mathcal{I} + \alpha \mathcal{Q}^{(0)} \right] \boldsymbol{\nabla}_{\boldsymbol{y}} \phi_0 \right) \cdot \hat{\boldsymbol{\nu}}_0 dl = 0, \qquad \boldsymbol{y} \in \Gamma_j, \qquad \forall j. \tag{4.61b}$$

If $\phi_0$ is independent of $\boldsymbol{y}$ then $\boldsymbol{e}_0$ is zero. Hence all of the above equations are satisfied by $\boldsymbol{a}_0 = \boldsymbol{a}_0(\boldsymbol{x})$ and $\phi_0 = \phi_0(\boldsymbol{x})$. However, as noted in chapter 3 for static particles, if $\phi_0$ varies on the macroscopic scale the potential across the metallic inclusions will not be constant. To overcome this we employ the same method as in chapter 3.3.3. As before we find appropriate boundary conditions $\phi_0$ and $\phi_1$ for fixed $j$,

$$\phi_0(\boldsymbol{x}_j) = C_{0j}, \tag{4.62a}$$

$$\phi_1 = -\left( \boldsymbol{y} - \boldsymbol{y}_j \right) \cdot \boldsymbol{\nabla}_{\boldsymbol{x}} \phi_0 + C_{1j}, \qquad \boldsymbol{y} \in \Gamma_j. \tag{4.62b}$$

Imposing $\phi_0 = \phi_0(\boldsymbol{x})$ and $\boldsymbol{a}_0 = \boldsymbol{a}_0(\boldsymbol{x})$ we find that the potential equation is automatically satisfied at this order.

### 4.4.4 First order correction

At order $\mathcal{O}(\eta)$ we find

$$\xi_0^2 \nabla_{\boldsymbol{y}}^2 \boldsymbol{a}_1 = 0, \qquad \boldsymbol{y} \in \Omega, \tag{4.63a}$$

$$\hat{\boldsymbol{\nu}}_0 \cdot \boldsymbol{\nabla}_y \boldsymbol{a}_1 + \hat{\boldsymbol{\nu}}_0 \cdot \boldsymbol{\nabla}_x \boldsymbol{a}_0 = 0, \qquad \boldsymbol{y} \in \Gamma. \tag{4.63b}$$

This is equivalent to the standard order one problem for diffusion of solutes in porous media [47], hence solvabillity is guaranteed. By making the ansatz $\boldsymbol{a}_1 = \chi_k \frac{\partial \boldsymbol{a}_0}{\partial x_k}$ and

substituting into equations (4.63) we obtain the cell problem for $\chi_k$, $k = 1, 2$,

$$\nabla^2_{\boldsymbol{y}} \chi_k = 0, \tag{4.64a}$$

$$\hat{\boldsymbol{\nu}}_0 \cdot \boldsymbol{\nabla}_{\boldsymbol{y}} \chi_k = -\hat{\boldsymbol{\nu}} \cdot \hat{\boldsymbol{e}}_k. \tag{4.64b}$$

Here $\hat{\boldsymbol{e}}_k$ is the $k$-th coordinate unit vector. These equations (with periodic boundary conditions) define $\chi_k$ up to a constant, hence $\boldsymbol{a}_1 = \chi_k \frac{\partial \boldsymbol{a}_0}{\partial x_k} + \overline{\boldsymbol{a}}_1(\boldsymbol{x})$. Maxwell's equation gives

$$\boldsymbol{\nabla}_{\boldsymbol{y}} \cdot \left[ (\mathcal{I} + \alpha \mathcal{Q}^{(0)}) \boldsymbol{\nabla}_{\boldsymbol{y}} \phi_1 \right] = 0, \tag{4.65a}$$

$$\phi_1 = -(\boldsymbol{y} - \boldsymbol{y}_i) \cdot \boldsymbol{\nabla}_{\boldsymbol{x}} \phi_0 + C_{1i}, \qquad \boldsymbol{y} \in \Gamma_i, \tag{4.65b}$$

$$\int_{\Gamma_i} \left[ \mathcal{I} + \alpha \mathcal{Q}^{(0)} \right] (\boldsymbol{\nabla}_{\boldsymbol{y}} \phi_1 + \boldsymbol{\nabla}_{\boldsymbol{x}} \phi_0) \cdot \hat{\boldsymbol{\nu}} \, dl = 0. \tag{4.65c}$$

Here $\mathcal{Q}^{(0)}$ is the order $\mathcal{O}(\eta^0)$ part of the $\mathcal{Q}$-tensor and has component vector $\boldsymbol{a}_0$. The solvability condition for equation (4.65a), found by integrating (4.65a) over an arbitrary cell, using the divergence theorem and condition (4.65c), is automatically satisfied. The cell problem for the electric field is derived by making the ansatz,

$$\phi_1 = \sum_{k=1}^{3} R_k(\boldsymbol{x}, \boldsymbol{y}) \frac{\partial \phi_0}{\partial x_k} + \bar{\phi}_1(\boldsymbol{x}). \tag{4.66}$$

By substituting this ansatz into equations (4.65) and setting $\bar{\phi}_1 = C_{1i}$ we find

$$\left[ \delta_{nm} + \alpha \mathcal{Q}^{(0)}_{nm} \right] \frac{\partial^2 R_k}{\partial y_n \partial y_m} = 0, \ \boldsymbol{y} \in \Omega_j, \tag{4.67a}$$

$$R_k = -(y_k - y_{0k}), \ \boldsymbol{y} \in \Gamma_j, \tag{4.67b}$$

$$\int_{\Gamma_i} \left[ \mathcal{I} + \alpha \mathcal{Q}^{(0)} \right] \boldsymbol{\nabla}_{\boldsymbol{y}} R_k(\boldsymbol{y}) \cdot \hat{\boldsymbol{\nu}} \, dl = 0, \tag{4.67c}$$

which must be solved numerically for varying particle orientations and realizations of $\mathcal{Q}^{(0)}$.

### 4.4.5 Homogenization

At order $\mathcal{O}(\eta^0)$ the nematic equations give

$$\xi_0^2 \left( \nabla^2_{\boldsymbol{x}} \boldsymbol{a}_0 + 2 \boldsymbol{\nabla}_{\boldsymbol{x}} \cdot \boldsymbol{\nabla}_{\boldsymbol{y}} \boldsymbol{a}_1 + \nabla^2_{\boldsymbol{y}} \boldsymbol{a}_2 \right) - T_0 \boldsymbol{a}_0 - 2 \boldsymbol{a}_0 |\boldsymbol{a}_0|^2 + \chi_a \boldsymbol{e}_2 = \frac{\partial \boldsymbol{a}_0}{\partial t}, \tag{4.68a}$$

$$\hat{\boldsymbol{\nu}}_0 \cdot \boldsymbol{\nabla}_{\boldsymbol{y}} \boldsymbol{a}_2 + \hat{\boldsymbol{\nu}}_0 \cdot \boldsymbol{\nabla}_{\boldsymbol{x}} \boldsymbol{a}_1 + \boldsymbol{\nu}_1 \cdot \boldsymbol{\nabla}_{\boldsymbol{x}} \boldsymbol{a}_0 + \boldsymbol{\nu}_1 \cdot \boldsymbol{\nabla}_{\boldsymbol{y}} \boldsymbol{a}_1 = W \left( \boldsymbol{a}_{S0} - \boldsymbol{a}_0 \right). \tag{4.68b}$$

The leading order operator is $\nabla_{\boldsymbol{y}}^2$ equipped with periodic boundary conditions on $\partial\hat{\Omega}$ and is self-adjoint. Hence its kernel is spanned by functions that depend only on $\boldsymbol{x}$. Projecting equation (4.68a) onto the kernel of the leading order operator we find that the homogenised equations take the form

$$\begin{aligned} &\frac{\xi_0^2}{|\Omega|} \int_\Omega \boldsymbol{\nabla}_{\boldsymbol{x}} \cdot \left( \boldsymbol{\nabla}_{\boldsymbol{x}} \boldsymbol{a}_0 + \boldsymbol{\nabla}_{\boldsymbol{y}} \boldsymbol{a}_1 \right) dS - T_0 \boldsymbol{a}_0 - 2\boldsymbol{a}_0 |\boldsymbol{a}_0|^2 + \chi_a \frac{1}{|\Omega|} \int_\Omega \boldsymbol{e}_2 dl \\ &+ \frac{\beta}{|\Omega|} \int_\Gamma \left( \boldsymbol{a}_{S0} - \boldsymbol{a}_0 \right) dl - \frac{\xi_0^2}{|\Omega|} \int_\Gamma \boldsymbol{\nu}_1 \cdot \boldsymbol{\nabla}_{\boldsymbol{x}} \boldsymbol{a}_0 + \boldsymbol{\nu}_1 \cdot \boldsymbol{\nabla}_{\boldsymbol{y}} \boldsymbol{a}_1 dl = \frac{\partial \boldsymbol{a}_0}{\partial t}. \end{aligned} \tag{4.69}$$

Here we have dropped the subscript on the domain $\Omega$ and the particle boundary $\Gamma$ and instead regard the domain of integration as a function of the slow variable $\boldsymbol{x}$. Next we use the transport theorem on the first integral (see appendix A.3)

$$\begin{aligned} \boldsymbol{\nabla}_{\boldsymbol{x}} \cdot \int_\Omega \left( \boldsymbol{\nabla}_{\boldsymbol{x}} \boldsymbol{a}_0 + \boldsymbol{\nabla}_{\boldsymbol{y}} \boldsymbol{a}_1 \right) dS = &\int_\Omega \boldsymbol{\nabla}_{\boldsymbol{x}} \cdot \left( \boldsymbol{\nabla}_{\boldsymbol{x}} \boldsymbol{a}_0 + \boldsymbol{\nabla}_{\boldsymbol{y}} \boldsymbol{a}_1 \right) dS \\ &+ \int_\Gamma \left( \boldsymbol{\nabla}_{\boldsymbol{x}} \boldsymbol{a}_0 + \boldsymbol{\nabla}_{\boldsymbol{y}} \boldsymbol{a}_1 \right) \cdot \left( \boldsymbol{\nabla}_{\boldsymbol{x}} \boldsymbol{r} \cdot \hat{\boldsymbol{\nu}}_0 \right) dl, \end{aligned} \tag{4.70}$$

and we use the level set representation to find

$$\boldsymbol{\nabla}_{\boldsymbol{x}} \boldsymbol{r} \cdot \hat{\boldsymbol{\nu}}_0 = -\frac{\boldsymbol{\nabla}_{\boldsymbol{x}} \chi_{LS}}{\| \boldsymbol{\nabla}_{\boldsymbol{y}} \chi_{LS} \|}. \tag{4.71}$$

Hence,

$$\begin{aligned} \int_\Omega \boldsymbol{\nabla}_{\boldsymbol{x}} \cdot \left( \boldsymbol{\nabla}_{\boldsymbol{x}} \boldsymbol{a}_0 + \boldsymbol{\nabla}_{\boldsymbol{y}} \boldsymbol{a}_1 \right) dS = &\boldsymbol{\nabla}_{\boldsymbol{x}} \cdot \int_\Omega \left( \boldsymbol{\nabla}_{\boldsymbol{x}} \boldsymbol{a}_0 + \boldsymbol{\nabla}_{\boldsymbol{y}} \boldsymbol{a}_1 \right) dS \\ &+ \int_\Gamma \left( \boldsymbol{\nabla}_{\boldsymbol{x}} \boldsymbol{a}_0 + \boldsymbol{\nabla}_{\boldsymbol{y}} \boldsymbol{a}_1 \right) \cdot \frac{\boldsymbol{\nabla}_{\boldsymbol{x}} \chi_{LS}}{\| \boldsymbol{\nabla}_{\boldsymbol{y}} \chi_{LS} \|} dl \end{aligned} \tag{4.72}$$

In addition, using boundary condition (4.63b) we see that on $\Gamma$

$$\boldsymbol{\nu}_1 \cdot \left( \boldsymbol{\nabla}_{\boldsymbol{x}} \boldsymbol{a}_0 + \boldsymbol{\nabla}_{\boldsymbol{y}} \boldsymbol{a}_1 \right) = \frac{\boldsymbol{\nabla}_{\boldsymbol{x}} \chi_{LS}}{\| \boldsymbol{\nabla}_{\boldsymbol{y}} \chi_{LS} \|} \cdot \left( \boldsymbol{\nabla}_{\boldsymbol{x}} \boldsymbol{a}_0 + \boldsymbol{\nabla}_{\boldsymbol{y}} \boldsymbol{a}_1 \right). \tag{4.73}$$

Substituting equations (4.72), (4.73) into (4.69) we obtain

$$\begin{aligned}&\xi_0^2\boldsymbol{\nabla}_{\boldsymbol{x}}\cdot\mathcal{K}\boldsymbol{\nabla}_{\boldsymbol{x}}\boldsymbol{a}_0-T_0\boldsymbol{a}_0-2\boldsymbol{a}_0|\boldsymbol{a}_0|^2+\chi_a\left[\boldsymbol{e}_M\left(1+2\frac{|\Omega_{np}|}{|\Omega|}\right)+\boldsymbol{p}\right]\\&+\frac{\beta}{|\Omega|}\int_\Gamma(\boldsymbol{a}_{S0}-\boldsymbol{a}_0)\,dl=\frac{\partial\boldsymbol{a}_0}{\partial t}.\end{aligned}\tag{4.74}$$

The new elasticity term is given by

$$\mathcal{K}_{ij}=\frac{1}{|\Omega|}\int_{\Omega(\boldsymbol{x})}\delta_{ij}+\frac{\partial\chi_j}{\partial y_i}dS,\tag{4.75a}$$

the macroscopic electric field is given by

$$e_{Mi}=\mathrm{Tr}\left(\sqrt{2}\left[\boldsymbol{\nabla}_{\boldsymbol{x}}\phi_0\otimes\boldsymbol{\nabla}_{\boldsymbol{x}}\phi_0\right]\mathcal{T}^{(i)}\right),\tag{4.76}$$

and the polarization is given by

$$p_i=\frac{1}{|\Omega|}\int_\Omega\mathrm{Tr}\left[\sqrt{2}\boldsymbol{\nabla}_{\boldsymbol{y}}R_k\otimes\boldsymbol{\nabla}_{\boldsymbol{y}}R_l\phi_{0,k}\phi_{0,l}\mathcal{T}^{(i)}\right]dS.\tag{4.77}$$

Having obtained a macroscopic equation for the alignment of the nematic, we now derive a macroscopic Maxwell equation for the electric potential. At this order Maxwell's equation for the electric potential and its boundary condition are

$$\begin{aligned}&\boldsymbol{\nabla}_{\boldsymbol{y}}\cdot[(\mathcal{I}+\alpha\mathcal{Q}^{(0)})(\boldsymbol{\nabla}_{\boldsymbol{y}}\phi_2+\boldsymbol{\nabla}_{\boldsymbol{x}}\phi_1)+\alpha\mathcal{Q}_1(\boldsymbol{\nabla}_{\boldsymbol{y}}\phi_1+\boldsymbol{\nabla}_{\boldsymbol{x}}\phi_0)+\alpha\mathcal{Q}_2\boldsymbol{\nabla}_{\boldsymbol{y}}\phi_0],\\&+\boldsymbol{\nabla}_{\boldsymbol{x}}\cdot[(\mathcal{I}+\alpha\mathcal{Q}^{(0)})(\boldsymbol{\nabla}_{\boldsymbol{x}}\phi_0+\boldsymbol{\nabla}_{\boldsymbol{y}}\phi_1)+\alpha\mathcal{Q}_1\boldsymbol{\nabla}_{\boldsymbol{y}}\phi_0]=0,\end{aligned}\tag{4.78a}$$

$$\begin{aligned}\int_\Gamma&\hat{\boldsymbol{\nu}}_0\cdot[(\mathcal{I}+\alpha\mathcal{Q}^{(0)})(\boldsymbol{\nabla}_{\boldsymbol{y}}\phi_2+\boldsymbol{\nabla}_{\boldsymbol{x}}\phi_1)+\alpha\mathcal{Q}_1(\boldsymbol{\nabla}_{\boldsymbol{y}}\phi_1+\boldsymbol{\nabla}_{\boldsymbol{x}}\phi_0)]\\&+\boldsymbol{\nu}_1\cdot[(\mathcal{I}+\alpha\mathcal{Q}^{(0)})(\boldsymbol{\nabla}_{\boldsymbol{x}}\phi_0+\boldsymbol{\nabla}_{\boldsymbol{y}}\phi_1)]dl=0.\end{aligned}\tag{4.78b}$$

Integrating equation (4.78a) using the divergence theorem, equation (4.78b) and the transport theorem A.3 we obtain a macroscopic equation for the potential,

$$\boldsymbol{\nabla}_{\boldsymbol{x}}\cdot\left[\left(\mathcal{I}+\alpha\mathcal{Q}^{(0)}\right)\boldsymbol{\nabla}_{\boldsymbol{x}}\phi_0\right]=0.\tag{4.79}$$

We see from (4.79) that, to first order, the electrostatic potential is not distorted by the presence of the particles. This is not true for the electric field which to leading order is given by $\boldsymbol{E}=-\boldsymbol{\nabla}_{\boldsymbol{x}}\phi_0-\boldsymbol{\nabla}_{\boldsymbol{y}}\phi_1$.

As the last step in deriving a set of macroscopic equations, we simplify the particle equation. Using $\boldsymbol{a}_0 = \boldsymbol{a}_0(\boldsymbol{x})$ and $\phi_0 = \phi_0(\boldsymbol{x})$ we can simplify the equation governing the particle dynamics considerably. The bulk elastic/screening torque becomes

$$\tau_B = -\xi_0^2 \int_\Gamma \left[ \frac{1}{2} \|\boldsymbol{\nabla}_{\boldsymbol{y}} \boldsymbol{a}_1\|^2 + \frac{1}{2} \|\boldsymbol{\nabla}_{\boldsymbol{x}} \boldsymbol{a}_0\|^2 + \boldsymbol{\nabla}_{\boldsymbol{x}} \boldsymbol{a}_0 \cdot \boldsymbol{\nabla}_{\boldsymbol{y}} \boldsymbol{a}_1 \right] (\hat{\boldsymbol{\nu}}_0 \cdot \boldsymbol{r}_\perp)\, dl + \mathcal{O}(\eta), \tag{4.80}$$

the surface torque

$$\tau_S = \beta \int_\Gamma \left[ \kappa (\hat{\boldsymbol{\nu}}_0 \cdot \boldsymbol{r}_\perp) \mathcal{I} - 2\mathcal{W} \right] \boldsymbol{a}_S dl \cdot \boldsymbol{a}_0 + \mathcal{O}(\eta), \tag{4.81}$$

where $\boldsymbol{a}_{S\perp 0} = -2\mathcal{W}\boldsymbol{a}_{S0}$ with $\mathcal{W} = \begin{bmatrix} 0 & -1 \\ 1 & 0 \end{bmatrix}$ and the electric torque

$$\tau_E = -\chi_c \int_\Gamma \boldsymbol{r}_\perp \cdot (\hat{\boldsymbol{\nu}}_0 \cdot T_{M2})\, dl + \mathcal{O}(\eta), \tag{4.82}$$

where the first non-zero contribution from the Maxwell stress tensor is given by

$$\hat{T}_{M2} = \boldsymbol{E}_1 \otimes \boldsymbol{D}_1 - \frac{1}{2} (\boldsymbol{E}_1 \cdot \boldsymbol{D}_1) \mathcal{I}. \tag{4.83}$$

Here $\boldsymbol{E}_1 = \boldsymbol{\nabla}_{\boldsymbol{x}} \phi_0 + \boldsymbol{\nabla}_{\boldsymbol{y}} \phi_1$ and $\boldsymbol{D}_1 = (\mathcal{I} + \alpha \mathcal{Q}^{(0)})(\boldsymbol{\nabla}_{\boldsymbol{x}} \phi_0 + \boldsymbol{\nabla}_{\boldsymbol{y}} \phi_1)$ are the first non-zero contributions to the electric potential and displacement. The final form of the particle equation reads,

$$\kappa_0' \frac{\partial \psi_0}{\partial t} = -\xi_0^2 \mathcal{B} : (\boldsymbol{\nabla}_{\boldsymbol{x}} \boldsymbol{a}_0 \cdot \boldsymbol{\nabla}_{\boldsymbol{x}} \boldsymbol{a}_0) - \beta \boldsymbol{q}_\kappa \cdot \boldsymbol{a}_0 - \chi_c P_{imlk} \epsilon_{il}^0 \phi_{0,m} \phi_{0,k}, \tag{4.84}$$

where

$$\begin{aligned} \mathcal{B}_{ij} &= \int_\Gamma \frac{1}{2} \left( \chi_{i,j} + \chi_{j,i} + \chi_{i,k} \chi_{j,k} \right) (\boldsymbol{r}_\perp \cdot \hat{\boldsymbol{\nu}}_0) dl, \\ P_{imlk} &= \int_\Gamma \left( \delta_{kl} + \frac{\partial R_l}{\partial y_k} \right) \left( \delta_{im} + \frac{\partial R_i}{\partial y_m} \right) (\boldsymbol{r}_\perp \cdot \hat{\boldsymbol{\nu}}_0) dl, \\ \boldsymbol{q}^{(\kappa)} &= -\int_\Gamma \left[ \kappa (\hat{\boldsymbol{\nu}}_0 \cdot \boldsymbol{r}_\perp) \mathcal{I} - 2\mathcal{W} \right] \boldsymbol{a}_{S0} dl, \\ \kappa_0' &= \int_{\Gamma_j} \boldsymbol{r}_\perp \cdot (\zeta' D_1' \hat{\boldsymbol{\nu}}_0 - \hat{\boldsymbol{\nu}}_0 P_0)\, dl. \end{aligned} \tag{4.85}$$

To summarize, equations (4.74), (4.79) and (4.84) capture the macroscopic behaviour of the system. Normally, the homogenization procedure would stop here. However, in the

specific case of liquid crystals a further simplification is possible, namely we can apply a second multiple scale expansion, this time in the time domain, to obtain a final set of macroscopic equations.

### 4.4.6 Reduced manifold dynamics

Looking at equations (4.74) and (4.84) we notice that $\xi_0^2$, $\chi_a$, $\chi_b$ and $\beta$ are extremely small parameters $\sim \mathcal{O}(10^{-7})$. Away from defects the elastic and particle driving terms are small in comparison to the thermotropic terms. As a results when equations (4.74) and (4.84) are integrated to equilibrium, the dynamics in the absence of defects roughly correspond to a rapid equilibration of the scalar order parameter followed by a slow elastic reorientation. We now follow the method of [34] and use multiple scale analysis to obtain equations governing the slow elastic reorientation. The slow reorientation dynamics are driven by terms of the order $\xi_0^2$. We simplify equations (4.74) by expanding in terms of $\eta_M = \xi_0^2$ and express $\beta = \eta_M \hat{\beta}$, $\chi_a = \eta_M \hat{\chi}_a$, $\chi_b = \eta_M \hat{\chi}_b$ and $\frac{\partial}{\partial t} = \eta_M \frac{\partial}{\partial \hat{t}}$. We assume that all dynamics on a faster time-scale than $\hat{t}$ have reached equilibrium. Equation (4.84) is driven solely by terms of order $\eta_M$, its dynamics are confined solely to the slow elastic time-scale $\hat{t}$. The first order part of equation (4.74) is

$$-T_0 \boldsymbol{a}_0 - 2\boldsymbol{a}_0 |\boldsymbol{a}_0|^2 = 0, \tag{4.86}$$

which defines an invariant manifold $|\boldsymbol{a}_0|^2 = -\frac{T_0}{2}$. At next order we find

$$\begin{aligned} &\boldsymbol{\nabla}_{\boldsymbol{x}} \cdot \mathcal{K} \boldsymbol{\nabla}_{\boldsymbol{x}} \boldsymbol{a}_0 + \hat{\chi}_a \left[ \boldsymbol{e}_M \left( 1 + 2\frac{|\Omega_{np}|}{|\Omega|} \right) + \boldsymbol{p} \right] \\ &+ \frac{\hat{\beta}}{|\Omega|} \int_\Gamma (\boldsymbol{a}_{S0} - \boldsymbol{a}_0)\, dl - \frac{\partial \boldsymbol{a}_0}{\partial \hat{t}} = 4\boldsymbol{a}_0 (\boldsymbol{a}_0 \cdot \boldsymbol{a}_1). \end{aligned} \tag{4.87}$$

To obtain the time and space dependence of $\boldsymbol{a}_0$ we require that (4.87) posses a solution for any $\boldsymbol{a}_1$. The solvability condition is that the left hand-side of (4.87) is orthogonal to $\boldsymbol{a}_\perp = \mathcal{W}\boldsymbol{a}_0$: this ensures that both the left and right hand-side of (4.87) are in the direction of $\boldsymbol{a}_0$. Applying the solvability condition and re-expressing the result on the

rapid time-scale we find

$$\begin{aligned}\boldsymbol{a}_\perp \cdot \frac{\partial \boldsymbol{a}_0}{\partial t} =& \xi_0^2 \boldsymbol{\nabla}_{\boldsymbol{x}} \cdot \mathcal{K} \boldsymbol{\nabla}_{\boldsymbol{x}} \boldsymbol{a}_0 \cdot \boldsymbol{a}_\perp \\ &+ \chi_a \left[ \boldsymbol{e}_M \left( 1 + 2\frac{|\Omega_{np}|}{|\Omega|} \right) + \boldsymbol{p} \right] \cdot \boldsymbol{a}_\perp + \frac{\beta}{|\Omega|} \int_\Gamma \boldsymbol{a}_{S0} dl \cdot \boldsymbol{a}_\perp, \qquad (4.88) \\ \boldsymbol{a}_0 \cdot \frac{\partial \boldsymbol{a}_0}{\partial t} =& 0.\end{aligned}$$

The first equation in (4.88) is the solvabillity condition, the second is obtained by differentiating (4.86). Together they define the dynamics of the nematic along the manifold of uniaxial $\mathcal{Q}$-tensors with scalar order parameter given by (4.86). Equation (4.79), (4.84) and (4.88) are the final macroscopic equations for a two-dimensional suspension of freely rotating metallic particles in a nematic liquid crystal in the absence of defects.

The torque the particle experiences due to the elastic free energy is captured by $\mathcal{B}_{ij}$ in equation (4.84) and represents a screening effect. This term tends to align a particle relative to the gradient in the $\mathcal{Q}$-tensor. This effect is illustrated in figure 4.2: particles align with their largest side orthogonal to the gradient, thereby screening the opposing boundary conditions. The surface interaction with the nematic is captured by $\boldsymbol{q}^{(\kappa)}$ in equation (4.84) and favours aligning the particle easy axis with the macroscopic director. The interaction with the electric field is determined by both the local field and the local alignment of the nematic. The term containing $P_{imlk}$ in equation (4.84) describes this coupling.

The terms in (4.88) offer a similar interpretation. In place of the screening effect we have an excluded volume effect given by $\mathcal{K}$. The surface interaction takes a slightly different form but still favours aligning the nematic with the local particle easy axis. The interaction with the electric field is split into two parts, the macroscopic field $\boldsymbol{e}_M$ and the polarization $\boldsymbol{p}$. The macroscopic field coupling is increased due to the volume occupied by metallic particles: the field is only non-zero outside the particles and the total change in potential due to an externally driven field remains constant regardless of the presence of metallic particles. The polarization captures the additional field due to induced surface charges on the dopant particles.

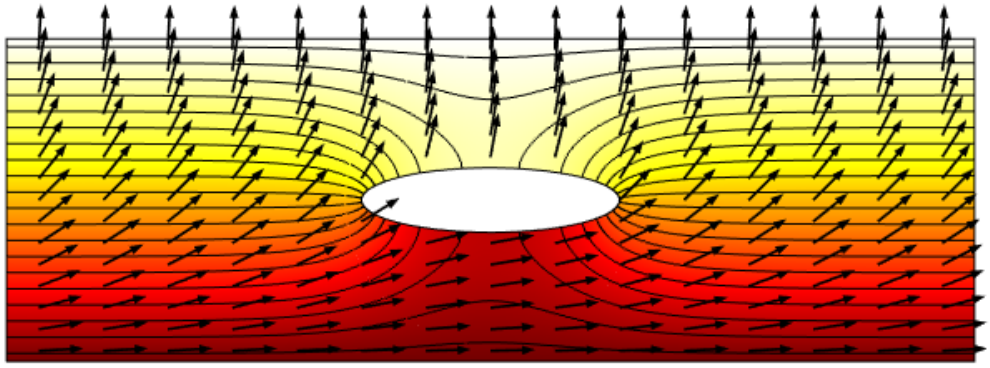

Figure 4.2: Illustration of the screening effect quantified by $\mathcal{B}_{ij}$. The director (black arrows) obeys hybrid anchoring conditions on the cells top and bottom surfaces and periodicity on the remaining sides. The anchoring energy is $\tilde{\mu} = 0$ and there is no externally applied field. The colour and contours indicate value of the director tilt angle $\theta$. With the particle horizontally aligned there is a reduced gradient in its vicinity.

## 4.5 Numerical validation

To check the accuracy of the macroscopic model derived in the previous section, we have compared its predictions with numerical simulations of realistic, but numerically manageable, colloidal suspensions. This required us to tackle two independent issues: the first was the integration of the cell problems, equations (4.53), (4.64) and (4.67), that define the parameters that appear in the macroscopic equations. Once these are known the integration of the macroscopic equations (4.79), (4.84) and (4.88) is relatively trivial. The second was the integration of the microscopic equations (4.33), (4.36), (4.38) and (4.39). We discuss these two issues in turn and then compare the results of the two sets of simulations.

To use the macroscopic equations (4.79), (4.84) and (4.88) we must first solve the set of cell problems (4.53), (4.64) and (4.67) to obtain the effective material parameters. This can be accomplished using the finite element package COMSOL multi physics. Figure 4.3 shows the solution of the cell problems for $\chi_k$ (4.64) and $R_k$ (4.67) for an asymmetric particle both implemented using the general form PDEs package. The solutions have the form of horizontal and vertically oriented dipole potentials which are by the particle shape, and, in the case of $R_k$ also distorted by the alignment of the nematic. We solve cell problems (4.64) and (4.67) for a range of particle orientations parameterized by the angle $\psi$. In the case of the cell problem (4.67) we also have to solve for a range of director orientations that we parameterize by an angle $\theta \in [0, \psi]$. Cubic spline interpolation is

used to compute the effective material parameters and torques for generic $\psi \in [0, 2\pi]$ and $\theta \in [0, \pi]$. To integrate the macroscopic equations we used a spectral collocation method [113] to discretize in space and the MATLAB variable order solver ode15s, which uses implicit numerical differentiation, to integrate in time.

The macroscopic equations (4.79), (4.84) and (4.88) can be integrated with relative ease numerically in arbitrarily large domains. However, for comparison with the microscopic equations (4.33), (4.36), (4.38) and (4.39) we have selected a one dimensional domain. The equivalent microscopic system is a stack of up to 64 unit cells, each containing one particle, that was solved using a finite element method. The number of particles is large enough to make the model realistic, but small enough that the integration of the microscopic equations takes no more than a few hours on a high spec PC (as opposed to a few seconds for the macroscopic equations).

The microscopic equations (4.33), (4.36), (4.38) and (4.39) were solved in a domain consisting of a $1 \times N$ array of unit cells each containing a single identical particle. Within each cell the particle is free to rotate and equations (4.33), (4.36), (4.38) and(4.39) are solved throughout the whole system. The long sides of the array are subject to periodic boundary conditions while the ends are subject to appropriate Dirichlet conditions. In all cases we have solved subject to zero pre-tilt and constant potential across the ends of the stack. Equation (4.33) is implemented as a general form PDE, the electrostatics package is used to compute the electric field, the particles motion is included as a set of global ODEs. To accommodate the particle motion the geometry is constructed as an assembly rather than a union. This allows each of the cell to be meshed independently as shown in figure 4.3 and removes the need to re-mesh to account for particle motion. The particle motion itself is implemented by the deformed geometry node.

A comparison between the homogenised equations and the large-scale finite element simulations is shown in figure 4.4 for a range of voltages $V = 2$ to $V = 5$. For each voltage 64 particles were used in the microscopic simulations. There is excellent agreement at all voltages.

Trends with increasing particle number for different anchoring regimes are shown in figure 4.5. The figure shows the convergence of the microscopic simulations for $N = 8, 16, 32$ (black, green and blue) to the solution of the homogenised equations (red). The broken black line represents the alignment of a pure liquid crystal. The top panels show the limiting behaviour under the constraint of constant anchoring energy density. In this case the anchoring energy density $\tilde{\mu}$ does not scale with $\eta$. In such a system the total surface free energy tends to infinity as the number of particles increases because the total surface area diverges. One consequence of this is that the particles are slaved to the

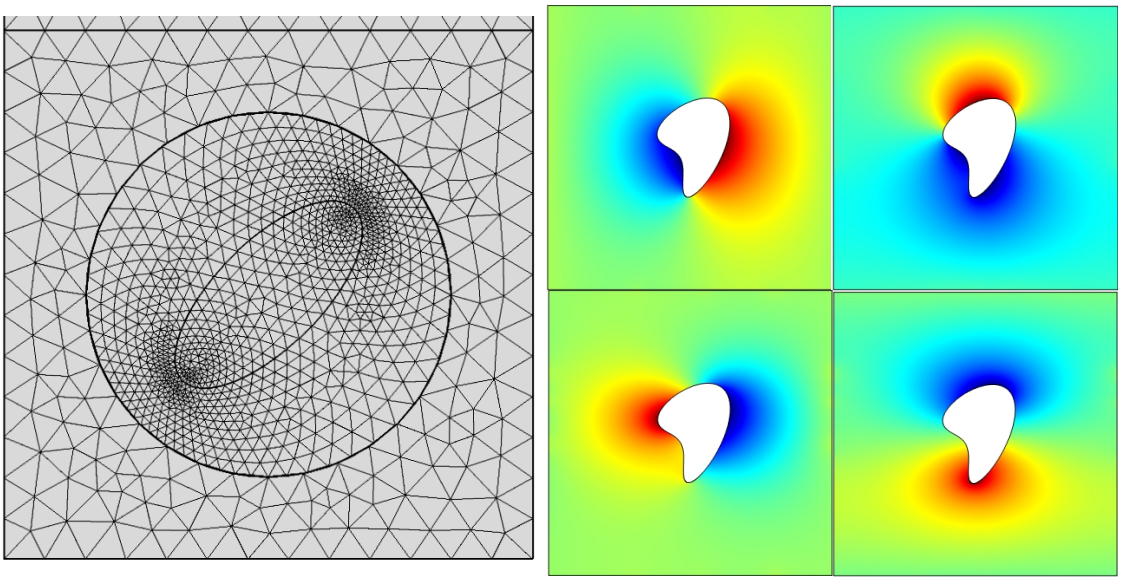

Figure 4.3: (Left) Example of the meshing scheme used when solving (4.33), (4.38), (4.36) and(4.39). The particle motion is achieved by the entire circular region rotating as a solid body motion. This removes the need to re-mesh while solving. (right)Solution of the cell problems (4.64) and (4.67) for asymmetric particles. Plots show from top right proceeding clockwise: $\chi_1$, $\chi_2$, $R_2$ and $R_1$. The solution to these problems is used to compute the material parameters needed to solve the homogenised equations.

nematic by the anchoring interaction as can be seen in the left-hand plot of figure 4.5. To obtain this limit from the homogenised equations the value of the dimensionless anchoring energy $\beta$ used in numerical simulations was increased by a factor of $\eta$ to undo the scaling postulated in section 4.4.1. This limit is distinct to that shown in the bottom panels in which the anchoring energy density $\tilde{\mu} = \mathcal{O}(\eta)$. In this regime as expected we find that the particle alignment is not dominated by the anchoring interaction and is additionally influenced by the applied field and screening effects, both of which favour $\psi = \pi/2$.

To further probe the validity of the theory we computed the alignment of asymmetric particles in a planar cell with and without an externally imposed field. The particles used are shown in figure 4.3. The results for two different applied voltages are shown in figure 4.6, both cases correspond to anchoring energies of $\tilde{\mu} = 10^{-6}$ Jm$^{-2}$. In this limit there is a non-uniform ground-state that differs from that predicted by our theory. However, the deviation from the ground state is small $\mathcal{O}(10^{-3})$ and from figure 4.6 we see that under an applied field the macroscopic and microscopic results agree well. For both the $V = 0$ and $V = 3$ case the final configuration of the particles exhibits a jump of $\pi$ radians. This is due to the incompatible symmetry of the particles and nematic, the location and potentially the number of jumps, is highly dependent on the initial conditions used. By using the

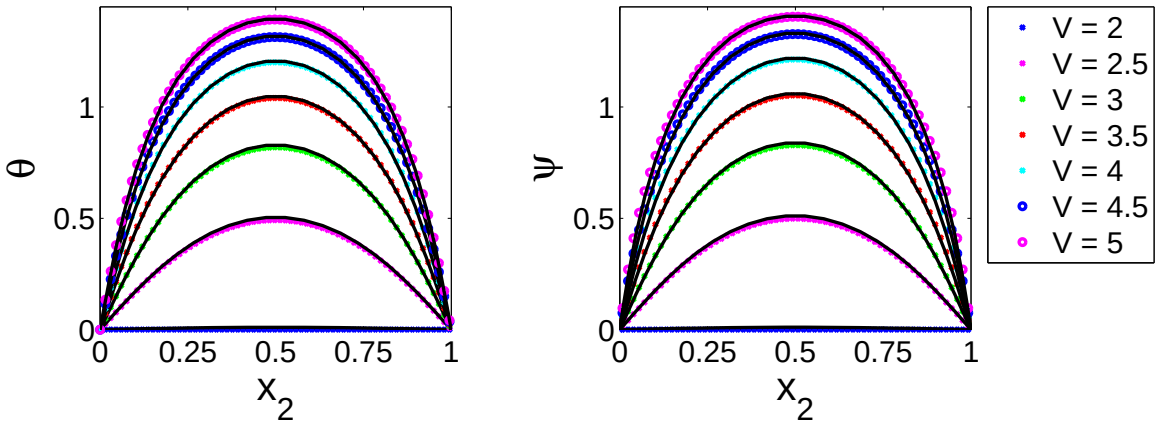


Figure 4.4: Solution of the homogenised/macroscopic equations for elliptic particles at $V = 2$ to $V = 5$ Volts in increments of 0.5 Volts for anchoring energy $\tilde{\mu} = 10^{-6}$ Jm$^{-2}$. Solid black lines are from the macroscopic equations, colored points and circles are solutions of the microscopic equations computed using Comsol with $N = 64$ particles.

same initial conditions for the microscopic and macroscopic systems we have found that the theory developed here is capable of capturing the apparent metastability shown in figure 4.6. It should be noted that optical experiments are sensitive to the alignment of the nematic and as a result the two alignments of $\theta$ shown in the bottom half of figure 4.6 would produce the same experimental results. It is anticipated that the deviations are due to the incompatible symmetry between the particles and the nematic, and, the postulate that $\tilde{\mu}$ scales linearly with $\eta$. If this constraint is dropped we obtain an additional set of cell problems which couples the elastic and surface interactions. This will be explored further in future work.

## 4.6 Discussion and conclusions

In this chapter we have studied the alignment of a nematic liquid crystal containing freely rotating metallic particles using the method of asymptotic homogenization. We have derived a set of macroscopic equations that include the shape and composition of the dopant particles directly. The model applies to particles of arbitrary shape. However, for asymmetric particles there is a small perturbation to the ground state of the nematic shown in figure 4.6 that will be explored further in future work. We have shown that the model developed here agrees well with large-scale numerical simulations. The main difference between the theory developed here and that developed in chapter 3 is the presence of particle dynamics. We find that the particles are aligned by elastic screening interactions with the LC, surface anchoring effects and a direct interaction with the electric field. As in

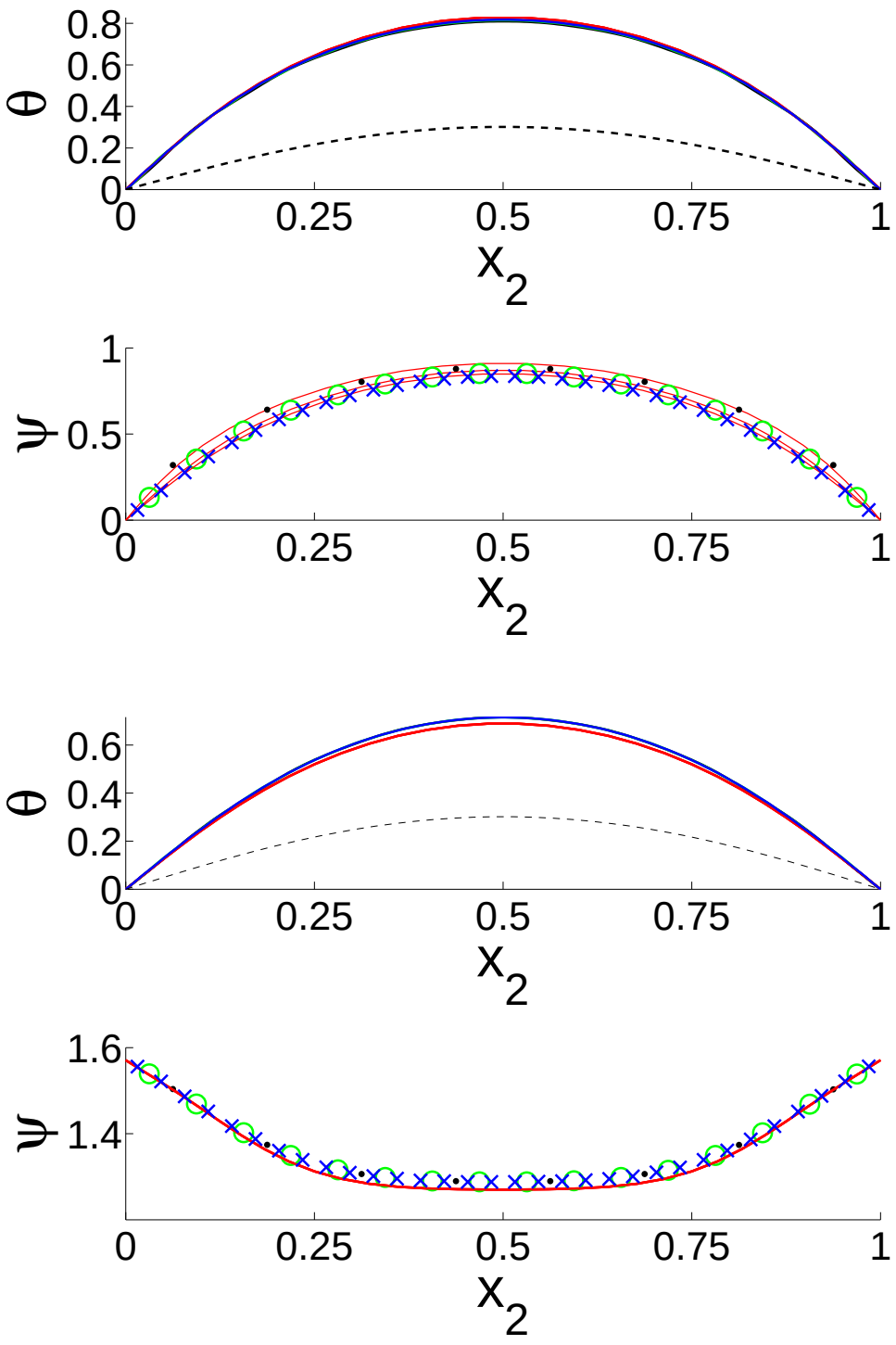


Figure 4.5: Comparison of the homogenised/macroscopic equation (red) to microscopic equations for $N = 8, 16, 32$ elliptic particles (black, green blue) at $V = 3$. Dimensional anchoring of $\tilde{\mu} = 10^{-6}$ Jm$^{-2}$ (top) and $\tilde{\mu} = \frac{10^{-6}}{N}$ Jm$^{-2}$ (bottom). The bottom set of plots shows the sequence of problems corresponding to finite total anchoring strength in the limit as $\eta \to 0$.

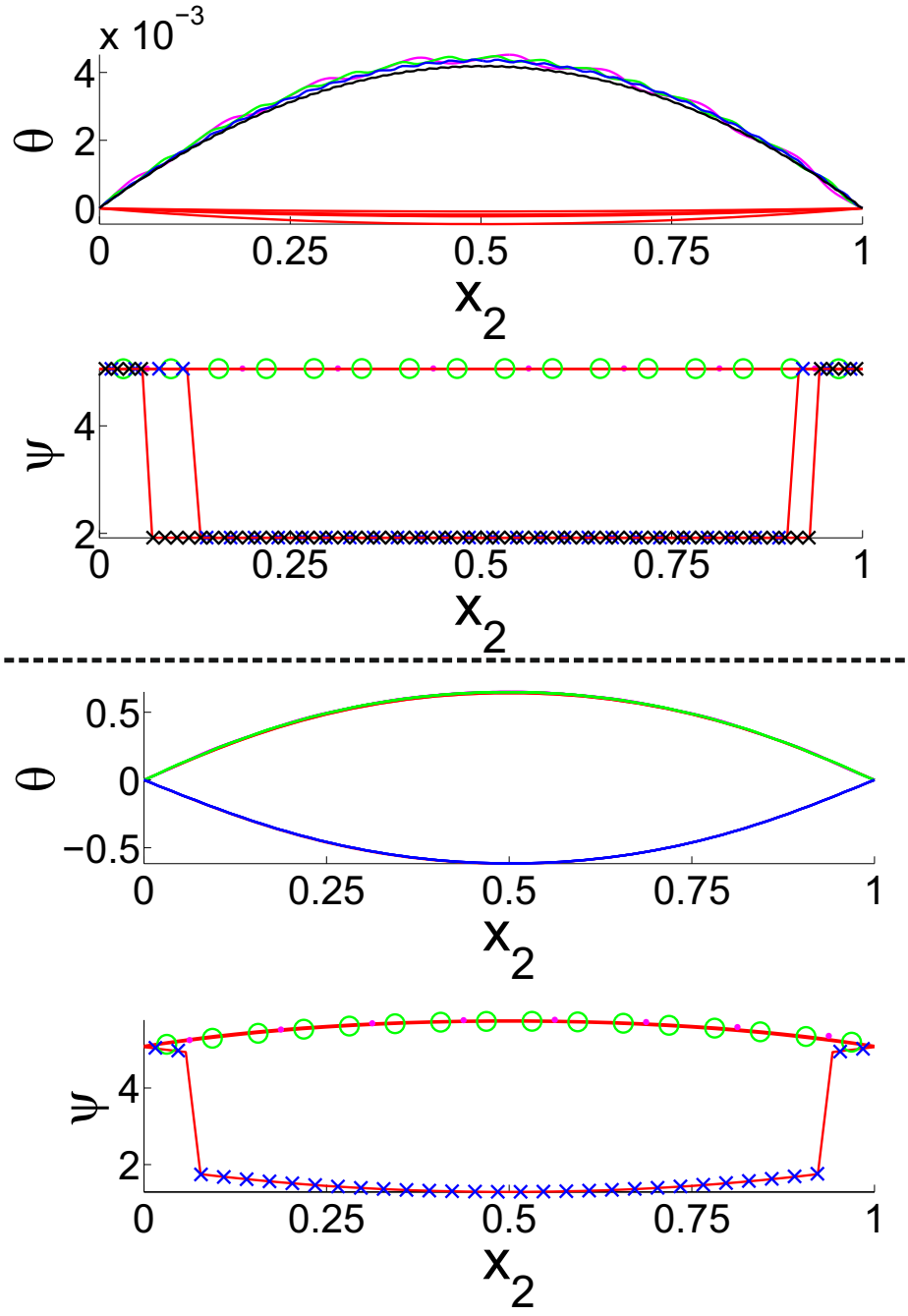


Figure 4.6: (Top) Comparison of the homogenised equation (red) to full equations for $N = 8, 16, 32, 64$ asymmetric particles (purple, green, blue and black) with $\tilde{\mu} = 10^{-6}$ Jm$^{-2}$ with an applied voltage of $V = 0$. (Bottom) As in top figure but for $N = 8, 16, 32$ asymmetric particles (purple, green and blue) with $V = 3$. The solutions to the homogenised equations are obscured by the solution to the microscopic equations, additionally the purple and green curves coincide nearly exactly. The uniform ground state is disturbed by the presence of the particles and this effect does not diminish as the particle number increases. The jump in $\psi$ shown in both cases is of magnitude $\pi$ radians.

chapter 3 the key advantage of using homogenization is the ability to link the macroscopic quantities such as susceptibilities, to the microstructure of the problem.

The main assumption we have made in deriving our model is that a separation of scales exists between the inter-particle spacing and the macroscopic size of the system. This is a valid assumption for low concentration colloids that are typically studied experimentally. One consequence of this assumption is that the alignment cannot vary significantly within the neighborhood of a particle. This precludes the study of defects. In addition we have assumed that the anchoring energy density is scaled with the concentration of particles in the system. This has some impact on the range of systems that may be modeled. Our model is valid for anchoring energies up to $\tilde{\mu} \approx 10^{-6}$ Jm$^{-2}$ for elliptic particles. We have observed that particles that do not obey $\boldsymbol{r} \to -\boldsymbol{r}$ symmetry show deviation from predicted values at higher anchoring energies $\tilde{\mu} \gtrsim 10^{-6}$ Jm$^{-2}$. These deviations are most apparent in the absence of an externally applied field. In this case the asymmetric particles force the nematic out of the uniform ground state with the magnitude of the distortion varying with anchoring energy. Preliminary work has shown that this results from higher order (non-linear) terms in the anchoring energy that do not appear in our model of weak anchoring.

Future work may explore extending this theory to the three dimensional case, incorporating fluid flow more completely and allowing for more general particle motion. Extending to three dimensions is expected to mostly increase the computational time needed to solve the cell problems and verify the model against large-scale numerical simulations. Incorporating the full dissipation function derived by Sonnet *et al.* [106] would couple the particle and nematic dynamics leading to a more complicated model. It may be possible to incorporate translating particles using the method employed by Richardson and Chapman [92]. This method involves making a change of coordinates that maps a seemingly non-periodic problem into a periodic problem in general curvilinear coordinates. Treating moving particles in this way may allow the particles to move away from the lattice configuration we are currently confined to.

In conclusions we have demonstrated that a theory of liquid crystal interaction with rotating colloidal particles can be derived based on a homogenisation formalism. The model we have obtained is accurate for a range of anchoring energies and particle species. In addition to the results presented here the model presented can be used to study the changes to the Frederiks that occur due to the metallic particles. We find a range of switching behaviours that depends delicately on the strength of the anchoring. Additionally it is possible to write the theory presented here in terms of homogenised free energies and dissipation functions.

# Chapter 5

# Conclusions

In this thesis we have considered two problems: the measurement of liquid crystal material parameters and deriving an effective medium theory for a liquid crystal colloid. In this chapter we summarise the results and suggest extensions to the work already pursued.

In chapter 2 we modelled the optical response of a liquid crystal cell to various applied fields. We found that the rotational viscosity could be obtained by using an amplitude modulated signal with an envelope oscillating at frequencies between 0.1 Hz to 10 Hz. Additional information about the combination of Leslie viscosities $\alpha_4 + \alpha_5$ can be extracted from high frequency high voltage measurements. In addition by combining multiple measurements of the CPI taken at different points on a planar cell we were able to resolve the variations in cell thickness and pre-tilt angle across a cell. These techniques were primarily developed to allow further investigation into the properties of existing liquid crystal cells manufactured in the Southampton physics department. These cells often contain exotic active polymer alignment layers which alter their behaviour when compared to traditional PI-PI cells. Alternatively these cells contain nematic liquid crystal doped with metallic, ferroelectric or dielectric particles. The wide area measurements are obviously applicable to testing cells with new alignment layers. The time response or viscosity measurements provide an alternative way to characterise doped systems. In these systems there are at least two time-scales for reorientation. This is known to have an impact on the transient response of the system [84]. By tuning the envelope frequency it may be possible to qualitative detect the changes to the dynamics. In order to obtain quantitative results from such an investigation an adequate theoretical description of the colloid would be required.

In chapters 3 and 4 we developed a model of a liquid crystal colloid. The model of static inclusions developed in chapter 3 was published in Physical Review E [11] and the model extended to include rotating particles has been submitted to the SIAM Journal on Applied Mathematics. Although we have not made any comparisons to experimental

results we have found excellent agreement with large-scale finite element simulations. The main advantages of these models over existing work is the ability to self consistently compute effective material parameters for a given dopant. As a by-product of using a $\mathcal{Q}$-tensor model we were also able to extract the slow time-scale dynamics using the DFQTA method of Daly *et al.* [34]. As a result our model can be solved in a fraction of the time needed to solve a finite element model of an equivalent system.

The project started in chapters 3 and 4 could be continued in a number of directions. Aside from considering dopants of different compositions, dielectric or ferroelectric for instance, the full details of the Sonnet and Virga [107] dynamic theory could be incorporated. A related problem is that of translating particles. Within a homogenisation framework one possible way that this could be realised is by allowing the periodic lattice to distort [93, 92, 21]. Alternatively the influence of elastic anisotropy, increased anchoring strength or the presence of defects could be investigated. The first two are relatively straightforward to implement. Elastic anisotropy would likely result in a larger number of cell problems to capture the differing energy costs of splay, twist and bend deformations. Preliminary results indicate that increasing the anchoring energy produces a model containing non-linear contributions in the anchoring energy, and, that the dynamics of the particles and nematic become tethered and we obtain a single evolution equation governing both. We have found that for highly symmetry particles, such as ellipses, these additional non-linear terms are identically zero.

It is not obvious if systems containing defects can be meaningfully treated using homogenisation. The main difficulty encountered when attempting to include defects is that the leading order alignment $\mathcal{Q}_0$ is not independent of the microscopic coordinate $\boldsymbol{y}$. This makes separating the scales difficult. This problem might be addressed by making a suitable ansatz separating the rapid $\boldsymbol{y}$ and slow $\boldsymbol{x}$ contribution to $\mathcal{Q}_0$ or else by diving the domain of the problem separating the rapid variations in the particle vicinity from the slow large scale variations over the macro-scale.

# Appendix A

## A.1 Matched asymptotics

In this section we derive the matched asymptotic expansions that approximate the director behaviour at high applied fields. The full nondimensional governing equations are

$$[1 - \gamma\cos(2\theta)]\frac{\partial^2\theta}{\partial\xi^2} + \gamma\Big(\frac{\partial\theta}{\partial\xi}\Big)^2\sin(2\theta) + \delta\psi^2\sin(2\theta)\cos^2(\omega\tau) - m(\theta)\frac{\partial v}{\partial\xi} = \frac{\partial\theta}{\partial\tau}, \quad \text{(A.1)}$$

$$\frac{\partial}{\partial\xi}\left[g(\theta)\frac{\partial v}{\partial\xi} + m(\theta)\frac{\partial\theta}{\partial\tau}\right] = N_r\frac{\partial v}{\partial\tau}, \quad \text{(A.2)}$$

$$m(\theta) = \mu_3\cos^2(\theta) - \mu_2\sin^2(\theta), \quad \text{(A.3)}$$

$$g(\theta) = \frac{1}{2}(\mu_4 + (\mu_5 - \mu_2)\sin^2(\theta) + (\mu_3 + \mu_6)\cos^2(\theta)) + \mu_1\sin^2(\theta)\cos^2(\theta), \quad \text{(A.4)}$$

$$\psi(\theta) = \frac{1}{1-\alpha\cos(2\theta)}\left(\int_{-1}^{+1}\frac{1}{1-\alpha\cos(2\theta)}dz\right)^{-1}, \quad \text{(A.5)}$$

The scalings used are given in table A.1 with $\mu_i = \alpha_i/\gamma_1$, $i = 1,..,6$ the nondimensional viscosities and $\omega$ the nondimensional frequency. As is discussed in [110] $N_r\frac{\partial v}{\partial\tau} \ll 1$ and so we set the inertial term in (A.2) to zero. This has the effect of slaving the velocity

| $\xi$ | $t$ | $u$ | $Re$ |
|---|---|---|---|
| $\frac{2z}{d} - 1$ | $\frac{\gamma_1 d^2}{2(K_1+K_3)}\tau$ | $\frac{K_1+K_3}{\gamma_1 d}v$ | $\frac{\rho U_0 d}{2\gamma_1}$ |
| $\gamma$ | $\delta$ | $N_r$ | $E_r$ |
| $\frac{K_3-K_1}{K_3+K_1}$ | $\frac{\epsilon_0\epsilon_a V^2}{K_1+K_3}$ | $\frac{Re}{Er}$ | $\frac{\gamma_1 U_0 d}{(K_1+K_3)}$ |

Table A.1: Nondimensionalisation

field to the liquid crystal director. The matched asymptotic approximation is arrived at by seeking a fourier series solution to (A.1)-(A.2) of the form,

$$\theta = \sum_{\forall n \in \mathbb{Z}} \theta_n \eta^{|n|} \exp(int), \tag{A.6}$$

and

$$v = \sum_{n \neq 0} \eta^{|n|-1} v_n \exp(int), \tag{A.7}$$

where $\eta = 1/\omega$ is a small parameter. Expanding in powers of $\eta$ and equating terms of equal order we can solve for the static part of the director alignment $\theta_0$ and the principal dynamic part (first harmonic) of the director and velocity field $\theta_1$ and $v_1$ respectively. At sufficiently high frequency only the first harmonic is needed to approximate the dynamics despite the non linear nature of the problem. An expression for the static alignment of the nematic is derived by Daly et al [32]. With a few changes in notation from [32] the final expression reads,

$$\begin{aligned}\theta_0 =& \tan^{-1}(\sinh(\sqrt{2}(\xi+1)/\sqrt{\nu} + \sinh^{-1}(\tan(\phi_{-1})))) \\ &+ \tan^{-1}(\sinh(\sqrt{2}(-\xi+1)/\sqrt{\nu} + \sinh^{-1}(\tan(\phi_{+1})))) \\ &- \frac{\pi}{2},\end{aligned} \tag{A.8}$$

where $\nu = \frac{4}{\delta}$ is a small parameter inversely proportional to the square of the voltage and $\phi_{-1}$ and $\phi_{+1}$ are the pre-tilt at $\xi = -1$ and $\xi = 1$ respectively. Equation (A.8) is obtained by making a matched asymptotic expansion and is valid at high voltage and assumes a uniform electric field. At large applied voltages only the nematic towards the sides of the cell is not aligned with the applied field. Therefore the approximation is valid throughout the bulk of the cell and yields good agreement with numerical solutions. Upon substituting equations (A.6) and (A.7) into (A.1) and (A.2), making the single elastic constant approximation and neglecting the fluid inertia we find the first harmonic of the director and velocity are governed by,

$$\eta \frac{d^2\theta_1}{d\xi^2} - 2i\theta_1 + \frac{\delta}{4}\psi(\theta_0)^2 \sin(2\theta_0) - m(\theta_0)\frac{dv_1}{d\xi} = 0, \tag{A.9}$$

$$\left[ g(\theta_0)\frac{dv_1}{d\xi} + 2i\, m(\theta_0)\theta_1 \right] = C, \tag{A.10}$$

where $C$ is an integration constant. This system is singular in the limit of $\eta \to 0$ and will have boundary layers at the edges of the cell. We now apply the method of matched

asymptotic expansions. The outer solution is governed by,

$$\begin{pmatrix} 2\,i & m(\theta_0) \\ 2\,i\,m(\theta_0) & g(\theta_0) \end{pmatrix} \begin{bmatrix} \theta_{1,out} \\ \frac{dv_{1,out}}{d\xi} \end{bmatrix} = \begin{bmatrix} \frac{\delta}{4}\psi(\theta_0)^2 \sin(2\theta_0) \\ C \end{bmatrix} \implies$$
$$\begin{bmatrix} \theta_{1,out} \\ \frac{dv_{1,out}}{d\xi} \end{bmatrix} = \frac{1}{g(\theta_0) - m^2(\theta_0)} \begin{pmatrix} -(1/2)i\,g(\theta_0) & (1/2)i\,m(\theta_0) \\ -m(\theta_0) & 1 \end{pmatrix} \begin{bmatrix} \frac{\delta}{4}\psi(\theta_0)^2 \sin(2\theta_0) \\ C \end{bmatrix} \tag{A.11}$$

Hence substituting equation (A.8) into (A.11) an expression for $\theta_{1,out}$ and $v_{1,out}$ can be found. The constant C can be found by integrating the expression for $dv_1/d\xi$ using the non-slip conditions. Together this gives the outer solution

$$C = \frac{1}{4} \frac{\int_{-1}^{+1} [\delta_0 \psi^2(\theta_0) m(\theta_0) \sin(2\theta_0)(g(\theta_0) - m^2(\theta_0))^{-1}]\, d\xi}{\int_{-1}^{+1} [(g(\theta_0) - m(\theta_0)^2)^{-1}]\, d\xi} \tag{A.12}$$

$$\theta_{1,out} = \frac{i}{2} \left[ \frac{m(\theta_0)C - (1/4)\delta_0 g(\theta_0)\psi^2(\theta_0)\sin(2\theta_0)}{g(\theta_0) - m^2(\theta_0)} \right] \tag{A.13}$$

$$v_{1,out} = \int_{-1}^{\xi} \frac{C - (1/4)\delta_0 m(\theta_0)\psi^2(\theta_0)\sin(2\theta_0)}{g(\theta_0) - m^2(\theta_0)} d\xi \tag{A.14}$$

Having found an outer solution we now turn to the boundary layers and seek an inner solution. Defining an inner variable $\xi = \pm 1 + \eta^\alpha x$, we also expand the harmonics of the velocity in powers of $\eta^\beta$.

$$v_{1,In} = v_{10,In} + \eta^\beta v_{11,In} + \mathcal{O}(\eta^{2\beta}) \tag{A.15}$$

Substituting we find an equation for the inner part of the first harmonic $\theta_{1,In}$

$$\begin{aligned} \frac{\eta}{\eta^{2\alpha}} \frac{d^2\theta_{1,In}}{dx^2} - 2i\theta_{1,In} + \frac{\delta}{4}\psi_{In}(\theta_{0,in})^2 \sin(2\theta_{0,In}) \\ - \frac{m_{In}(\theta_{0,In})}{\eta^\alpha} \frac{dv_{10,In}}{dx} - \frac{\eta^\beta m_{In}(\theta_{0,In})}{\eta^\alpha} \frac{dv_{11,In}}{dx} = 0, \end{aligned} \tag{A.16}$$

and

$$\frac{g(\theta_{0,In})}{\eta^\alpha} \frac{dv_{10,In}}{dx} + \frac{\eta^\beta g_{In}(\theta_{0,In})}{\eta^\alpha} \frac{dv_{11,In}}{dx} + 2i\, m_{In}(\theta_{0,In})\theta_{1,In} = c_{In}. \tag{A.17}$$

Balancing the dominant terms suggests that $\alpha = \beta = 1/2$, this way the highest order derivative balances the driving electric field and also enters at the same order as the first order correction to the flow. By equating terms of equal order in $\alpha$ from equations (A.16)

and (A.17) we have,

$$\frac{dv_{10,In}}{dx} = 0, \tag{A.18}$$

$$\frac{d^2\theta_{1,In}}{dx^2} - 2i\,\theta_{1,In} + \frac{\delta}{4}\psi_{In}(\theta_{0,In})^2\sin(2\theta_{0,In}) - m_{In}(\theta_{0,In})\frac{dv_{11,In}}{dx} = 0, \tag{A.19}$$

and

$$g(\theta_{0,In})\frac{dv_{11,In}}{dx} + 2i\,m_{In}(\theta_{0,In})\theta_{1,In} = c_i. \tag{A.20}$$

We see that this choice gives $v_{10,In} = 0$ as we impose non-slip boundary conditions, giving no correction to the velocity. There are corrections to the first harmonic of the director. In order to arrive at a simple analytical result rather than including the full boundary layer structure of $\theta_0$ we approximate $\theta_{0,In}$ by its value at the boundary, this will reduce the accuracy of the approximation. Denoting this as $\theta_{0,In}(\xi = -1)$ we have a system of equations for the inner expansion at $\xi = -1$.

$$\frac{d^2\theta_{1,In}}{dx^2} - 2i\,\theta_{1,In} + \frac{\delta}{4}\psi^2\sin(2\theta_0(\xi = -1)) - m\frac{dv_{11,In}}{dx} = 0, \tag{A.21}$$

and

$$g\frac{dv_{11,In}}{dx} + 2i\,m\theta_{1,In} = c_i. \tag{A.22}$$

where $\psi = \psi_{0,In}(\xi = -1)$ is the value of the potential at the boundary and $g = g(\theta_{0,In})), m = (\theta_{0,In})$.

Eliminating the velocity we obtain an equation for $\theta_{1,In}$ only,

$$\frac{d^2\theta_{1,In}}{dx^2} - 2i\,(1 - m^2/g)\theta_{1,In} + \frac{\delta_0}{4}\psi^2\sin(2\theta_{0,In}(\xi = -1)) - mc_i/g = 0 \tag{A.23}$$

This has solution,

$$\theta_{1In} = \theta_p(1 - \exp(-(1+i)(1 - (m^2/g))^{1/2}x)) \tag{A.24}$$

$$\theta_p = \frac{i}{2}\Big(\frac{mc_i - (1/4)\delta_0\psi^2\sin(2\theta_0(\xi = -1))g}{g - m^2}\Big) \tag{A.25}$$

The equation satisfied by the velocity is,

$$g\frac{dv_{11}}{dx} + 2i\,m\theta_p[1 - \exp(-(1+i)(1 - (m^2/g))^{1/2}x)] = c_i. \tag{A.26}$$

In order to match this to the outer solution for the velocity a higher order outer solution would be required. As there is good agreement between the velocity profile and the first order outer expansion and we already satisfy the boundary conditions on the velocity we

will not persue this.
A uniform approximation for $\theta_1$ can be obtained in the normal way, the end result is,

$$\theta_1 = \frac{1}{\omega}\left(\theta_{1,out} - \theta_p \exp\left(-(1+i)(1-(m^2/g))^{1/2}\frac{(\xi+1)}{\sqrt{\omega}}\right)\right.$$
$$\left. - \theta_p \exp\left((1+i)(1-(m^2/g))^{1/2}\frac{(\xi-1)}{\sqrt{\omega}}\right)\right), \tag{A.27}$$

Where matching with the outer solution has given $c_i = C$.

## A.2 Wide area measurements data

In this appendix we present all of the CPI traces used for the wide are measurement project. The elastic constants for the E7 cell are $K_1 = 11.8$ pN and $K_3 = 15.7$ pN and for TL205 $K_1 = 16.6$ pN, $K_3 = 23$ pN. The cell thickness and pre-tilt vary between measurement points, the CPI traces corresponding to each measurement point are shown in figure figures A.1 to A.6. The changes in the low voltage intensity indicate the variations in cell thickness and pre-tilt found in figures 2.16 and 2.17.

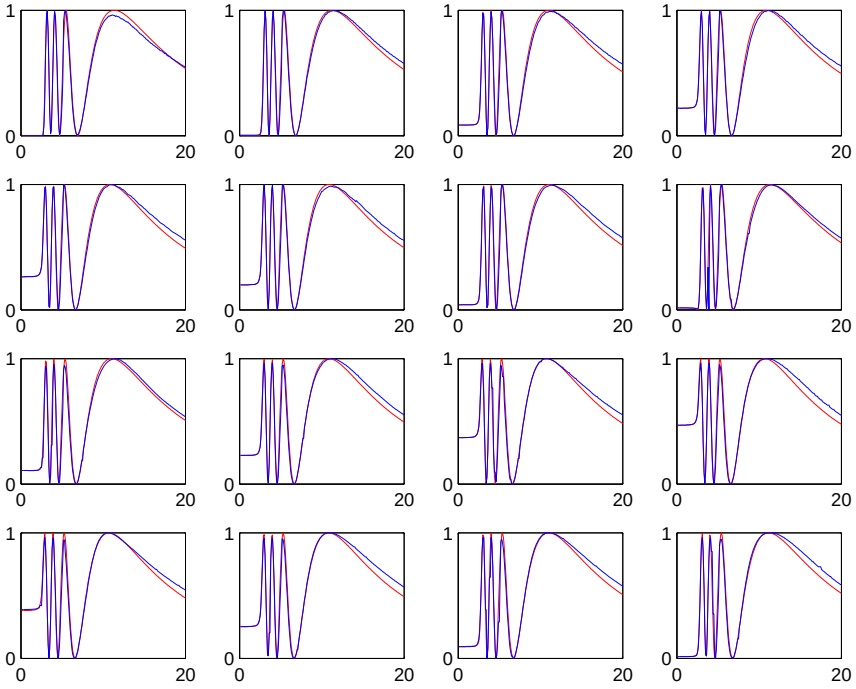


Figure A.1: Cross polarised intensity for E7 as a function of applied voltage measured at different point in the cell, traces 1 to 16.

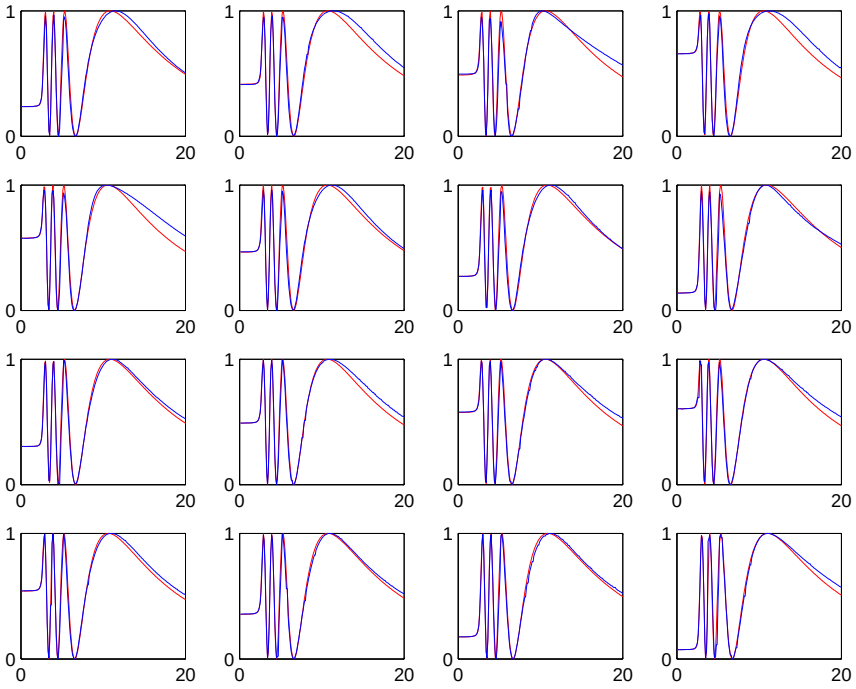


Figure A.2: As in A.1 traces 17 to 32.

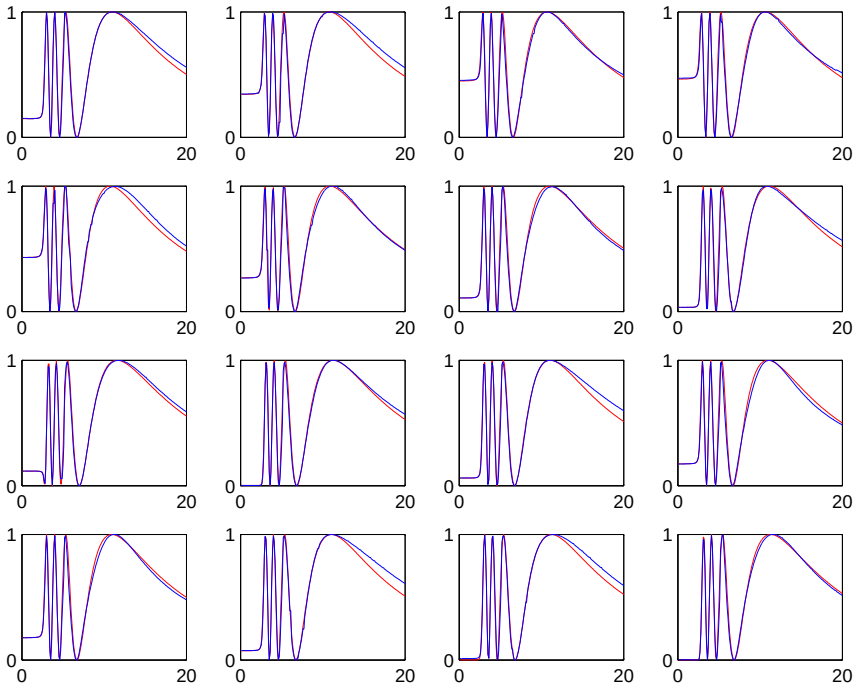

Figure A.3: As in A.1 traces 33 to 48.

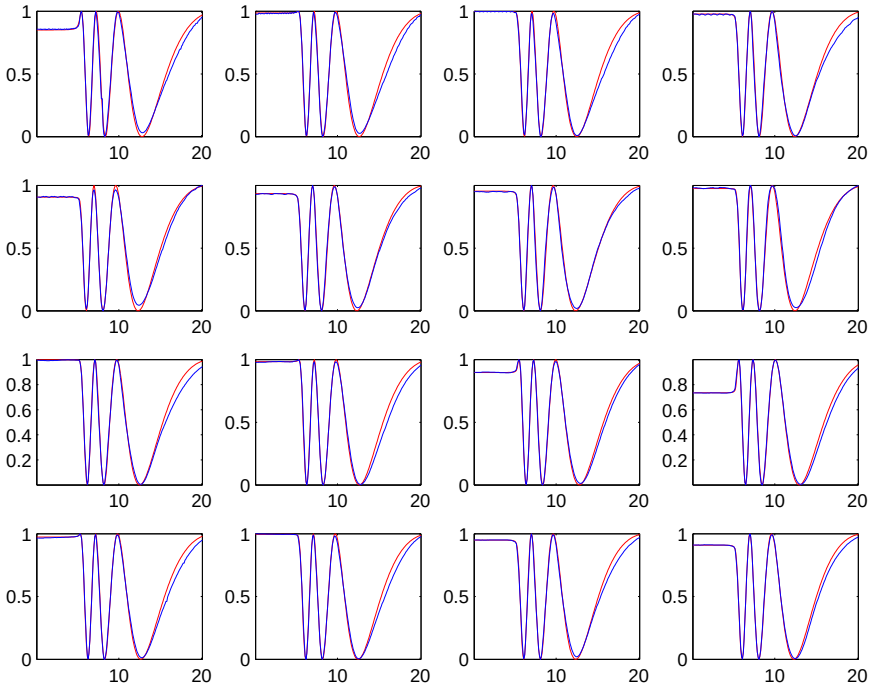

Figure A.4: As in A.1 but for TL205, traces 1 to 16.

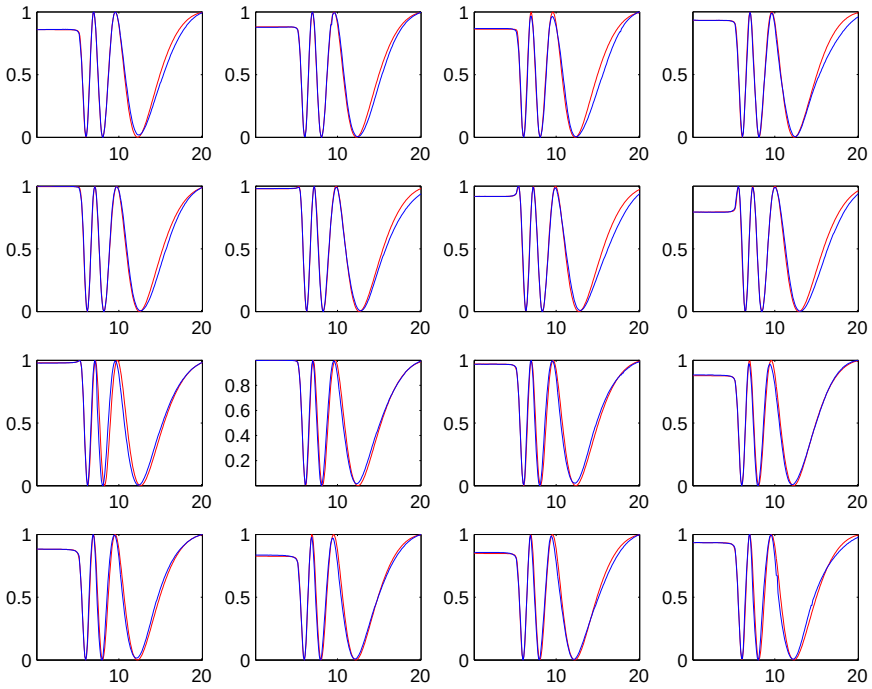

Figure A.5: As in A.4 traces 17 to 32.

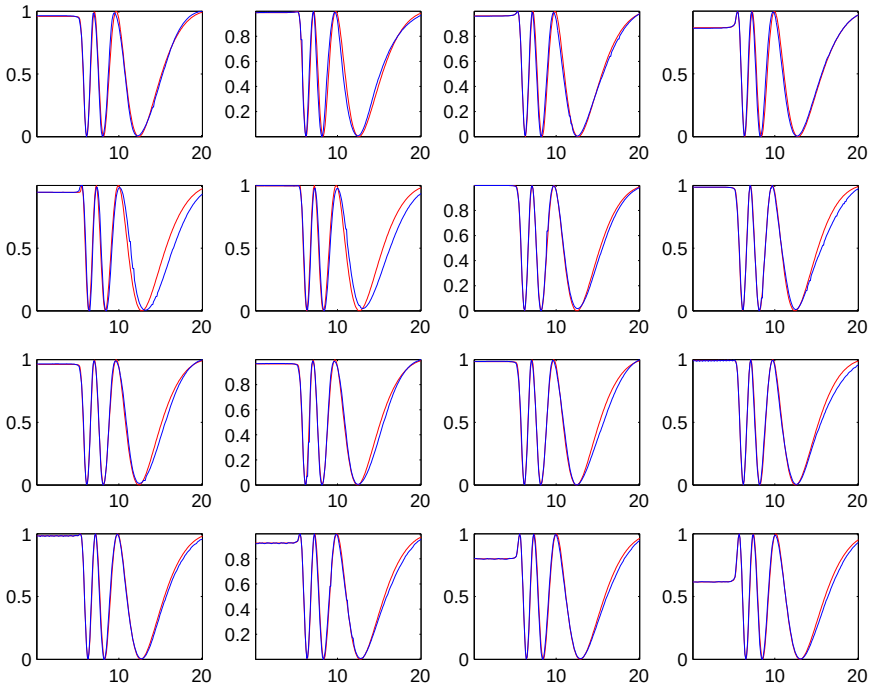

Figure A.6: As in A.4 traces 33 to 48.

## A.3 Reynolds Transport theorem

The two versions of the transport theorem that we need are [77]

$$\frac{d}{dt}\int_{\Omega} F dS = \int_{\Omega} \frac{\partial F}{\partial t} dS + \int_{\partial\Omega} F(\boldsymbol{v}_b \cdot \hat{\boldsymbol{n}}) dl, \tag{A.28}$$

and

$$\frac{d}{dt}\int_{\partial\Omega} F dl = \int_{\partial\Omega} \frac{\partial F}{\partial t} + (\boldsymbol{v}_b \cdot \hat{\boldsymbol{n}})\hat{\boldsymbol{n}} \cdot \boldsymbol{\nabla} F - \boldsymbol{v}_b \cdot \hat{\boldsymbol{n}} \kappa F dl, \tag{A.29}$$

where $\boldsymbol{v}_b$ is the velocity of the boundary and $\kappa$ is the principal curvature of the boundary. From these equations we see that only the normal component of the boundary velocity contributes to the derivatives.

# Bibliography


[1] G. Allaire. Homogenization and two-scale convergence. *SIAM Journal on Mathematical Analysis*, 23(6):1482–1518, 1992.

[2] G. Allaire and A. Piatnitski. Homogenization of the schrödinger equation and effective mass theorems. *Communications in Mathematical Physics*, 258(1):1–22, 2005.

[3] T. Araki and H. Tanaka. Colloidal aggregation in a nematic liquid crystal: Topological arrest of particles by a single-stroke disclination line. *Phys. Rev. Lett.*, 97:127801, Sep 2006.

[4] I. Babuka. Solution of interface problems by homogenization. i. *SIAM Journal on Mathematical Analysis*, 7(5):603–634, 1976.

[5] I. Babuka. Solution of interface problems by homogenization. ii. *SIAM Journal on Mathematical Analysis*, 7(5):635–645, 1976.

[6] I. Babuka. Solution of interface problems by homogenization. iii. *SIAM Journal on Mathematical Analysis*, 8(6):923–937, 1977.

[7] E. Bahat-Treidel, B. Apter, and U. Efron. Simple method for controlled variation of liquid crystal cell thickness. *Optical Engineering*, 43(12):3021–3025, 2004.

[8] W. W. Beens and W. H. de Jeu. Flow-measurements of viscosity coefficients of two nematic liquid crystalline azoxybenzenes. *Le Journal de Physique*, 44(2):129–136, February 1983.

[9] V. V. Belyaev. Physical methods for measuring the viscosity coefficients of nematic liquid crystals. *Physics - Uspekhi*, 44:255–284, 2001.

[10] M. Bender, P. Holstein, and D. Geschke. Electrically induced dynamic processes in nematic liquid crystals: 1h nuclear magnetic resonance investigations. *The Journal of Chemical Physics*, 113(6):2430–2439, 2000.

[11] T. P. Bennett, G. D'Alessandro, and K. R. Daly. Multiscale models of colloidal dispersion of particles in nematic liquid crystals. *Phys. Rev. E*, 90:062505, Dec 2014.

[12] T. P. Bennett, G. D'Alessandro, and K. R. Daly. Multiscale models of metallic particles in nematic liquid crystals. Submitted to SIAM Journal on Applied Mathematics, July 2016.

[13] T. P. Bennett, Y. Murugesan, K. R. Daly, G. De Matteis, and G. D'Alessandro. Fast algorithms for liquid crystal modelling. In I. C. Khoo, editor, *Liquid Crystals XVIII*, volume 9182 of *Proc. SPIE*, pages 918208–918208–15, 2014.

[14] L. Berlyand, D. Cioranescu, and D. Golovaty. Homogenization of a Ginzburg-Landau model for a nematic liquid crystal with inclusions. *J Math Pure Appl*, 84(1):97 – 136, 2005.

[15] L. Berlyand and E. Khruslov. Ginzburg–Landau model of a liquid crystal with random inclusions. *J Math Phys*, 46(9):99–136, 2005.

[16] D. W. Berreman. Optics in stratified and anisotropic media: $4 \times 4$-matrix formulation. *J. Opt. Soc. Am.*, 62(4):502–510, Apr 1972.

[17] D. W. Berreman and A. Sussman. Net lateral flow during a twist-cell cycle. *Journal of Applied Physics*, 50(12):8016–8018, 1979.

[18] M. Born and E. Wolf. *Principles of Optics*. Cambridge Univ. Press, Cambridge, England, 6 edition, 1997.

[19] F. Brochard and P. G. de Gennes. Theory of magnetic suspensions in liquid crystals. *J. Phys, France*, 31(7):691–708, July 1970.

[20] F. Brochard, P. Pieranski, and E. Guyon. Dynamics of the orientation of a nematic-liquid-crystal film in a variable magnetic field. *Phys. Rev. Lett.*, 28:1681–1683, Jun 1972.

[21] M. Bruna and S. J. Chapman. Diffusion in spatially varying porous media. *SIAM Journal on Applied Mathematics*, 75(4):1648–1674, 2015.

[22] A. Buka and W. de Jeu. Diamagnetism and orientational order of nematic liquid crystals. *J. Phys. France*, 43(2):361–367, 1982.

[23] S. V. Burylov and Y. L. Raikher. Macroscopic Properties of Ferronematics Caused by Orientational Interactions on the Particle Surfaces. I. Extended Continuum Model. *Mol. Cryst. Liq. Cryst.*, 258:107–122, 1995.

[24] S. V. Burylov and Y. L. Raikher. Macroscopic Properties of Ferronematics Caused by Orientational Interactions on the Particle Surfaces. II. Behavior of Real Ferronematics in External Fields. *Mol. Cryst. Liq. Cryst.*, 258:123–141, 1995.

[25] M. C. Calderer, A. DeSimone, D. Golovaty, and A. Panchenko. An effective model for nematic liquid crystal composites with ferromagnetic inclusions. *SIAM Journal on Applied Mathematics*, 74(2):237–262, 2014.

[26] F. Castles, S. C. Green, D. J. Gardiner, S. M. Morris, and H. J. Coles. Flexoelectric coefficient measurements in the nematic liquid crystal phase of 5cb. *AIP Advances*, 2(2), 2012.

[27] S. Chandrasekhar. *Liquid Crystals*. Cambridge University Press, 1992.

[28] Y. F. Chen and Y. P. Lan. Transverse pattern formation of optical vortices in a microchip laser with a large Fresnel number. *Phys. Rev. A*, 65(1):013802, 2002.

[29] D. Cioranescu, A. Damlamian, and G. Griso. The periodic unfolding method in homogenization. *SIAM Journal on Mathematical Analysis*, 40(4):1585–1620, 2008.

[30] G. Cook, V. Y. Reshetnyak, R. F. Ziolo, S. A. Basun, P. P. Banerjee, and D. R. Evans. Asymmetric freedericksz transitions from symmetric liquid crystal cells doped with harvested ferroelectric nanoparticles. *Opt. Express*, 18(16):17339–17345, Aug 2010.

[31] K. R. Daly. *Light-matter interaction in liquid crystal cells*. PhD thesis, School of Mathematics, University of Southampton, School of Mathematics, University of Southampton, January 2011.

[32] K. R. Daly, S. Abbott, G. D'Alessandro, D. C. Smith, and M. Kaczmarek. Theory of hybrid photorefractive plasmonic liquid crystal cells. *J. Opt. Soc. Am. B*, 28(8):1874–1881, Aug 2011.

[33] K. R. Daly, S. B. Abbott, D. C. Smith, and G. D'Alessandro. Optimization of plasmon-plasmon coupling in photorefractive layered media. *J. Opt. Soc. Am. B*, 30(8):2090–2099, Aug 2013.

[34] K. R. Daly, G. D'Alessandro, and M. Kaczmarek. An Efficient $\mathcal{Q}$-Tensor-Based Algorithm for Liquid Crystal Alignment away from Defects. *SIAM J. Appl. Math.*, 70(8):2844–2860, 2010.

[35] P. G. de Gennes. Physique des solides - types de singularités permises dans une phase ordonnée. *C. R. Acad. Sc. Paris B*, 275:319–320, 1972.

[36] P. G. de Gennes. *The Physics of Liquid Crystals*. Clarendon press Oxford, 1974.

[37] W. H. de Jeu. *Physical properties of liquid crytalline materials*. Gordon and Breach new york, New York, 1980.

[38] J. L. Ericksen. Conservation laws for liquid crystals. *Transactions of The Society of Rheology (1957-1977)*, 5(1):23–34, 1961.

[39] J. B. Fournier and P. Galatola. Modeling planar degenerate wetting and anchoring in nematic liquid crystals. *EPL (Europhysics Letters)*, 72:403–409, nov 2005.

[40] F. C. Frank. On the theory of liquid crystals. *Discuss. Faraday Soc.*, 25:19–28, 1958.

[41] H. Goldstein. *Classical mechanics*. Pearson Education, 3rd edition, 2002.

[42] M. V. Gorkunov and M. A. Osipov. Mean-field theory of a nematic liquid crystal doped with anisotropic nanoparticles. *Soft Matter*, 7:4348–4356, 2011.

[43] M. Grinfeld, M. Langer, and N. Mottram. Nematic viscosity estimation using director kickback dynamics. *Liquid Crystals*, 38(8):981–987, 2011.

[44] W. Haiss, N. T. K. Thanh, J. Aveyard, and D. G. Fernig. Determination of size and concentration of gold nanoparticles from uv-vis spectra. *Anal. Chem.*, 79(11):4215–4221, 2007. PMID: 17458937.

[45] I. Haller. Elastic constants of the nematic liquid crystalline phase of p-methoxybenzylidene-p-n-butylaniline (MBBA). *The Journal of Chemical Physics*, 57(4):1400–1405, 1972.

[46] I. Haller. Thermodynamic and static properties of liquid crystals. *Progress in Solid State Chemistry*, 10:103–12, 1975 1975.

[47] U. Hornung. *Homogenization and Porous Media*. Springer, 1996.

[48] O. Iliev, A. Mikelic, and P. Popov. On upscaling certain flows in deformable porous media. *Multiscale Model Sim*, 7(1):93–123, 2008.

[49] H. Imura and K. Okano. Temperature dependence of the viscosity coefficients of liquid crystals. *Japanese Journal of Applied Physics*, 11(10):1440–1445, 1972.

[50] W. H. D. Jeu, W. A. P. Claassen, and A. M. J. Spruijt. The determination of the elastic constants of nematic liquid crystals. *Molecular Crystals and Liquid Crystals*, 37(1):269–280, 1976.

[51] J. Katriel, G. F. Kventsel, G. R. Luckhurst, and T. J. Sluckin. Free Energies in the Landau and Molecular Field Approaches. *Liq. Cryst.*, 1(4):337–355, 1986.

[52] J. Kelly, S. Jamal, and M. Cui. Simulation of the dynamics of twisted nematic devices including flow. *J. Appl. Phys.*, 86(8):4091, October 1999.

[53] Kiry, F. and Martinoty, P. Ultrasonic investigation of anisotropic viscosities in a nematic liquid-crystal. *J. Phys. France*, 38(2):153–157, 1977.

[54] O. V. Kuksenok, R. W. Ruhwandl, S. V. Shiyanovskii, and E. M. Terentjev. Director structure around a colloid particle suspended in a nematic liquid crystal. *Phys. Rev. E*, 54(5):5198–5203, Nov 1996.

[55] C. P. Lapointe, T. G. Mason, and I. I. Smalyukh. Shape-controlled colloidal interactions in nematic liquid crystals. *Science*, 326(5956):1083–1086, 2009.

[56] C. K. Lee and C. C. Mei. Re-examination of the equations of poroelasticity. *International Journal of Engineering Science*, 35(4):329 – 352, 1997.

[57] F. M. Leslie. Some constitutive equations for liquid crystals. *Archive for Rational Mechanics and Analysis*, 28(4):265–283, 1968.

[58] A. Lien. Extended Jones matrix representation for the twisted nematic liquid crystal display at oblique incidence. *Applied Physics Letters*, 57(26):2767–2769, 1990.

[59] L. Longa, D. Monselesan, and H. Trebin. An extension of the Landau-Ginzburg-de Gennes theory for liquid crystals. *Liq. Cryst.*, 2(6):769–796, 1987.

[60] L. Longa and H. Trebin. Integrity basis approach to the elastic free energy functional of liquid crystals - I. Classification of elastic modes. *Liq. Cryst.*, 5(2):617–622, 1989.

[61] L. M. Lopatina and J. V. Selinger. Theory of Ferroelectric Nanoparticles in Nematic Liquid Crystals. *Phys. Rev. Lett.*, 102:197802, May 2009.

[62] L. M. Lopatina and J. V. Selinger. Maier-Saupe-type theory of ferroelectric nanoparticles in nematic liquid crystals. *Phys. Rev. E*, 84:041703, Oct 2011.

[63] Luc Tartar. *The General Theory of Homogenization: A Personalized Introduction*. Springer Berlin Heidelberg, 2010.

[64] A. Majumdar. Equilibrium order parameters of nematic liquid crystals in the Landau-de Gennes theory. *Eur. J. Appl Math.*, 21:181–203, 2010.

[65] A. Martinez, M. Ravnik, B. Lucero, R. Visvanathan, S. Žumer, and I. I. Smalyukh. Mutually tangled colloidal knots and induced defect loops in nematic fields. *Nat Mater*, 13(3):258–263, 2014.

[66] D. Meyerhofer. Elastic and dielectric constants in mixtures of nematic liquid crystals. *Journal of Applied Physics*, 46(12):5084–5087, 1975.

[67] M. Miesowicz. The three coefficients of viscosity of anisotropic liquids. *Nature*, 158:27, 1946.

[68] M. Miesowicz. Liquid crystals in my memories and now-the role of anisotropic viscosity in liquid crystals research. *Molecular Crystals and Liquid Crystals*, 97:1–11, 1983.

[69] T. Miyama, J. Thisayukta, H. Shiraki, Y. Sakai, Y. Shiraishi, N. Toshima, and S. Kobayashi. Fast Switching of Frequency Modulation Twisted Nematic Liquid Crystal Display Fabricated by Doping Nanoparticles and Its Mechanism. *Jpn. J. Appl. Phys.*, 43(5A):2580–2584, 2004.

[70] N. J. Mottram, J. T. Pinto, and G. McKay. Decoupling of the Ericksen-Leslie equations. *Liquid Crystals*, 40(6):787–798, 2013.

[71] I. Muševič, M. Škarabot, U. Tkalec, M. Ravnik, and S. Žumer. Two-dimensional nematic colloidal crystals self-assembled by topological defects. *Science*, 313(5789):954–958, 2006.

[72] G. Nguetseng. A general convergence result for a functional related to the theory of homogenization. *SIAM Journal on Mathematical Analysis*, 20(3):608–623, 1989.

[73] G. Nguetseng. Homogenization in perforated domains beyond the periodic setting. *Journal of Mathematical Analysis and Applications*, 289(2):608 – 628, 2004.

[74] M. Nobili and G. Durand. Disorientation-induced disordering at a nematic-liquid-crystal-solid interface. *Phys. Rev. A*, 46:R6174–R6177, Nov 1992.

[75] O. Oleinik, A. Shamaev, and G. Yosifian. *Mathematical Problems in Elasticity and Homogenization*. Studies in Mathematics and its Applications. Elsevier Science, 1992.

[76] C. W. Oseen. The theory of liquid crystals. *Trans. Faraday Soc.*, 29:883–899, 1933.

[77] S. Paolucci. *Continuum Mechanics and Thermodynamics of Matter*. Cambridge University Press, 2016.

[78] O. Parodi. Stress tensor for a nematic liquid crystal. *J. de Physique*, 31:581–584, 1970.

[79] G. Pavliotis and A. Stuart. *Multiscale methods: averaging and homogenization*. Springer-Verlag, New York, 1 edition, 2007.

[80] P. Pieranski, F. Brochard, and E. Guyon. Static and dynamic behavior of a nematic liquid crystal in a magnetic field. Part II : Dynamics. *Journal de Physique*, 34(1):35–48, 1973.

[81] N. Podoliak. *Magneto-optic effects in colloids of ferromagnetic nanoparticles in nematic liquid crystals*. PhD thesis, University of Ssouthampton, Faculty of Physical and Applied Sciences, Physics and Astronomy, 2012.

[82] N. Podoliak, D. Bartczak, O. Buchnev, A. G. Kanaras, and M. Kaczmarek. High optical nonlinearity of nematic liquid crystals doped with gold nanoparticles. *J. Phys. Chem. C*, 116(23):12934–12939, 2012.

[83] N. Podoliak, O. Buchnev, O. Buluy, G. D'Alessandro, M. Kaczmarek, Y. Reznikov, and T. J. Sluckin. Macroscopic optical effects in low concentration ferronematics. *Soft Matter*, 7(10):4742–4749, 2011.

[84] N. Podoliak, O. Buchnev, M. Herrington, E. Mavrona, M. Kaczmarek, A. G. Kanaras, E. Stratakis, J.-F. Blach, J.-F. Henninot, and M. Warenghem. Elastic constants, viscosity and response time in nematic liquid crystals doped with ferroelectric nanoparticles. *RSC Adv.*, 4:46068–46074, 2014.

[85] S. K. Prasad, K. L. Sandhya, G. G. Nair, U. S. Hiremath, C. V. Yelamaggad, and S. Sampath. Electrical conductivity and dielectric constant measurements of liquid crystal-gold nanoparticle composites. *Liq. Cryst.*, 33(10):1121–1125, 2006.

[86] R. Pratibha, K. Park, I. I. Smalyukh, and W. Park. Tunable optical metamaterial based on liquid crystal-gold nanosphere composite. *Opt. Express*, 17(22):19459–19469, Oct 2009.

[87] J. Prost and H. Gasparoux. Determination of twist viscosity coefficient in the nematic mesophases. *Physics Letters A*, 36:245–246, Aug. 1971.

[88] H. Qi, B. Kinkead, and T. Hegmann. Unprecedented Dual Alignment Mode and Freedericksz Transition in Planar Nematic Liquid Crystal Cells Doped with Gold Nanoclusters. *Adv. Funct. Mater.*, 18(2):212–221, 2008.

[89] T. Qian and P. Sheng. Generalized hydrodynamic equations for nematic liquid crystals. *Phys. Rev. E*, 58(6):7475–7485, 1998.

[90] A. Rapini and M. Papoular. Distorsion d'une lamelle nématique sous champ magntique conditions d'ancrage aux parois. *J. Phys. Colloques*, 30(4):54–56, 1969.

[91] V. Y. Reshetnyak, S. M. Shelestiuk, and T. J. Sluckin. Fredericksz transition threshold in nematic liquid crystals filled with ferroelectric nano-particles. *Mol. Cryst. Liq. Cryst.*, 454(1):201/[603]–206/[608], 2006.

[92] G. Richardson and S. J. Chapman. Derivation of the bidomain equations for a beating heart with a general microstructure. *SIAM Journal on Applied Mathematics*, 71(3):657–675, 2011.

[93] G. Richardson, G. Denuault, and C. P. Please. Multiscale modelling and analysis of lithium-ion battery charge and discharge. *Journal of Engineering Mathematics*, 72(1):41–72, 2011.

[94] R. W. Ruhwandl and E. M. Terentjev. Long-range forces and aggregation of colloid particles in a nematic liquid crystal. *Phys. Rev. E*, 55:2958–2961, Mar 1997.

[95] R. W. Ruhwandl and E. M. Terentjev. Monte Carlo simulation of topological defects in the nematic liquid crystal matrix around a spherical colloid particle. *Phys. Rev. E*, 56(5):5561–5565, Nov 1997.

[96] A. Sawada, K. Tarumi, and S. Naemura. Novel Characterization Method of Ions in Liquid Crystal Materials by Complex Dielectric Constant Measurements. *Jap. J. Appl. Phys.*, 38(Part 1, No. 3A):1423–1427, 1999.

[97] N. Schopohl and T. J. Sluckin. Defect core structure in nematic liquid crystals. *Phys. Rev. Lett.*, 59(22):2582–2585, 1987.

[98] R. H. Self. *Mathematical models of some nematic and cholesteric liquid crystal devices*. PhD thesis, School of Mathematics, University of Southampton, November 1998.

[99] A. K. Sen and D. E. Sullivan. Landau ˘ de gennes theory of wetting and orientational transitions at a nematic-liquid ˘ substrate interface. *Phys. Rev. A*, 35:1391–1403, Feb 1987.

[100] B. Senyuk, J. S. Evans, P. J. Ackerman, T. Lee, P. Manna, L. Vigderman, E. R. Zubarev, J. v. d. Lagemaat, and I. I. Smalyukh. Shape-dependent oriented trapping and scaffolding of plasmonic nanoparticles by topological defects for self-assembly of colloidal dimers in liquid crystals. *Nano Lett.*, 12(2):955–963, 2012.

[101] B. Senyuk, Q. Liu, S. He, R. D. Kamien, R. B. Kusner, T. C. Lubensky, and I. I. Smalyukh. Topological colloids. *Nature*, 493(7431):200–205, 2013. 10.1038/nature11710.

[102] S. Sergio. Convergence in energy for elliptic operat ors. *Numerical solution of partial differential equations. Proceedings of the 3rd Symposium on the Numerical Solution of Partial Differential Equations.*, pages 469–498, 1976.

[103] S. M. Shelestiuk, V. Y. Reshetnyak, and T. J. Sluckin. Frederiks transition in ferroelectric liquid-crystal nanosuspensions. *Phys. Rev. E*, 83(4):041705, Apr 2011.

[104] Q. Shen and M. C. Calderer. A relaxed model and its homogenization for nematic liquid crystals in composite materials. *Math Method Appl Sci*, 27(10):1125–1143, 2004.

[105] A. Sonnet, A. Kilian, and S. Hess. Alignement tensor versus director: Description of defects in nematic liquid crystals. *Phys. Rev. E*, 52(1):718–722, 1995.

[106] A. Sonnet, P. Maffettone, and E. Virga. Continuum theory for nematic liquid crystals with tensorial order. *J. Non-Newtonian Fluid Mech.*, 119:51 – 59, 2004.

[107] A. M. Sonnet and E. G. Virga. *Dissipative ordered fluids: Theories for liquid crystals.* Springer, New York, 1st edition, 2012.

[108] H. Stark. Director field configurations around a spherical particle in a nematic liquid crystal. *Eur. Phys. J. B*, 10(2):311–321, 1999.

[109] H. Stark. Physics of colloidal dispersions in nematic liquid crystals. *Physics Reports*, 351:387–474, 2001.

[110] I. W. Stewart. *The static and dynamic continuum theory of liquid crystals: a mathematical introduction.* Taylor & Francis, 2004.

[111] K. Tarumi, U. Kinkenzeller, and B. Schuler. Dynamic behaviour of twisted nematic liquid crystals. *Jpn. J. Appl. Phys*, 31:2829–2836, Sept 1992.

[112] S. A. Thomas. *Likelihood Methods in Statistics*. Oxford University Press, 2000.

[113] L. N. Trefethen. *Spectral Methods in Matlab*. SIAM, Philadelphia, 2000.

[114] S. Čopar and S. Žumer. Nematic Braids: Topological Invariants and Rewiring of Disclinations. *Phys. Rev. Lett.*, 106:177801, Apr 2011.

[115] H. Wang, T. X. Wu, S. Gauza, J. R. Wu, and S. T. Wu. A method to estimate the Leslie coefficients of liquid crystals based on MBBA data. *Liq. Crys.*, 33(1):91–98, January 2006.

[116] S. T. Wu and C. S. Wu. Experimental confirmation of the Osipov-Terentjev theory on the viscosity of nematic liquid crystals. *Phys. Rev. A*, 42:2219–2227, Aug 1990.

[117] F. H. Yu and H. S. Kwok. Comparison of extended Jones Matrices for twisted nematic liquid-crystal displays at oblique angles of incidence. *J. Opt. Soc. Am. A*, 16(11):2772–2780, Nov 1999.

[118] V. I. Zadorozhnii, A. N. Vasilev, V. Y. Reshetnyak, K. S. Thomas, and T. J. Sluckin. Nematic director response in ferronematic cells. *EPL*, 73(3):408–414, 2006.

[119] H. Zocher. The effect of a magnetic field on the nematic state. *Trans. Faraday Soc.*, 29:945–957, 1933.